NICKEL EXSOLUTION EFFECT ON THE CATALYTIC BEHAVIOR OF RUDDLESDEN-POPPER MANGANITES IN SOFC CONDITIONS USING COLOMBIAN NATURAL GAS

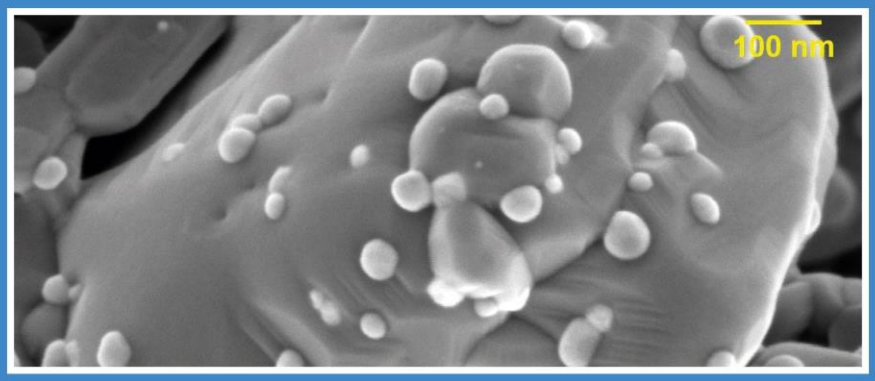

Thesis submitted by

Juan Sebastián Vecino Mantilla

to apply for the degree of Doctor

Supervisors

Prof. María Paola Maradei García

Prof. Gilles Henri Gauthier

Prof. José Manuel Serra Alfaro

Valencia
July
2020

UNIVERSIDAD INDUSTRIAL DE SANTANDER
GRUPO DE INVESTIGACIÓN INTERFASE
UNIVERSITAT POLITÈCNICA DE VALÈNCIA
INSTITUTO DE TECNOLOGÍA QUÍMICA

NICKEL EXSOLUTION EFFECT ON THE CATALYTIC BEHAVIOR OF RUDDLESDEN-POPPER MANGANITES IN SOFC CONDITIONS USING COLOMBIAN NATURAL GAS

DOCTORAL THESIS

Submitted by

JUAN SEBASTIÁN VECINO MANTILLA

Supervisors

Ph.D. Maria Paola Maradei García

Ph.D. Gilles Henri Gauthier

Ph.D. José Manuel Serra Alfaro

Valencia
Spain
July
2020

"Footsteps approaching the door or only the heartbeat in his ears?"

The shining, Stephen King, 1977

To God

To Héctor, Gloria, Camilo, Silvia, Margarita y Lucía

To my family

To my friends

To those who are no longer here…

Dedicado a ustedes, dedicat a vostès, dédié à vous, dedicated to you

Acknowledgment

Han sido largos años de continuo trabajo, de altos y bajos, de alegrías y tristezas, de logros y fracasos y a su vez han sido muchas personas las que ayudaron a que este camino, que yo mismo decidí empezar, haya sido más llevadero.

Agradezco a Dios por la vida, la salud y todas las cosas buenas y no tan buenas que a lo largo de estos 29 años ha dispuesto para mí, para hacerme grande, llegar lejos y triunfar, sé que soy su hijo bobo, no me desampare nunca. Lo quiero mucho.

A mi papi y a mi mami, Héctor y Gloria, ejemplo de amor, esfuerzo y éxito para mí, mis hermanos, mi familia y la sociedad, por ustedes estoy donde estoy, su apoyo, sus palabras, sus regaños me han hecho la persona que soy, quizás no he sido el mejor hijo, pero siempre he dado lo mejor de mí. Los quiero mucho.

Al Calvo, Silva, Marga y la Chuca gracias por hacer parte de mi mundo, los mejores momentos de mi vida los he pasado junto a ustedes, las peleas, la molestadera, las risas, su apoyo y su cariño no tienen comparación, la vida les tiene muchas cosas buenas guardadas, espero estar ahí para celebrarlas a su lado. Los quiero mucho.

A la familia Vecino y familia Mantilla, su apoyo en este largo proceso fue fundamental, no puedo ser más feliz al haber nacido siendo parte de estas dos grandes familias, son los mejores. Los quiero mucho.

A Julián, Liliana, Zulma y Liseth, mi mano, a ustedes muchas gracias por tantos y tantos años de loca amistad, para despejar la mente siempre es buena una reunión con ustedes, gracias por su apoyo y su buena energía, que sean muchos años más de locura. Los quiero mucho.

A mis chicas INTERFASE, Mónica (monaca), Silvia (…Durán Durán de Durán), Carolina (carola), Claudia (clauducky) cómo no decirles gracias por esas largas conversaciones, desorden, onces y esos momentos de desahogo interminable durante todo este tiempo, de no ser por ustedes, no sé dónde me habría llevado el estrés. Las quiero mucho.

A mis padres adoptivos, profe Gilles y profe María Paola (Maradei), por depositar en mí su confianza y darme la oportunidad de la realización de este proyecto, su sencillez y su ejemplo hacen parte del conocimiento adquirido durante estos años. Los quiero mucho.

A mi combo latino de doctoras colombianas en Valencia, Dalje, Cecilia, Karen, Lina, Carolina, y a todas las que en esa primera y segunda estancia conocí y que hicieron

mucho más amena mi estadía lejos de casa, no saben cuánto lo valoro; que los caminos de la vida nos vuelvan a reunir a todos en algún momento. Las quiero mucho.

A mis hijos de pregrado Iván, Santiago, Carolina, Margarita, Camilo y Erika muchas gracias por su apoyo y paciencia en la realización de este trabajo, este libro también es de ustedes chicos.

A mi alma mater la Universidad Industrial de Santander, la Escuela de Ingeniería Química y al grupo de investigación INTERFASE por transmitirme el conocimiento y permitirme las herramientas necesarias para el desarrollo de las actividades contempladas en esta tesis.

A los ya no tan nuevos miembros del grupo INTERFASE, Karol, Deyanira, Omar, Isacc y Raúl, por su compañía en la última etapa de este proyecto, espero que también lleven a feliz término cada uno de sus trabajos, hay que meterle ganas, ánimo.

Agraïments a la Universitat Politècnica de València i al grup d'investigació en energies renovables de l'ITQ, al professor José Manuel Serra Alfaro per acollir-me en el seu laboratori, a María B., Laura, Raquel, Sara, Fidel, David, Julio, Nuria, Sonia, Juan B., Juan E., Marwan, Mateusz els meus companyes de laboratori i en especial a María F. i Álvaro per tota la seua valuosa col·laboració, ajuda i paciència.

Al Departamento Administrativo de Ciencia, Tecnología e Innovación (COLCIENCIAS) por la beca de estudios de Doctorados Nacionales Conv. 647 y el proyecto # 110265842833 “Symmetrical high temperature Fuel Cell operating with Colombian natural gas”. Al Consejo Superior de Investigaciones Científicas por el apoyo con la ayuda económica para la estancia mediante la convocatoria I-coop Project # COOPA20112.

A los laboratorios de Difracción de Rayos X, Microscopía y de Ciencia de Superficies de la Universidad Industrial de Santander, por las caracterizaciones que se hicieron para este trabajo.

A Diana “Dianirris” Uribe (sí la de los podcasts), quien sin saberlo y durante largos días, noches y madrugadas hizo más amena la redacción de esta tesis doctoral, sus podcast, audios, grabaciones y entrevistas sobre la historia del mundo fueron mi gran compañía en esa última etapa. Q gran trabajo!!!.

…Y finalmente a todos los que hicieron parte de esta historia, sencillamente gracias.

Sebas

Table of contents

List of tables

List of figures

List of appendices

Summary Resumen
Resum

Summary

Several major problems have to be solved before Solid Oxide Fuel Cells (SOFC) can operate continuously using hydrocarbon fuels such as natural gas. The risk of low catalytic behavior for fuel reforming, the carbon formation/deposition on the anode material at high operating temperatures and the presence of impurities in the fuel (in particular sulfides) can dramatically reduce the performance and durability of the cells. Taking all this into account, new anode materials with adequate (electro)catalytic properties are required. Recently, manganite compounds with Ruddlesden-Popper (RP) structure have been studied as potential new anode materials in INTERFASE group at Universidad Industrial de Santander (UIS). Their electrochemical performance have been described in previous works with promising results, but a fundamental knowledge was missing concerning the catalytic properties of such materials and the way to improve them by the addition of nickel metallic particles on the electrode surface.

The current Ph.D. thesis was focused on the synthesis, characterization and catalytic study for steam reforming in SOFC anode conditions (low steam content) of a new RP manganite ($La_{1.5}Sr_{1.5}Mn_{1.5}Ni_{0.5}O_{7\pm\delta}$), which, in reducing atmosphere at high operating temperatures promotes via an exsolution mechanism the formation of two phases, *i.e.* an RP manganite of composition $LaSrMnO_{4\pm\delta}$ decorated with metallic active Ni nanoparticles embedded in the surface; such strategy can be viewed as an original way to improve the (electro)catalytic properties of the anode materials and then a promising option for future SOFC systems operating with Colombian natural gas.

The first chapter deals with the synthesis and characterization of the RP n= 2 phase $La_{1.5}Sr_{1.5}Mn_{1.5}Ni_{0.5}O_{7\pm\delta}$ using the Pechini method. In agreement with SOFC operating temperature, Ni exsolution has been studied in diluted H_2 at different temperatures (750, 800 and 850 °C) and reduction times. Ni nanoparticles decorating an RP n= 1 manganite is confirmed by XRD, TEM-EDS analysis and the size of the metallic particles on the oxide surface, below 100 nm, is characterized as a function of the exsolution conditions.

The second chapter presents the catalytic behavior for the methane steam reforming reaction of the exsolved material applying the Gradual Internal Reforming concept adapted to SOFC operation (*i.e.* low water content, steam to carbon ratio equal to 0.15) at different reaction temperatures (750, 800 and 850 °C). The catalytic properties of Ni impregnated samples using a similar $(La,Sr)_2MnO_{4\pm\delta}$ ceramic support are also presented for comparison. The exsolved material exhibits better performance than the impregnated manganite for the reaction, especially at 850 °C, with higher conversion, conversion rate, and H_2 production rate. Concerning the steam reforming of light alkane gas mixtures

(CH_4-C_2H_6, and CH_4-C_3H_8), the behavior is affected due to the competition between the molecules and low available metallic active sites, but without affecting the H_2 production. In addition, at long reaction times, the activity over the exsolved material is stable even with 100 h of reaction, without formation of carbonaceous species on the Ni particles, as confirmed by TEM and TGA/MS analysis.

In the third and last chapter, the possible coke formation and sulfide poisoning are presented. Despite the high and stable catalytic behavior for methane steam reforming reaction with considerable carbon formation resistance, the exsolved material exhibits a high level of sensitivity to H_2S poisoning, similar to the case of state-of-the-art Ni/YSZ anodic cermet and or Ni impregnated catalyst, with a drop of the activity to almost zero. Nevertheless, the exceptional overall results obtained for the exsolution-based material are promising for a possible use as SOFC anode operating with sulfur-free Colombian natural gas.

Resumen

Muchos son los problemas que deben resolverse antes de que las celdas de combustible de óxido sólido (SOFC por sus siglas en inglés) puedan operar continuamente usando combustibles hidrocarbonados como por ejemplo el gas natural. El riesgo de una baja actividad catalítica para el reformado del combustible, la formación y depósito en el material de ánodo a elevadas temperaturas de operación y la presencia de impurezas en el combustible empleado (en particular de sulfuros) pueden reducir dramáticamente el desempeño y la durabilidad de las celdas. Teniendo todo esto en cuenta, nuevos materiales de ánodo con adecuadas propiedades (electro)catalíticas son necesarios. Recientemente, en el grupo INTERFASE de la Universidad Industrial de Santander (UIS), compuestos de tipo manganita con estructura Ruddlesden-Popper (RP) han sido estudiados como potenciales materiales de ánodo. Su desempeño electrocatalítico ha sido descrito en trabajos previos con promisorios resultados, pero el conocimiento fundamental sobre las propiedades catalíticas de dichos materiales y la forma de mejorarlos mediante la adición de partículas metálicas de níquel en la superficie del electrodo aún faltaba.

La presente tesis doctoral se enfocó en la síntesis, caracterización y estudio catalítico en el reformado con vapor en condiciones de ánodo de celdas SOFC (bajo contenido de vapor) de una nueva manganita de tipo RP ($La_{1.5}Sr_{1.5}Mn_{1.5}Ni_{0.5}O_{7\pm\delta}$), la cual, en atmósfera reductora y a elevadas temperaturas de operación, promueven a través del mecanismo de exsolución la formación de dos fases: una manganita tipo RP de composición $LaSrMnO_{4\pm\delta}$ decorada con nanopartículas metálicas y activas de Ni incrustadas en la superficie; dicha estrategia puede ser vista como una manera muy original de mejorar las propiedades (electro)catalíticas de los materiales de ánodo y por lo tanto ser consideradas como una opción prometedora para sistemas SOFC operados con gas natural colombiano.

El primer capítulo trata sobre la síntesis de la fase RP n= 2 $La_{1.5}Sr_{1.5}Mn_{1.5}Ni_{0.5}O_{7\pm\delta}$ usando el método de Pechini y su caracterización. De acuerdo con la temperatura de operación de las celdas SOFC, la exsolución del Ni en atmósfera de H_2 diluido a diferentes temperaturas (750, 800 y 850 °C) y tiempos de reducción fue estudiada. Las nanopartículas de Ni decorando la manganita de estructura RP n= 1 es confirmada a través de análisis de DRX, MET-EDS y el tamaño de las partículas metálicas en la superficie del óxido, inferiores a 100 nm, es caracterizado en función de las condiciones de exsolución.

El segundo capítulo presenta el comportamiento catalítico del material exsuelto en la reacción de reformado de metano aplicando el concepto de reformado interno gradual (GIR por sus siglas en inglés) adaptado a celdas SOFC (en otras palabras, bajo contenido de agua, relación vapor carbono igual a 0.15) a diferentes temperaturas de reacción (750, 800 y 850 °C). Las propiedades catalíticas de las muestras impregnadas con Ni utilizando como soporte un material cerámico similar $(La,Sr)_2MnO_{4\pm\delta}$, son también presentados como comparación. El material exsuelto exhibe un mejor desempeño catalítico en la reacción de reformado que la manganita impregnada, especialmente a 850 °C, mostrando una más alta conversión, velocidad de conversión y de producción de H_2. Con respecto al reformado de la mezcla de alcanos ligeros (CH_4 -C_2H_6, y CH_4 -C_3H_8), el comportamiento catalítico es afectado debido a la competición entre moléculas y la baja disponibilidad de sitios activos metálicos, sin afectar la producción de H_2. Adicionalmente, a tiempos de reacción prolongados, la actividad en el material exsuelto es estable incluso con 100 h de reacción, sin formación de especies carbonáceas sobre las partículas de Ni como lo confirman las imágenes MET y el ATG/MS.

En el tercer y último capítulo, la posible formación y depósito de carbón y el envenenamiento con sulfuros son presentados. Sin embargo, a pesar de la elevada y estable actividad catalítica en la reacción de reformado de metano con vapor con una considerable resistencia a la formación de carbón, el material exsuelto tiene un alto nivel de sensibilidad al envenenamiento con H_2S, similar al Ni/YSZ (material de referencia de la literatura) o al material impregnado con Ni, con una disminución de la actividad catalítica a prácticamente cero No obstante, el excepcional resultado global obtenido en el material exsuelto es prometedor para un posible uso como material de ánodo en sistemas SOFC alimentados con gas natural colombiano libre de H_2S

Resum

Molts són els problemes que han de ser resolts abans que les cel·les de combustible d'òxid sòlid (SOFC per les seues sigles en anglès) puguen operar contínuament usant combustibles hidrocarbonats com per exemple el gas natural. El risc d'una baixa activitat catalítica per al reformat del combustible, la formació i depòsit en el material d'ànode a elevades temperatures d'operació i la presència d'impureses en el combustible emprat (en particular de sulfurs) poden reduir dramàticament l'acompliment i la durabilitat de les cel·les. Tenint tot això en compte, nous materials d'ànode amb propietats (electro)catalítiques adequades són necessaris. Recentment, en el grup d'investigació INTERFASE de la Universitat Industrial de Santander (UIS), compostos de tipus manganita amb estructura Ruddlesden-Popper (RP) han sigut estudiats com a potencials materials anòdics. El seu acompliment electroquímiques ha sigut tractades en treballs previs amb resultats promissoris, però el coneixement fonamental sobre les característiques catalítiques d'aquests materials i la manera de millorar-los mitjançant l'addició de partícules metàl·liques de níquel en la superfície de l'elèctrode encara faltava.

La present tesi de doctorat es va enfocar en la síntesi, caracterització i estudi d'activitat catalítica en el reformat amb vapor en condicions d'ànode de cel·les SOFC (sota contingut de vapor) d'una nova manganita de d'estructura RP ($La_{1.5}Sr_{1.5}Mn_{1.5}Ni_{0.5}O_{7\pm\delta}$), la qual, en atmosfera reductora i a elevades temperatures d'operació, promouen, a través del mecanisme de exsolució; la formació de dues fases: una manganita de composició $LaSrMnO_{4\pm\delta}$ decorada amb nanopartícules metàl·liques i actives de Ni incrustades en la superfície; aquesta estratègia pot ser vista com una manera molt original de millorar les propietats (electro)catalítiques dels materials d'ànode i per tant, ser considerades com una prometedora opció per a futurs usos en sistemes SOFC alimentats amb gas natural colombià.

El primer capítol tracta sobre la síntesi de la fase RP n= 2 $La_{1.5}Sr_{1.5}Mn_{1.5}Ni_{0.5}O_{7\pm\delta}$ usant el mètode de Pechini i la seua caracterització. D'acord amb la temperatura d'operació de les cel·les SOFC, la exsolució del Ni en atmosfera d'H_2 diluït a diferents temperatures (750, 800 i 850 °C) i temps de reducció va ser estudiada. Les nanopartícules de Ni decorant la manganita d'estructura RP n= 1 és confirmada a través d'anàlisi de DRX, MET-EDS i la grandària de les partícules metàl·liques en la superfície de l'òxid, inferiors a 100 nm, és caracteritzat en funció de les condicions de exsolució.

El segon capítol presenta el comportament catalític del material d'exsolució en la reacció de reformat de metà amb vapor aplicant el concepte de reformat gradual intern (GIR per

les seues sigles en anglès) adaptat a cel·les SOFC (en altres paraules, sota contingut de vapor, relació vapor-carboni de 0.15) a diferents temperatures de reacció (750, 800 i 850 °C). Les propietats catalítiques de les mostres impregnades amb Ni utilitzant com a suport un material ceràmic similar $(La,Sr)_2MnO_{4\pm\delta}$, són també presentats com a comparació. El material d'exsolució exhibeix un millor resultat catalític en la reacció de reformat que la manganita impregnada, especialment a 850 °C, mostrant una més alta conversió, velocitat de conversió i de producció d'H_2. En el reformat de la mescla d'alcans lleugers (CH_4 -C_2H_6, i CH_4 -C_3H_8), el comportament catalític és afectat per la competició entre molècules i la baixa disponibilitat de llocs actius metàl·lics, sense afectar la producció d'H_2. Addicionalment, a temps de reacció llargs, l'activitat en el material d'exsolució és estable fins i tot després de 100 h de reacció, sense formació d'espècies carbòniques sobre les partícules de Ni, com ho confirmen les imatges MET i el ATG/MS.

En el tercer i últim capítol, la possible formació i depòsit de carbó i l'enverinament amb sulfurs són presentats. No obstant això, malgrat l'elevada i estable activitat catalítica en la reacció de reformat de metà amb vapor amb una considerable resistència a la formació de carbó, el material d'exsolució té un alt nivell de sensibilitat a l'enverinament amb H_2S, similar al Ni/YSZ (material de referència de la literatura) o el material impregnat amb Ni, amb una disminució de l'activitat catalítica a pràcticament zero No obstant això, l'excepcional resultat global obtingut aquest nou material és prometedor per a un possible ús futur com a material d'ànode en sistemes SOFC alimentats amb gas natural colombià lliure d'H_2S.

Introduction

1. Introduction

Considering the current environmental problems and the energetic context, technological development and many research works performed during the 20th century and part of the 21st have been focused on energetic alternatives and efficient energy conversion devices. Fuel cells (FC) are the product of this research development and one of the most important technologies proposed for future H_2 economy, considered as a promising alternative that will allow the change of the current energy system. FC are open thermodynamic systems, with a high-power efficiency (40 - 85 %) compared with conventional distributed energy systems such as diesel engines, wind turbines, photovoltaic panels and turbine generators [1].

These electrochemical energetic conversion devices have four main components: two electrodes (anode and cathode), the electrolyte and the external circuit. According to the type of electrolyte, it has been defined 6 major groups: Alkaline Fuel Cell (AFC), Phosphoric Acid Fuel Cell (PAFC), Direct Methanol Fuel Cell (DMFC), Molten Carbonate Fuel Cell (MCFC), Proton Exchange Membrane Fuel Cell (PEMFC) and Solid Oxide Fuel Cell (SOFC) [1–3]. Among all this variety, the SOFC is currently the most promising and interesting fuel cell system due to the low emission of pollutant gas, resistance to high operating conditions, high electrochemical reaction rate, high efficiency, fuel flexibility and the potential application in electricity power plants, heat and electricity domestic units and trucks [4–9].

The Solid Oxide Fuel Cells (SOFC, Figure 1) are ceramic-based energetic conversion devices that transform the chemical energy from a particular fuel and oxidant gas directly into electricity and heat through electrochemical reactions without combustion or intermediate steps. These devices operate at high temperatures (600 – 1000°C) and utilize a solid dense ceramic as electrolyte *e.g.* yttria-stabilized zirconia – YSZ ($(ZrO_2)_{0.92}(Y_2O_3)_{0.08}$) or gadolinia-doped ceria – CGO ($Ce_{0.9}Gd_{0.1}O_{1.95}$) [4,10,11].

The electrolyte is located in the middle of the two electrodes, the anode and the cathode, interconnected by the external circuit. These electrochemical systems operate using oxygen (O_2) from the air on the cathode side. The O_2 is reduced in this electrode (Equation 1) and the anions (O^{2-}) that are produced diffuse selectively through the electrolyte to the anode side and react with the fuel *e.g.* H_2 (Equation 2), producing H_2O, heat and electrons (e^-). The e^- will flow via the external circuit, producing the electricity and starting the cycle again [12,13].

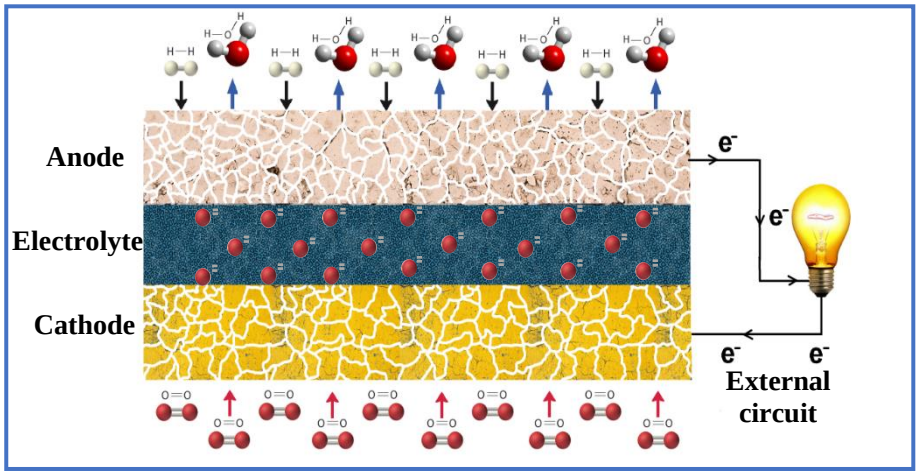

Figure 0.1 Solid oxide fuel cell (SOFC) scheme. Modified from [1]

$$O_2(g)+4e^- \longrightarrow 2O^{2-} \qquad \textbf{Equation 1}$$

$$2H_2(g)+2O^{2-} \longrightarrow 2H_2O(v)+4e^- \qquad \textbf{Equation 2}$$

The H_2 fed on the anode side is produced by electrolysis of water [14] or reforming of hydrocarbon fuels (natural gas, alcohols, glycerol, etc) in external units [15]. However, the H_2 can be also produced *in situ* when the electrode (anode) acts simultaneously as a catalyst for the reforming reactions, omitting intermediate steps and then, reducing the operating costs [16]. Therefore, the anode material must satisfy a number of requirements to operate efficiently in the fuel cell, including: redox stability, physical and chemical compatibility with the others cell components, high ionic and electronic conductivity, low cost, stability at high temperatures and (electro)catalytic activity for fuel oxidation, including the catalytic reforming of hydrocarbon fuels and then the resistance to carbon formation/deposition and sulfur poisoning [17–20].

In conclusion, the identification of a material that meets all these characteristics is a big challenge. The cermets form an important family of composites employed in SOFC anode. They are porous materials constituted by a mixture of at least one ceramic (ionic conductor) and one metal (electronic conductor); Ni/YSZ is the most commonly used material for such anode application because it satisfies many of the requirements described above [21–23]. However, in spite of its many advantages, Ni/YSZ still exhibits

some issues, such as redox instability, carbon formation in deficient steam/carbon ratio and sensibility to sulfur poisoning when using hydrocarbon fuels [24,25], which must be solved before this kind of cells can operate continuously using hydrocarbon fuels *e.g.* natural gas.

Additional studies have been carried out to find new materials that can satisfy the anode material requirements in SOFC systems and among the most promising alternative materials are the Mixed Ionic and Electronic Conductors (MIEC), most of them exhibit the perovskite structure (ABO_3, where *A* represents an alkali, alkaline earth, or rare-earth metal cation, *B* refers to transition metal cations occupying the anionic octahedral coordination and *O* the oxygen) [21,26,27], *e.g.* $La_{1-x}Sr_xCrO_{3\pm\delta}$ or $La_xSr_{1-x}TiO_{3\pm\delta}$ [10]. In MIEC materials, the active zone for the electrocatalytic reaction is extended over the entire electrode material (or at least in the volume of the electrode in contact with the electrolyte) improving the reaction efficiency; it is not limited to specific points (triple phase boundary or TPB, *i.e.* the contact points between the ion conductor (ceramic), the electron conductor (metal) and gaseous phase) as in the case of cermet materials (Figure 2) [4,21,28].

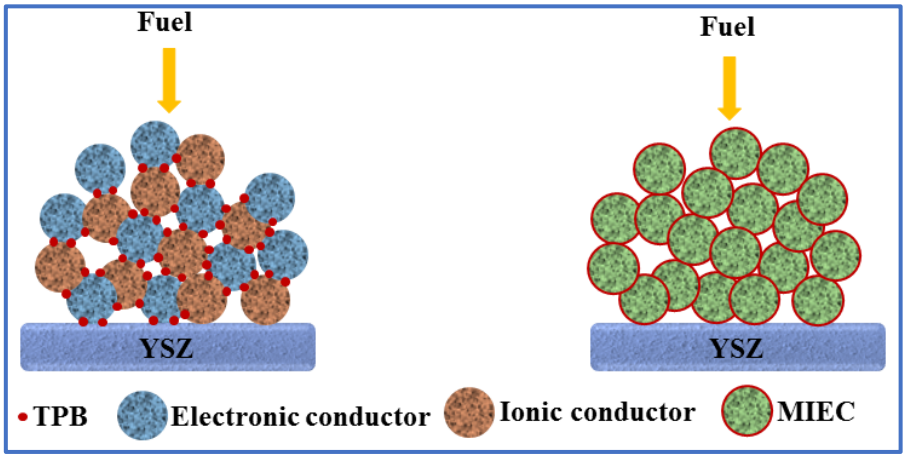

Figure 2 Comparison between a cermet and a MIEC anode material. Modified from [26]

Apart from the perovskite mixed oxides, the Ruddlesden-Popper (RP) phases have also demonstrated a MIEC behavior, with desirable results in terms of thermomechanical stability, redox cycles, ionic and electronic conductivity, structural properties, in several concerns better than their parent perovskites, they are considered as an interesting option

in a variety of catalytic and electrocatalytic processes like those occurring at both electrodes of a SOFC (symmetrical cells) [29–37].

RP phases are materials whose structure results from the intergrowth of one or several perovskite-type blocks (ABO_3) separated by one rock-salt structure layer (AO). Their general formula is $A_{n+1}B_nO_{3n+1}$ or $(AO)(ABO_3)_n$, where n is the number of octahedra's layers in the perovskite block [38] (Figure 3). For n= 1, the K_2NiF_4-type structure can exhibit a large amount of interstitial oxygen anions into the rock-salt block (case of nickelates) or vacancy diffusion mechanism (case of lanthanum strontium cuprates) in the perovskites layers favoring the ionic diffusivity [39–41]; in this case, their main use is as cathode materials. Their possible use as anode material has been only recently described [42,43]. Then, the manganite series of composition (La,Sr)MnO_4 has been proposed as particularly promising, for which several compositions have demonstrated a possible use as both anode and cathode material in symmetrical SOFC, due to and the resulting manganite family could be a feasible option. Several compositions have shown an exceptional potential as electrode (both anode and cathode) in symmetrical SOFC, due to their stability in oxidizing and reducing atmospheres, thermo-mechanical and chemical compatibility with common electrolytes *e.g.* CGO, and acceptable electrochemical properties, high-temperature resistance, redox stability and favorable total conductivity [44–47]. Notwithstanding, some authors suggest that some compositions, *e.g.* $La_{0.6}Sr_{1.4}MnO_4$, are poor catalysts for direct use of hydrocarbon (HC) fuels like methane [48]. Therefore, find a way to improve the catalytic properties of RP manganites for SOFC anodes operating with HC fuels is mandatory.

To enhance the catalytic behavior of such mixed oxides, the addition of some catalytic active metal nanoparticles (Ni, Ru, Rh, Co, Fe, Cu, Pd, Pt, others) on the MIEC surface is commonly employed and the vast majority of supported particles are prepared by impregnation technique due to the relative simple procedure (Figure 4) [49–54]. Nevertheless, as confirmed by different authors [55–58], a homogeneous particles distribution on the support is sometimes problematic, as well as limitations in the particle size and the imminent cell degradation and deactivation caused by the coalescence and agglomeration of the metallic particles due to the weak interaction with the oxide support and the carbon formation/deposition on the metallic surface.

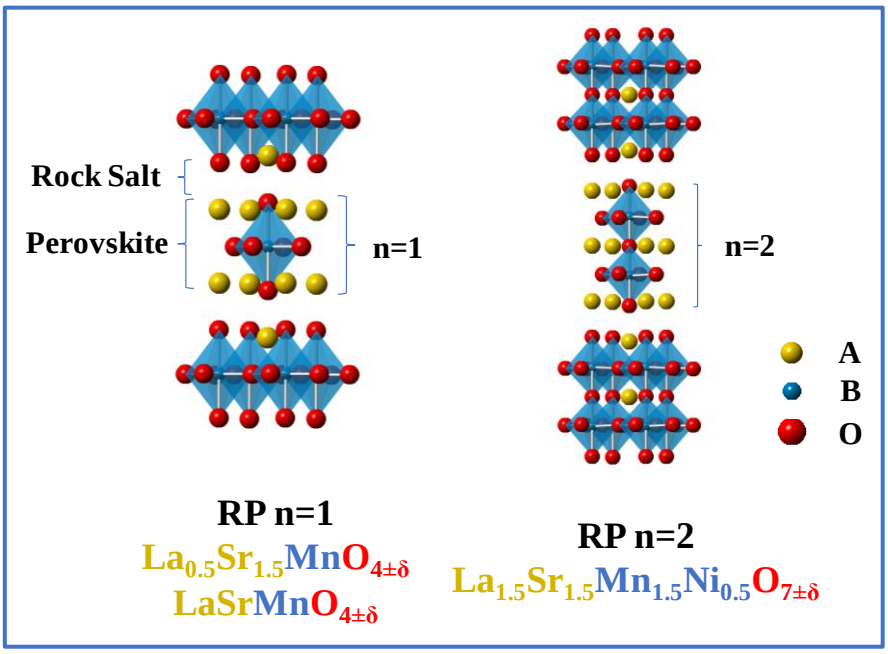

Figure 3 Ruddlesden-Popper structure. Modified from [38].

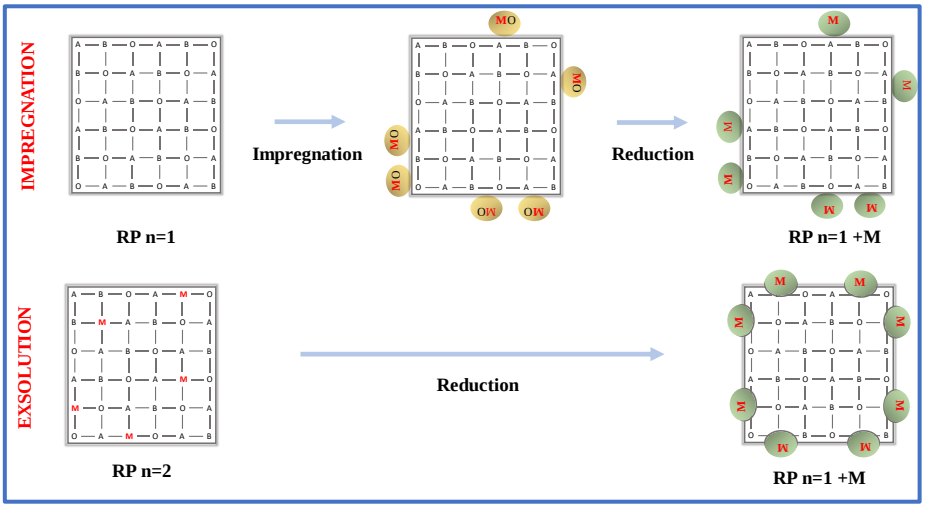

Figure 4 Impregnation vs exsolution. Modified from [54].

To overcome these issues, an alternative method to create heterogeneous surface systems with a more-uniformly distributed metal nano-socketed particles has been developed: exsolution or *in situ* growth of metal nanoparticles (Figure 4). In the exsolution methodology active elements (transition metals [59,60] or precious metals [61,62]) are dissolved in their oxidized form within the electrode material phase during the synthesis step; then, in a single reduction step at high temperature (driven force), the solid state precipitation of metal nanoparticles is induced from the bulk to the oxide surface. Those particles provide active sites with larger specific surface area able to considerably promote metal catalyzed reactions like steam reforming. According to several authors, such catalytic system seems to provide desirable thermal stability, an anti-coking behavior and mitigate the problem of particle agglomeration due to the strong interaction between the metallic particles and the mixed oxide support, which limit their mobility (the nanoparticles are socketed or embedded on the surface) [54,58,63–66]. Finally, if necessary, the regeneration of the nanostructure has been described as theoretically and practically possible using adequate redox cycles [67,68]. Therefore, compared to impregnation methods, the exsolution shows a better cost and time efficiency.

As described above, the exsolution process is a chemically driven heterogeneous phase transformation and, therefore, results from four main sequential steps: diffusion, reduction, nucleation and particle growth (Figure 5) [69]. It has been demonstrated that the driving force for the exsolution from an $A(B_{1-x}M_x)O_3$ perovskite (or perovskite-layer in the case of Ruddlesden-Popper structure) is the change in the Gibbs free energy (ΔG) from M^{n+} to M^0 in an easily reducible oxide (*e.g.* NiO), meanwhile the elements A and B need to remain oxidized during the reduction to retain the stability of the structure (*e.g.* metal oxides of La, Sr, Sc and Mn). Then, the M^{n+} ions diffuse from the bulk to the surface (mass transport) where the segregation energy is lower and where they are exposed to the reducing gas; the reduction step can thus occurs and the particle nucleation starts, which is affected by the surface defects or roughness of the material, dislocations, oxygen vacancies (intrinsic factors) or the reduction time, temperature and even the concentration of the reducing gas (extrinsic factors). Once the nucleation has begun, the particle growth take place in different regions of the surface and the final particle size will be determined by the amount of M^{n+} in the solid solution, the diffusion rate from the bulk to the surface, the reduction time and the particle-support interactions [69].

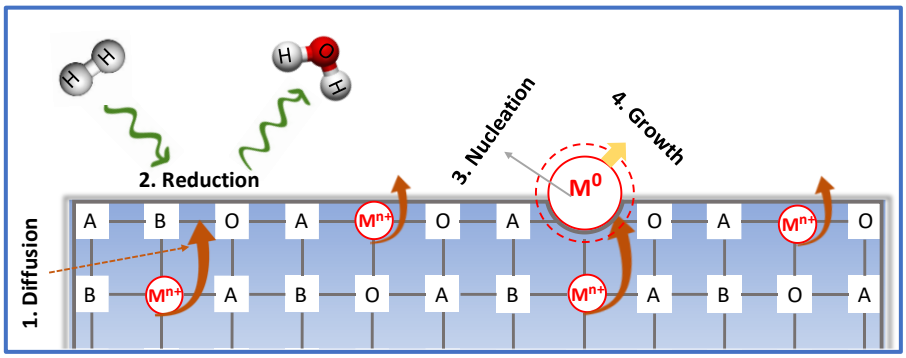

Figure 5 Schema of exsolution process. Modified from [69].

Historically, the preparation of such sophisticated structural systems was developed in the field of catalysis as an alternative way to avoid carbon formation or sintering problems, looking for a homogeneous distribution of metallic active particles on the catalyst surface to be employed in commercial reactions such as partial oxidation of methane to obtain syngas [70]. In this way, and considering the application, the only interest was to get the active phase without particular regard to the structure of the resulting support (except its chemical properties, such as basicity). In this regard, catalysts with perovskite-type (ABO_3) compositions or perovskite-layered compounds *e.g.* Ruddlesden-Popper phases were considered, due to its easy synthesis. Shiozaki *et al.* [70] reported the solid phase crystallization (exsolution) of Ni using $BaTi_{1-x}Ni_xO_3$ compounds with the formation of additional phases for the oxidation of methane reaction, while Hayakawa *et al.* [71] suggest the exsolution of Co from the bulk of $Ca_{0.8}Sr_{0.2}Ti_{0.8}Co_{0.2}O_3$ for the same application. On the other hand, Batiot-Dupeyrat *et al.* [72] proposed the complete material decomposition (and framework destruction) of the RP n= 1 La_2NiO_4 through its reduction at high temperature as a way to obtain La_2O_3 support decorated with Ni nanoparticles to be employed as catalyst for methane dry reforming (Figure 6 step 1).

More recently, and this time for the application as SOFC anode, the literature reports the use of exsolution of a B-site metallic cation from a perovskite system in which A/B ratio is 1, but trying to keep, in this case, a support in the form of perovskite phase (for electrical conduction and possibly electrocatalytic properties of the support itself), with the restriction that such B cation should be easily reducible (Ni^{2+}, Ru^{4+}, Pd^{4+}, others) [59,68,73–76]. It is worth noting that, in this case, the process is necessarily limited to a few elements and low content of exsolved B-type metallic nanoparticles in order to avoid the perovskite decomposition and the segregation of AO_x oxide, as recently reported for Ni in $(La,Sr)(Ti,Ni)O_3$ materials [77]. Indeed, in the case of SOFC anode, the formation

of additional phases with low/null ionic and electronic conductivity would be problematic as blocking electrons/ions, *i.e.* the electrocatalytic process of fuel oxidation. This case is depicted in Figure 6, step 2 in which the AO_x phase can remain in the form of defects within the perovskite structure until it precipitates as nanodomains for higher exsolution rate.

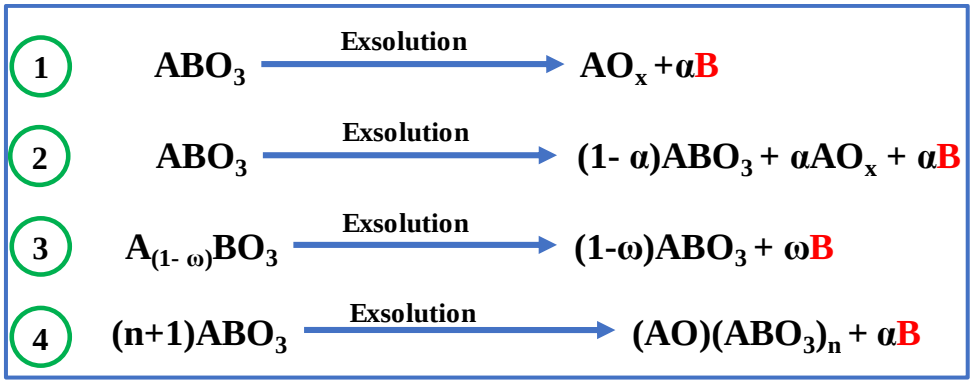

Figure 6 Exsolution in cation stoichiometric perovskites compared to A-site deficiency perovskites. Adapted from [78].

To avoid the latter issue, and broaden the range of possible materials able to exsolve a reducible cation two recent strategies has been designed, opening possibilities to work with hardly reducible B cations and obtain a more stable resulting support:

- The first one (step 3 in Figure 6) is to used compositions with a cation deficiency at the A-site (A/B< 1), which is relatively possible for perovskites. In this way, the A-site deficiency together with the cation reducibility will act as the driving force to propitiate the exsolution as a way to stabilize a defect-free ABO_3 perovskite phase [69,78] (*e.g.* Ni exsolution from $La_{0.6}Sr_{0.3}Cr_{0.85}Ni_{0.15}O_3$).

- Finally, a very recent concept, in which this work can be classified, report the use of compositions, which have the possibility to be transformed from on structure (*e.g.* perovskite) to a different one with interesting electrical or electrocatalytical properties, *e.g.* a Ruddlesden-Popper-type phase. For example, Chung *et al.* proposed the use of Fe exsolution from the perovskite $La_{0.6}Sr_{0.4}Mn_{0.2}Fe_{0.8}O_3$ to finally obtain a composite of Fe nanaoparticles over $La1.2Sr_{0.8}Mn_{0.4}Fe_{0.6}O_4$ (RP n= 1) oxide [58]; this type of mechanism is a

particularity interesting option to design electrode materials for symmetric cells (Figure 6, step 4 but not limited to a perovskite into RP phase).

Considering the aforementioned literature and the opportunity to develop a performant material for fuel cells and catalytic applications, the INTERFASE research group from Universidad Industrial de Santander decided to embark with this thesis on the complete study of a new compound, $La_{1.5}Sr_{1.5}Mn_{1.5}Ni_{0.5}O_{7\pm\delta}$, designed to transform via a mechanism of exsolution to a material that would exhibit not only catalytic properties for the steam reforming of natural gas but also electrocatalytic activity for the oxidation of hydrogen resulting from the fuel reforming.

2. Outline

The current Ph.D. thesis deals with the synthesis, characterization and catalytic study of a new Ruddlesden-Popper (RP) manganite ($La_{1.5}Sr_{1.5}Mn_{1.5}Ni_{0.5}O_{7\pm\delta}$), which, in reducing atmosphere and at high operating temperatures would result in the formation of two phases that correspond to the RP manganite $LaSrMnO_{4\pm\delta}$ decorated with metallic active Ni nanoparticles embedded in the surface, a promising option for future use as the anode in a SOFC fed with Colombian natural gas.

Chapter 1 describes the preparation of the new RP material, $La_{1.5}Sr_{1.5}Mn_{1.5}Ni_{0.5}O_{7\pm\delta}$, which has been designed using a retrosynthetic approach similar to organic chemistry in order to be able to form, in reducing conditions, a biphasic material made of electrocatalytic active metallic nanoparticles on a n= 1 RP manganite of the type $La_xSr_{2-x}MnO_{4\pm\delta}$. It is worth noting that the latter manganite series has been previously studied in the group (and in literature) for hydrogen oxidation. The synthesis, proof of exsolution and its catalytic behavior for the methane steam reforming reaction using Colombian natural gas composition in low water content are presented. It is worth to notice that this chapter was published recently in ChemCatChem Journal [79].

Chapter 2 concerns the study of catalytic behavior for the Steam Reforming reaction using Colombian natural gas composition (methane, ethane, and propane) with low water content, comparing the behavior of the exsolved material ($La_{1.5}Sr_{1.5}Mn_{1.5}Ni_{0.5}O_{7\pm\delta}$ reduced at a high operating temperature) to the conventional Ni impregnated manganite of the same RP structure. Recently, this chapter was submitted in ChemCatChem journal in a special collection of the French Conference of Catalysis (FCCat).

Chapter 3 provides continuity to the previous chapters, dealing with an in-depth study of the catalyst resistance to carbon formation/deposition as well as to H_2S poisoning, the two main issues of an anode material operating with realistic fuels. The study has been performed for a long period of time considering the Methane Steam Reforming reaction in water-deficient conditions. A comparison is made with the conventional Ni impregnated material and the state-of-the art SOFC anode, the Ni/YSZ cermet. The results obtained in this chapter will be submitted in the Journal of Hydrogen Energy.

3. References

[1] S. Mekhilef, R. Saidur, A. Safari, Comparative study of different fuel cell technologies, Renew. Sustain. Energy Rev. 16 (2012) 981–989. doi:10.1016/j.rser.2011.09.020.

[2] A. Kirubakaran, S. Jain, R.K. Nema, A review on fuel cell technologies and power electronic interface, Renew. Sustain. Energy Rev. 13 (2009) 2430–2440. doi:10.1016/j.rser.2009.04.004.

[3] S. Hardman, A. Chandan, R. Steinberger-Wilckens, Fuel cell added value for early market applications, J. Power Sources. 287 (2015) 297–306. doi:10.1016/j.jpowsour.2015.04.056.

[4] B. Shri Prakash, S. Senthil Kumar, S.T. Aruna, Properties and development of Ni/YSZ as an anode material in solid oxide fuel cell: A review, Renew. Sustain. Energy Rev. 36 (2014) 149–179. doi:10.1016/j.rser.2014.04.043.

[5] Y.D. Lee, K.Y. Ahn, T. Morosuk, G. Tsatsaronis, Environmental impact assessment of a solid-oxide fuel-cell-based combined-heat-and-power-generation system, Energy. 79 (2015) 455–466. doi:10.1016/j.energy.2014.11.035.

[6] C. Sun, U. Stimming, Recent anode advances in solid oxide fuel cells, J. Power Sources. 171 (2007) 247–260. doi:10.1016/j.jpowsour.2007.06.086.

[7] M. Andersson, H. Paradis, J. Yuan, B. Sundén, Review of catalyst materials and catalytic steam reforming reaction in SOFC anodes, Int. J. Energy Res. 35 (2011) 1340–1350. doi:10.1002/er.

[8] H. Paradis, M. Andersson, J. Yuan, B. Sundén, Simulation of alternative fuels for potential utilization in solid oxide fuel cells, Int. J. Energy Res. 35 (1011) 1107–1117. doi:10.1002/er.

[9] O. Yamamoto, Solid oxide fuel cells: Fundamental aspects and prospects, Electrochim. Acta. 45 (2000) 2423–2435. doi:10.1016/S0013-4686(00)00330-3.

[10] S.P.S. Shaikh, A. Muchtar, M.R. Somalu, A review on the selection of anode

materials for solid-oxide fuel cells, Renew. Sustain. Energy Rev. 51 (2015) 1–8. doi:10.1016/j.rser.2015.05.069.

[11] J.W. Fergus, Electrolytes for solid oxide fuel cells, J. Power Sources. 162 (2006) 30–40. doi:10.1016/j.jpowsour.2006.06.062.

[12] A.B. Stambouli, E. Traversa, Solid oxide fuel cells (SOFCs): A review of an environmentally clean and efficient source of energy, Renew. Sustain. Energy Rev. 6 (2002) 433–455. doi:10.1016/S1364-0321(02)00014-X.

[13] N. Mahato, A. Banerjee, A. Gupta, S. Omar, K. Balani, Progress in Materials Science Progress in material selection for solid oxide fuel cell technology : A review, Prog. Mater. Sci. 72 (2015) 141–337. doi:10.1016/j.pmatsci.2015.01.001.

[14] C. Lamy, From hydrogen production by water electrolysis to its utilization in a PEM fuel cell or in a SO fuel cell: Some considerations on the energy efficiencies, Int. J. Hydrogen Energy. 41 (2016) 15415–15425. doi:10.1016/j.ijhydene.2016.04.173.

[15] A.L. Dicks, Advances in catalysts for internal reforming in high temperature fuel cells, J. Power Sources. 71 (1998) 111–122. doi:10.1016/S0378-7753(97)02753-5.

[16] K. Girona, J. Laurencin, J. Fouletier, F. Lefebvre-Joud, Carbon deposition in CH4/CO2 operated SOFC: Simulation and experimentation studies, J. Power Sources. 210 (2012) 381–391. doi:10.1016/j.jpowsour.2011.12.005.

[17] H. Ghezel-Ayagh, B. Borglum, Review of Progress in Solid Oxide Fuel Cells at FuelCell Energy, ECS Trans. 78 (2017) 77–86. doi:10.1149/07801.0077ecst.

[18] B.H. Park, G.M. Choi, Ex-solution of Ni nanoparticles in a $La_{0.2}Sr_{0.8}Ti_{1-x}Ni_xO_{3-\delta}$ alternative anode for solid oxide fuel cell, Solid State Ionics. 262 (2014) 345–348. doi:10.1016/j.ssi.2013.10.016.

[19] L.S. Mahmud, A. Muchtar, M.R. Somalu, Review on anode material development in solid oxide fuel cells, AIP Conf. Proc. 1660 (2015) 6–11. doi:10.1063/1.4915812.

[20] M. Mukhopadhyay, J. Mukhopadhyay, R.N. Basu, Functional Anode Materials for Solid Oxide Fuel Cell - A Review, Trans. Indian Ceram. Soc. 72 (2013) 145–168. doi:10.1080/0371750X.2013.851625.

[21] A. Atkinson, S. Barnett, R.J. Gorte, J.T.S. Irvine, A.J. McEvoy, M. Mogensen, et al., Advanced anodes for high-temperature fuel cells., Nat. Mater. 3 (2004) 17–27. doi:10.1038/nmat1040.

[22] S.K. Pratihar, A. Dassharma, H.S. Maiti, Processing microstructure property correlation of porous Ni-YSZ cermets anode for SOFC application, Mater. Res. Bull. 40 (2005) 1936–1944. doi:10.1016/j.materresbull.2005.06.002.

[23] D. Sarantaridis, A. Atkinson, Redox cycling of Ni-based solid oxide fuel cell anodes: A review, Fuel Cells. 7 (2007) 246–258. doi:10.1002/fuce.200600028.

[24] M. Kogler, E.M. Köck, M. Stöger-Pollach, S. Schwarz, T. Schachinger, B. Klötzer, et al., Distinct carbon growth mechanisms on the components of Ni/YSZ materials,

Mater. Chem. Phys. 173 (2016) 508–515. doi:10.1016/j.matchemphys.2016.02.046.

[25] H. Chen, F. Wang, W. Wang, D. Chen, S.D. Li, Z. Shao, H_2S poisoning effect and ways to improve sulfur tolerance of nickel cermet anodes operating on carbonaceous fuels, Appl. Energy. 179 (2016) 765–777. doi:10.1016/j.apenergy.2016.07.028.

[26] R.N. Basu, Materials for solid oxide fuel cells, in: S. Basu (Ed.), Recent Trends Fuel Cell Sci. Technol., 1st ed., Springer-Verlag New York, New Delhi, India, 2007: pp. 286–331. doi:10.1007/978-0-387-68815-2.

[27] S.P.S. Badwal, S. Giddey, C. Munnings, A. Kulkarni, Review of progress in high temperature solid oxide fuel cells, J. Aust. Ceram. Soc. 50 (2014) 23–37.

[28] S.W. Tao, P.I. Cowin, R. Lan, Novel anode materials for solid oxide fuel cells, Woodhead Publishing Limited, 2012. doi:10.1533/9780857096371.3.445.

[29] S.J. Skinner, J.A. Kilner, Oxygen diffusion and surface exchange in $La_{2-x}Sr_xNiO_{4+\delta}$, Solid State Ionics. 135 (2000) 709–712. doi:10.1016/S0167-2738(00)00388-X.

[30] H.W. Nie, T.L. Wen, S.R. Wang, Y.S. Wang, U. Guth, V. Vashook, Preparation, thermal expansion, chemical compatibility, electrical conductivity and polarization of $A_{2-\alpha}A'_{\alpha}MO_4$ (A = Pr, Sm; A′ = Sr; M = Mn, Ni; α = 0.3, 0.6) as a new cathode for SOFC, Solid State Ionics. 177 (2006) 1929–1932. doi:10.1016/j.ssi.2006.01.003.

[31] V. V. Kharton, A.A. Yaremchenko, A.L. Shaula, M. V. Patrakeev, E.N. Naumovich, D.I. Logvinovich, J.R. Frade, F.M.B. Marquez, Transport properties and stability of Ni-containing mixed conductors with perovskite- and K_2NiF_4-type structure, J. Solid State Chem. 177 (2004) 26–37. doi:10.1016/S0022-4596(03)00261-5.

[32] S.Y. Jeon, M.B. Choi, H.N. Im, J.H. Hwang, S.J. Song, Oxygen ionic conductivity of La 2NiO 4δ via interstitial oxygen defect, J. Phys. Chem. Solids. 73 (2012) 656–660. doi:10.1016/j.jpcs.2012.01.006.

[33] J. Dailly, S. Fourcade, A. Largeteau, F. Mauvy, J.C. Grenier, M. Marrony, Perovskite and A_2MO_4-type oxides as new cathode materials for protonic solid oxide fuel cells, Electrochim. Acta. 55 (2010) 5847–5853. doi:10.1016/j.electacta.2010.05.034.

[34] P. V. Balachandran, D. Puggioni, J.M. Rondinelli, Crystal-chemistry guidelines for noncentrosymmetric A_2BO_4 Ruddlesden-Popper oxides, Inorg. Chem. 53 (2014) 336–348. doi:10.1021/ic402283c.

[35] C. Autret, C. Martin, M. Hervieu, R. Retoux, B. Raveau, G. André, F. Bourée, Structural investigation of Ca_2MnO_4 by neutron powder diffraction and electron microscopy, J. Solid State Chem. 177 (2004) 2044–2052. doi:10.1016/j.jssc.2004.02.012.

[36] M. Al Daroukh, V. V. Vashook, H. Ullmann, F. Tietz, I. Arual Raj, Oxides of the AMO_3 and A_2MO_4-type: Structural stability, electrical conductivity and thermal expansion, Solid State Ionics. 158 (2003) 141–150. doi:10.1016/S0167-2738(02)00773-7.

[37] E. Lay, G. Gauthier, L. Dessemond, Preliminary studies of the new Ce-doped La/Sr chromo-manganite series as potential SOFC anode or SOEC cathode materials, Solid State Ionics. 189 (2011) 91–99. doi:10.1016/j.ssi.2011.02.004.

[38] A. Das, E. Xhafa, E. Nikolla, Electro- and thermal-catalysis by layered, first series Ruddlesden-Popper oxides, Catal. Today. 277 (2016) 214–226. doi:10.1016/j.cattod.2016.07.014.

[39] V. V. Vashook, I.I. Yushkevich, L. V. Kokhanovsky, L. V. Makhnach, S.P. Tolochko, I.F. Kononyuk, H. Ullmann, H. Altenburg, Composition and conductivity of some nickelates, Solid State Ionics. 119 (1999) 23–30. doi:10.1016/S0167-2738(98)00478-0.

[40] V. V. Kharton, A.P. Viskup, A. V. Kovalevsky, E.N. Naumovich, F.M.B. Marques, Ionic transport in oxygen-hyperstoichiometric phases with K_2NiF_4-type structure, Solid State Ionics. 143 (2001) 337–353. doi:10.1016/S0167-2738(01)00876-1.

[41] Y. Hu, Y. Bouffanais, L. Almar, A. Morata, A. Tarancon, G. Dezanneau, $La_{2-x}Sr_xCoO_{4-\delta}$ (x = 0.9, 1.0, 1.1) Ruddlesden-Popper-type layered cobaltites as cathode materials for IT-SOFC application, Int. J. Hydrogen Energy. 38 (2013) 3064–3072. doi:10.1016/j.ijhydene.2012.12.047.

[42] C. Jin, Z. Yang, H. Zheng, C. Yang, F. Chen, $La_{0.6}Sr_{1.4}MnO_4$ layered perovskite anode material for intermediate temperature solid oxide fuel cells, Electrochem. Commun. 14 (2012) 75–77. doi:10.1016/j.elecom.2011.11.008.

[43] S. Liping, H. Lihua, Z. Hui, L. Qiang, C. Pijolat, La substituted Sr_2MnO_4 as a possible cathode material in SOFC, J. Power Sources. 179 (2008) 96–100. doi:10.1016/j.jpowsour.2007.12.090.

[44] M. V. Sandoval, C. Pirovano, E. Capoen, R. Jooris, F. Porcher, P. Roussel, G.H. Gauthier, In-depth study of the Ruddlesden-Popper $La_xSr_{2-x}MnO_{4\pm\Delta}$ family as possible electrode materials for symmetrical SOFC, Int. J. Hydrogen Energy. 42 (2017) 21930–21943. doi:10.1016/j.ijhydene.2017.07.062.

[45] S. Li-Ping, L. Qiang, H. Li-Hua, Z. Hui, Z. Guo-Ying, L. Nan, J.P. Viricelle, C. Pijolat, Synthesis and performance of $Sr_{1.5}La_xMnO_4$ as cathode materials for intermediate temperature solid oxide fuel cell, J. Power Sources. 196 (2011) 5835–5839. doi:10.1016/j.jpowsour.2011.03.016.

[46] M. V. Sandoval, C. Cárdenas, E. Capoen, C. Pirovano, P. Roussel, G.H. Gauthier, Performance of $La_{0.5}Sr_{1.5}MnO_{4\pm\delta}$ Ruddlesden-Popper manganite as electrode material for symmetrical solid oxide fuel cells. Part A. The oxygen reduction reaction, Electrochim. Acta. 304 (2019) 415–427. doi:10.1016/j.electacta.2019.03.037.

[47] M. V. Sandoval, S. Durán, A. Prada, C. Pirovano, O. Gardoll, P. Roussel, G.H. Gauthier, Synthesis and preliminary study of $Nd_xAE_{2-x}MnO_{4\pm\delta}$ (AE: Ca, Sr) for symmetrical SOFC electrodes, Solid State Ionics. 317 (2018) 194–200. doi:10.1016/j.ssi.2018.01.025.

[48] J. Shen, G. Yang, Z. Zhang, W. Zhou, W. Wang, Z. Shao, Tuning layer-structured $La_{0.6}Sr_{1.4}MnO_{4+\delta}$ into a promising electrode for intermediate-temperature symmetrical solid oxide fuel cells through surface modification, J. Mater. Chem. A. 4 (2016) 10641–10649. doi:10.1039/c6ta02986h.

[49] R. Xing, Y. Wang, Y. Zhu, S. Liu, C. Jin, Co-electrolysis of steam and CO_2 in a solid oxide electrolysis cell with La0.75Sr0.25Cr0.5Mn0.5O3-δ -Cu ceramic composite electrode, J. Power Sources. 274 (2015) 260–264. doi:10.1016/j.jpowsour.2014.10.066.

[50] Y. Gan, Q. Qin, S. Chen, Y. Wang, D. Dong, K. Xie, Y. Wu, Composite cathode $La_{0.4}Sr_{0.4}TiO_{3-\delta}$ - $Ce_{0.8}Sm_{0.2}O_{2-\delta}$ impregnated with Ni for high-temperature steam electrolysis, J. Power Sources. 245 (2014) 245–255. doi:10.1016/j.jpowsour.2013.06.107.

[51] Y. Li, Y. Gan, Y. Wang, K. Xie, Y. Wu, Composite cathode based on Ni-loaded $La_{0.75}Sr_{0.25}Cr_{0.5}Mn_{0.5}O_{3-\delta}$ for direct steam electrolysis in an oxide-ion-conducting solid oxide electrolyzer, Int. J. Hydrogen Energy. 38 (2013) 10196–10207. doi:10.1016/j.ijhydene.2013.06.057.

[52] L. Thommy, O. Joubert, J. Hamon, M.T. Caldes, Impregnation versus exsolution: Using metal catalysts to improve electrocatalytic properties of LSCM-based anodes operating at 600 °C, Int. J. Hydrogen Energy. 41 (2016) 14207–14216. doi:10.1016/j.ijhydene.2016.06.088.

[53] J.T.S. Irvine, D. Neagu, M.C. Verbraeken, C. Chatzichristodoulou, C. Graves, M.B. Mogensen, Evolution of the electrochemical interface in high-temperature fuel cells and electrolysers, Nat. Energy. 1 (2016) 1–13. doi:10.1038/nenergy.2015.14.

[54] D. Neagu, T.S. Oh, D.N. Miller, H. Ménard, S.M. Bukhari, S.R. Gamble, .R.J. Gorte, J.M. Vohs, J.T.S. Irvine, Nano-socketed nickel particles with enhanced coking resistance grown in situ by redox exsolution, Nat. Commun. 6 (2015) 8120. doi:10.1038/ncomms9120.

[55] S. Park, Y. Kim, H. Han, Y.S. Chung, W. Yoon, J. Choi, W.B. Kim, In situ exsolved Co nanoparticles on Ruddlesden-Popper material as highly active catalyst for CO_2 electrolysis to CO, Appl. Catal. B Environ. (2019) 147–156. doi:10.1016/j.apcatb.2019.02.013.

[56] D. Papargyriou, D.N. Miller, J.T.S. Irvine, Exsolution of Fe-Ni alloy nanoparticles from $(La,Sr)(Cr,Fe,Ni)O_3$ perovskites as potential oxygen transport membrane catalysts for methane reforming, J. Mater. Chem. A. 7 (2019) 15812–15822. doi:10.1039/c9ta03711j.

[57] H. Han, J. Park, S.Y. Nam, K.J. Kim, G.M. Choi, S.S.P. Parkin, H.M. Jang, J.T.S. Irvin, Lattice strain-enhanced exsolution of nanoparticles in thin films, Nat. Commun. 10 (2019) 1–8. doi:10.1038/s41467-019-09395-4.

[58] Y.S. Chung, T. Kim, T.H. Shin, H. Yoon, S. Park, N.M. Sammes, W.B. Kim, J.S. Chung, In situ preparation of a $La_{1.2}Sr_{0.8}Mn_{0.4}Fe_{0.6}O_4$ Ruddlesden-Popper phase with

exsolved Fe nanoparticles as an anode for SOFCs, J. Mater. Chem. A. 5 (2017) 6437–6446. doi:10.1039/c6ta09692a.

[59] C. Arrivé, T. Delahaye, O. Joubert, G. Gauthier, Exsolution of niquel nanoparticles at the surface of a conducting titanate as potential hydrogen electrode materialfor solid oxide electrochemical cells, J. Power Sources. 223 (2013) 341–348. doi:10.1016/j.jpowsour.2012.09.062.

[60] V.B. Vert, F. V. Melo, L. Navarrete, J.M. Serra, Redox stability and electrochemical study of nickel doped chromites as anodes for H_2/CH_4-fueled solid oxide fuel cells, Appl. Catal. B Environ. 115–116 (2012) 346–356. doi:10.1016/j.apcatb.2011.12.033.

[61] W. Kobsiriphat, B.D. Madsen, Y. Wang, M. Shah, L.D. Marks, S.A. Barnett, Nickel- and ruthenium-doped lanthanum chromite anodes: Effects of nanoscale metal precipitation on solid oxide fuel cell performance, J. Electrochem. Soc. 157 (2010) 6–11. doi:10.1149/1.3269993.

[62] Y. Nishihata, J. Mizuki, T. Akao, H. Tanaka, M. Uenishi, M. Kimura, et al., Self-regeneration of a Pd-perovskite catalyst for automotive emissions control, Nature. 418 (2002) 164–167. doi:10.1038/nature00893.

[63] G. Tsekouras, D. Neagu, J.T.S. Irvine, Step-change in high temperature steam electrolysis performance of perovskite oxide cathodes with exsolution of B-site dopants, Energy Environ. Sci. 6 (2013) 256–266. doi:10.1039/c2ee22547f.

[64] G. Dimitrakopoulos, A.F. Ghoniem, B. Yildiz, In situ catalyst exsolution on perovskite oxides for the production of CO and synthesis gas in ceramic membrane reactors , Sustain. Energy Fuels. 3 (2019) 2347–2355. doi:10.1039/c9se00249a.

[65] S. Liu, Q. Liu, X.Z. Fu, J.L. Luo, Cogeneration of ethylene and energy in protonic fuel cell with an efficient and stable anode anchored with in-situ exsolved functional metal nanoparticles, Appl. Catal. B Environ. 220 (2018) 283–289. doi:10.1016/j.apcatb.2017.08.051.

[66] D. Zubenko, S. Singh, B.A. Rosen, Exsolution of Re-alloy catalysts with enhanced stability for methane dry reforming, Appl. Catal. B Environ. 209 (2017) 711–719. doi:10.1016/j.apcatb.2017.03.047.

[67] T. Screen, Platinum group metal perovskite catalysts: Preparation and applications, Platin. Met. Rev. 51 (2007) 87–92. doi:10.1595/147106707X192645.

[68] H. Tanaka, M. Uenishi, M. Taniguchi, I. Tan, K. Narita, M. Kimura, et al., The intelligent catalyst having the self-regenerative function of Pd, Rh and Pt for automotive emissions control, Catal. Today. 117 (2006) 321–328. doi:10.1016/j.cattod.2006.05.029.

[69] Y. Gao, D. Chen, M. Saccoccio, Z. Lu, F. Ciucci, From material design to mechanism study: Nanoscale Ni exsolution on a highly active A-site deficient anode material for solid oxide fuel cells, Nano Energy. 27 (2016) 499–508.

doi:10.1016/j.nanoen.2016.07.013.

[70] R. Shiozaki, A.G. Andersen, T. Hayawaka, S. Hamakawa, K. Suzuki, M. Shimizu, K. Takehira, Sustainable Ni/$BaTiO_3$ catalysts for partial oxidation of methane to synthesis gas, Stud. Surf. Sci. Catal. 110 (1997) 701–710. doi:https://doi.org/10.1016/S0167-2991(97)81032-4.

[71] T. Hayakawa, A.G. Andersen, M. Shimizu, K. Suzuki, K. Takehira, Partial oxidation of methane to synthesis gas over some titanates based perovskite oxides, Catal. Letters. 22 (1993) 307–317. doi:10.1007/BF00807238.

[72] C. Batiot-Dupeyrat, G. Valderrama, A. Meneses, F. Martinez, J. Barrault, J.M. Tatibouët, Pulse study of CO_2 reforming of methane over $LaNiO_3$, Appl. Catal. A Gen. 248 (2003) 143–151. doi:10.1016/S0926-860X(03)00155-8.

[73] B.D. Madsen, W. Kobsiriphat, Y. Wang, L.D. Marks, S.A. Barnett, Nucleation of nanometer-scale electrocatalyst particles in solid oxide fuel cell anodes, J. Power Sources. 166 (2007) 64–67. doi:10.1016/j.jpowsour.2006.12.080.

[74] B.D. Madsen, W. Kobsiriphat, Y. Wang, L.D. Marks, S.A. Barnett, SOFC anode performance enhancement through precipitation of nanoscale catalysts, ECS Trans. 7 (2007) 1339–1348.

[75] D.M. Bierschenk, E. Potter-Nelson, C. Hoel, Y. Liao, L. Marks, K.R. Poeppelmeier, S.A. Barnett, Pd-substituted (La,Sr)$CrO_{3-\delta}$-$Ce_{0.9}Gd_{0.1}O_{2-\delta}$ solid oxide fuel cell anodes exhibiting regenerative behavior, J. Power Sources. 196 (2011) 3089–3094. doi:10.1016/j.jpowsour.2010.12.050.

[76] T. Jardiel, M.T. Caldes, F. Moser, J. Hamon, G. Gauthier, O. Joubert, New SOFC electrode materials: The Ni-substituted LSCM-based compounds $(La_{0.75}Sr_{0.25})(Cr_{0.5}Mn_{0.5-x}Ni_x)O_{3-\delta}$ and $(La_{0.75}Sr_{0.25})(Cr_{0.5-x}Ni_xMn_{0.5})O_{3-\delta}$, Solid State Ionics. 181 (2010) 894–901. doi:10.1016/j.ssi.2010.05.012.

[77] C. Arrivé, T. Delahaye, O. Joubert, G.H. Gauthier, Study of (La,Sr)(Ti,Ni)$O_{3-\delta}$ materials for symmetrical Solid Oxide Cell electrode - Part B: Conditions of Ni exsolution, Ceram. Int. (2019). doi:10.1016/j.ceramint.2019.06.015.

[78] D. Neagu, G. Tsekouras, D.N. Miller, H. Ménard, J.T.S. Irvine, In situ growth of nanoparticles through control of non-stoichiometry, Nat. Chem. 5 (2013) 916–923. doi:10.1038/nchem.1773.

[79] S. Vecino-Mantilla, P. Gauthier-Maradei, M. Huvé, J.M. Serra, P. Roussel, G.H. Gauthier, Nickel exsolution-driven phase transformation from an n = 2 to an n= 1 Ruddlesden-Popper manganite for methane steam reforming reaction in SOFC conditions, ChemCatChem. 11 (2019) 4631–4641. doi:10.1002/cctc.201901002.

Chapter 1
Nickel exsolution from a new Ruddlesden-Popper manganite for methane steam reforming reaction in SOFC conditions

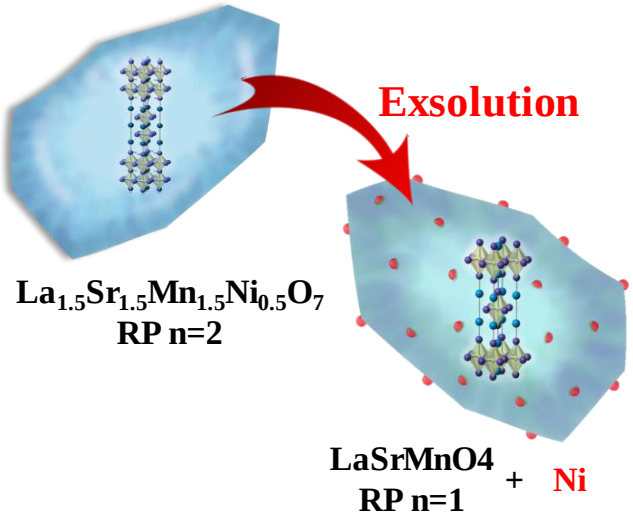

1.1. Abstract

In this study, an original way to perform the exsolution of Ni nanoparticles on ceramic support was explored for the development of SOFC anode material. The Ruddlesden-Popper (RP) phase n= 2 $La_{1.5}Sr_{1.5}Mn_{1.5}Ni_{0.5}O_{7\pm\delta}$ has been synthesized by the Pechini method and subsequently reduced with an H_2-N_2 mixture at different temperatures and reduction times to induce the formation of two phases that correspond to the RP n= 1 structure $LaSrMnO_{4\pm\delta}$ decorated with metallic Ni nanoparticles with different average particle sizes. Preliminary measurements of catalytic behavior for the steam reforming have been carried out in a reduction-reaction process with a mixture of 82 mol% CH_4, 18 mol% N_2 and low steam to carbon content (S/C= 0.15). The catalyst exhibits a selectivity for CO production (0.97), 14.60 mol% of CH_4 conversion and 24.19 mol% of H_2 production. Such catalytic behavior was maintained for more than 4 h, with a constant rate of hydrogen production and a stable CH_4 conversion rate. This study demonstrates that such Ni-doped manganite can be considered as a promising option for the development of new types of anode materials for SOFC.

1.2. Introduction

Given the current environmental problems and the global energetic context, it is necessary to develop and implement new, clean, safe and reliable energetic alternatives, which ensure a high and sustainable quality of life and, at the same time, avoid a possible crisis. Presently, the Solid Oxide Fuel Cells (SOFCs) are studied as potential devices to produce electricity and heat in a clean and efficient way (chemical to electrical yield > 60 %), better than conventional thermomechanical processes, converting directly the chemical energy of an oxidant gas and a large range of fuels (fuel flexibility), without combustion as intermediate step [1,2]. Nevertheless, the massive commercialization of SOFCs is blocked mainly by cost and durability issues, such as stability at high temperature (600 – 1000 °C), compatibility with the other components of the cell, electrochemical activity at low temperature and direct operation with hydrocarbon fuels without coking or poisoning (catalytic behavior) [3,4]. In particular, the conventional cermet based on nickel and yttria-stabilized zirconia (Ni/YSZ) still presents many issues as SOFC anode material [5,6]. Therefore, one of the current interests in this field is the search for new materials that can solve these problems in the cells and allow their proper operation.

One of the most promising alternatives is the development of Mixed Ionic and Electronic Conducting (MIEC) anodes. Apart from the perovskite mixed oxides, the Ruddlesden-Popper (RP) phases have demonstrated such kind of behavior and generated great expectation, historically as SOFC cathodes [7,8]. Due to their varied and exceptional transport and structural properties, together with their high thermal and mechanical stabilities, those materials are considered as an interesting option in a variety of catalytic and electrocatalytic processes like those occurring at both electrodes of a SOFC [9–18].

RP phases are materials whose structure results from the intergrowth of one or several perovskite-type blocks (ABO_3) separated by one rock-salt structure layer (AO). Their general formula is $A_{n+1}B_nO_{3n+1}$ or $(AO)(ABO_3)_n$, where A represents alkali, alkaline earth, or rare-earth metal cations located in the perovskite and rock salt slabs, B refers to transition metal cations occupying the anionic octahedral coordination of the perovskite block, and n is the number of octahedra's layers in the perovskite block [19]. Their possible use as anode material has been only recently described and studied [20,21] and the resulting manganite family could be a viable option. Several compositions have shown an exceptional potential as an electrode (both anode and cathode) in symmetrical SOFCs due to their stability in oxidizing and reducing atmospheres, thermo-mechanical compatibility with common electrolytes *e.g.* gadolinium-doped ceria (CGO), and acceptable electrochemical properties, high-temperature resistance, redox stability and favorable total conductivity [22,23]. Notwithstanding, some authors suggest that some compositions, *e.g.* $La_{0.6}Sr_{1.4}MnO_{4\pm\delta}$, are poor catalysts for direct use of methane [24].

It is however well known that electrochemical characteristics and catalytic behavior of a mixed oxide anode can be improved by the addition of small metallic nanoparticles (Ni, Ru, Rh, others) on the surface of the MIEC using, for example, the impregnation technique. Nevertheless, the use of impregnated material followed by a heat-treatment at high temperature (> 700 °C) does not guarantee a homogeneous distribution, size and strong metal-support interaction (nanoparticles anchorage) [25,26] to avoid sintering problems *in operando*. As an alternative method to create heterogeneous surface systems, it is possible to dissolve active metals in their oxidized form within the electrode material phase during the synthesis step. Then, under reducing atmosphere and high temperature (driven force), nanosized metallic particles can precipitate from the bulk to the surface. This phenomenon is called *in situ* growth or exsolution [8,25,27–29] and, as is previously presented, it could be considered as the basis for the design and development of more sophisticated oxide materials with advanced functionality [30]. Even though such mechanism has been applied mainly for perovskite structural oxides [31–34] and until now a few examples of exsolution in RP compounds have been reported [27,29].

This study describes the preparation of a new RP material, $La_{1.5}Sr_{1.5}Mn_{1.5}Ni_{0.5}O_{7\pm\delta}$, which has been designed using a retrosynthetic approach similar to organic chemistry [35,36], in order to be able to form, in reducing conditions, a biphasic material made of electrocatalytic active metallic nanoparticles on a RP n= 1 manganite of the type $La_xSr_{2-x}MnO_4$. The synthesis, proof of exsolution and its catalytic behavior for the methane steam reforming reaction using Colombian natural gas composition in low water content are presented.

1.3. **Methodology**

1.3.1. ***Synthesis***

Powder of $La_{1.5}Sr_{1.5}Mn_{1.5}Ni_{0.5}O_{7\pm\delta}$ composition (hereafter referred to as LSMN) powder was synthesized by a Pechini o citrate complexation route [37] using stoichiometric amounts of La_2O_3 (≥ 99.9 % Alfa Aesar), $SrCO_3$ (≥ 99.9 % Sigma Aldrich), $MnCO_3$ (≥ 99.9 % Sigma Aldrich) and $NiCO_3$ (≥ 99.9 % Alfa Aesar). Before using La_2O_3 and $SrCO_3$, they were calcined in air at 1000 and 500 °C, respectively, for 1 hour. Such pre-treatments were performed to remove hydration products (and carbonation in the case of lanthanum oxide) to facilitate the weighing of the precursors in correct proportions. The precursors were initially dissolved in a solution made of concentrated nitric acid (HNO_3, ≥ 65 vol% Merck) in excess and citric acid (CA, ≥99.5 %Merck), added in the molar ratio CA:$(\text{metal ion})_{total}$= 3:1. Under constant stirring, the resulting solution was slowly heated from room temperature to 120 °C using a hot plate, to reduce the volume of liquid. Polyethylene glycol (≥ 99 %, Panreac) was added as a polymerizing agent (1.5 mL per gram of targeted product). Then, the resulting mixture was stirred and heated at 150 °C just to form a viscous gel, which was subsequently dried and heat-treated in the air at 300 °C (2 h) and 500 °C (3 h) to ensure total organic matter decomposition. Finally, the product was subsequently sintered in air at 1000 °C (6 h), 1100 °C (6 h) and 1300 °C (12 h), with intermediate grinding and pelletizing steps. Figure 1.1 schematizes the synthesis steps.

In order to assure a good homogeneity in the particle size of LSMN material, the powder was ball-milled in acetone:powder:3 mm-sized zirconia balls dispersion (5:1:5 weight ratio) during 12 h at a speed of 50 rpm. After the milling step, the balls were separated, and the resulting mixture was dried. Homogenous powders with a particle size distribution between 125 and 200 μm, were re-obtained by sieving through steel sieves of the referred mesh size.

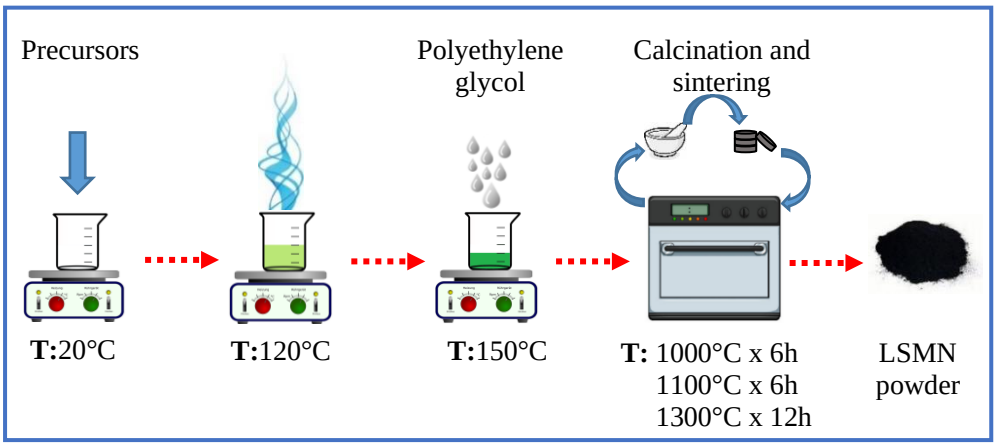

Figure 1.1 LSMN synthesis scheme. Source author.

1.3.2. *Characterization*

Each synthesized powder (~3 g per synthesis) was characterized by X-ray diffraction (XRD) at room temperature (RT) using a BrukerD8-ADVANCE powder diffractometer operated in Bragg-Brentano geometry, equipped with a Lineal LynxEye detector and a beam of $CuK_{\alpha 1,2}$ radiation (λ= 1.5418 Å). The diffractometer was operated over the angular range 2θ = 2 - 70° for qualitative analysis and 2θ= 2-90° for Rietveld analysis (Appendix A) with a measurement step of 0.020353° (2θ). The X-ray diffraction data were processed using JANA 2006 software package [38]. The elemental analysis was confirmed by X-Ray Fluorescence spectroscopy (XRF) in an S2 Ranger Bruker spectrometer equipped with a Pd X-ray tube.

1.3.3. *Exsolution study*

1.3.3.1 *Thermogravimetric measurement in reducing atmosphere*

Thermogravimetric analysis (TGA) in reducing atmosphere was carried out to understand the LSMN reduction behavior. The test was performed using a gravimetric analyzer Hiden-Isochema model IGA-003, applying the first cycle in N_2 at 5 °C min^{-1} that aims to suppress any further influence of moisture and/or adsorbed species and then, a second cycle one at 2 °C min^{-1} in 3 mol% H_2/N_2; both from RT to 1000 °C.

1.3.3.2 *Reduction study*

The operating temperatures (T) for the reduction study were selected considering the results obtained by TGA. Around 0.5 g of fresh LSMN powder was reduced in a tubular furnace CARBOLITE CTF 12/65/550 using a gas mixture 3 mol% H_2/N_2 (Cryogas) with a flow of 55 mL (STP) min^{-1} and different reduction times (t_r= 1, 4, 8, 16, 24 and 48 h). The powder obtained at each temperature - reduction time point was characterized by XRD at RT as described in Section 1.3.2. Additional microstructural characterization was performed on the reduced powder by field-emission scanning electron microscopy (FE-SEM) in a ZEISS microscope model ULTRA 55 and transmission electron microscopy in the TEM FEI TITAN Themis 300 equipped with a Super-X quad EDS for elemental analysis. The powder was crushed and dropped in the form of alcohol suspension on carbon-supported copper grids followed by evaporation under ambient conditions.

1.3.4. ***Catalytic test***

1.3.4.1 *Experimental set-up*

Steam reforming reaction with low steam content was studied on the LSMN powder for selected reducing conditions to explore its potential as a catalyst for this reaction. In Chapter 2 this topic will be studied into detail. The measurements of catalytic behavior for the reforming of methane were carried out in an experimental set-up described in Figure 1.2. It is divided into 4 main sections: the first one is the gases zone in which N_2 (grade 5.0, Cryogas), 3 mol% H_2/N_2 mixture (Cryogas) and CH_4 (grade 4.0, Cryogas) cylinders are available. In addition, this zone presents two analog manometers (Bourdon-Haenni® 0-100 psi and Ashcroft® 0-100 psi), two Cole-Parmer® 150 mm correlated and calibrated flowmeters with high-resolution valves and a Cole-Parmer® digital mass flowmeter (0 - 256 mL (STP) min^{-1}) for the precise control flow that passes to the next zones.

The second zone is the gas saturation zone (humidification), which consists of a stainless-steel bubbler with a capacity of 300 mL, equipped with a type J immersion thermocouple and a clamp-on heater connected to its control system. Additionally, a 50 cm heating cord, also with its control system, wraps the bubbler outlet line to prevent the steam condensation before entering the reactor.

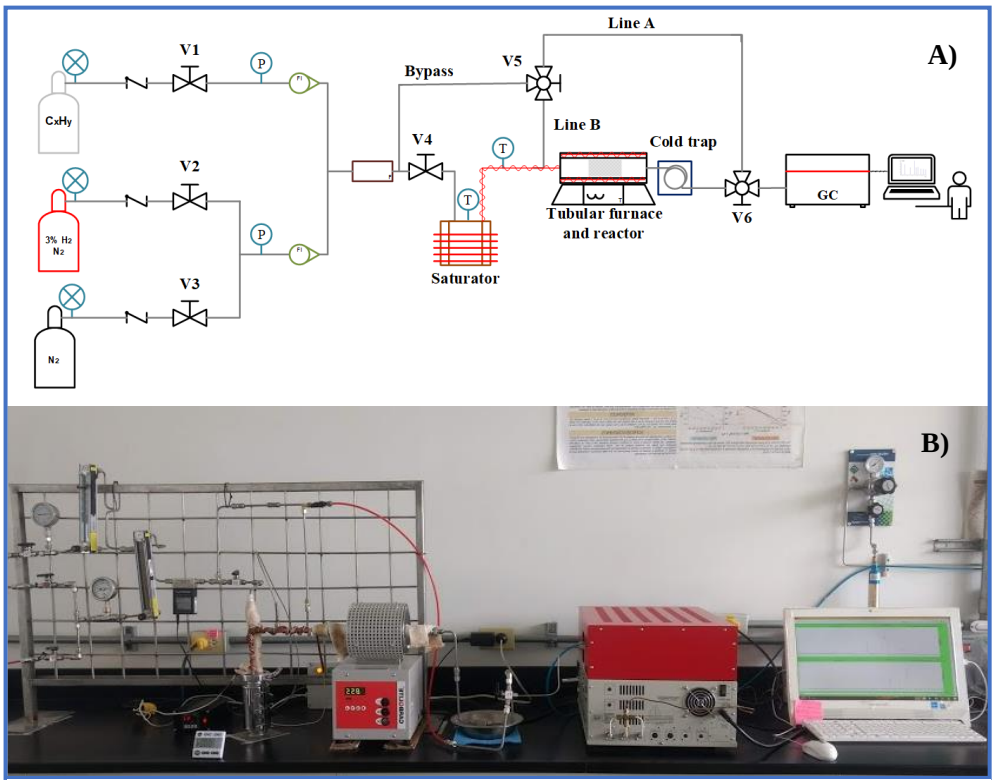

Figure 1.2 Experimental set-up A) scheme, B) photo. Source author.

The third zone is the reduction/reaction zone integrated by a tubular quartz reactor ($ø_I$: 9 mm, $ø_E$: 12 mm and L: 300 mm) heated by a tubular furnace (CARBOLITE MTF 10/15/130) and a cold trap to condense the steam excess after the reaction and before entering the gas chromatograph. According to the need (reduction step, reaction step or reagents analysis step) the bypass, line A or B will be used.

Finally, the last zone is the analysis one, integrated by a gas chromatograph (GC, SRI instruments 8610C) using He (grade 5.0, CRYOGAS) as mobile phase, equipped with a solenoid gas sampling valve heated at 60 °C, two packed columns (molecular sieve 13X 6 in and hayesep D 6 in), a thermal conductivity detector (TCD) heated at 150 °C and controlled by PeakSimple 4.44 free software. Standard gas cylinders with different gas compositions were employed for the outlet product quantification.

1.3.4.2 *Operating conditions*

Around 100 mg of catalyst (LSMN) was diluted in SiC (SiC:LSMN 10:1 weight ratio) and introduced in the reactor as fixed-bed between catalyst-free SiC and two pieces of quartz wool. Prior to the behavior test, the catalyst sample was reduced *in situ* (55 mL (STP) min^{-1} of 3 mol% H_2/N_2 mixture, Cryogas) according to the results obtained in the reduction study (Section 1.3.3.2). The catalytic behavior was measured during 8 h at the same reducing temperature under atmospheric pressure. The reaction mixture corresponds to 82 mol% CH_4 (N_2 as balance) humidified in steam to carbon ratio (S/C) of 0.15 according to the SOFC anode conditions suggested by the Gradual Internal Reforming concept or GIR [39]. The steam content was adjusted by flowing the adequate dry CH_4-N_2 mixture throughout the bubbler containing distilled water maintained exactly 46 °C. The total dry flow rate was 128 mL (STP) min^{-1} and the system was operating at a volume hourly space velocity (VHSV) of 86200 mL (STP) min^{-1} g_{cat}^{-1}. The composition in each effluent constituent (CH_4, CO, H_2, CO_2, and N_2) was obtained at regular time intervals (each 20 min) using online GC analysis (method described in Appendix B). The CH_4 conversion (X_{CH_4}), CH_4 conversion rate and H_2 formation rate were calculated using Equation 1.1, Equation 1.2 and Equation 1.3 respectively, where $n_{CH_4}^{In}$ and $n_{CH_4}^{Out}$ are the CH_4 molar flow rate at the inlet and outlet of the reactor (mmol min^{-1}), W_{Cat} is the catalyst weight (g), and $n_{H_2}^{Out}$ is the H_2 molar flow rate at the outlet of the reactor (mmol min^{-1}). Blank tests were performed at different temperatures using SiC only, and no conversion was observed for methane.

$$X_{CH_4}=\frac{n_{CH_4}^{In}-n_{CH_4}^{Out}}{n_{CH_4}^{In}}\times 100 \quad [\text{mol\%}] \qquad \textbf{Equation 1.1}$$

$$CH_4 \text{ conversion rate}=\frac{n_{CH_4}^{In}-n_{CH_4}^{Out}}{W_{Cat}} \quad \left[\text{mmol } min^{-1} g^{-1}\right] \qquad \textbf{Equation 1.2}$$

$$H_2 \text{ formation rate}=\frac{n_{H_2}^{Out}}{W_{Cat}} \quad \left[\text{mmol } min^{-1} g^{-1}\right] \qquad \textbf{Equation 1.3}$$

The CO and CO_2 selectivities (S_{CO_2} and S_{CO_2}) were defined as the molar flow rate ratios of the specified component in the outlet (n_{CO}^{Out} or $n_{CO_2}^{Out}$) to the total produced CO and CO_2 molar flow rate ($n_{CO_2}^{Out}+n_{CO}^{Out}$) (Equation 1.4 and Equation 1.5). The H_2 to CO ratio is defined as is shown in Equation 1.6.

$$S_{CO_2} = \frac{n_{CO_2}^{Out}}{n_{CO_2}^{Out} + n_{CO}^{Out}} \quad \text{[dimensionless]} \qquad \textbf{Equation 1.4}$$

$$S_{CO} = \frac{n_{CO}^{Out}}{n_{CO_2}^{Out} + n_{CO}^{Out}} \quad \text{[dimensionless]} \qquad \textbf{Equation 1.5}$$

$$\frac{H_2}{CO} = \frac{n_{H_2}^{Out}}{n_{CO}^{Out}} \quad \text{[dimensionless]} \qquad \textbf{Equation 1.6}$$

1.4. **Results**

1.4.1. ***LSMN study***

The LSMN material exhibits a Ruddlesden-Popper (RP) structure with 2 layers of octahedra in the perovskite-like stack and tetragonal space group *I4/mmm* (No. 139). A total of 24 sets of ~3 g of corresponding material, were synthesized as described in the Methodology section. For each synthesis, the lattice parameters (*a=b*, *c*) and the unit-cell volume were determined from the XRD data using structure refinement based on the Full Pattern Matching – Le Bail method. The comparison of the results allowed the selection of the samples to be mixed (or discarded), obtaining a final homogeneous stock of around 40 g of pure phase material (Appendix C).

The structure of the as-obtained LSMN powder was successfully refined as a single-phase using Rietveld method based on X-ray diffraction data and pseudo-Voigt peak shape function with reasonable reliability factors of R_p= 4.35%, R_{wp}= 5.77%, and χ^2= 1.51 and very few residual intensity, as observed graphically in Figure 1.3, suggesting an effective structural analysis. The refined lattice parameters are shown in Table 1.1 and those results agree well with those reported for parent compounds such as $La_{1.4}Sr_{1.6}Mn_2O_7$ obtained at 1450 °C [40], $LaSr_2Mn_{1.6}Ni_{0.4}O_7$ prepared at 1500 °C [41] and, to a greater extent, $La_{1.5}Sr_{1.5}Mn_{1.25}Ni_{0.75}O_{6.67}$ [42] synthesized at a higher temperature (1450 °C). In fact, the small differences are especially associated with the stoichiometric La/Sr and/or Mn/Ni ratio, the synthesis method, or the sintering temperature. As often the case of transition metal oxides, the substitution at the A or B-sites of the structure is correlated with a mechanism of charges compensation, which implies changes in the unit cell size. Finally, this material was analyzed by XRF with a result of 0.057 ± 0.002 weight fraction, confirming the adequate stoichiometric Ni amount in the solid-state solution (Appendix D).

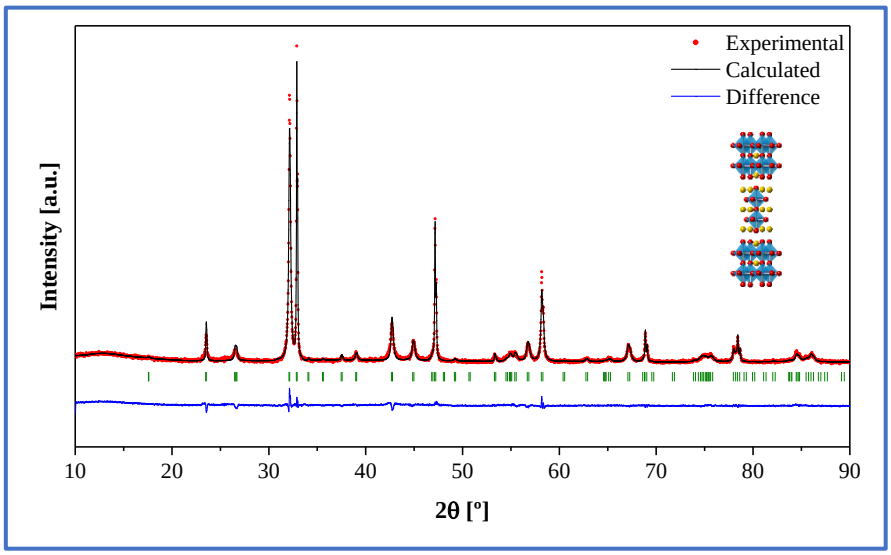

Figure 1.3 LSMN Rietveld refinement.

TGA performed from RT until 1000 °C in diluted H_2 is presented in Figure 1.4. In the whole temperature range, two weight losses are evidenced in a distinct temperature range, that must be attributed to the reduction of Mn and/or Ni. In similar compositions of perovskite structure type, stabilized in addition by Cr at the B site, Ni^{2+} and mixed $Mn^{3+/4+}$ oxidation states have been clearly established [43]. We assume the same kind of equilibrium effect is also present in the LSMN material. Indeed, the first weight loss is observed between around 400 and 600 °C; this is the same temperature range for which Mn^{4+} is reduced to exactly Mn^{3+} in the $(La,Sr)_2MnO_{4\pm\delta}$ series synthesized in air and treated in the same conditions as the present work [22]. Consequently, the first weight loss can be assigned to the reduction of Mn^{4+} to Mn^{3+}, with the consecutive formation of oxygen vacancies (δ), in agreement with the material charge balance. The second weight loss in reducing atmosphere is observed between 750 and 850 °C and is associated with the reduction of Ni^{2+} to Ni^0. Such attribution is based on the fact that the reduction of Mn^{3+} to Mn^{2+} in $(La,Sr)_2MnO_{4\pm\delta}$ parent compounds have been observed only for temperatures higher than 900 °C in similar conditions [22]. Certainly, this second weight loss measured between 730 and 860 °C corresponds to Δm/m=-1.43%. This is in very close agreement with the theoretical weight loss (Δm/m=-1.42%) calculated from the following equation, considering a fixed 3+ oxidation state for Mn (Equation 1.7).

$La_{1.5}Sr_{1.5}Mn_{1.5}Ni_{0.5}O_{7\pm\delta}$ (LSMN)			
	This study		
R_p [%]	3.80		
R_{wp}[%]	4.92		
χ^2	1.29		
a [Å]	3.8546(2)		
c [Å]	20.1911(14)		
V [Å^3]	300.01(3)		
	$La_{1.4}Sr_{1.6}Mn_2O_7$ [40]	$LaSr_2Mn_{1.6}Ni_{0.4}O_7$ [41]	$La_{1.5}Sr_{1.5}Mn_{1.25}Ni_{0.75}O_{6.67}$ [42]
R_p	9.53	N.R.	10.6
R_{wp}	12.36	N.R.	12.9
χ^2	1.4	N.R.	N.R.
a [Å]	3.8686(6)	3.8502(1)	3.847(2)
c [Å]	20.238(4)	20.1134(6)	20.137(1)
V [Å^3]	302.88(3)	298.17(2)	298.02

N.R.: Not reported

Table 1.1 LSMN structure parameters calculated by Rietveld refinement using XRD data.

$$La_{1.5}Sr_{1.5}Mn_{1.5}Ni_{0.5}^{2+}O_{6.5} + 0.5H_2 \rightarrow 1.5LaSrMnO_4 + 0.5Ni + 0.5H_2O \quad \textbf{Equation 1.7}$$

It is worth noting that the reduction to metal of Ni cations only is confirmed by thermodynamic calculations for the reduction of binary metal oxides of corresponding constituting elements (see Appendix E). As expected, metal oxides such as La_2O_3, SrO, and MnO show positive Gibbs free energy (ΔG) in the selected temperature range; consequently, and in agreement with chemical knowledge of the corresponding elements, these oxides are very difficult to reduce using H_2. On the other hand, the three other manganese oxides *i.e.* Mn_3O_4, Mn_2O_3, and MnO_2, as well as NiO shall be the only easily reducible oxides, because of their calculated negative ΔG, what is in concordance with the thermogravimetric analysis [6,44–46]. If such weight loss assignment is correct, Ni exsolution should be evidenced for temperature treatment in reducing conditions between T=750 °C and T=850 °C. According to these results, the operating temperatures (T) for reduction (and subsequent catalytic tests) were selected as T= 750, 800 and 850 °C, together with the following reduction times: t_r= 1, 4, 8, 16, 24 and 48 h as established in the methodology.

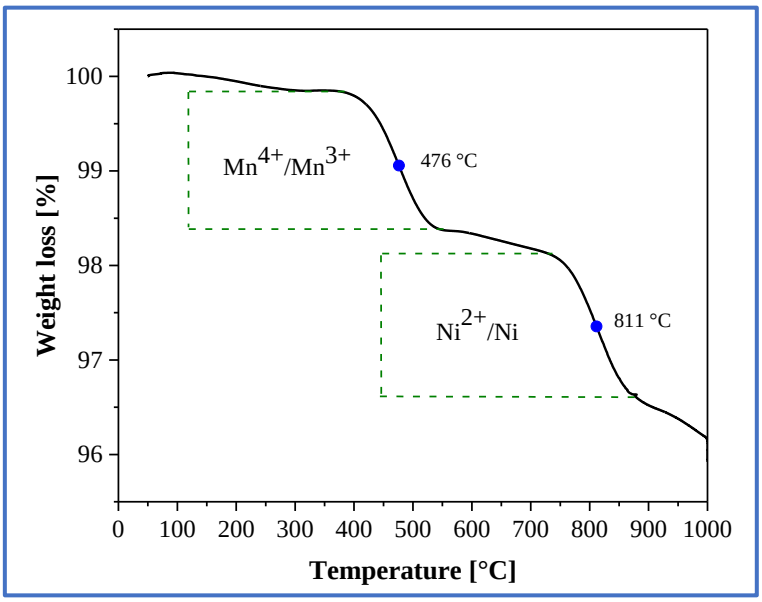

Figure 1.4 LSMN thermogravimetric analysis in reducing atmosphere.

1.4.2. *Exsolution study*

The XRD patterns of LSMN after reduction at 750 °C in 3 mol% H_2/N_2 are shown in Figure 1.5 as a function of the reduction time (t_r). By heating LSMN oxide in reducing atmosphere at 750 °C and short reduction times, a mixture of phases is obtained. During the first hour the LSMN phase changes and, although it is still visible in a large proportion, the formation of a new phase in a smaller quantity is also observed. At 4 h of reduction, it is evident that the ratio is slowly reversed, decreasing the amount of the RP n= 2 phase. However, after 8 h of treatment, the sample exhibits two well-defined phases, completely different than the starting one, which can be indexed as a reduced Ruddlesden-Popper phase of the $LaSrMnO_{4\pm\delta}$ type (hereafter referred to as LSM) and metallic Ni (the characteristic peaks of Ni phase at around 44.5 and 51.9 °, as shown as red dots in Figure 1.5 [47]). The formation of LSM n= 1 seems reasonable since the synthesis conditions of $La_xSr_{2-x}MnO_{4\pm\delta}$ ($x \geq 1$) materials have been reported under reducing conditions [48–50]. Thus, the products of the reaction can be proposed according to Equation 1.7.

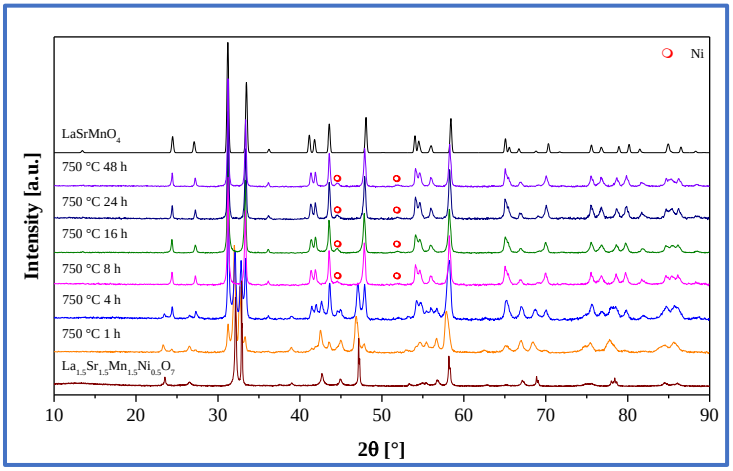

Figure 1.5 XRD patterns of LSMN reduced at 750 °C during different times (t_r).

The reduced samples in which the two LSM n= 1 and Ni phases are clearly evidenced (t_r from 8 to 48 h at 750 °C) are apparently identical, indicating the process and material stability upon reduction. A complete quantitative Rietveld refinement using XRD data was carried out considering a K_2NiF_4-type structure with a tetragonal unit cell and *I4/mmm* space group for the LSM n= 1 structure and FCC cubic cell with *Fm-3m* space group for Ni. The results of the lattice parameters of both phases and their weight fraction are shown in Figure 1.6 (A–E). The refinements present correct reliability factors, R_p= 4.26-5.12 %, R_{wp}= 5.34-6.67 % and "goodness of fit (GOF)" or χ^2= 1.28-1.93 (value between 1.0 and 2.9 is generally considered satisfactory [51]), confirmed by the graphical analysis of each refinement. Very slight evolution of the lattice parameters can be evidenced along with the reduction duration with an apparent *a* decrease while *c* parameter increases for the LSM n=1 up to t_r= 24 h. The phenomenon seems to stabilize for larger reduction times. Nonetheless, neither the refined Ni lattice parameter nor the Ni weight fraction exhibits any change along with the reduction duration, what means the cell parameter changes for the n= 1 Ruddlesden-Popper phase is possibly related to the presence of defects formed during Ni exsolution that disappear within the crystal structure or the further slow reduction of the same manganite with time. It is worth noting that for t_r= 24 h the refined values for the LSM n= 1 lattice parameters are in good correspondence with the calculated for the same material synthesized by other authors [52–55].

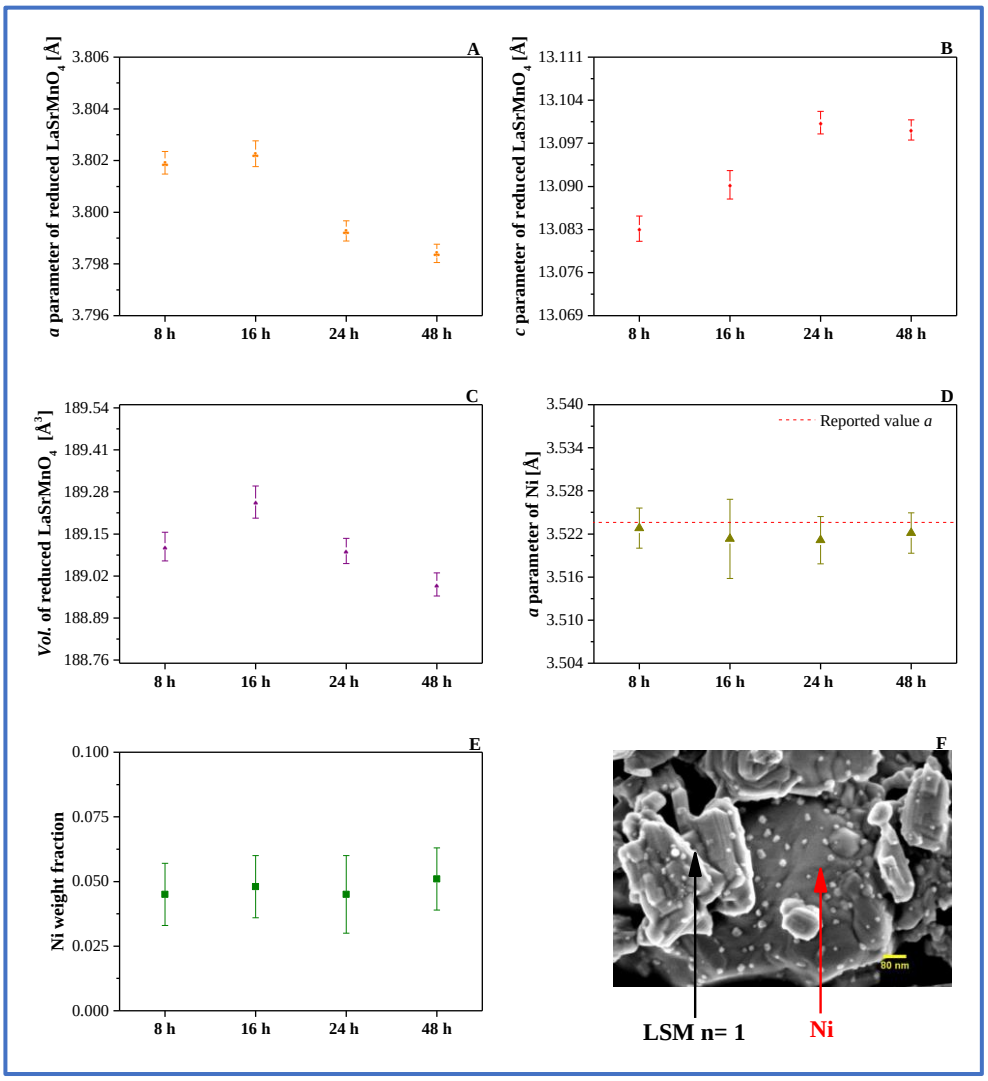

Figure 1.6 XRD Rietveld refinement of LSMN reduced at 750 °C during 8, 16, 24 and 48 h. A) *a* parameter of reduced $LaSrMnO_4$. B) *c* parameter of reduced $LaSrMnO_4$. C) *Vol.* of reduced $LaSrMnO_4$ D) *a* parameter of Ni compared with the reported one E) Ni weight fraction F) SEM image of LSMN reduced at 750 °C and 4 h.

The refined *a* lattice parameter calculated for metallic nickel in all four studied points match very well with the reported values (*a*= 3.5236(3) Å [56]), confirming that exsolved nanoparticles are probably pure Ni, what makes sense in the chemical point of view. In addition, the refined weight fraction of around 0.050 for metallic Ni, identical for all studied points at the precision level of the refinement (at 3 times the standard deviation), is in a very good agreement with the maximum stoichiometric and theoretical values calculated using the above-mentioned Equation 1.7 (0.946 LSM n= 1 and 0.054 Ni) as well in accordance with the amount of metallic Ni in LSMN, *i.e.* suggesting that all Ni^{2+} was completely reduced and exsolved from the crystal structure and visible as hemispherical nanoparticles on the surface of the manganite (Figure 1.6 F).

The XRD patterns of LSMN after reduction in 3 mol% H_2/N_2 at 800 and 850 °C using the same values of t_r are shown in Figure 1.7 and Figure 1.8, respectively. In these cases, the intermediate mixture of phases is only visible for 1 h of reduction and, for t_r= 4 h, the LSM n= 1 and Ni phases are already formed with an increasing crystallinity when T and/or t_r raises. This result can be associated with faster kinetics of exsolution at higher temperatures due to the fact that such kind of process requires solid-state diffusion within the crystal framework [57].

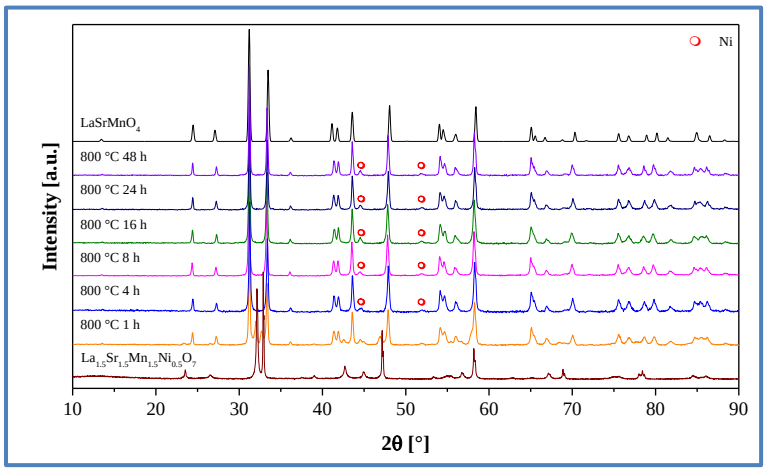

Figure 1.7 XRD patterns of LSMN reduced at 800 °C during different times (t_r).

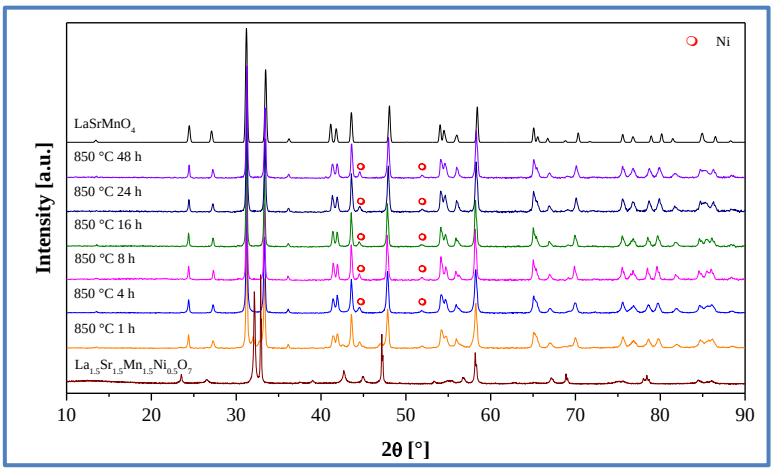

Figure 1.8 XRD patterns of LSMN reduced at 850 °C during different times (t_r).

The same conclusions can be obtained as in the previous case (T= 750 °C), *i.e.* two phases are observed for reduction times between 4 and 48 h, which are almost identical along the series, except the slight change in the lattice parameters for the LSM n= 1 phase, already described in the low-temperature exsolution conditions. For all reduction times, no difference can be evidenced for metallic Ni lattice parameter and weight fraction, as shown in Figure 1.9 (A–E) and Figure 1.10 (A–E), suggesting the complete Ni reduction and exsolution from the crystal structure and LSM n= 1 formation, as can be also confirmed in SEM results (Figure 1.9 F and Figure 1.10 F). Globally, in any reducing conditions ($t_r \geq 4$h), all the lattice parameters (*a*, *c* and cell volume) for LSM n= 1 phase, calculated by Rietveld refinement, remain coherent with the values reported by other authors [52–55,58–62]; the same can be concluded for Ni *a* lattice parameter and weight fraction.

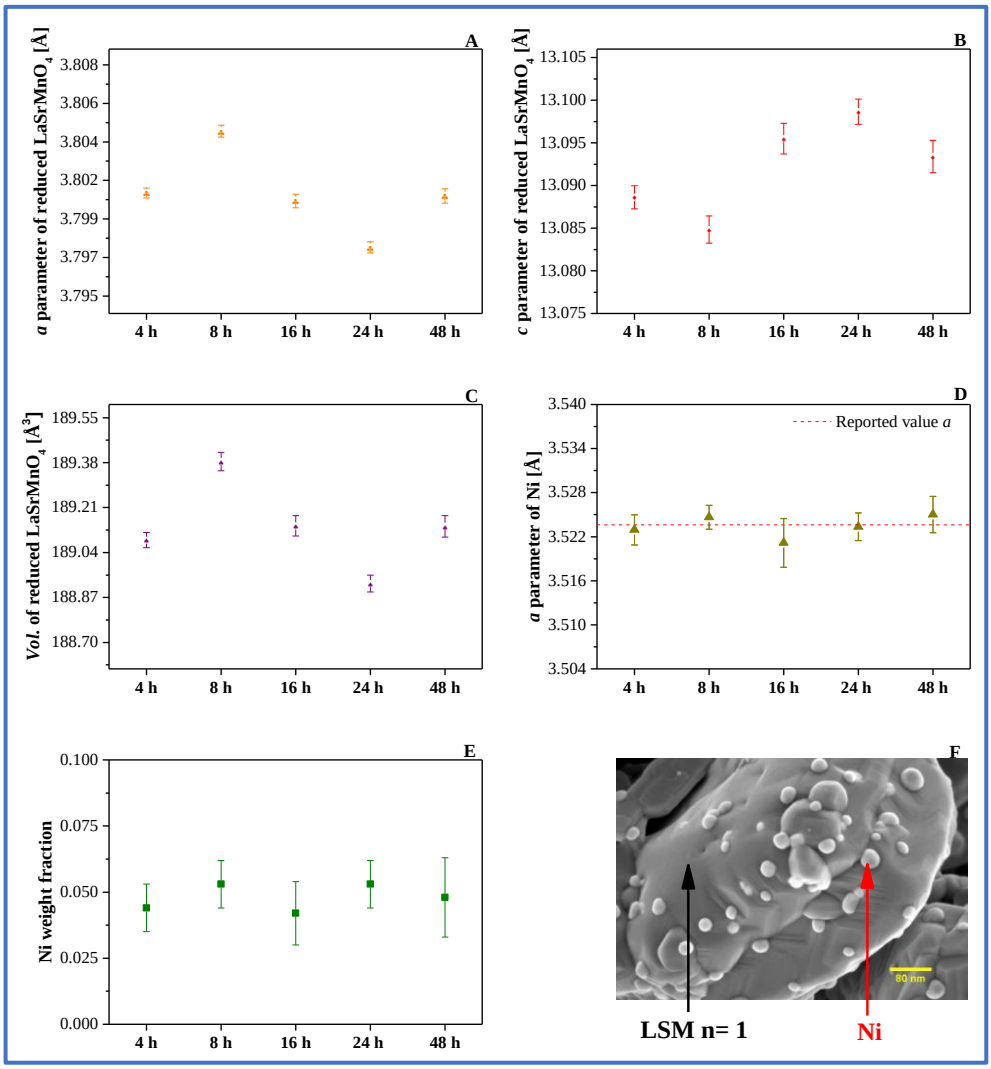

Figure 1.9 XRD Rietveld refinement of LSMN reduced at 800 °C during 4, 8, 16, 24 and 48 h. A) *a* parameter of reduced $LaSrMnO_4$. B) *c* parameter of reduced $LaSrMnO_4$. C) *Vol.* of reduced $LaSrMnO_4$. D) *a* parameter of Ni compared with the reported one E) Ni weight fraction F) SEM image of LSMN reduced at 800 °C and 4 h.

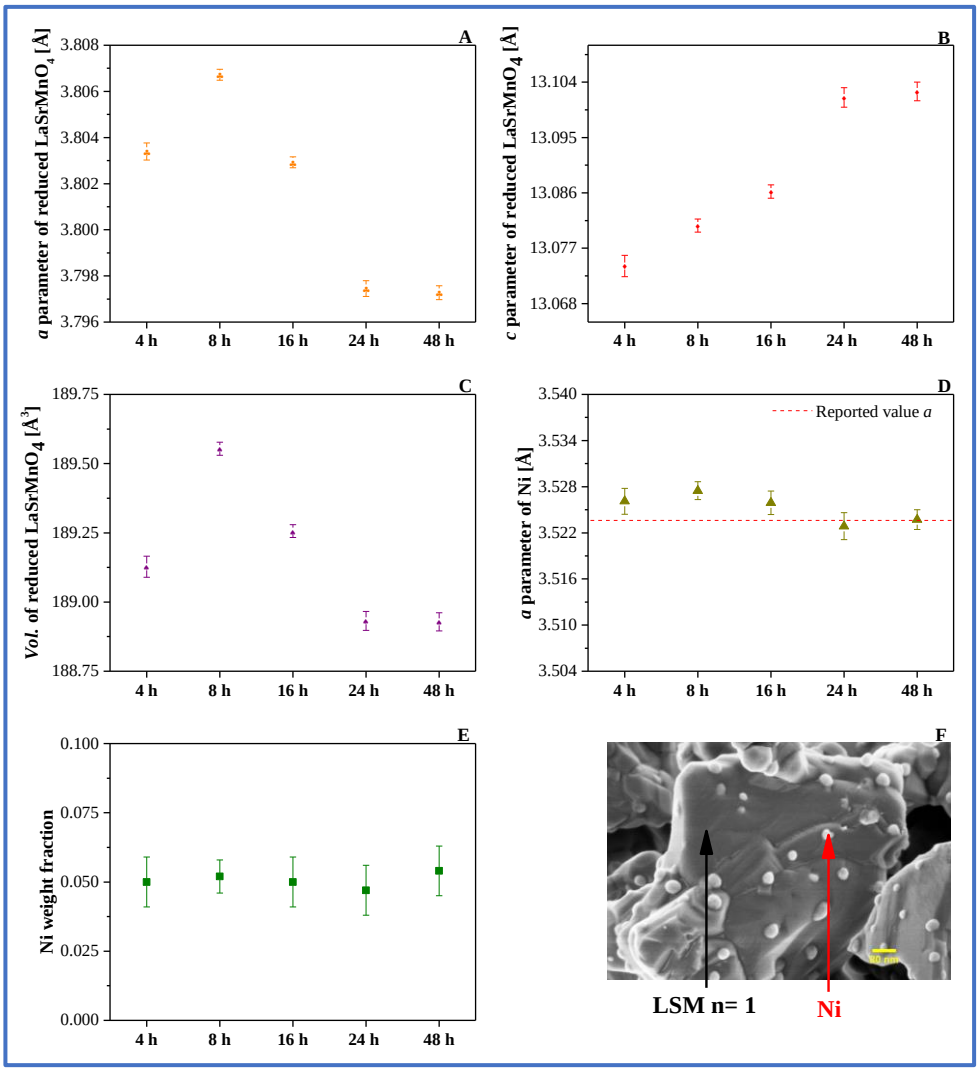

Figure 1.10 XRD Rietveld refinement of LSMN reduced at 850 °C during 4, 8, 16, 24 and 48 h. A) *a* parameter of reduced $LaSrMnO_4$ B) *c* parameter of reduced $LaSrMnO_4$. C) *Vol.* of reduced $LaSrMnO_4$. D) *a* parameter of Ni compared with the reported one E) Ni weight fraction F) SEM image of LSMN reduced at 850 °C and 4 h.

TEM and STEM images of the exsolved nanoparticles and its perovskite matrix associated with energy dispersive spectroscopy (EDS) mapping of the main elements for a characteristic zone of LSMN powder after reduction at 850 ºC for 4 h are shown in Figure 1.11. The elemental mapping (Figure 1.11-C) confirms the grain composition, *i.e.* La, Sr, and Mn are homogeneously distributed in the entire grain and few tenths of nanometer-sized highly concentered spots (in red) confirm the chemical nature of the nanoparticles, which consists in pure and dense metallic Ni. The only trace of Ni is detected in the area without Ni segregation, which suggests that most of the Ni is exsolved on the surface. The complete morphology of the reduced sample can be observed in Figure 1.11-D: the LSM n= 1 surface is decorated with some anchored small and uniformly distributed crystallized Ni hemispherical nanoparticles with strong particle - oxide matrix interaction [57,63,64]. The spacing between the lattice fringe is consistent with the (111) interreticular distance of Ni and the [001] zone axis of the perovskite. Such kind of morphological results (nanoparticles embedded on the surface), are similar and coherent with those reported for Ni exsolution from perovskites structures such as $La_{0.9}Mn_{0.8}Ni_{0.2}O_3$ [65], $La_{0.4}Sr_{0.4}Sc_{0.9}Ni_{0.1}O_3$ [33] and $La_{0.5}Sr_{0.5}Ti_{0.75}Ni_{0.25}O_3$ [32].

It has been established that the particle size distribution and average particle size values can be associated to many extrinsic aspects (oxygen partial pressure P_{O_2} of the reduction gas mixture, etc) or intrinsic aspects (surface features [66], mechanical stresses and strains [67], wetting angles [68], defects such as vacancies and dislocations [69,70]), affecting the formation (nucleation) and growth of the Ni particles [33], it was considered in this study only the main effects of reduction temperature (T) and time (t_r).

The influence of T and t_r on the Ni particle size was examined using precise image analysis of the scanning electron micrographs (FE-SEM) based on about 100 particles to obtain a characteristic frequency histogram in each selected (T, t_r) conditions. The grouped particle size data were analyzed using as likelihood fitting method a lognormal distribution (Equation 1.8) as it is reported in the literature [71–73] and treated in OriginPro8® with the iteration algorithm named Orthogonal Distance Regression.

$$f(D) = \frac{A}{(2\pi)^{0.5} w D} e^{-\frac{\ln\left(D/D_0\right)^2}{2w^2}} \qquad \textbf{Equation 1.8}$$

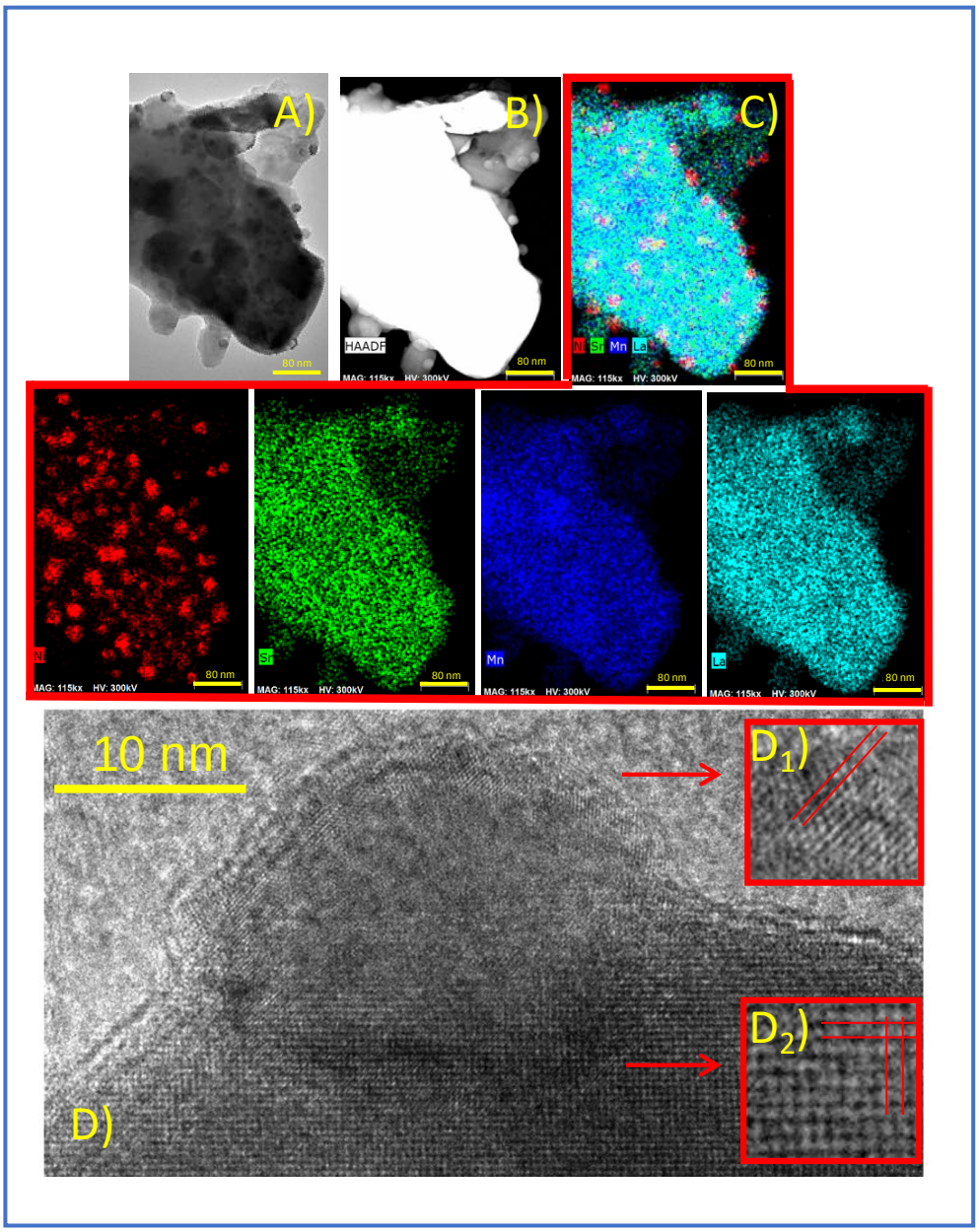

Figure 1.11 LSMN powder reduced at 850 °C and 4 h A) TEM image B) HAADF images showing nanoparticles on the surface C) Corresponding EDS mapping identify them as Ni D) HR TEM image of the exsolved nanoparticle and its perovskite matrix. The lattice fringe spacings are D_1) closest to 2 Å which correspond to d111 of Ni and D_2) closest to 3.8x3.8 Å which match well with the [001] zone axis of the perovskite.

In this case, A is the area of the size distribution, w the scale parameter defining the width of the size distribution (multiplicative standard deviation) and D_0 the median diameter. The average particle size ($\overline{D}_p$) of the lognormal distribution and its standard deviation (σ_{ln}) were determined using the following equations:

$$\overline{D}_p = D_0 e^{\frac{w^2}{2}} \qquad \textbf{Equation 1.9}$$

$$\sigma_{ln} = D_0 \sqrt{e^{2w^2} - e^{w^2}} \qquad \textbf{Equation 1.10}$$

The results of the 14 lognormal distributions are shown in Appendix F and they were used to determine the statistical significance of the different studied variables (T and t_r) on the average Ni particle size ($\overline{D}_p$). A statistical ANOVA analysis was performed through the Generalized Linear Models available in the STATGRAPHICS Centurion XVII package with a confidence level of 95% and a Square Sum Type III analysis, allowing measurement of the contribution of each variable (see Appendix G). The results are presented in Table 1.2, showing that p-value was lower than 0.05 for both cases, which means that t_r and T have a statistically significant influence on the average Ni particle size in perfect agreement with Gao *et al.* [33], Lai *et al.* [57] and Oh *et al.* [67].

Variable	Sum of squares	D.F.*	Mean square	F-test	p-value
Temperature (T)	724.435	1	724.435	34.36	0.0001
Reduction time (tr)	520.277	1	520.277	24.67	0.0004
Residual	231.94	11	21.0855		
Total (Corrected)	1366.44	13			

*D.F.: Degree of freedom

Table 1.2 Temperature and reduction time effect on $\overline{D}_p$ (ANOVA result).

The $\overline{D}_p$ results obtained from the distributions were used to generate the contour plot by a physical interpolating method (Thin Plate Spline, TPS) using the OriginPro8® software. Figure 1.12 graphically shows the T and t_r effect on the average Ni particle size and confirms the results obtained with ANOVA (Table 1.2), in which both variables have a high influence on the particle size. Nevertheless, it is worth noting that the temperature effect is apparently stronger than the reduction time, *i.e.* high temperatures induce the rapid exsolution of Ni particles with a wide distribution. During the exsolution process, the self-grown nanoparticles are "anchored" and highly dispersed on the oxide surface, displaying a higher tendency to avoid their agglomeration and coarsening during

the reduction/reaction steps; this resulting material consists in an excellent option to improve the catalytic behavior, prevent the sulfur poisoning and carbon formation when hydrocarbons are used as fuels [74].

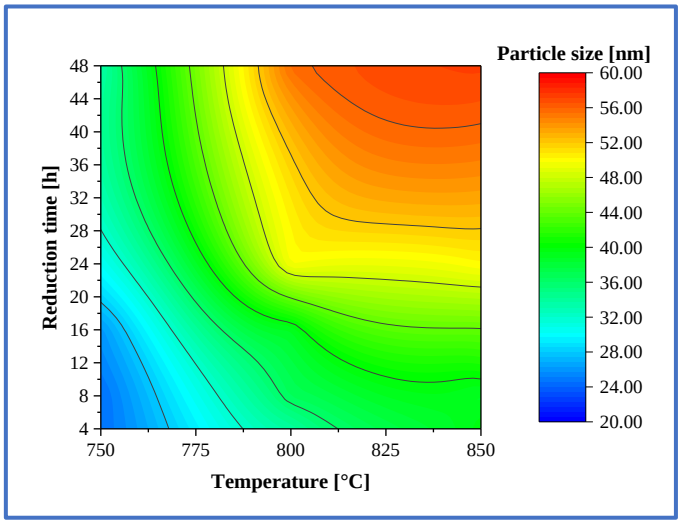

Figure 1.12 Influence of the reduction temperature (T) and time (t_r) on the Ni exsolved particle size.

The variation in the particle size and its slow increase with time at any studied reduction temperature could be associated with the fact that the metal exsolution equilibria has not been reached. Nevertheless, such hypothesis must be discarded, as it was already demonstrated with the complete Ni exsolution according to Equation 1.7. Therefore, two mechanisms are possible to explain the evolution of the particle size due to sintering: particle migration followed by coalescence or Ostwald-ripening [75]. The first hypothesis is the coalescence that only occurs between very close particles [57,63,64], a process strongly T dependent [75–77] mainly when the Tamman temperature is exceeded ($0.5T_{melting}$ [K], Ni: 864 K) [78].

When the nanoparticle-matrix oxide interaction is poor, the particle exhibits a spherical shape, generally observed *e.g.* using a typical metallic impregnation method. This case is more propitious to particle/crystallite migration and coalescence. However, it has been demonstrated that a strong interaction between the particles and the matrix turns the particle shape to hemispherical [57,63,64], explained, in this case, by the fact that the exsolved phase is embedded into the oxide matrix [67,74]. Such characteristic makes them less mobile on the surface and the coalescence rate is considerably decreased,

occurring only when the particles are very close to each other. This is the case of exsolve nanoparticles, as mentioned before and therefore cannot be the dominant mechanism [57,79,80]. Consequently, the only mechanism that could explain the observed increase in nanoparticle size is probably the Ostwald ripening process (atomic migration). This mechanism describes the growth of a larger particle by consuming a smaller one without a direct connection, here, clusters of atoms from a small particle migrate through the oxide surface and merge into other large particles just to reach the equilibrium; this effect becomes much serious when the temperature increases [79,81]. As indeed for the coalescence process, the driving force is the minimization of the total surface energy of the system. Despite the possible presence of Ni particle sintering, the average particle size values and distributions obtained in the present study are similar (< 100 nm) to what has been described by other authors using the exsolution of Ni or other metallic elements from an oxide matrix [5,33,57,70,74,82,83].

1.4.3. ***Preliminary catalytic study***

Preliminary catalytic properties of the material were studied in only one selected operating condition for exsolution *e.g.:* T= 850 °C and t_r= 16 h. The reaction was performed at the same temperature as for the reduction, T= 850 °C, using only a small amount of water for the methane reforming, *i.e.* low steam to carbon ratio (S/C) (GIR concept [39]). According to the literature, S/C ratios higher than 1 are necessary to avoid the coke formation/deposition on the anode surface. Nevertheless, such high S/C ratios dilute the fuel content and may lead to thermomechanical damages due to large temperature gradients in the anode side (reforming reaction strongly endothermic, while electrochemical reactions are exothermic) and the requirements to produce steam in excess and condense the unreacted products are energetically unfavorable. Therefore, with low S/C ratios, the process needs a small amount of steam at the inlet and the excess is produced *in situ* by the electrochemical oxidation of the hydrogen obtained during the steam reforming reaction in the anode side [39,84]; this requires the development of specific materials.

During 8 h of reaction, CH_4 molar conversion was calculated (Figure 1.13 A) and the outlet gas compositions (H_2, CO, and CO_2) was analyzed (Figure 1.13 B). In those figures, two main zones are clearly evidenced with a first region in which a low conversion and low products composition are measured but gradually increase until they reach the second region of stable behavior. The latter, which corresponds to steady-state operation and starts after around 200 min, was used to determine the average values of conversion, gas compositions and selectivity, similrly as presented by other authors [85].

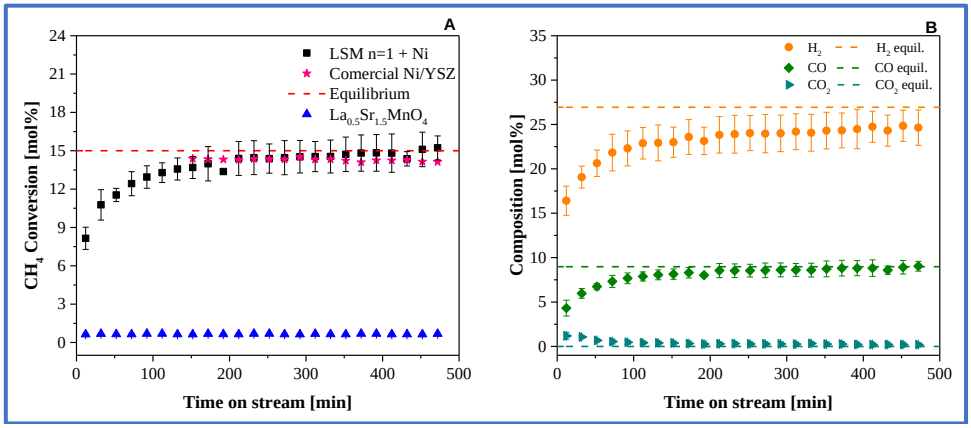

Figure 1.13 Catalytic behavior of LSMN reduced at T=850 °C for 16 h A) CH_4 molar conversion at 850 °C (theoretical equilibrium as dashed line), compared with $La_{0.5}Sr_{1.5}MnO_{4\pm\delta}$. B) H_2, CO and CO_2 molar composition in comparison to theoretical equilibrium (dashed lines).

The direct influence of the Ni particles on the catalytic behavior is evident by the comparison with a pure LSM material (similar in composition to the support of the exsolved material), the latter having very poor catalytic activity. The resulting LSM n= 1 + Ni exhibits an exceptional activity: 24.19 mol% H_2, 0.26 mol % CO_2, 8.65 mol% CO corresponding to a stable CH_4 conversion (14.60 mol%). The obtained values are very close to the maximum CH_4 conversion, H_2, CO_2 and CO content that should be obtained with the selected operating conditions (equilibrium) or those obtained using Ni/YSZ material (Figure 1.13 A). The latter, comparable only from a purely catalytic behavior point of view and during few hours, because in previous works have been demonstrated that the major difficulty of a direct natural gas (methane) operation over Ni/YSZ is the possible formation/deposition of carbon species on the Ni surface due to cracking of hydrocarbons resulting in the loss of cell performance and low durability [86–89].

Notwithstanding these results, it is not possible a complete and direct comparison between both materials (reduced LSMN and Ni/YSZ) because they are on the thermodynamic equilibrium. However, this preliminary result shows the high catalytic potential of the exsolved LSMN for the steam reforming reaction in the selected operating conditions and therefore to be considered as anode materials for SOFC; in a forthcoming study (Chapter 2), the influence of the exsolution conditions on the catalytic behavior and stability over longer times (coke formation/deposition) will be presented.

In addition, the presented results, together with the low CO_2 production (0.26 mol%) and the calculated H_2/CO ratio (2.80) measured in the effluent stream suggest a practically null contribution of Water-Gas Shift reaction (Equation 1.11 [90]) and the total selectivity towards the steam reforming reaction (Equation 1.12 [90]) using the exsolved material as catalyst (see Table 1.3). The catalytic behavior was maintained for more than 4 h, with a stable CH_4 conversion and H_2 formation rate, a much better behavior as other catalysts studied in similar S/C and temperature conditions, *e.g.* $Ce_{0.9}Gd_{0.1}O_{2-x}$ (0.047 mmol min^{-1} g^{-1}) [91] or $Ir/Ce_{0.9}Gd_{0.1}O_{1.95}$ (0.43 mmol min^{-1} g^{-1}) [92] (Table 1.3). This apparent stability could be a sign of potentially good resistance to coke formation/deposition in severe operating conditions (S/C= 0.15), which could be the result of the fine metal dispersion, associated to the strong basicity of the La/Sr-containing support grant less sensitivity to coking [32,93]. Future studies with longer reaction time will be carried out to confirm such hypothesis.

H_2 formation rate [mmol min^{-1} g^{-1}]	**CH_4 conversion rate [mmol min^{-1} g^{-1}]**	**S_{CO_2}**	**S_{CO}**	**H_2/CO ratio**
16.7 ± 1.45	6.15 ± 0.42	0.03 ± $5x10^{-3}$	0.97 ± $5 x10^{-3}$	2.80 ± 0.03

Table 1.3 Catalytic results of exsolved LSMN n = 2.

$$CO + H_2O \leftrightarrow CO_2 + H_2 \quad \Delta H^o = -41.2 \text{ kJ mol}^{-1} \qquad \textbf{Equation 1.11}$$

$$CH_4 + H_2O \leftrightarrow CO + 3H_2 \quad \Delta H^o = 206.1 \text{ kJ mol}^{-1} \qquad \textbf{Equation 1.12}$$

1.5. **Conclusions**

In conclusion, the new material LSMN with Ruddlesden-Popper n= 2 structure was successfully synthesized by the Pechini method as a single phase in air. In reducing atmosphere (H_2), at high temperature (750, 800 and 850°C) and different reduction times (4, 8 16, 24 and 48 h), an exsolution reaction occurs, resulting in the formation of LSM n= 1 together with embedded metallic Ni nanoparticles without any other impurity, as demonstrated by XRD analysis, TEM, and SEM, and with a direct influence on the particle size distributions and their average values. According to the preliminary test, and based on the catalytic behavior, the exsolved LSMN material appears to be an interesting option to be considered as anode materials for SOFC fed with natural gas (methane) in low steam conditions, due to its high CH_4 conversion, H_2 production, selectivity to steam reforming reaction and a constant behavior once the steady-state is

reached. These catalytic properties could be an important proof to believe in the resistance of the new materials to coke formation/deposition, but this is only a hypothesis for which a deeper and adequate study, is now required to support such conclusion.

1.6. References

[1] S. Shaikh, A. Muchtar, M. Somalu, A review on the selection of anode materials for solid-oxide fuel cells, Renew. Sustain. Energy Rev. 51 (2015) 1–8. doi:10.1016/j.rser.2015.05.069.

[2] B. Shri Prakash, S. Senthil Kumar, S. Aruna, Properties and development of Ni/YSZ as an anode material in solid oxide fuel cell: A review, Renew. Sustain. Energy Rev. 36 (2014) 149–179. doi:10.1016/j.rser.2014.04.043.

[3] H. Ghezel-Ayagh, B. Borglum, Review of Progress in Solid Oxide Fuel Cells at FuelCell Energy, ECS Trans. 78 (2017) 77–86. doi:10.1149/07801.0077ecst.

[4] B. Park, G. Choi, Ex-solution of Ni nanoparticles in a $La_{0.2}Sr_{0.8}Ti_{1-x}Ni_xO_{3-\delta}$ alternative anode for solid oxide fuel cell, Solid State Ionics. 262 (2014) 345–348. doi:10.1016/j.ssi.2013.10.016.

[5] Y. Chung, T. Kim, T. Shin, H. Yoon, S. Park, N. Sammes, W. Kim, J. Chung, In situ preparation of a $La_{1.2}Sr_{0.8}Mn_{0.4}Fe_{0.6}O_4$ Ruddlesden-Popper phase with exsolved Fe nanoparticles as an anode for SOFCs, J. Mater. Chem. A. 5 (2017) 6437–6446. doi:10.1039/c6ta09692a.

[6] Y. Sun, J. Li, Y. Zeng, B. Amirkhiz, M. Wang, Y. Behnamian, J. Luo, A-site deficient perovskite: The parent for in situ exsolution of highly active, regenerable nano-particles as SOFC anodes, J. Mater. Chem. A. 3 (2015) 11048–11056. doi:10.1039/c5ta01733e.

[7] Y. Hu, Y. Bouffanais, L. Almar, A. Morata, A. Tarancon, G. Dezanneau, $La_{2-x}Sr_xCo_{4-\delta}$ (x=0.9, 1.0, 1.19 Ruddlesden-Popper-type layered cobaltites as cathode materials for IT-SOFC application, Int. J. Hydrogen Energy. 38 (2013) 3064–3072. doi:http://dx.doi.org/10.1016/j.ijhydene.2012.12.047.

[8] Y. Li, W. Zhang, Y. Zheng, J. Chen, B. Yu, Y. Chen, M. Liu, Controlling cation segregation in perovskite-based electrodes for high electro-catalytic activity and durability, Chem. Soc. Rev. 46 (2017) 6345–6378. doi:10.1039/c7cs00120g.

[9] V. Kharton, A. Yaremchenko, A. Shaula, M. Patrakeev, E. Naumovich, D. Logvinovich, J. Frade, F. Marques, Transport properties and stability of Ni-containing mixed conductors with perovskite- and K_2NiF_4-type structure, J. Solid State Chem. 177 (2004) 26–37. doi:10.1016/S0022-4596(03)00261-5.

[10] S. Skinner, J. Kilner, Oxygen diffusion and surface exchange in $La_{2-x}Sr_xNiO_{4+\delta}$, Solid

State Ionics. 135 (2000) 709–712. doi:10.1016/S0167-2738(00)00388-X.

[11] P. Balachandran, D. Puggioni, J. Rondinelli, Crystal-chemistry guidelines for noncentrosymmetric A_2BO_4 Ruddlesden-Popper oxides, Inorg. Chem. 53 (2014) 336–348. doi:10.1021/ic402283c.

[12] C. Autret, C. Martin, M. Hervieu, R. Retoux, B. Raveau, G. André, F. Bourée, Structural investigation of Ca_2MnO_4 by neutron powder diffraction and electron microscopy, J. Solid State Chem. 177 (2004) 2044–2052. doi:10.1016/j.jssc.2004.02.012.

[13] J. Dailly, S. Fourcade, A. Largeteau, F. Mauvy, J. Grenier, M. Marrony, Perovskite and A_2MO_4-type oxides as new cathode materials for protonic solid oxide fuel cells, Electrochim. Acta. 55 (2010) 5847–5853. doi:10.1016/j.electacta.2010.05.034.

[14] H. Zhao, F. Mauvy, C. Lalanne, J. Bassat, S. Fourcade, J. Grenier, New cathode materials for ITSOFC: Phase stability, oxygen exchange and cathode properties of $La_{2-x}NiO_{4+\delta}$, Solid State Ionics. 179 (2008) 2000–2005. doi:10.1016/j.ssi.2008.06.019.

[15] M. Al Daroukh, V. Vashook, H. Ullmann, F. Tietz, I. Arual Raj, Oxides of the AMO_3 and A_2MO_4-type: Structural stability, electrical conductivity and thermal expansion, Solid State Ionics. 158 (2003) 141–150. doi:10.1016/S0167-2738(02)00773-7.

[16] S. Jeon, M.B. Choi, H.N. Im, J.H. Hwang, S.J. Song, Oxygen ionic conductivity of $La_2NiO_{4-\delta}$ via interstitial oxygen defect, J. Phys. Chem. Solids. 73 (2012) 656–660. doi:10.1016/j.jpcs.2012.01.006.

[17] H.W. Nie, T.L. Wen, S.R. Wang, Y.S. Wang, U. Guth, V. Vashook, Preparation, thermal expansion, chemical compatibility, electrical conductivity and polarization of $A_{2-\alpha}A'_{\alpha}MO_4$ (A = Pr, Sm; A′ = Sr; M = Mn, Ni; α = 0.3, 0.6) as a new cathode for SOFC, Solid State Ionics. 177 (2006) 1929–1932. doi:10.1016/j.ssi.2006.01.003.

[18] Y.S. Yoo, M. Choi, J.H. Hwang, H.N. Im, B. Singh, S.J. Song, $La_2NiO_{4+\delta}$ as oxygen electrode in reversible solid oxide cells, Ceram. Int. 41 (2015) 6448–6454. doi:10.1016/j.ceramint.2015.01.083.

[19] A. Das, E. Xhafa, E. Nikolla, Electro- and thermal-catalysis by layered, first series Ruddlesden-Popper oxides, Catal. Today. 277 (2016) 214–226. doi:10.1016/j.cattod.2016.07.014.

[20] S. Liping, H. Lihua, Z. Hui, L. Qiang, C. Pijolat, La substituted Sr_2MnO_4 as a possible cathode material in SOFC, J. Power Sources. 179 (2008) 96–100. doi:10.1016/j.jpowsour.2007.12.090.

[21] C. Jin, Z. Yang, H. Zheng, C. Yang, F. Chen, $La_{0.6}Sr_{1.4}MnO_4$ layered perovskite anode material for intermediate temperature solid oxide fuel cells, Electrochem. Commun. 14 (2012) 75–77. doi:10.1016/j.elecom.2011.11.008.

[22] M. V. Sandoval, C. Pirovano, E. Capoen, R. Jooris, F. Porcher, P. Roussel, G.H. Gauthier, In-depth study of the Ruddlesden-Popper $La_xSr_{2-x}MnO_{4\pm\Delta}$ family as

possible electrode materials for symmetrical SOFC, Int. J. Hydrogen Energy. 42 (2017) 21930–21943. doi:10.1016/j.ijhydene.2017.07.062.

[23] S. Li-Ping, L. Qiang, H. Li-Hua, Z. Hui, Z. Guo-Ying, L. Nan, J.P. Viricelle, C. Pijolat, Synthesis and performance of $Sr_{1.5}La_xMnO_4$ as cathode materials for intermediate temperature solid oxide fuel cell, J. Power Sources. 196 (2011) 5835–5839. doi:10.1016/j.jpowsour.2011.03.016.

[24] J. Shen, G. Yang, Z. Zhang, W. Zhou, W. Wang, Z. Shao, Tuning layer-structured $La_{0.6}Sr_{1.4}MnO_{4+\delta}$ into a promising electrode for intermediate-temperature symmetrical solid oxide fuel cells through surface modification, J. Mater. Chem. A. 4 (2016) 10641–10649. doi:10.1039/c6ta02986h.

[25] L. Thommy, O. Joubert, J. Hamon, M.T. Caldes, Impregnation versus exsolution: Using metal catalysts to improve electrocatalytic properties of LSCM-based anodes operating at 600 °C, Int. J. Hydrogen Energy. 41 (2016) 14207–14216. doi:10.1016/j.ijhydene.2016.06.088.

[26] J. Irvine, D. Neagu, M.C. Verbraeken, C. Chatzichristodoulou, C. Graves, M.B. Mogensen, Evolution of the electrochemical interface in high-temperature fuel cells and electrolysers, Nat. Energy. 1 (2016) 1–13. doi:10.1038/nenergy.2015.14.

[27] J. Zhou, T.H. Shin, C. Ni, G. Chen, K. Wu, Y. Cheng, K. Wu, Y. Cheng, J.T.S. Irvine, In Situ Growth of Nanoparticles in Layered Perovskite $La_{0.8}Sr_{1.2}Fe_{0.9}Co_{0.1}O_{4-\delta}$ as an Active and Stable Electrode for Symmetrical Solid Oxide Fuel Cells, Chem. Mater. 28 (2016) 2981–2993. doi:10.1021/acs.chemmater.6b00071.

[28] B. Hua, M. Li, Y.F. Sun, J.H. Li, J.L. Luo, Enhancing Perovskite Electrocatalysis of Solid Oxide Cells Through Controlled Exsolution of Nanoparticles, ChemSusChem. 10 (2017) 3333–3341. doi:10.1002/cssc.201700936.

[29] C. Yang, J. Li, Y. Lin, J. Liu, F. Chen, M. Liu, In situ fabrication of CoFe alloy nanoparticles structured $(Pr_{0.4}Sr_{0.6})_3(Fe_{0.85}Nb_{0.15})_2O_7$ ceramic anode for direct hydrocarbon solid oxide fuel cells, Nano Energy. 11 (2015) 704–710. doi:10.1016/j.nanoen.2014.12.001.

[30] W. Zhang, W. Zheng, Exsolution-mimic heterogeneous surfaces: Towards unlimited catalyst design, ChemCatChem. 7 (2015) 48–50. doi:10.1002/cctc.201402757.

[31] S. Liu, W. Zhang, T. Deng, D. Wang, X. Wang, X. Zhang, C. Zhang, W. Zheng, Mechanistic origin of enhanced CO catalytic oxidation over $Co_3O_4/LaCoO_3$ at lower temperature, ChemCatChem. 9 (2017) 3102–3106. doi:10.1002/cctc.201700937.

[32] C. Arrivé, T. Delahaye, O. Joubert, G. Gauthier, Exsolution of nickel nanoparticles at the surface of a conducting titanate as potential hydrogen electrode material for solid oxide electrochemical cells, J. Power Sources. 223 (2013) 341–348. doi:10.1016/j.jpowsour.2012.09.062.

[33] Y. Gao, D. Chen, M. Saccoccio, Z. Lu, F. Ciucci, From material design to mechanism study: Nanoscale Ni exsolution on a highly active A-site deficient anode material for

solid oxide fuel cells, Nano Energy. 27 (2016) 499–508. doi:10.1016/j.nanoen.2016.07.013.

[34] Y.F. Sun, Y.Q. Zhang, J. Chen, J.H. Li, Y.T. Zhu, Y.M. Zeng, B.S. Amirkhiz, J. Li, B. Hua, J.L. Luo, New Opportunity for in Situ Exsolution of Metallic Nanoparticles on Perovskite Parent, Nano Lett. 16 (2016) 5303–5309. doi:10.1021/acs.nanolett.6b02757.

[35] M. Henry, Retrosynthesis in inorganic crystal structures: application to nesosilicate and inosilicate networks, Coord. Chem. Rev. 178–180 (1998) 1109–1163. doi:10.1016/S0010-8545(98)00167-2.

[36] R.J. Ouellette, J.D. Rawn, Organometallic Chemistry of Transition Metal Elements and Introduction to Retrosynthesis, Org. Chem. (2014) 567–593. doi:10.1016/B978-0-12-800780-8.00017-6.

[37] M.P. Pechini, Method of preparing lead and alkaline earth titanates and niobates and coating method using the same to form a capacitor, US3330697A, 1967.

[38] V. Petrícek, M. Dušek, L. Palatinus, Crystallographic computing system JANA2006: General features, Zeitschrift Fur Krist. 229 (2014) 345–352. doi:10.1515/zkri-2014-1737.

[39] P. Vernoux, J. Guindet, M. Kleitz, Gradual Internal Methane Reforming in Intermediate-Temperature Solid Oxide Fuel Cell, J. Electrochem. Soc. 145 (1998) 3487–3492.

[40] E. Chi, Y. Kwon, N.H. Hur, Crystal chemistry of layered manganites $Ln_{1.4}Sr_{1.6}Mn_2O_7$ (Ln = La, Pr, Nd, Sm, Eu, and Gd), Bull. Korean Chem. Soc. 21 (2000) 259–263.

[41] A.A. Yaremchenko, D.O. Bannikov, A. V. Kovalevsky, V.A. Cherepanov, V. V. Kharton, High-temperature transport properties, thermal expansion and cathodic performance of Ni-substituted $LaSr_2Mn_2O_{7-\delta}$, J. Solid State Chem. 181 (2008) 3024–3032. doi:10.1016/j.jssc.2008.07.038.

[42] T.I. Chupakhina, G. V. Bazuev, E. V. Zabolotskaya, Synthesis and magnetic properties of a new layered oxide $La_{1.5}Sr_{1.5}Mn_{1.25}Ni_{0.75}O_{6.67}$, Russ. J. Inorg. Chem. 55 (2010) 247–253. doi:10.1134/S0036023610020178.

[43] T. Jardiel, M.T. Caldes, F. Moser, J. Hamon, G. Gauthier, O. Joubert, New SOFC electrode materials: The Ni-substituted LSCM-based compounds $(La_{0.75}Sr_{0.25})(Cr_{0.5}Mn_{0.5-x}Ni_x)O_{3-\delta}$ and $(La_{0.75}Sr_{0.25})(Cr_{0.5-x}Ni_xMn_{0.5})O_{3-\delta}$, Solid State Ionics. 181 (2010) 894–901. doi:10.1016/j.ssi.2010.05.012.

[44] K. Svoboda, A. Siewiorek, D. Baxter, J. Rogut, M. Pohořelý, Thermodynamic possibilities and constraints for pure hydrogen production by a nickel and cobalt-based chemical looping process at lower temperatures, Energy Convers. Manag. 49 (2008) 221–231. doi:10.1016/j.enconman.2007.06.036.

[45] O. Kwon, S. Sengodan, K. Kim, G. Kim, H.Y. Jeong, J. Shin, Y. Ju, J. Han, G. Kim, Exsolution trends and co-segregation aspects of self-grown catalyst nanoparticles in

perovskites, Nat. Commun. 8 (2017) 1–7. doi:10.1038/ncomms15967.

[46] J. Zhu, H. Li, L. Zhong, P. Xiao, X. Xu, X. Yang, Z. Zhao, J. Li, Perovskite oxides: Preparation, characterizations, and applications in heterogeneous catalysis, ACS Catal. 4 (2014) 2917–2940. doi:10.1021/cs500606g.

[47] I.K. Suh, H. Ohta, Y. Waseda, High-temperature thermal expansion of six metallic elements measured by dilatation method and X-ray diffraction, J. Mater. Sci. 23 (1988) 757–760. doi:10.1007/BF01174717.

[48] T. Broux, C. Prestipino, M. Bahout, O. Hernandez, D. Swain, S. Paofai, T. Hansen, C. Greaves, Unprecedented high solubility of oxygen interstitial defects in $La_{1.2}Sr_{0.8}MnO_{4+\delta}$ up to $\delta \sim 0.42$ revealed by in situ high temperature neutron powder diffraction in flowing O_2, Chem. Mater. 25 (2013) 4053–4063. doi:10.1021/cm402194q.

[49] C. Munnings, S. Skinner, G. Amow, P. Whitfield, I. Davidson, Structure, stability and electrical properties of the $La_{(2-x)}Sr_xMnO_{4\pm\delta}$ solid solution series, Solid State Ionics. 177 (2006) 1849–1853. doi:10.1016/j.ssi.2006.01.009.

[50] R.K. Li, C. Greaves, Synthesis and Characterization of the Electron-Doped Single-Layer Manganite $La_{1.2}Sr_{0.8}MnO_{4-\delta}$ and Its Oxidized Phase $La_{1.2}Sr_{0.8}MnO_{4+\delta}$, J. Solid State Chem. 153 (2000) 34–40. doi:10.1006/jssc.2000.8735.

[51] Y. Wang, K. Shih, X. Jiang, Phase transformation during the sintering of γ-alumina and the simulated Ni-laden waste sludge, Ceram. Int. 38 (2012) 1879–1886. doi:10.1016/j.ceramint.2011.10.015.

[52] D. Senff, P. Reutler, M. Braden, O. Friedt, D. Bruns, A. Cousson, F. Bourée, M. Merz, B. Büchner, A. Revcolevschi, Crystal and magnetic structure of $La_{1-x}Sr_{1+x}MnO_4$: Role of the orbital degree of freedom, Phys. Rev. B - Condens. Matter Mater. Phys. 71 (2005) 024425(1)-024425(8). doi:10.1103/PhysRevB.71.024425.

[53] S. Larochelle, A. Mehta, L. Lu, P.K. Mang, O.P. Vajk, N. Kaneko, J. W. Lynn, L. Zhou, M. Greven, Structural and magnetic properties of the single-layer manganese oxide $La_{1-x}Sr_{1+x}MnO_4$, Phys. Rev. B. 71 (2005) 024435(1)-024435(18). doi:10.1103/PhysRevB.71.024435.

[54] M. Bieringer, J.E. Greedan, Structure and magnetism in $BaLaMnO_{4+/-\delta}$ (δ = 0.00, 0.10) and $Ba_xSr_{1-x}LaMnO_4$. Disappearance of magnetic order for x > 0.30, J. Mater. Chem. 12 (2002) 279–287. doi:10.1039/b104405m.

[55] H.J. Kitchen, I. Saratovsky, M.A. Hayward, Syntheses and characterization of some solid-state actinide (Th, U, Np) compounds, Dalt. Trans. 39 (2010) 6098–6105. doi:10.1039/b927026d.

[56] J. Bandyopadhyay, K.P. Gupta, Low temperature lattice parameter of nickel and some nickel-cobalt alloys and Grüneisen parameter of nickel, Cryogenics (Guildf). 17 (1977) 345–347. doi:10.1016/0011-2275(77)90130-8.

[57] K.Y. Lai, A. Manthiram, Evolution of Exsolved Nanoparticles on a Perovskite Oxide

Surface during a Redox Process, Chem. Mater. 30 (2018) 2838–2847. doi:10.1021/acs.chemmater.8b01029.

[58] G. Blasse, New compositions with K_2NiF_4 structure, J. Inorg. Nucl. Chem. 27 (1965) 2683–2684.

[59] Y. Moritomo, Y. Tomioka, A. Asamitsu, Y. Tokura, Magnetic and electronic properties in hole-doped manganese oxides with layered structures: $La_{1-x}Sr_{1+x}MnO_4$, Phys. Rev. B. 51 (1995) 3297–3301.

[60] P. Ganguly, C.N.R. Rao, Crystal Chemistry and Magnetic Properties of Layered Possessing the K2NiF4 or Related Structures, J. Solid State Chem. 53 (1984) 193–216.

[61] A. Benabad, A. Daoudi, Les phases $SrLnMnO_4$ (Ln=La, Nd, Sm, Gd), $BaLnMnO_4$ (Ln= La, Nd) et M1+xLa1-xMnO4 (M= Sr, Ba), J. Solid State Chem. 22 (1977) 121–126.

[62] W.B. Wu, D.J. Huang, G.Y. Guo, H.J. Lin, T.Y. Hou, C.F. Chang, C.T. Chen, A. Fujimori, T. Kimura, H.B. Huang, A. Tanaka, T.Jo, Orbital polarization of $LaSrMnO_4$ studied by soft X-ray linear dichroism, J. Electron Spectros. Relat. Phenomena. 137–140 (2004) 641–645. doi:10.1016/j.elspec.2004.02.072.

[63] V.M. Gonzalez-DelaCruz, J.P. Holgado, R. Pereñíguez, A. Caballero, Morphology changes induced by strong metal-support interaction on a Ni-ceria catalytic system, J. Catal. 257 (2008) 307–314. doi:10.1016/j.jcat.2008.05.009.

[64] O. Dulub, W. Hebenstreit, U. Diebold, Imaging cluster surfaces with atomic resolution: The strong metal-support interaction state of pt supported on TiO_2 (110), Phys. Rev. Lett. 84 (2000) 3646–3649. doi:10.1103/PhysRevLett.84.3646.

[65] T. Wei, L. Jia, H. Zheng, B. Chi, J. Pu, J. Li, LaMnO3-based perovskite with in-situ exsolved Ni nanoparticles: a highly active, performance stable and coking resistant catalyst for CO_2 dry reforming of CH_4, Appl. Catal. A Gen. 564 (2018) 199–207. doi:10.1016/j.apcata.2018.07.031.

[66] A. Adamson, A. Gat, Physical chemistry of surfaces, 6th editio, John Wiley & Sons, Inc., New York, 1997.

[67] T.S. Oh, E.K. Rahani, D. Neagu, J.T.S. Irvine, V.B. Shenoy, R.J. Gorte, J.M. Vohs, Evidence and Model for Strain-Driven Release of Metal Nanocatalysts from Perovskites during Exsolution, J. Phys. Chem. Lett. 6 (2015) 5106–5110. doi:10.1021/acs.jpclett.5b02292.

[68] M. Blander, J.L. Katz, Bubble nucleation in liquids, AIChE J. 21 (1975) 833–848. doi:10.1002/aic.690210502.

[69] C.L. Kelchner, S. Plimpton, Dislocation nucleation and defect structure during surface indentation, Phys. Rev. B - Condens. Matter Mater. Phys. 58 (1998) 11085–11088. doi:10.1103/PhysRevB.58.11085.

[70] D. Neagu, G. Tsekouras, D.N. Miller, H. Ménard, J.T.S. Irvine, In situ growth of nanoparticles through control of non-stoichiometry, Nat. Chem. 5 (2013) 916–923. doi:10.1038/nchem.1773.

[71] O.G. Raabe, Particle size analysis utilizing grouped data and the log-normal distribution, J. Aerosol Sci. 2 (1971) 289–303. doi:10.1016/0021-8502(71)90054-1.

[72] B.R. Pauw, C. Kästner, A.F. Thünemann, Nanoparticle size distribution quantification: Results of a small-angle X-ray scattering inter-laboratory comparison, J. Appl. Crystallogr. 50 (2017) 1280–1288. doi:10.1107/S160057671701010X.

[73] G. Bergeret, P. Gallezot, Particle Size and Dispersion Measurements, in: G. Ertl, H. Knözinger, F. Schüth, J. Weitkamp (Eds.), Handb. Heterog. Catal. Online, 15 March 2, Wiley-VCH Verlag GmbH & Co. KGaA, Online, 2008: pp. 738–765. doi:https://doi.org/10.1002/9783527610044.hetcat0038.

[74] D. Neagu, T.S. Oh, D.N. Miller, H. Ménard, S.M. Bukhari, S.R. Gamble, et al., Nano-socketed nickel particles with enhanced coking resistance grown in situ by redox exsolution, Nat. Commun. 6 (2015) 1–8. doi:10.1038/ncomms9120.

[75] T.W. Hansen, A.T. Delariva, S.R. Challa, A.K. Datye, Sintering of catalytic nanoparticles: Particle migration or Ostwald ripening?, Acc. Chem. Res. 46 (2013) 1720–1730. doi:10.1021/ar3002427.

[76] J. Lif, M. Skoglundh, L. Löwendahl, Sintering of nickel particles supported on γ-alumina in ammonia, Appl. Catal. A Gen. 228 (2002) 145–154. doi:10.1016/S0926-860X(01)00957-7.

[77] F.N. Agüero, A.M. Beltrán, M.A. Fernández, L.E. Cadús, Surface nickel particles generated by exsolution from a perovskite structure, J. Solid State Chem. 273 (2019) 75–80. doi:10.1016/j.jssc.2019.02.036.

[78] R.T.K. Baker, The relationship between particle motion on a graphite surface and Tammann temperature, J. Catal. 78 (1982) 473–476. doi:10.1016/0021-9517(82)90332-3.

[79] S.E. Wanke, P.C. Flynn, The Sintering of Supported Metal Catalysts, Catal. Rev. Sci. Eng. 12 (1975) 93–135. doi:https://doi.org/10.1080/01614947508067523.

[80] G. Palasantzas, T. Vystavel, S.A. Koch, J.T.M. De Hosson, Coalescence aspects of cobalt nanoparticles during in situ high-temperature annealing, J. Appl. Phys. 99 (2006) 024307(1)-024307(5). doi:10.1063/1.2163983.

[81] M.A. Asoro, P.J. Ferreira, D. Kovar, In situ transmission electron microscopy and scanning transmission electron microscopy studies of sintering of Ag and Pt nanoparticles, Acta Mater. 81 (2014) 173–183. doi:10.1016/j.actamat.2014.08.028.

[82] Z. Du, H. Zhao, S. Yi, Q. Xia, Y. Gong, Y. Zhang, X. Cheng, Y. Li, L. Gu, K. Swierczek, High-Performance Anode Material $Sr_2FeMo_{0.65}Ni_{0.35}O_{6-\delta}$ with in Situ Exsolved Nanoparticle Catalyst, ACS Nano. 10 (2016) 8660–8669. doi:10.1021/acsnano.6b03979.

[83] D. Papargyriou, J.T.S. Irvine, Nickel nanocatalyst exsolution from (La,Sr)(Cr,M,Ni)O_3 (M=Mn,Fe) perovskites for the fuel oxidation layer of Oxygen Transport Membranes, Solid State Ionics. 288 (2016) 120–123. doi:10.1016/j.ssi.2015.11.007.

[84] K. Girona, S. Sailler, P. Gélin, N. Bailly, S. Georges, Y. Bultel, Modelling of gradual internal reforming process over Ni-YSZ SOFC anode with a catalytic layer, Can. J. Chem. Eng. 93 (2015) 285–296. doi:10.1002/cjce.22113.

[85] W. Ramli, Exsolved base metal catalyst systems with anchored nanoparticles for carbon monoxide (CO) and nitric oxides (NO_x) oxidation, Newcastle University, 2017.

[86] N. Laosiripojana, S. Assabumrungrat, Catalytic steam reforming of methane, methanol, and ethanol over Ni/YSZ: The possible use of these fuels in internal reforming SOFC, J. Power Sources. 163 (2007) 943–951. doi:10.1016/j.jpowsour.2006.10.006.

[87] V. Sadykov, N. Mezentseva, G. Alikina, R. Bunina, V. Pelipenko, A. Lukashevich, S. Tikhov, V. Usoltsev, Z. Vostrikov, O. Bobrenok, A. Smirnova, J. Ross, O. Smorygo, B. Rietveld, Nanocomposite catalysts for internal steam reforming of methane and biofuels in solid oxide fuel cells: Design and performance, Catal. Today. 146 (2009) 132–140. doi:10.1016/j.cattod.2009.02.035.

[88] A. Atkinson, S. Barnett, R. Gorte, J. Irvine, A. McEvoy, M. Mogensen, S. Singhal, J. Vohs, Advanced anodes for high-temperature fuel cells., Nat. Mater. 3 (2004) 17–27. doi:10.1038/nmat1040.

[89] A. Dicks, Advances in catalysts for internal reforming in high temperature fuel cells, J. Power Sources. 71 (1998) 111–122. doi:10.1016/s0140-6701(98)96936-3.

[90] P.S. Roy, N.K. Park, K. Kim, Metal foam-supported Pd-Rh catalyst for steam methane reforming and its application to SOFC fuel processing, Int. J. Hydrogen Energy. 39 (2014) 4299–4310. doi:10.1016/j.ijhydene.2014.01.004.

[91] G. Postole, F. Bosselet, G. Bergeret, S. Prakash, P. Gélin, On the promoting effect of H_2S on the catalytic H_2 production over Gd-doped ceria from CH_4/H_2O mixtures for solid oxide fuel cell applications, J. Catal. 316 (2014) 149–163. doi:10.1016/j.jcat.2014.05.011.

[92] S. Cheah, L. Massin, M. Aouine, M.C. Steil, J. Fouletier, P. Gélin, Methane steam reforming in water deficient conditions on Ir/$Ce_{0.9}Gd_{0.1}O_{2-x}$ catalyst: Metal-support interactions and catalytic activity enhancement, Appl. Catal. B Environ. 234 (2018) 279–289. doi:10.1016/j.apcatb.2018.04.048.

[93] C.H. Bartholomew, Catalysis reviews : science and reforming and methanation carbon deposition in steam reforming and methanation, Catal. Rev. Sci. Eng. 24 (1982) 67–112. doi:http://dx.doi.org/10.1080/03602458208079650.

Chapter 2

Natural gas steam reforming in water deficient conditions on a new Ni exsolved Ruddlesden-Popper manganite: catalytic behavior

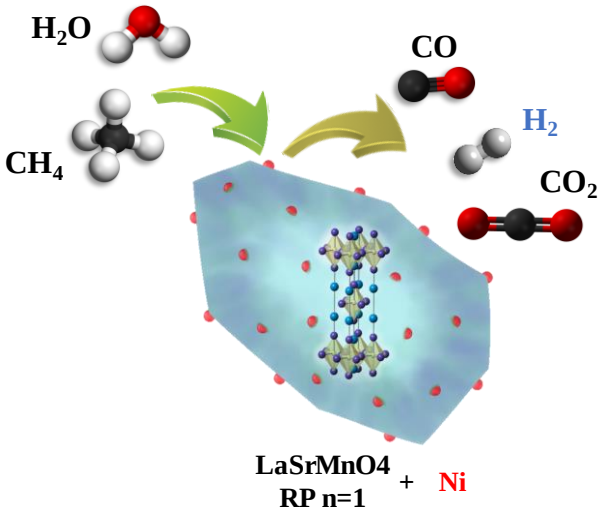

2.1. **Abstract**

In this research work, the complete catalytic behavior for the reforming reaction on the new Ni exsolved Ruddlesden-Popper (RP) manganite ($La_{1.5}Sr_{1.5}Mn_{1.5}Ni_{0.5}O_{7\pm\delta}$ LSMN n= 2) was studied. This material was synthesized by the Pechini method and reduced to induce the formation of two phases that correspond to the n = 1 RP structure $LaSrMnO_4$ decorated with metallic Ni nanoparticles. Ni impregnation on a similar $(La,Sr)_2MnO_{4\pm\delta}$ ceramic support was also prepared for comparison. The catalytic measurements for the steam reforming reactions were carried out in a reduction-reaction process with low water content (S/C = 0.15) and at different reaction temperatures (700, 800 and 850 °C). The exsolved material exhibits a better performance than the impregnated manganite for the methane steam reforming reaction, especially at 850 °C with higher conversion, conversion rate, and H_2 production rate. However, in light alkane gas mixtures (CH_4 - C_2H_6, and CH_4 -C_3H_8), the behavior is affected due to the competition between reactions and low available metallic active sites, without affecting the H_2 production. The exceptional overall results obtained in this new material are promising for future use as the anode in a SOFC fed with Colombian natural gas.

2.2. **Introduction**

Given the global energetic context, the solid oxide fuel cells (SOFC) appears as an interesting "clean" technology to produce electricity with high efficiency from different kind of hydrocarbon fuels [1]. Instead of the direct use of hydrogen which is still problematic because of remaining issues related to its handling, storage and distribution infrastructure, the direct internal steam reforming of hydrocarbons at the SOFC anode side is relevant [2]. This fuel flexibility in SOFC systems is possible due to high operating temperatures (T > 600 °C) allowing the "*in situ*" H_2 production by direct internal reforming at the anode side, which is consumed simultaneously by the electrochemical oxidation reaction, generating electricity and heat [3].

The most interesting and widely studied fuel for SOFC is the natural gas [3–5] consisting mainly of methane (CH_4), *e.g.* around 82 mol% in the Cusiana gas available in Colombia (Table 2.1) [6]. The methane steam reforming (MSR) is a highly endothermic reaction and is presented in Equation 2.1. In parallel to MSR reaction, the excessive addition of H_2O will further convert CO to CO_2 by the slightly exothermic Water Gas Shift (WGS) reaction represented as Equation 2.2. Methane overall steam reforming (Equation 2.3)

and methane dry reforming (MDR, Equation 2.4) could also be present, but they are dependent reactions [7].

Cusiana gas (Colombia)	
Compounds	**Composition [%mol]**
CH_4	82.195
C_2H_6	10.841
C_3H_8	3.510
CO_2	1.900
Minority hydrocarbons	1.035
N_2	0.519
H_2S	2-50 ppm

Table 2.1 Colombian natural gas (Cusiana) composition [6].

$$CH_4 + H_2O \leftrightarrow CO + 3H_2 \quad \Delta H^o = 206.1 \text{ kJ mol}^{-1} \qquad \textbf{Equation 2.1}$$

$$CO + H_2O \leftrightarrow CO_2 + H_2 \quad \Delta H^o = -41.2 \text{ kJ mol}^{-1} \qquad \textbf{Equation 2.2}$$

$$CH_4 + 2H_2O \leftrightarrow CO_2 + 4H_2 \quad \Delta H^o = 165.0 \text{ kJ mol}^{-1} \qquad \textbf{Equation 2.3}$$

$$CH_4 + CO_2 \leftrightarrow 2CO + 2H_2 \quad \Delta H^o = 247.3 \text{ kJ mol}^{-1} \qquad \textbf{Equation 2.4}$$

Nevertheless, the direct internal reforming is still facing two major issues: carbon deposition due to parasitic reactions such as methane cracking and thermomechanical problems [3]. According to the literature, steam to carbon ratios (S/C) higher than 1.0 are necessary to avoid the coke formation on the anode surface. However, such high S/C ratios dilute the amount of fuel and may lead to thermomechanical damages due to large temperature gradients in the anode side (the reforming reaction is strongly endothermic whereas the electrochemical reactions are exothermic) and condensation process of unreacted products due to presence of excess steam which are energetically unfavorable. Therefore, the process should be fed with low S/C ratios to produce an *in situ* additional steam by the electrochemical oxidation of the hydrogen obtained during the steam reforming reaction in the anode side [8,9]. This alternative strategy is called Gradual Internal Reforming - GIR (schematized in Figure 2.1), proposed by Vernoux *et al*. to avoid those problems [10], which were experimentally and theoretically demonstrated to result in the long-term stability of the cell operating without water excess [11,12]. On

the other hand, to improve the coke resistance and allow the cell's prolonged use, the development of new materials with specific (electro-)catalytic properties is necessary.

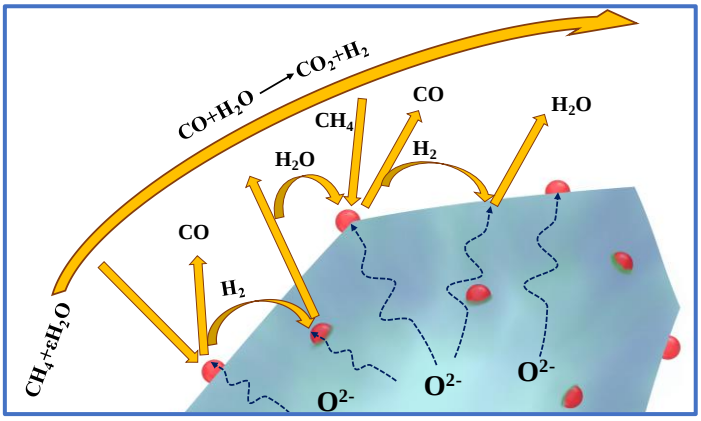

Figure 2.1 Diagram of the Gradual Internal Reforming process. Modified by the author from [10].

The conventional cermet based on nickel and yttria-stabilized zirconia (Ni/YSZ) exhibits unsatisfactory performance during operation with natural gas (methane) [13–15]. As described in Chapter 1 [16], one of the most promising alternatives is the development of Mixed Ionic and Electronic Conducting (MIEC) anode materials, in particular with Ruddlesden-Popper (RP) structure ($A_{n+1}B_nO_{3n+1}$ or $(AO)(ABO_3)_n$ consisting of n perovskite-like layers, ABO_3, separated by single rock salt-like layers, AO) [17]. The interesting transport properties of those materials coupled to their high thermal and mechanical stability not only in the air but in reducing atmosphere, make them now a valuable option for an application as SOFC electrode (cathode or anode) [18–26]. However, some authors recently pointed out their poor catalysis performance for direct use of methane (*e.g.* $La_{0.6}Sr_{1.4}MnO_{4\pm\delta}$ [27]).

The catalytic behavior of a MIEC anode can be improved by the addition of metallic nanoparticles. Most of the reported active metal are based on transition metals like Pt, Ru or Rh [28–30], however, compared to precious metals, nickel-based catalysts are desirable for SOFC industrial applications considering the availability and cost of such a metal. The addition of metallic nanoparticles can be realized by different methods. The exsolution technique leading generally to better performance and less degradation than conventional impregnation [31].

Previously, in Chapter 1 [16], the synthesis and exsolution conditions of a new RP material, $La_{1.5}Sr_{1.5}Mn_{1.5}Ni_{0.5}O_{7\pm\delta}$ (LSMN n= 2), was reported, with the aim to obtain, in reducing atmosphere, a biphasic material made of electrocatalytic active Ni metallic nanoparticles decorating a n= 1 RP $LaSrMnO_{4\pm\delta}$ manganite using *in situ* exsolution technique for short reduction times and high temperatures (up to 850 °C). The present work deals with the study of catalytic behavior for the steam reforming reaction using Colombian natural gas composition (methane, ethane, and propane) at low water content, comparing the behavior of the exsolved material to the conventional Ni impregnated manganite of the same RP structure.

2.3. **Methodology**

2.3.1. ***Materials Synthesis***

The manganite powders were synthesized by the Pechini or citrate complexation route [32]. In the case of $La_{1.5}Sr_{1.5}Mn_{1.5}Ni_{0.5}O_{7\pm\delta}$ (hereafter referred to as LSMN n= 2), the procedure is described in Chapter 1, section 1.3.1 [16]. For $La_{0.5}Sr_{1.5}MnO_{4\pm\delta}$ (LSMO n= 1), stoichiometric amounts of La_2O_3 (≥ 99.9 % Alfa Aesar), $SrCO_3$ (≥ 99.9 % Sigma Aldrich) and $MnCO_3$ (≥ 99.9 % Sigma Aldrich) were used. Before weighing La_2O_3 and $SrCO_3$, those reagents were calcined in air at 1000 and 500 °C, respectively, for 1 hour, to remove hydration products (and carbonation in the case of lanthanum oxide). The precursors were initially dissolved in a solution made of concentrated nitric acid (HNO_3, ≥ 65 vol% Merck) in excess and citric acid (CA, ≥99.5%Merck), added in the molar ratio $CA:(metal\ ion)_{total}$= 3:1. Under constant stirring, the resulting solution was slowly heated from room temperature to 120 °C using a hot plate to reduce the volume of liquid. Polyethylene glycol (≥ 99 %, Panreac) was added as a polymerizing agent (1.5 mL per gram of targeted product). Then, the resulting mixture was stirred and heated at 150 °C just to form a viscous gel, which was subsequently dried and heat-treated in air at 300 °C (2 h) and 500 °C (3 h) to ensure total organic matter decomposition Finally, the product was calcined in air at 1000 °C (6 h) and 1100 °C (6 h) with intermediate grinding and pelletizing steps.

In order to ensure a good homogeneity in the particle size of the synthesized materials (LSMN n= 2 and LSMO n= 1), the powders were individually ball-milled during 12 h at a speed of 50 rpm in a dispersion made of acetone:powder:3 mm-sized zirconia balls in a 5:1:5 weight ratio. After the milling step, the ceramic balls were removed, and the resulting mixtures were dried. Homogenous powders with a particle size distribution between 125 and 200 μm were finally obtained by adequate sieving, with the objective to eliminate intra-particle diffusion effects during the catalytic reactions [33].

2.3.2. *Fresh materials characterization*

Fresh LSMN n= 2 and LSMO n= 1 powders were characterized by powder X-ray diffraction (XRD) at room temperature (RT) using a Bruker D8-ADVANCE powder diffractometer operated in Bragg-Brentano geometry, equipped with a Lineal Lynx Eye detector and a beam of $CuK_{\alpha 1,2}$ radiation ($\lambda = 1.5418$ Å). The diffractometer was operated over the angular range $2\theta = 2 - 70°$ for qualitative analysis and $2\theta = 2 - 90°$ for Rietveld analysis with a measurement step of 0.020353° (2θ). The X-ray diffraction data were processed using JANA 2006 software package [34].

2.3.3. *Incipient wetness impregnation*

As the objective was to compare the behavior of exsolved LSMN n= 2 material to the catalyst produced by a more classical method, LSMO n= 1 powder was impregnated with Ni using Incipient Wetness Impregnation (IWI) technique, also known as pore volume impregnation. In the case of Ni, an aqueous nitrate solution ($Ni(NO_3)_2$) is normally used; in this case, a smaller Ni particle size has been reported in the literature, respect to other salts [35]. In this case, the Ni content was the same as obtained by the exsolution, *i.e.* ~0.05 mass fraction, as shown in Chapter 1 [16]. Into details, a solution of $Ni(NO_3)_2$ was prepared using stoichiometric amounts of $NiCO_3$ (≥ 99.9 % Alfa Aesar) and concentrated nitric acid (HNO_3, ≥ 65 %vol Merck), diluted in an ethanol:deionized water solution (20:80 mol%) to decrease the surface tension of pure water and increase the material´s wettability (Appendix H) [36]. The LSMO n= 1was impregnated with the correct volume (defined previously), dried at 110 °C during 12 h and after that, calcinated in the air at 500 °C during 90 min [37–40] to obtain the NiO/LSMO n= 1 material.

2.3.3.1 *Reduction study*

The operating temperatures (T) for the reduction study were selected considering the conditions of exsolution of LSMN n= 2 (750, 800 and 850 °C) described in Chapter 1 [16]. Around of 0.5 g of fresh NiO/LSMO n= 1 material was reduced in a tubular furnace CARBOLITE CTF 12/65/550 using a 3 mol% H_2/N_2gas mixture (Cryogas) with a flow of 55 mL (STP) min^{-1} and the lowest reduction times to obtain the complete exsolution different reduction times (t_r: 4 and 8 h); also selected considering the lowest times to obtain the complete exsolution (t_r= 4 or 8 h) [16]. The powder obtained at each temperature-reduction time point (Ni/LSMO n= 1) was characterized by XRD at RT as is described in Section 2.3.2. Besides, the material was analyzed by X-Ray Fluorescence spectroscopy (XRF) in an S2 Ranger Bruker spectrometer equipped with a Pd X-ray

tube, to confirm the correct amount of impregnated Ni. A morphological characterization was performed on the reduced powder by scanning electron microscopy (FEG-SEM) in a FEG Quanta 650 microscope at high vacuum, acceleration voltage of 25 kV, secondary electrons (SE) signal, Everhart Thomeley Detector (ETD) and by transmission electron microscopy (TEM) in an FEI TITAN Themis 300 equipped with a Super-X quad EDS for elemental analysis. In this case, the powder was crushed and dropped in the form of alcohol suspension on carbon-supported copper grids followed by evaporation under ambient conditions.

2.3.4. ***Catalytic test***

2.3.4.1 *Experimental set-up*

The measurements of the catalytic behavior for steam reforming were carried out using the experimental set-up described in Chapter 1 section 1.3.4.1 [16]. The composition of each effluent constituent was obtained by a gas chromatograph (GC, SRI instruments 8610C) using He (grade 5.0, CRYOGAS) as mobile phase, equipped with a solenoid gas sampling valve heated at 60 °C, two packed columns (molecular sieve 13X 6 in and hayesep D 6 in), a thermal conductivity detector (TCD) heated at 150 °C and controlled by PeakSimple 4.44 free software. Standard gas cylinders with different gas compositions were employed for the outlet products quantification.

2.3.4.2 *Preliminary tests: conditions for intrinsic kinetics*

Preliminary tests were carried out to confirm that the experiments correspond to the region of intrinsic kinetics, in which the heat and mass transport resistances are negligible, and for which the changes observed on molar concentrations are exclusively due to chemical reactions applied in the process. Therefore, to ensure a plug flow pattern and minimize back mixing, the recommendations described in the literature suggest, on one hand, a ratio between the catalyst bed length (L) and the particle size (d_p) upper than 50 ($L/d_p > 50$) and on the other hand, a ratio between the inner diameter of the reactor (D_r) and d_p upper than 10 ($D_r/d_p > 10$) [41–43].

LSMN n= 2 material was diluted with SiC grains (SiC:catalyst 10:1 weight ratio) to minimize heat-transfer effects [44] and introduced in the reactor as fixed-bed between catalyst-free SiC and two pieces of quartz wool. Considering the results obtained in the last section of Chapter 1 [16], the amount of catalyst was fixed to 50 mg to ensure both

the CH_4 conversion and the composition of products being far from the thermodynamic equilibrium.

Finally, to avoid external diffusional limitations, *i.e.* interphase concentration gradients between gas and solid surface, preliminary experiments were performed, based on the principle that the reactant conversion at any space velocity (*e.g.* Volume Hourly Space Velocity, VHSV) should be independent of the linear velocity through the catalyst bed when the external diffusional conditions are negligible. Therefore, different tests were performed keeping the VHSV value as a constant, while increasing both, the input volumetric flow rate (volume of inlet gas per unit time) and catalyst volume (or weight). During those tests, the reactant conversion is expected to change while the interphase limitations (external diffusion) are present [33,45]. The range of input volumetric flow rate that avoids external diffusional limitation is thus obtained when the reactant conversion does not change, which allow to determine the correct operating conditions, *i.e.* volumetric flow rate and catalyst amount. Considering that CH_4 is the most abundant hydrocarbon in Cusiana gas, Colombia, (Table 2.1), these tests were carried out using only a dry mixture of 82 mol% CH_4 (N_2 as balance) humidified to a steam to carbon ratio (S/C) of 0.15 at different reactor inlet flow rates. It is worth noting that before this test, the catalyst sample was *in situ* reduced using 55 mL (STP) min^{-1} of 3 mol% H_2/N_2 mixture (Cryogas) during 4 h at T= 850 °C, as defined in Chapter 1 [16].

2.3.4.3 *Operating conditions for catalytic tests*

LSMN n= 2 catalyst was preliminarily reduced (*in situ* conditions) using 55 mL (STP) min^{-1} of 3 mol% H_2/N_2 mixture (Cryogas) at previously selected temperatures of 750, 800 or 850 °C. At 750 °C, the reduction time was t_r=8 h, *i.e.* the minimum condition to reach the complete Ni exsolution (Chapter 1 Section 1.4 [16]). In the case of 800 and 850 °C, t_r was fixed to 4 h that corresponds to the completion of the exsolution process, and 8 h for better comparison with T=750 °C.

The catalytic behavior at each operating condition was measured during 8 h using atmospheric pressure and the same reducing temperature as for the catalytic test. The starting reaction mixture was fixed to 82 mol% CH_4 (N_2 as balance) humidified up to S/C= 0.15 according to the SOFC anode conditions suggested by the GIR concept [10]. The steam content was adjusted by flowing the adequate dry CH_4-N_2 mixture throughout the bubbler containing distilled water maintained exactly 46 °C. The composition in each effluent constituent was obtained at regular time intervals (each 20 min) using online GC analysis (method described in Appendix B). For the NiO/LSMO n= 1 (impregnated material) the reaction procedure was the same described for exsolution material (LSMN

n= 2). In the case of LSMO n= 1 material, the steam reforming reaction was started without a prior reduction step.

Considering the composition of Colombian natural gas in which ethane (C_2H_6) and propane (C_3H_8) are also present with methane but in lower concentration, additional tests were carried out at their respective molar compositions (Table 2.1). Therefore, this study used mixtures of ethane – N_2 (10 mol% C_2H_6), propane – N_2 (4 mol% C_3H_8), CH_4-C_2H_6 and CH_4-C_3H_8 mixtures.

The individual light hydrocarbons conversion $\left(X_{C_nH_{2n+2}}\right)$, their conversion rate, and H_2 formation rate were calculated as is shown in Equation 2.5, Equation 2.6 and Equation 2.7 respectively.

$$X_{C_nH_{2n+2}} = \frac{n^{In}_{C_nH_{2n+2}} - n^{Out}_{C_nH_{2n+2}}}{n^{In}_{C_nH_{2n+2}}} \times 100 \quad [\text{mol\%}] \qquad \textbf{Equation 2.5}$$

$$C_nH_{2n+2} \text{ conversion rate} = \frac{n^{In}_{C_nH_{2n+2}} - n^{Out}_{C_nH_{2n+2}}}{W_{Cat}} \quad [\text{mmol min}^{-1}\text{g}^{-1}] \qquad \textbf{Equation 2.6}$$

$$H_2 \text{ formation rate} = \frac{n^{Out}_{H_2}}{W_{Cat}} \quad [\text{mmol min}^{-1}\text{g}^{-1}] \qquad \textbf{Equation 2.7}$$

Where, W_{Cat} is the catalyst weight (g), $n^{In}_{C_nH_{2n+2}}$ and $n^{Out}_{C_nH_{2n+2}}$ are the individual light hydrocarbons molar flow rate at the inlet and outlet of the reactor (mmol min^{-1}) and $n^{Out}_{H_2}$ is the H_2 molar flow rate at the outlet of the reactor (mmol min^{-1}).

Besides, the selectivities $\left(S_j\right)$ of CO, CO_2, C_2H_4, C_2H_6, and C_3H_6, were defined as the ratio between the molar flow rate of all carbon atoms in the outlet of the selected *j* product and, that of the reacted light hydrocarbons *i* employed as reactants as Equation 2.8 shows, where φ is the carbon number of the selected j product or *i* reactive and *n* the molar flow rate.

$$S_j = \frac{\varphi_j \, n_j^{Out}}{\sum_{i=1}^{N} \varphi_i \left(n_i^{In} - n_i^{Out}\right)} \quad [\text{dimensionless}] \qquad \textbf{Equation 2.8}$$

Finally, H_2 to CO ratio was defined by Equation 2.9.

$$\frac{H_2}{CO} = \frac{n_{H_2}^{Out}}{n_{CO}^{Out}} \quad [\text{dimensionless}] \qquad \textbf{Equation 2.9}$$

It is worth noting that blank tests were done at different temperatures using only SiC, and no conversion was observed for methane and the other light hydrocarbon compounds.

2.4. **Results**

2.4.1. ***Catalysts study***

As shown in Chapter 1 [16], the LSMN n= 2 material exhibits a Ruddlesden-Popper (RP) structure with 2 layers of octahedra in the perovskite-like stack and tetragonal space group *I4/mmm* (No. 139). The calculated parameters by Rietveld refinement are *a*=*b*= 3.8543(2) Å, *c*= 20.1898(19) Å and *Vol.*= 299.93(4). On the other hand, the LSMO n= 1 material was selected to be synthesized and subsequently impregnated due to its structural similarity with the $LaSrMnO_4$ (hereafter referred to as LSM n= 1) obtained as support after the Ni exsolution in LSMN n= 2 and the simplicity to be prepared in air. This material also exhibits a RP structure with 1 layer of octahedra in the perovskite-like stack and tetragonal space group *I4/mmm* (No. 139). A total of 9 sets of ~3 g of corresponding material, were synthesized according to the methodology. For each synthesis, the lattice parameters (*a*=*b*, *c*) and the unit-cell volume were determined from the XRD data using structure refinement based on the Full Pattern Matching – Le Bail method. The comparison of the results allowed the selection of the samples to be mixed (or discarded), obtaining a final homogeneous stock of around 20 g of pure phase material (Appendix I).

The structure of the as-obtained LSMO n= 1 powder was successfully refined using Rietveld method based on X-ray diffraction data and pseudo-Voigt peak shape function with reasonable reliability factors of R_p = 5.40 %, R_{wp} = 3.78 %, and χ^2 = 1.99 and very few residual intensity, as observed graphically in Figure 2.2. The refined lattice parameters are *a*=*b*= 3.8605(9) Å, *c*= 12.4143(30) Å and *Vol.*= 185.020(8) $Å^3$, these results are in satisfactory agreement with literature [46–51]. In addition, the sample exhibits a small peak of $SrCO_3$ impurity around 25 º, which could be removed increasing

the sintering temperature to 1300 ºC [46] but possibly affecting the microstructural properties; hence in this research, it was decided to remain with a slightly impure LSMO n= 1 sample.

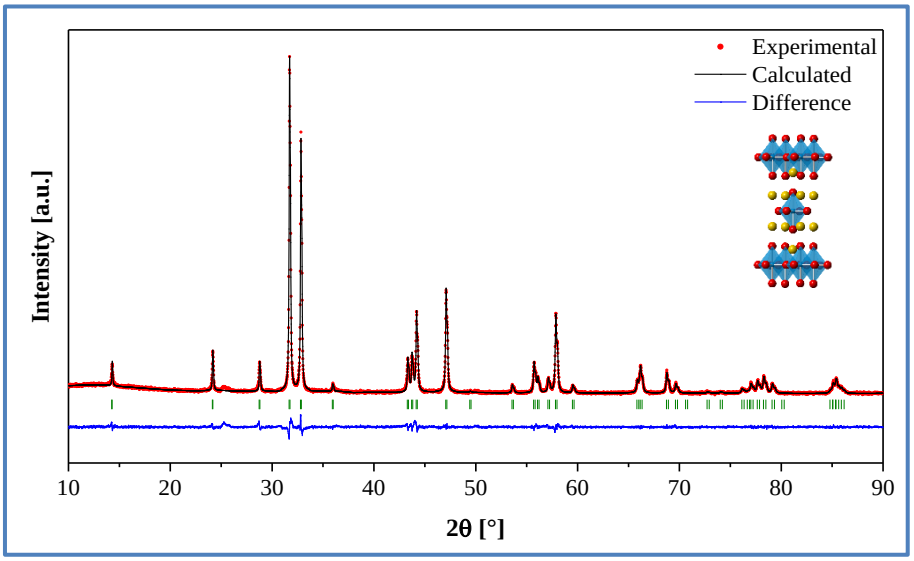

Figure 2.2 LSMO n= 1 Rietveld refinement using XRD data.

Once the LSMO n= 1 has been obtained, the powder was impregnated according to the methodology and after that, reduced at the selected T and t_r. The XRD patterns of these results are presented in Figure 2.3. Extra peaks are evidenced at 2θ= 44.5 and 51.9° (highlighted as red dots), which are associated with the presence of Ni [52]. Additionally, it can be observed that the support structure remains stable; so, in each case, a structure refinement based on the Full Pattern Matching – Le Bail method was successfully carried out, employing a tetragonal system with *I4/mmm* space group, like the as-synthesized sample, and an FCC cubic cell with *Fm-3m* space group for Ni.

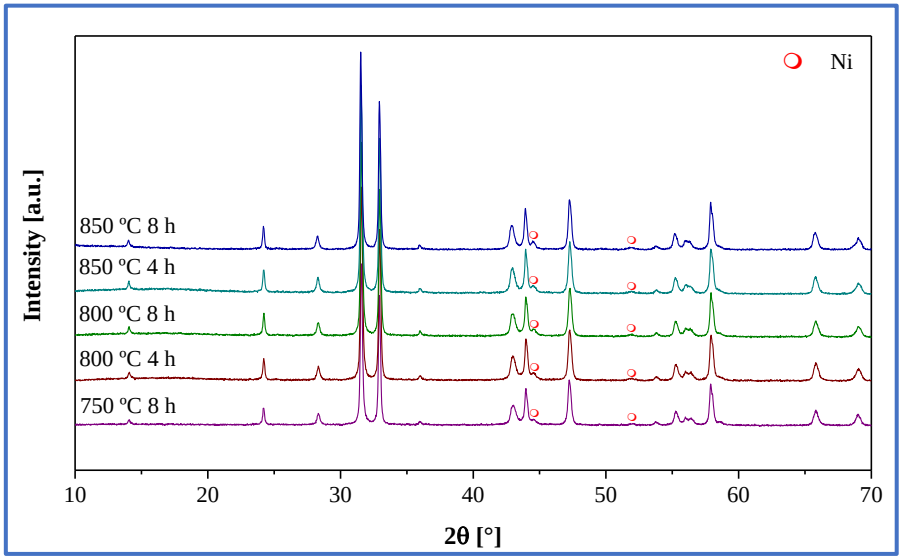

Figure 2.3 Ni/LSMO n = 1 material obtained at different temperature (T) and reduction time (t_r).

The refined lattice parameters of both phases (LSMO n= 1 and Ni) are presented in Figure 2.4 (A–C) with reasonable reliability factors of R_p= 3.97 – 4.18 %, R_{wp}= 5.57 - 5.61 % and "goodness of fit (GOF)" or χ^2= 1.56 - 1.68 (χ^2 values between 1.0 and 2.9 are generally considered satisfactory [53]) also confirmed by the graphical analysis of each refinement. By comparison with the values obtained in the oxidized phase LSMO n= 1, an expansion of the *c*-parameter and the unit-cell volume is evidenced, in agreement with Sandoval *et al.* [46]; such effect is related to the reduction of Mn^{4+} to Mn^{3+} and the generation of oxygen vacancies (δ) in the oxide structure. However, although the calculated values are not exactly the same as reported by those authors (*a*=*b*= 3.8378(3) Å, *c*= 12.7286(13) Å, *Vol.*= 187.48(3) $Å^3$ [46]), the trend remains, the small deviations being probably related to the difference of reduction time employed (16 h at 850 ºC) and therefore to the sample reduction degree. In the case of Ni, in all samples, the lattice parameters remain the same and agree well with the literature values [52]. The amount of impregnated Ni was confirmed by XRF using the sample reduced at 850 ºC for 4 h. The measured Ni mass fraction is 0.059 ± 0.004 (Appendix J), in reasonable agreement with the desired theoretical Ni concentration (~0.05 mass fraction) [16].

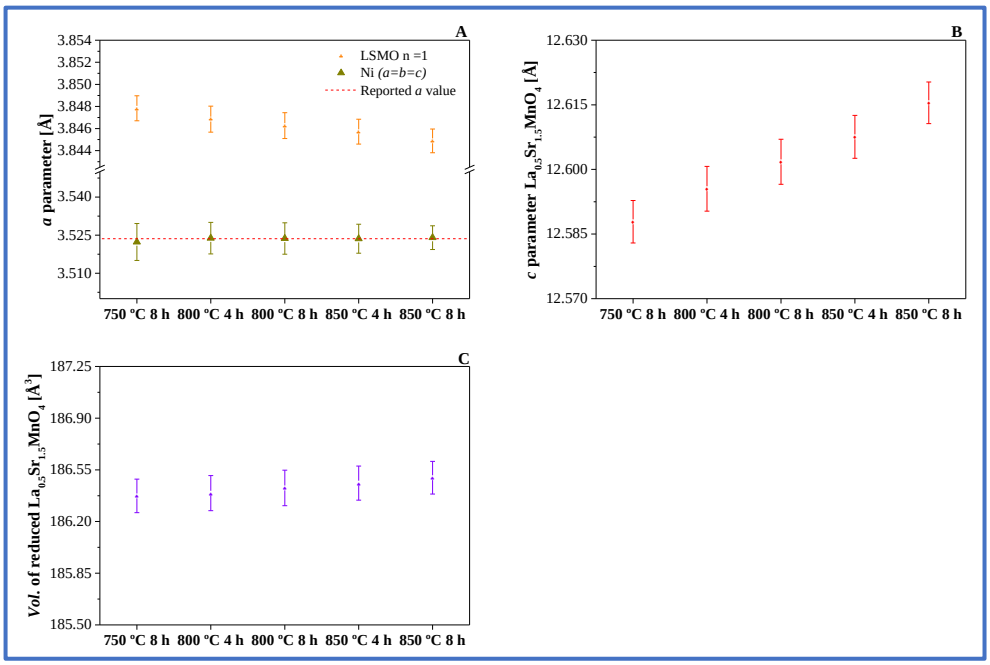

Figure 2.4 Full Pattern Matching refinement using XRD data for impregnated LSMO n= 1 reduced at 750, 800 and 850 °C during 4 and 8 h. A) *a* parameter of reduced LSMO n= 1 and Ni B) *c* parameter of reduced LSMO n= 1 C) Unit-cell volume of reduced LSMO n= 1.

To complete the XRD results, FEG-SEM images (Figure 2.5 A–C) exhibit the presence of nickel spherical nanoparticles with less than 50 nm of average size, decorating the surface of the manganite oxide, confirming the successful impregnation of the support. In addition, a TEM image and energy dispersive X-ray (EDX) concentration mapping of the main elements for a characteristic zone of the Ni-impregnated LSMO n= 1 powder after reduction at 850 °C for 4 h are shown in Figure 2.6. The corresponding elemental mapping confirms the composition for the manganite support, *i.e.* La, Sr, and Mn are homogeneously distributed in the entire grain. The presence of Ni is evidenced as a few isolated spots which consist of metallic Ni. It is worth noting that nickel is deposited as hemispherical Ni particles in only specific zones of the surface, suggesting that, using impregnation method, the active phase is not uniformly distributed on the support, as has been reported in the literature [54–56]; such results differ from those obtained in the case of exsolution, for which the surface is covered with anchored (strong particle - oxide matrix interaction) small and uniformly distributed Ni nanoparticles (less than 40 nm Chapter 1 [16]). These differences will be key factors that probably influence the materials´ performance, activity, selectivity, and stability during the steam reforming reactions.

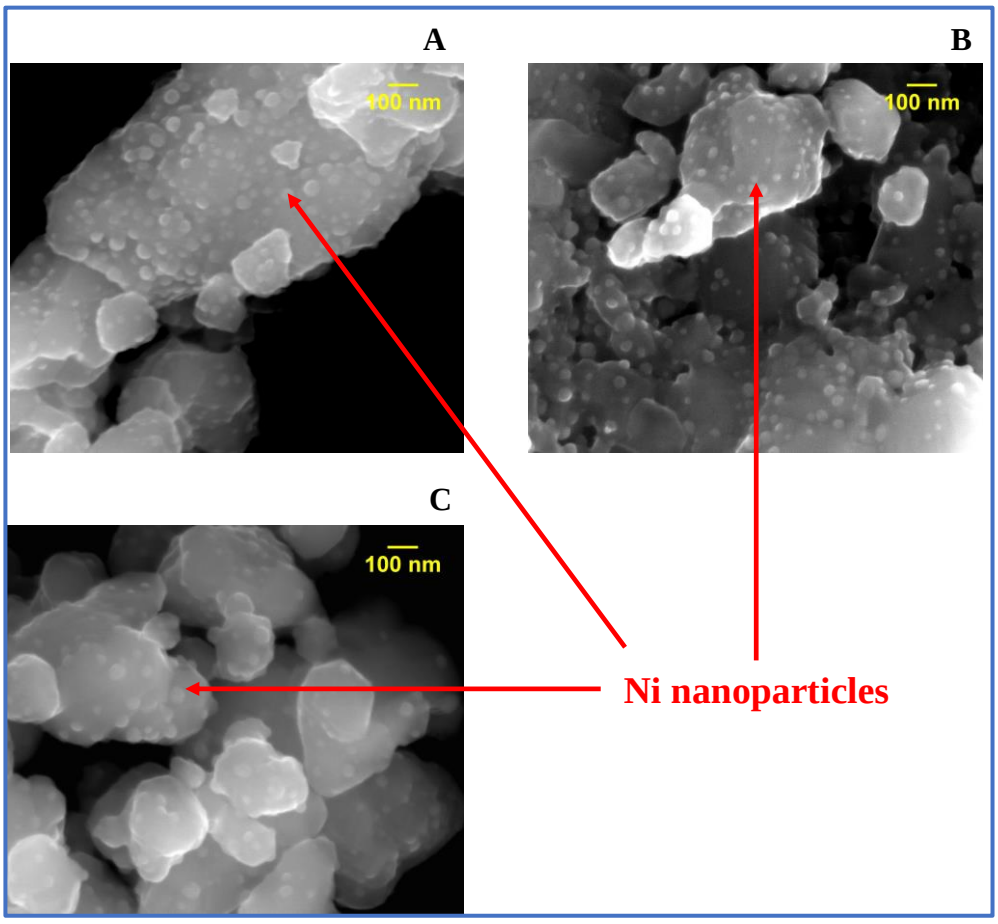

Figure 2.5 SEM image of reduced material at A) 750 °C for 8 h, B) 800 °C for 4 h and C) 850 °C for 4 h.

The average Ni particle size ($\overline{D}_p$) was determined at different reduction conditions (T and t_r) using the scanning electron micrographs (SEM), based on about 100 particles in four selected T – t_r conditions to obtain characteristic frequency histograms. The grouped particle size data were analyzed using as likelihood fitting method a lognormal distribution as already described in Chapter 1 [16] for exsolved material; the selected distributions are shown in Appendix K. In the impregnated LSMO n= 1 material, reduced at 850 °C during 4 h, the calculated $\overline{D}_p$ value is 38.20 ± 2.43 nm, similar to the value obtained for an 8 h treatment ($\overline{D}_p$=38.68 ± 2.13 nm); the material nanostructure seems not to be significative affected by the reduction treatment duration. However, when the

temperature decreases to 800 and 750 °C, the calculated $\overline{D}_p$ value is significative smaller (34.84 ± 1.46 nm and 32.85 ± 1.62 nm, respectively). As a conclusion, the temperature seems to have more influence on the particle size, in agreement with what has been described by other authors [54,57,58]; this is also coherent with the results we presented and discussed in Chapter 1 [16] for Ni exsolution.

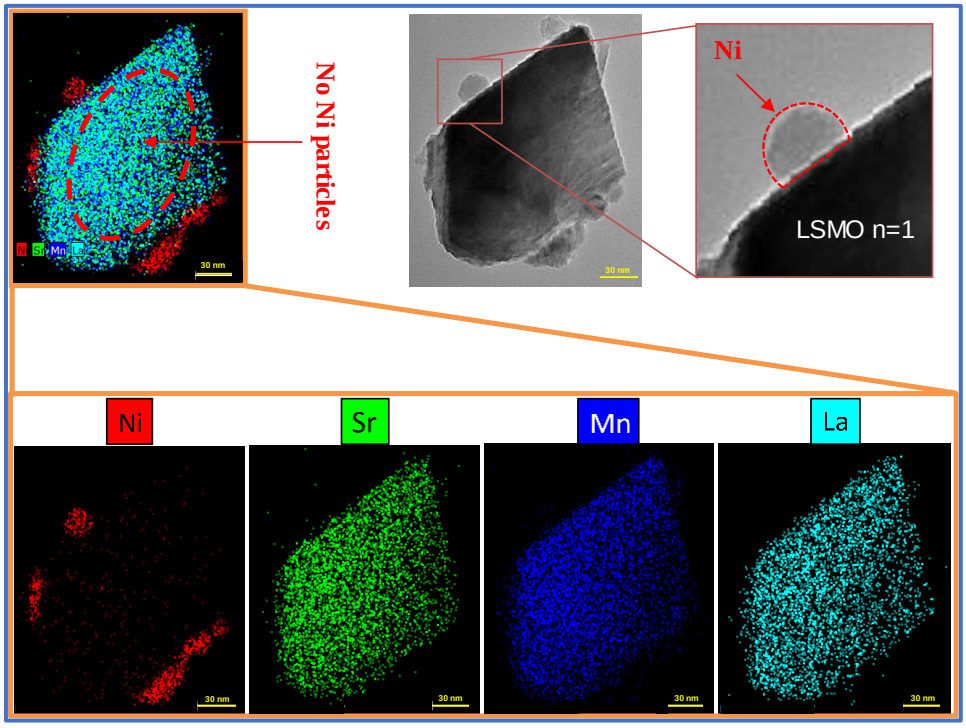

Figure 2.6 TEM image of Ni-impregnated LSMO n= 1 reduced at 850 °C for 4 h, On top, zoom of a Ni nanoparticle (bright field). On the bottom, the elemental grain mapping (dark field).

2.4.2. *Preliminary tests: conditions for intrinsic kinetics*

A preliminary test was carried out to guarantee that the experiments will be carried out within a region of intrinsic kinetics, and to define the adequate flow to be used at the reactor inlet. The selected reagent flow rate was first fixed at the same value as for the exploratory test presented in Chapter 1, *i.e.* 128 mL (STP) min^{-1} dry basis or 143.7 mL (STP) min^{-1} wet basis [16]. The other two points to evaluate the kinetic regime were

defined by multiplying and dividing the flow rate by a factor 1.5. For these tests, the VHSV value was 172000 mL (STP) g^{-1} h^{-1}. The corresponding results are illustrated in Figure 2.7.

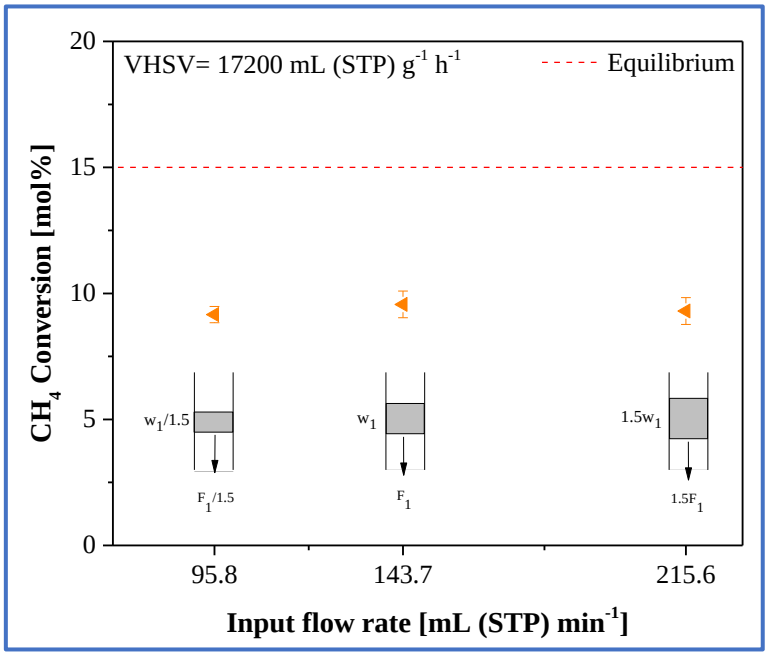

Figure 2.7 Influence of the input flow rate on CH_4 conversion at constant space velocity.

In the steady-state conditions, an average CH_4 conversion of 9.30 ± 0.40 mol% was reached without significant variation between the three evaluated points, indicating a kinetic regime, with no limitations by external diffusion, in this range of operating conditions and for the selected VHSV value. Based on these results and considering the thermodynamic equilibrium, a volumetric flow rate of 143.7 mL (STP) min^{-1} wet basis was chosen for the following catalytic study.

2.4.3. *Methane catalytic steam reforming reaction*

A series of catalytic tests were performed with CH_4 at a total exposure time of 8 h. The performance of the 3 synthesized catalytic materials, LSMO n= 1 (support), Ni/LSMO

n= 1 (impregnation) and Ni/LSM n=1 (exsolution), was evaluated in terms of CH_4 molar conversion. The results are shown in Figure 2.8.

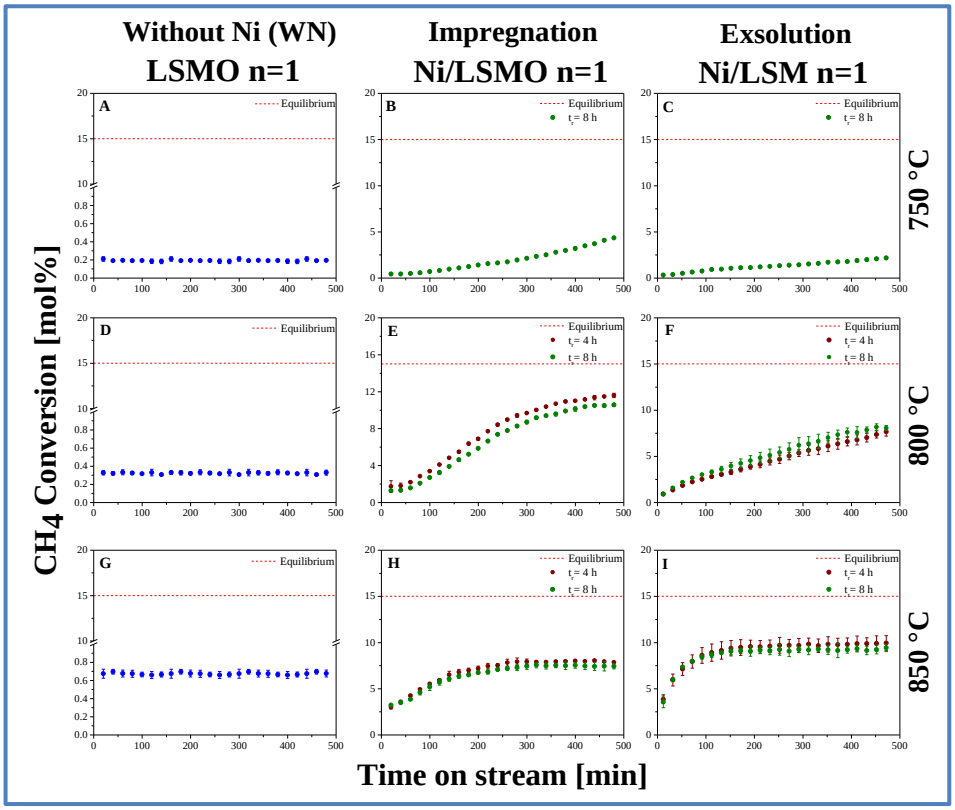

Figure 2.8 CH_4 conversion at different reaction temperatures (750, 800 and 850 °C) during 4 and 8 h of exposure to reactive gas and employing LSMO n= 1 (support), Ni/LSMO n= 1 (impregnation) and Ni/LSM n= 1 (exsolution) as catalysts.

First, low catalytic activity is evidenced for the support material, reaching less than 1 mol % of CH_4 conversion values at different temperatures (T= 750, 800 and 850 °C), which is stable during the time on stream (8 h). Such result indicates the lack of influence of the supporting manganite on the catalytic properties of Ni-impregnated or exsolved catalysts. Tao *et al.* [59] also reported, for the manganite oxide $La_{0.75}Sr_{0.25}Cr_{0.5}Mn_{0.5}O_{3\pm\delta}$, an insignificant catalytic behavior of the perovskite for the same reaction, even at higher S/C ratio. Generally speaking, such doped lanthanum manganites are not very active and are not employed as a pure phase for CH_4 reforming reactions, but their secondary role

to promote nickel-based reforming catalysts has been recognized, making them very good candidates as catalytic support [60].

For all the Ni-containing catalysts, the catalytic behavior at different exposure times is represented by two different zones: the CH_4 conversion is initially low but gradually increases until it reaches a constant value corresponding to steady-state conditions. In a similar way as presented by other authors [61–65], such behavior is maybe related to surface modifications during the steam reforming reaction. Therefore, the analysis of the results was performed considering the average values from data measured in this stable zone for conversion, *i.e.* conversion rate, H_2 formation rate, selectivities of C compounds formed and H_2 to CO ratio (Equation 2.5 to Equation 2.9).

A reason to explain such catalytic behavior of the Ni-containing materials (Figure 2.8) would be the partial reoxidation of the Ni particle surface as reported in the literature [66–68]. Such phenomenon could be attributed in this case to the increasing oxygen partial pressure (PO_2) due to the presence of steam in the reactor, despite being in low concentration. This partial oxidation is probably reversed while H_2 is produced and H_2O consumed, even though it is slow at low temperature *e.g.* 750 and 800 °C, in which the catalytic behavior did not reach a stable zone during the 8 h of the test.

In the steady-state conditions, impregnated and exsolved materials show a CH_4 conversion much higher than that obtained for LSMO n= 1 (support) for all reaction temperatures (T= 750, 800 and 850 °C); however, the steady-state conditions are achieved at different rates. At 750 °C, the conversion increases slowly in both samples, reaching values below 5 mol% without a visible steady-state condition after 8 h of exposure to reactive gas. The results show that a stable value of CH_4 conversion at this temperature and using impregnated material is achieved faster than that observed for exsolved material. The catalytic behavior improves significantly at 800 °C compared with that obtained at 750 °C. The reaction is promoted by the temperature. However, during the 8 h of exposure to reactive gas, a steady-state condition is still not reached hindering an adequate comparison between catalysts. The steady-state condition is obtained for both materials at 850 °C, being faster for the exsolved material. On the other hand, it is worth noting that the catalytic behavior observed for both materials indicates that the reduction times (t_r) used during the pretreatment of materials (4 and 8 h) do not have a significant effect on CH_4 conversion at a temperature higher than 800 °C. Hence, a 4 h treatment for pre-reduction seems high enough to get a stable performance of the catalyst.

At 850 °C and in steady-state conditions (Table 2.2), the CH_4 conversion reaches 9.71 mol% using exsolved material with a conversion rate of 8.17 mmol min^{-1} g^{-1} and H_2 formation rate of 23.5 mmol min^{-1} g^{-1}, while the impregnated material allows a CH_4 conversion of 7.89 mol% with a conversion rate of 6.65 mmol min^{-1} g^{-1} and H_2 formation rate of 19.6 mmol min^{-1} g^{-1}.

	Reduction time [h]	**Impregnated**	**Exsolved**
CH_4 conversion [mol%]	4	7.89 ± 0.20	9.71 ± 0.50
	8	7.40 ± 0.14	9.19 ± 0.50
CH_4 conversion rate [mmol min^{-1} g^{-1}]	4	6.65 ± 0.10	8.17 ± 0.40
	8	6.24 ± 0.10	7.90 ± 0.10
H_2 production rate [mmol min^{-1} g^{-1}]	4	19.6 ± 0.5	23.5 ± 1.00
	8	18.3 ± 0.30	22.4 ± 0.30
Outlet dry gas composition [mol%]			
N_2	4	16.36 ± 0.20	16.03 ± 0.10
	8	16.77 ± 0.20	16.09 ± 0.20
H_2	4	15.80 ± 0.13	18.31 ± 0.20
	8	14.86 ± 0.20	17.61 ± 0.18
CH_4	4	62.49 ± 0.16	59.29 ± 0.30
	8	63.31 ± 0.36	60.22 ± 0.36
CO	4	4.39 ± 0.08	5.51 ± 0.10
	8	4.09 ± 0.10	5.23 ± 0.06
CO_2	4	0.96 ± 0.02	0.86 ± 0.02
	8	0.97 ± 0.02	0.86 ± 0.02
S_{CO}	4	0.80 ± 0.01	0.86 ± 0.01
	8	0.79 ± 0.01	0.86 ± 0.01
S_{CO_2}	4	0.20 ± 0.01	0.14 ± 0.01
	8	0.21 ± 0.01	0.14 ± 0.01
H_2/CO ratio	4	3.60 ± 0.04	3.32 ± 0.03
	8	3.63 ± 0.04	3.36 ± 0.03

Table 2.2 Methane steam reforming catalytic results at 850 °C: exsolved material vs impregnated material pretreated at 850 °C during 4 and 8 h.

The exsolved material exhibits better catalytic performance than the catalyst prepared by Ni-impregnation in the working operating conditions. It is worth mentioning the particular behavior observed for the impregnated material at 850 °C. At this temperature, CH_4 conversion is lower than the apparent value reached for the same material at 800 °C. This behavior can be attributed to the Ni particle coarsening due to the increase of the temperature, reducing the number of catalytic active sites, as suggested by various authors [54,57,58]. To confirm such assumption, the impregnated materials (Ni/LSMO n= 1 reduced during 4 h) were analyzed by Scanning Electron Microscopy (SEM) after reaction at 800 and 850 °C and compared to fresh materials; the results are presented in Figure 2.9 (Appendix L). A rise in the average particle size is clearly evidenced for a reaction temperature of 850 °C ($\overline{D}_p$ =38.20 ± 2.43 nm vs $\overline{D}_p$ =62.97 ± 3.02 nm before and after reaction, respectively) while at 800 °C, the Ni particle size does not significantly change ($\overline{D}_p$ =34.86 ± 1.46 nm vs $\overline{D}_p$ =35.62 ± 1.62 nm before and after reaction, respectively). In this way, the effect of temperature on the coarsening of Ni nanoparticles is particularly critical for the impregnated material, explaining the decrease in the CH_4 conversion of the sample operating at 850 °C.

The improvement of CH_4 conversion when the exsolved material is used, by comparison to impregnation, can be attributed to the strong nanoparticle-matrix oxide interaction given by the exsolution mechanism. In an exsolved material, the metallic active particles are embedded into the oxide support contrary to the impregnated active phases in which the particles are just deposited on the support surface [58,69]. Such characteristic makes the exsolved particles less mobile on the surface and the coalescence rate is considerably decreased; this phenomenon can only occur when the particles are very close to each other. This phenomenon is evidenced by SEM, in the case of exsolved material pretreated at 850 °C during 4 h: there is no statistically difference between both values of the average particle size, so the sintering effect is not appreciable ($\overline{D}_p$= 39.81 ± 2.21 nm vs $\overline{D}_p$= 41.83 ± 1.99 nm before and after reaction, respectively, Appendix L). Consequently, particle migration cannot be the dominant mechanism due to the strong nanoparticle-matrix oxide interaction with practically null sintering by crystallite migration [70–72]. However, as explained in Chapter 1 [16], the particle coarsening does not completely disappear, as another mechanism may take place known as atomic migration or Ostwald ripening process. Such mechanism is slower than the particle migration and describes the growth of a larger particle by consuming a smaller one without direct connection; clusters of atoms from a small particle migrate through the oxide surface and merge into another large particle to reach the equilibrium. This effect becomes much serious when the temperature increases [71,73].

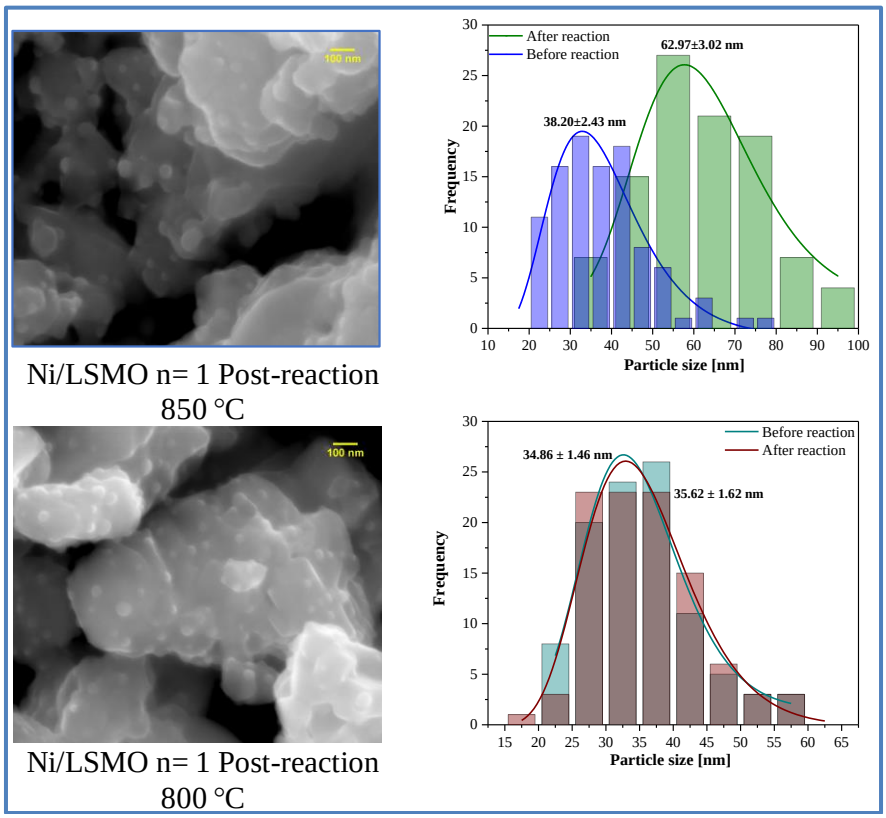

Figure 2.9 Ni particle size distribution in Ni/LSMO n= 1 (impregnation) before and after the methane steam reforming reaction at 800 and 850 °C.

Concerning the selectivity towards C-containing products present in the reaction (CO and CO_2), the comparison for T= 850 °C and t_r= 4 and 8 h is presented in Table 2.2. In the case of CO, the obtained values for calculated average selectivity seems to be higher than for CO_2, in both cases of exsolved and impregnated materials. It globally means that Ni metal exhibits a high activity as reported previously [74–76] and that selectivity is not affected by the reduction time (t_r). These results also indicate that the Methane Steam Reforming (MSR) reaction (Equation 2.1) dominates on Water Gas-Shift (WGS) reaction (Equation 2.2), in agreement with the conditions of low S/C ratio (low S/C ratio will increase the CO selectivity and the CO_2 selectivity for higher ratios [77]). To confirm such analysis, the H_2/CO ratio was calculated for both materials in the same operating conditions (Table 2.2). Those values are higher than 3.00 (stoichiometric value for MSR reaction), confirming that the WGS reaction is well present, to a lesser extent, during the catalytic test, which consumes CO and produces H_2 as well as CO_2, being

particularly the case for the impregnated material. In conclusion, although for both materials the selectivity to MSR reaction is higher, the impregnated material is significative less selective than the exsolved material, the latter case being more interesting for a SOFC anode application.

The results presented above are coherent with the thermodynamic data of the most important reactions occurring during methane reforming as shown by the behavior of Gibbs free energies (ΔG) as a function of temperature (Figure 2.10). At 850 °C and 1 atm, MSR and MDR are the most preponderant reactions due to their endothermicity, being spontaneous at temperatures higher than 620 and 641 °C, respectively. On the other hand, the WGS reaction is only favored at high steam and low H_2 content [78] and thermodynamically promoted at low temperatures (lower than 823 °C), as it is moderately exothermic. Then, in the present operating conditions, a low CO_2 production is expected, indicating the moderate participation of MDR; it results in a high CO concentration and, thereby, a greater selectivity to the MSR reaction with respect to other reactions.

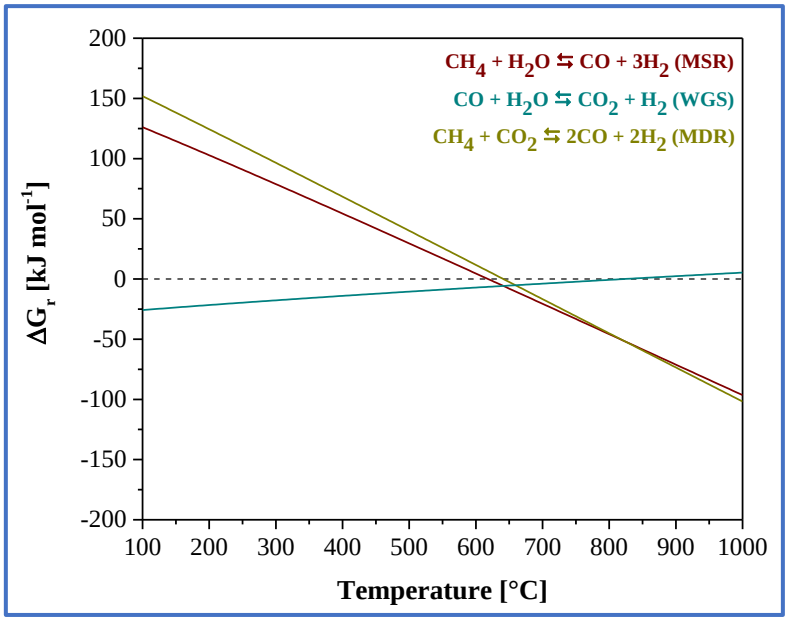

Figure 2.10 Variation of the Gibbs free energy (ΔG) with the temperature of all possible reactions during methane (CH_4) reforming reactions: Methane Steam Reforming (MSR), Water Gas Shift (WGS), Methane Dry Reforming (MDR). (Data taken from [79]).

Then, as a partial conclusion, both catalysts are clearly active for H_2 production, but the exsolved material seems a better option due to the higher CH_4 conversion, H_2 production, selectivity for the MSR reaction. This is probably due to a lower propensity for Ni-particles coarsening.

2.4.4. *Catalytic tests: Other light hydrocarbon steam reforming reactions*

Considering the composition of Colombian natural gas in which other minor hydrocarbon compounds such as ethane (C_2H_6) and propane (C_3H_8) are also present (Table 2.1), additional experiments were performed using CH_4 – C_2H_6, and CH_4 – C_3H_8 mixtures. Steam deficient conditions were kept constant in agreement with the GIR concept (S/C= 0.15). The tests were carried out at different reaction temperatures (750, 800 and 850 °C) using exsolved material after reduction at 850 °C during 4 h as the catalyst. The gas mixtures that were used for these tests could not be adjusted at the exact CH_4 composition of Colombian natural gas (80 mol%) due to system restrictions. Nevertheless, the CH_4 composition was always much greater than that of the other light hydrocarbon compounds in the mixture. An additional test, operated only with CH_4 in a new composition (the lowest one defined by the CH_4 - C_3H_8 mixture, *i.e.* 43.26 mol%) and keeping constant the other operating conditions, confirms that no significant variations are observed in the conversion, selectivities or H_2/CO ratio when the CH_4 composition in the feed stream is modified (see Appendix M); the only change is to alter the molar distribution of products in the outlet gas composition.

As for methane steam reforming (Section 2.4.3), the catalytic behavior for hydrocarbon mixtures at different exposure time exhibits two different zones: the hydrocarbon compound conversion is initially low but gradually increases until it reaches a constant value corresponding to steady-state conditions. In this region, the average amount of products, selectivities, H_2 production rate, hydrocarbon conversion, and conversion rates are calculated to compare between the reactions.

The first reactive dry gas composition tested was 10 mol% C_2H_6 – 49.92 mol% CH_4 – balance N_2, the results are presented in Table 2.3. H_2 is formed as the major product with an important production rate, similar to the results presented for methane catalytic steam reforming reaction (Table 2.2); such behavior is of great interest for SOFC application directly fed with natural gas. Other products such as CH_4, CO and C_2H_6 are also present in significant amounts whereas CO_2 and C_2H_4 were quantified in much less quantity.

		Temperature [°C]		
		750	**800**	**850**
C_2H_6 conversion rate [mmol min^{-1} g^{-1}]		3.74 ± 0.05	5.27 ± 0.05	8.13 ± 0.03
CH_4 conversion rate [mmol min^{-1} g^{-1}]		3.73± 0.10	3.05 ± 0.06	1.21 ± 0.16
H_2 production rate [mmol min^{-1} g^{-1}]		22.6 ± 0.10	22.3 ± 0.20	24.6 ± 0.20
Outlet dry gas composition	**N_2**	31.31 ± 0.16	31.46 ± 0.16	30.58 ± 0.28
	H_2	17.18 ± 0.08	16.93 ± 0.13	18.25 ± 0.10
	CH_4	38.52 ± 0.18	39.21 ± 0.22	39.51 ± 0.29
	CO	6.42 ± 0.12	5.88 ± 0.09	6.11 ± 0.02
	CO_2	0.61 ± 0.05	0.67 ± 0.03	0.51 ± 0.02
	C_2H_4	0.73 ± 0.03	1.90 ± 0.01	3.17 ± 0.02
	C_2H_6	5.25 ± 0.03	4.015 ± 0.04	1.87 ± 0.01
Selectivity	**CO**	0.76 ± $7x10^{-3}$	0.57 ± $4x10^{-3}$	0.47 ± $1x10^{-3}$
	CO_2	0.07 ± $5x10^{-3}$	0.06 ± $2x10^{-3}$	0.04 ± $1x10^{-3}$
	C_2H_4	0.17 ± $2x10^{-3}$	0.37 ± $4x10^{-3}$	0.49 ± $2x10^{-3}$

Table 2.3 Cataytic behavior for the steam reforming using methane-ethane mixture at different temperatures over exsolved material pretreated at 850 °C during 4 h.

The complexity of the products stream increase with the carbon chain length of the compounds in the feedstock in agreement with ethane and propane possible reforming reactions (Table 2.4 [80–83]. The value of Gibbs free energies (ΔG) as a function of temperature for the most important reactions occurring during ethane reforming shows that ethylene (C_2H_4) and CH_4 are spontaneously produced in operating conditions (Figure 2.11, data taken from [79]). However, it is worth noting that the CH_4 production during ethane reforming makes the same MSR reaction will be also present. On the other hand, C_2H_4 formation was confirmed through individual experiments of ethane steam reforming reaction (Appendix M).

Finally, as indicated before, the WGS reaction is only promoted at high steam and low H_2 content [78] and thermodynamically favored at low temperatures (lower than 823 °C, exothermically moderate). Therefore, in dry operating conditions, CO_2 production is lower while CO is higher (see Table 2.3).

	Reactions	Name		ΔH° [kJ mol^{-1}]
ETHANE	$C_2H_6+2H_2O \leftrightarrows 2CO+5H_2$	Ethane steam reforming	ESR	352.6
	$C_2H_6+2CO_2 \leftrightarrows 4CO+3H_2$	Ethane dry reforming	EDR	438.6
	$C_2H_6 \leftrightarrows C_2H_4+H_2$	Ethane dehydrogenation	EDhy.	137.9
	$C_2H_6+H_2 \dashrightarrow 2CH_4$	Ethane hydrogenolysis	EHyd.	-83.8
	$C_2H_4+2H_2O \leftrightarrows 2CO+4H_2$	Ethylene steam reforming	Et.SR	214.6
PROPANE	$C_3H_8+3H_2O \leftrightarrows 3CO+7H_2$	Propane steam reforming	PSR	497.9
	$C_3H_8+3CO_2 \leftrightarrows 6CO+4H_2$	Propane dry reforming	PDR	620.9
	$C_3H_8 \leftrightarrows C_3H_6+H_2$	Propane dehydrogenation	PDhy.	126.9
	$C_3H_8 \leftrightarrows C_2H_4+CH_4$	Propane cracking 1	PCrk.	84.7
	$C_3H_6+3H_2O \leftrightarrows 3CO+6H_2$	Propylene steam reforming	Pr.SR	381.1
	$2C_3H_8 \leftrightarrows C_3H_6+C_2H_6+CH_4$	Propane cracking 2	PCrk.2	73.7

Table 2.4 Expected ethane and propane reforming reactions according to [80–83].

According to Figure 2.10 and Figure 2.11, MSR and ethane steam reforming (ESR) are thermodynamically favored by temperatures higher than 620 and 475 °C, respectively, and due to the endothermicity of these reactions, the conversion should be favored at a higher temperature. However, Figure 3.12 and Table 2.3 show that C_2H_6 conversion and its conversion rate increase with the temperature, as expected, while the behavior for the CH_4 conversion and its conversion rate follow an inverse trend affecting the CO selectivity, but not the H_2 production rate (Table 2.2 and Table 2.3). Those results indicate that CH_4 conversion is significative affected by the presence of other hydrocarbon compounds; *e.g.* at 850 °C, methane conversion changes from 9.67 mol% in CH_4 feed stream (Table 2.2) to 2.21 mol% and in the CH_4 - C_2H_6 mixture feed stream (Figure 2.12). A competition between reactions and low available metallic active sites (5 wt% metallic Ni on the surface) can probably explain such behavior. Few studies have

tried to explain the reactivity of CH_4 vs C_2H_6 during steam reforming of gas mixtures [84–86]; in many cases, contradictory results are described which are mainly focused on the use of methane as the model reactant [86].

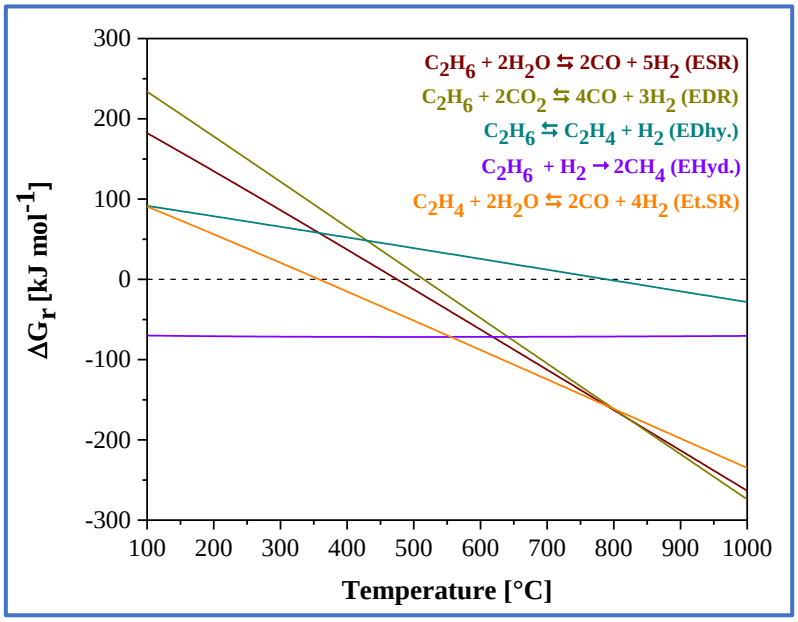

Figure 2.11 Variation of the Gibbs free energy (ΔG) with the temperature of all possible reactions during ethane (C_2H_6) reforming: Ethane Steam Reforming (ESR), Ethane Dry Reforming (EDR), Ethane Dehydrogenation (EDhy.), Ethane Hydrogenolysis (EHyd.), Ethylene Steam Reforming (Et.SR). (Data taken from [79]).

Today, the most accepted reaction mechanism for MSR, still under discussion, can be represented by 3 main steps: 1) CH_4 decomposition on the metallic surface to chemisorbed carbon atoms (C) and hydrogen fragments 2) dissociative adsorption of water to H and OH species and 3) OH or O species combine with C to form CO. The first step requires the C-H activation on the metal surface (*e.g.* Ni), which, according to Wei and Iglesia [87], is the limiting step in the mechanism of catalytic MSR. The results indicate that the presence of C_2H_6 promotes a decrease in the CH_4 conversion rate that seems to be due to a greater difficulty in the C-H activation of methane; at 850 °C, it changes from 8.17 mmol min^{-1} g^{-1} using a CH_4 feed stream to 1.21 mmol min^{-1} g^{-1} in a CH_4 - C_2H_6 mixed feed stream (Table 2.2 and Table 2.3). In this vein, when CH_4 and C_2H_6 are fed together, the activation of C_2H_6 C-H bonds occurs more easily than that of CH_4 [88] and it is related to the difference of energy bond strength (421.77 kJ mol^{-1} vs

438.89 kJ mol^{-1}, respectively [89]). Thus, the formation of ethyl radicals (C_2) will occur to a large degree, occupying first the available metallic active sites and hence promoting the C_2H_6 reforming reactions.

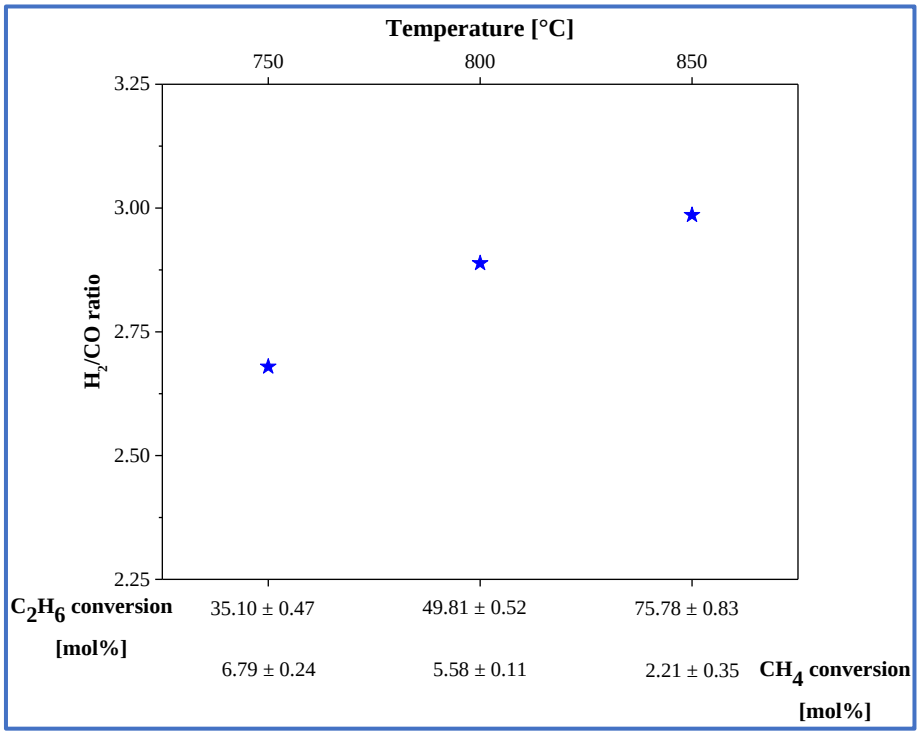

Figure 2.12 H_2/CO ratio, C_2H_6 and CH_4 conversion at different reaction temperatures in the methane-ethane mixture steam reforming reaction over exsolved material pretreated at 850 °C during 4 h.

C_2H_6 conversion is, thereby, higher than that of CH_4 and is promoted advantageously by an increase of temperature (Figure 2.12). Concerning the particular trend for CH_4, the results must be analyzed carefully, since the ESR is also producing CH_4 (Table 2.4) and, in this way, distorts the effect of the temperature on CH_4 conversion rate. CH_4 production is given by ethane hydrogenolysis (EHyd.) and stems from the scission of the C-C bond of an adsorbed C_2 radical, whose energy bond is weaker than C-H bond (376.66 kJ mol^{-1} [89]). Thus, the additional CH_4 formation leads to a decrease of CH_4 conversion in all operating conditions (Figure 2.12) when C_2H_6 is present in the reaction mixture. This behavior becomes more important when the temperature increases. Additionally, the calculated experimental H_2/CO mole ratio variation is presented in Figure 2.12 as a

function of the reaction temperature. This ratio increases proportionally with the reaction temperature; such behavior is related to the system deficient steam conditions and the inhibition of the WGS with the temperature, which reduces CO consumption and favors the H_2 production by the reforming reactions, especially the ethane reforming reactions (ESR, EDhy. and Et.SR).

In conclusion, it is possible to affirm that the ethane reforming reactions are more favored in severe reforming conditions (steam deficient conditions) than methane reforming when CH_4 – C_2H_6 mixture is used. Besides, this trend is exacerbated at high temperatures, for which CH_4 and C_2H_4 productions are promoted as observed by the drop of CH_4 conversion and increase of C_2H_4 composition and selectivity (Table 2.3).

The second tested dry gas composition was 4 mol% C_3H_8 – 43.26 mol% CH_4 – balance N_2. As for the other cases, the catalytic behavior is split into two characteristic two steps: the hydrocarbon compounds conversion is initially low but gradually increases (faster than for CH_4 or CH_4-C_2H_6 mixture) until it reaches a constant value corresponding to steady-state conditions. At this point, the average amounts of products, selectivities, H_2 production rate, hydrocarbon conversion, and conversion rates are calculated. The H_2 is formed as the major product with an important production rate (Table 2.5); however, these values are lower than those obtained in the case of CH_4 and CH_4 - C_2H_6 mixture. On the other hand, in a similar way as before, the low CO_2 production is expected due to the thermodynamically unfavored WGS reaction in the current operating conditions.

As for the MSR and ESR, the propane steam reforming (PSR) is also thermodynamically favored with a temperature higher than 441 °C (Figure 2.13) due to its endothermicity. However, and similarly to the results obtained for the steam reforming of CH_4 - C_2H_6 mixture, the CH_4 conversion, and conversion rate tends to decrease with a rise of temperature, and even reaches negative values at 850 °C, while the C_3H_8 conversion and conversion rate increase with the temperature, as expected, the conversion reaching almost 100 mol% (Figure 2.14). Such trend confirms that CH_4 conversion is significative affected by the presence of other hydrocarbon compounds, as in the case of ethane mixture.

		Temperature [°C]		
		750	**800**	**850**
C_3H_8 conversion rate [mmol min^{-1} g^{-1}]		2.14 ± 0.02	3.17 ± 0.02	4.11 ± 0.02
H_2 production rate [mmol min^{-1} g^{-1}]		15.70x ± 0.20	16.00 ± 0.20	17.8 ± 0.10
Outlet dry gas composition [mol%]	**N_2**	43.13 ± 0.19	42.94 ± 0.07	41.70 ± 0.17
	H_2	12.27 ± 0.06	12.20 ± 0.12	13.43 ± 0.08
	CH_4	36.76 ± 0.27	37.44 ± 0.07	37.40 ± 0.08
	CO	5.08 ± 0.05	5.07 ± 0.04	5.90 ± 0.04
	CO_2	0.60 ± 0.02	0.56 ± 0.01	0.27 ± 0.01
	C_2H_4	0.24 ± $3x10^{-3}$	0.63 ± 0.01	0.90 ± 0.02
	C_2H_6	0.03 ± $2x10^{-4}$	0.10 ± $9x10^{-4}$	0.15 ± $2x10^{-3}$
	C_3H_6	0.23 ± $1x10^{-3}$	0.20 ± $1x10^{-3}$	0.10 ± $2x10^{-3}$
	C_3H_8	1.67 ±0.01	0.87 ± $2x10^{-3}$	0.15 ± $3x10^{-3}$
Selectivity	**CO**	0.74 ± $5x10^{-3}$	0.74 ± $4x10^{-3}$	0.74 ± $5x10^{-3}$
	CO_2	0.09 ± $2x10^{-3}$	0.07 ± $2x10^{-3}$	0.02 ± $2x10^{-3}$
	C_2H_4	0.07 ± $7x10^{-4}$	0.14 ± $2x10^{-3}$	0.18 ± $4x10^{-3}$
	C_2H_6	0.01 ± $6x10^{-5}$	0.02 ± $3x10^{-4}$	0.03 ± $5x10^{-4}$
	C_3H_6	0.01 ± $6x10^{-5}$	0.03 ± $3x10^{-4}$	0.03 ± $1x10^{-3}$

Table 2.5 Catalytic behavior for the steam reforming using methane-propane mixture at different temperatures over exsolved material pretreated at 850 °C during 4 h.

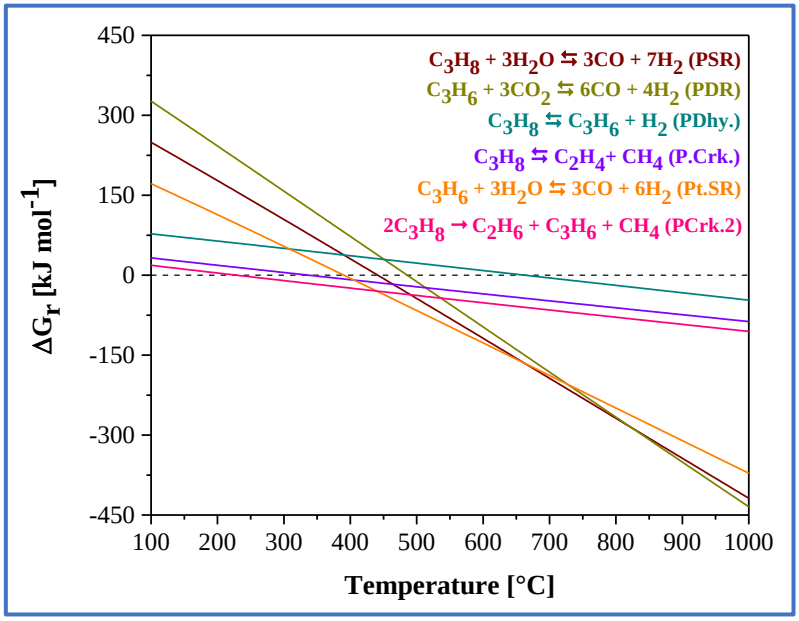

Figure 2.13 Variation of the Gibbs free energy (ΔG) with the temperature of all possible reactions during propane (C_3H_8) reforming: Propane Steam Reforming (PSR), Propane Dry Reforming (PDR), Propane Dehydrogenation (PDhy.), Propane Cracking 1 (P.Crk.), Propylene Steam Reforming (Pt.SR), Propane Cracking 2(PCrk.2). (Data taken from [79]).

In agreement with some other authors [90,91], high temperatures result in enhanced production of CH_4, C_2H_4, C_2H_6 and C_3H_6 due to a significant thermal decomposition of C_3H_8, evidenced in the present study by individual experiments concerning propane steam reforming reaction (Appendix M). In this case, the activation of C_3H_8 first C-H bond is easier than for CH_4 and even than C_2H_6 (C-H bond in CH_3 group 417 kJ mol^{-1} and C-H bond in CH_2 group 398 kJ mol^{-1} [92]); the dehydrogenation of these two kinds of bond is favored as well as the rupture of adsorbed C_3 radicals due to the weakness of the C-C bond (347 kJ mol^{-1} [92]), which improves the formation of methyl, ethyl, vinyl and propyl radicals occupying metallic Ni active sites and promotes the C_3H_8 related propane cracking and the reforming reactions *e.g.* ESR, Et.SR, Pt.SR. The possible change in the H_2/CO ratio depends on the degree of competition between these reactions. In the current operating conditions, no significant variation in the H_2/CO (Figure 2.14) is observed, remaining practically constant with an increase of the reaction temperature. This behavior is also related to the system deficient steam conditions, the C_3H_8 composition in the feed stream and the inhibition of the WGS with the temperature, which reduces the CO consumption and favor proportionally the H_2 production by the reforming reactions.

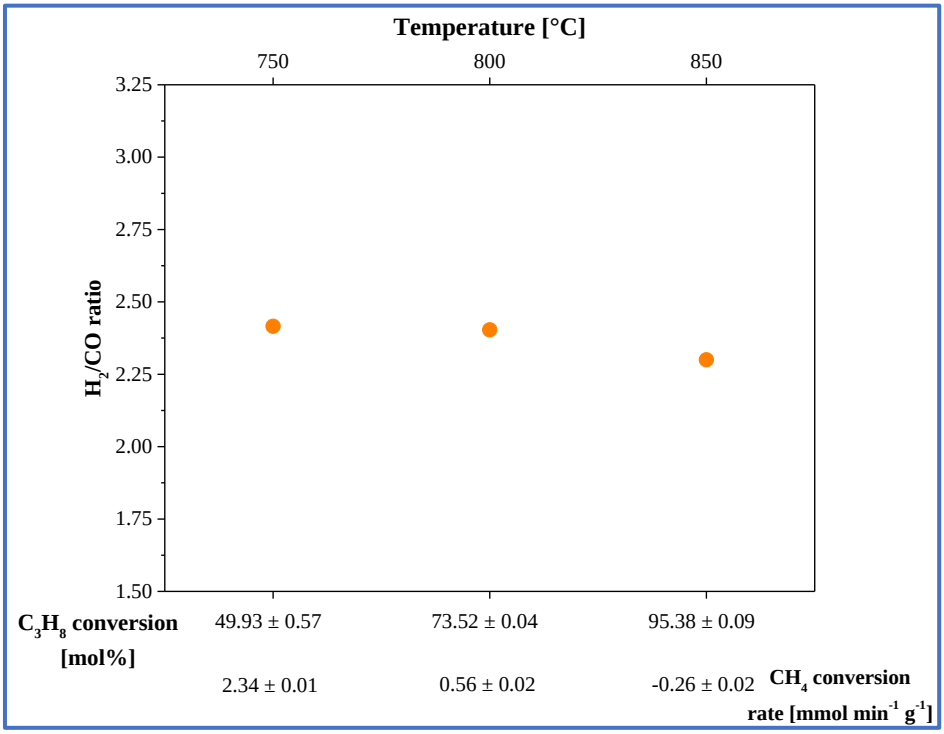

Figure 2.14 H_2/CO ratio at different reaction temperatures in the methane-propane mixture steam reforming reaction over exsolved material pretreated at 850 °C during 4 h.

In conclusion, the C_3H_8 will be significatively more reactive, than CH_4 for the steam reforming reactions when the temperature increases, promoting parallel reactions, including the CH_4 formation (PCrk., PCrk.2, EHyd and EDhy.) which steam reforming will not be kinetically favored (even if it is thermodynamically favored); it explains the significant decrease of CH_4 conversion rate when the temperature rises: CH_4 is produced faster from higher hydrocarbons than reformed, due to its lower reactivity.

2.5. **Conclusions**

The catalytic steam reforming of natural gas (methane) in low steam conditions is of special interest for the development of SOFC systems. Therefore, new anode materials with a high and stable catalytic behavior are requested to design systems that would be

directly fed with hydrocarbon fuels. Ni-decorated Ruddlesden-Popper manganite catalyst (prepared by exsolution or impregnation) are clearly effective for H_2 production through methane steam reforming (MSR) reaction due to the presence of the metallic active phase on the oxide support. However, the results obtained with the new proposed material *i.e.* $La_{1.5}Sr_{1.5}Mn_{1.5}Ni_{0.5}O_{7\pm\delta}$ reduced to Ni-exsolved $LaSrMnO_4$, suggest that this catalyst is a better option due to the high CH_4 conversion, H_2 production, selectivity for the MSR reaction and stability during 8 h of reaction time. This behavior is largely due to a lower propensity to Ni coarsening of the exsolved manganite because the metallic particles are embedded in the ceramic support; in comparison for the impregnated material, the particles are only deposited on the surface and makes them easily mobile.

Besides, it was proved that the reforming reactions in severe reforming conditions of other hydrocarbon compounds such as ethane and propane are favored with respect to methane using feed gas mixtures. Their presence promotes parallel reactions (PCrk., PCrk.2, EHyd, EDhy., etc), which produce H_2 and, in turn, an additional amount of CH_4. The methane steam reforming being not kinetically favored, a consequence is the significative drop of CH_4 conversion rate when the temperature is raised: CH_4 is produced faster from higher hydrocarbons than reformed, due to its lower reactivity.

As conclusion, the newly developed material, based on the Ni exsolution process in which the remaining oxide is a Mixed Ionic and Electronic Conductor [46,93,94] can be considered as a potentially interesting SOFC anode in a system that would run with the main hydrocarbon compounds present in natural gas. A last two issues to be considered would be the sensitivity of the catalyst to the formation of coke and the presence of sulfide impurities, issues that will be addressed in a forthcoming study.

2.6. **References**

[1] E.D. Wachsman, C.A. Marlowe, K.T. Lee, Role of solid oxide fuel cells in a balanced energy strategy, Energy Environ. Sci. 5 (2012) 5498–5509. doi:10.1039/c1ee02445k.

[2] R.F. Service, Bringing fuel cells down to earth, Science (80-.). 285 (1999) 682–685. doi:10.1126/science.285.5428.682.

[3] A. Atkinson, S. Barnett, R.J. Gorte, J.T.S. Irvine, A.J. Mcevoy, M. Mogensen, S.C. Singhal, J. Vohs, Advanced anodes for high-temperature fuel cells, Mater. Sustain. Energy. 3 (2004) 17–27. doi:10.1142/9789814317665_0030.

[4] J. Meusinger, E. Riensche, U. Stimming, Reforming of natural gas in solid oxide fuel cell systems, J. Power Sources. 71 (1998) 315–320. doi:10.1016/S0378-

7753(97)02763-8.

[5] T.M. Gür, Comprehensive review of methane conversion in solid oxide fuel cells: Prospects for efficient electricity generation from natural gas, Prog. Energy Combust. Sci. 54 (2016) 1–64. doi:10.1016/j.pecs.2015.10.004.

[6] Ecopetrol, Composición del gas entregado al SNT desde la planta de gas Cusiana, Dep. Logística Energía y Gas-Gerencia Logística y Contratación. (2019). https://www.ecopetrol.com.co/wps/portal/es (accessed April 11, 2019).

[7] P.S. Roy, N.K. Park, K. Kim, Metal foam-supported Pd-Rh catalyst for steam methane reforming and its application to SOFC fuel processing, Int. J. Hydrogen Energy. 39 (2014) 4299–4310. doi:10.1016/j.ijhydene.2014.01.004.

[8] J. Toyir, P. Gélin, H. Belatel, A. Kaddouri, Ir/$Ce_{0.9}Gd_{0.1}O_{2-x}$ as a new potential anode component in solid oxide fuel cells integrating the concept of gradual internal reforming of methane, Catal. Today. 157 (2010) 451–455. doi:10.1016/j.cattod.2010.03.066.

[9] K. Girona, S. Sailler, P. Gélin, N. Bailly, S. Georges, Y. Bultel, Modelling of gradual internal reforming process over Ni-YSZ SOFC anode with a catalytic layer, Can. J. Chem. Eng. 93 (2015) 285–296. doi:10.1002/cjce.22113.

[10] P. Vernoux, J. Guindet, M. Kleitz, Gradual Internal Methane Reforming in Intermediate-Temperature Solid Oxide Fuel Cell, J. Electrochem. Soc. 145 (1998) 3487–3492.

[11] S.D. Nobrega, M. V. Galesco, K. Girona, D.Z. De Florio, M.C. Steil, S. Georges, F.C. Fonseca, Direct ethanol solid oxide fuel cell operating in gradual internal reforming, J. Power Sources. 213 (2012) 156–159. doi:10.1016/j.jpowsour.2012.03.104.

[12] J.M. Klein, M. Hénault, C. Roux, Y. Bultel, S. Georges, Direct methane solid oxide fuel cell working by gradual internal steam reforming: Analysis of operation, J. Power Sources. 193 (2009) 331–337. doi:10.1016/j.jpowsour.2008.11.122.

[13] Y.S. Chung, T. Kim, T.H. Shin, H. Yoon, S. Park, N.M. Sammes, W.B. Kim, J.S. Chung, In situ preparation of a $La_{1.2}Sr_{0.8}Mn_{0.4}Fe_{0.6}O_4$ Ruddlesden-Popper phase with exsolved Fe nanoparticles as an anode for SOFCs, J. Mater. Chem. A. 5 (2017) 6437–6446. doi:10.1039/c6ta09692a.

[14] Y. Sun, J. Li, Y. Zeng, B.S. Amirkhiz, M. Wang, Y. Behnamian, J. Luo, A-site deficient perovskite: The parent for in situ exsolution of highly active, regenerable nano-particles as SOFC anodes, J. Mater. Chem. A. 3 (2015) 11048–11056. doi:10.1039/c5ta01733e.

[15] S. McIntosh, R.J. Gorte, Direct Hydrocarbon Solid Oxide Fuel Cells, Chem. Rev. 104 (2004) 4845–4866. doi:10.1021/cr020725g.

[16] S. Vecino-Mantilla, P. Gauthier-Maradei, M. Huvé, J.M. Serra, P. Roussel, G.H. Gauthier, Nickel exsolution-driven phase transformation from an n = 2 to an n= 1

Ruddlesden-Popper manganite for methane steam reforming reaction in SOFC conditions, ChemCatChem. 11 (2019) 4631–4641. doi:10.1002/cctc.201901002.

[17] A. Das, E. Xhafa, E. Nikolla, Electro- and thermal-catalysis by layered, first series Ruddlesden-Popper oxides, Catal. Today. 277 (2016) 214–226. doi:10.1016/j.cattod.2016.07.014.

[18] J. Dailly, S. Fourcade, A. Largeteau, F. Mauvy, J.C. Grenier, M. Marrony, Perovskite and A_2MO_4-type oxides as new cathode materials for protonic solid oxide fuel cells, Electrochim. Acta. 55 (2010) 5847–5853. doi:10.1016/j.electacta.2010.05.034.

[19] P. V. Balachandran, D. Puggioni, J.M. Rondinelli, Crystal-chemistry guidelines for noncentrosymmetric A_2BO_4 Ruddlesden-Popper oxides, Inorg. Chem. 53 (2014) 336–348. doi:10.1021/ic402283c.

[20] S.Y. Jeon, M.B. Choi, H.N. Im, J.H. Hwang, S.J. Song, Oxygen ionic conductivity of La 2NiO 4δ via interstitial oxygen defect, J. Phys. Chem. Solids. 73 (2012) 656–660. doi:10.1016/j.jpcs.2012.01.006.

[21] H.W. Nie, T.L. Wen, S.R. Wang, Y.S. Wang, U. Guth, V. Vashook, Preparation, thermal expansion, chemical compatibility, electrical conductivity and polarization of $A_{2-\alpha}A'_{\alpha}MO_4$ (A = Pr, Sm; A′ = Sr; M = Mn, Ni; α = 0.3, 0.6) as a new cathode for SOFC, Solid State Ionics. 177 (2006) 1929–1932. doi:10.1016/j.ssi.2006.01.003.

[22] Y.S. Yoo, M. Choi, J.H. Hwang, H.N. Im, B. Singh, S.J. Song, $La_2NiO_{4+\delta}$ as oxygen electrode in reversible solid oxide cells, Ceram. Int. 41 (2015) 6448–6454. doi:10.1016/j.ceramint.2015.01.083.

[23] V. Kharton, A.A. Yaremchenko, A.L. Shaula, M. V. Patrakeev, E.N. Naumovich, D.I. Logvinovich, J.R.Frade, F.M.B. Marques, Transport properties and stability of Ni-containing mixed conductors with perovskite- and K_2NiF_4-type structure, J. Solid State Chem. 177 (2004) 26–37. doi:10.1016/S0022-4596(03)00261-5.

[24] M. Al Daroukh, V. V. Vashook, H. Ullmann, F. Tietz, I. Arual Raj, Oxides of the AMO_3 and A_2MO_4-type: Structural stability, electrical conductivity and thermal expansion, Solid State Ionics. 158 (2003) 141–150. doi:10.1016/S0167-2738(02)00773-7.

[25] C. Autret, C. Martin, M. Hervieu, R. Retoux, B. Raveau, G. André, F. Baourée, Structural investigation of Ca_2MnO_4 by neutron powder diffraction and electron microscopy, J. Solid State Chem. 177 (2004) 2044–2052. doi:10.1016/j.jssc.2004.02.012.

[26] S.J. Skinner, J.A. Kilner, Oxygen diffusion and surface exchange in $La_{2-x}Sr_xNiO_{4+\delta}$, Solid State Ionics. 135 (2000) 709–712. doi:10.1016/S0167-2738(00)00388-X.

[27] J. Shen, G. Yang, Z. Zhang, W. Zhou, W. Wang, Z. Shao, Tuning layer-structured $La_{0.6}Sr_{1.4}MnO_{4+\delta}$ into a promising electrode for intermediate-temperature symmetrical solid oxide fuel cells through surface modification, J. Mater. Chem. A. 4 (2016) 10641–10649. doi:10.1039/c6ta02986h.

[28] N.R. Peela, D. Kunzru, Oxidative steam reforming of ethanol over Rh based catalysts in a micro-channel reactor, Int. J. Hydrogen Energy. 36 (2011) 3384–3396. doi:10.1016/j.ijhydene.2010.12.091.

[29] D.K. Liguras, D.I. Kondarides, X.E. Verykios, Production of hydrogen for fuel cells by steam reforming of ethanol over supported noble metal catalysts, Appl. Catal. B Environ. 43 (2003) 345–354. doi:10.1016/S0926-3373(02)00327-2.

[30] M.J. Saeki, H. Uchida, M. Watanabe, Noble metal catalysts highly-dispersed on Sm-doped ceria for the application to internal reforming solid oxide fuel cells operated at medium temperature, Catal. Letters. 26 (1994) 149–157. doi:10.1007/BF00824040.

[31] O. Kwon, S. Sengodan, K. Kim, G. Kim, H. Jeong, J. Shin, Y. Ju, J.W. Han, G. Kim, Exsolution trends and co-segregation aspects of self-grown catalyst nanoparticles in perovskites, Nat. Commun. 8 (2017) 1–7. doi:10.1038/ncomms15967.

[32] M.P. Pechini, Method of preparing lead and alkaline earth titanates and niobates and coating method using the same to form a capacitor, US3330697A, 1967.

[33] K. Hou, R. Hughes, The kinetics of methane steam reforming over a Ni / alpha - Al_2O_3 catalyst, Chem. Eng. J. 82 (2001) 311–328.

[34] V. Petrícek, M. Dušek, L. Palatinus, Crystallographic computing system JANA2006: General features, Zeitschrift Fur Krist. 229 (2014) 345–352. doi:10.1515/zkri-2014-1737.

[35] M.A. Rhamdhani, E. Jak, P.C. Hayes, Basic nickel carbonate: Part I. Microstructure and phase changes during oxidation and reduction processes, Metall. Mater. Trans. B Process Metall. Mater. Process. Sci. 39 (2008) 218–233. doi:10.1007/s11663-007-9124-4.

[36] S. Khosharay, S. Tourang, F. Tajfar, Modeling surface tension and interface of (water+methanol), (water+ethanol), (water+1-propanol), and (water+MEG) mixtures, Fluid Phase Equilibria J. 454 (2017) 99–110. doi:10.1016/j.fluid.2017.09.017.

[37] M. Tao, X. Meng, Y. Lv, Z. Bian, Z. Xin, Effect of impregnation solvent on Ni dispersion and catalytic properties of Ni/SBA-15 for CO methanation reaction, Fuel. 165 (2016) 289–297. doi:10.1016/j.fuel.2015.10.023.

[38] D. Eliche-Quesada, J. Mérida-Robles, P. Maireles-Torres, E. Rodriguéz-Castellón, A. Jiménez-López, Hydrogenation and ring opening of tetralin on supported nickel zirconium-doped mesoporous silica catalysts. Influence of the nickel precursor, Langmuir. 19 (2003) 4985–4991. doi:10.1021/la020865l.

[39] P. Biswas, D. Kunzru, Steam reforming of ethanol for production of hydrogen over Ni/CeO2-ZrO2 catalyst: Effect of support and metal loading, Int. J. Hydrogen Energy. 32 (2007) 969–980. doi:10.1016/j.ijhydene.2006.09.031.

[40] M.H. Youn, J.G. Seo, I.K. Song, Hydrogen production by auto-thermal reforming of

ethanol over nickel catalyst supported on metal oxide-stabilized zirconia, Int. J. Hydrogen Energy. 35 (2010) 3490–3498. doi:10.1016/j.ijhydene.2010.01.121.

[41] F.M. Dautzenberg, Ten Guidelines for Catalyst Testing, Charact. Catal. Dev. 411 (1989) 99–119. doi:10.1021/bk-1989-0411.ch011.

[42] G.F. Froment, K.B. Bischoff, J. De Wilde, Chemical reactor analysis and design, 3rd editio, John Wiley & Sons Inc., United States of America, 2011.

[43] C. Perego, S. Peratello, Experimental methods in catalytic kinetics, 1999. doi:10.1016/S0920-5861(99)00071-1.

[44] C. Duong-Viet, H. Ba, Z. El-Berrichi, J. Nhut, M.J. Ledoux, Y. Liu, C. Pham-Huu, Silicon carbide foam as a porous support platform for catalytic applications, New J. Chem. 40 (2016) 4285–4299. doi:10.1039/c5nj02847g.

[45] C. Perego, S. Peratello, Experimental methods in catalytic kinetics, Catal. Today. 52 (1999) 133–145.

[46] M. V. Sandoval, C. Pirovano, E. Capoen, R. Jooris, F. Porcher, P. Roussel, G.H. Gauthier, In-depth study of the Ruddlesden-Popper $La_xSr_{2-x}MnO_{4\pm\Delta}$ family as possible electrode materials for symmetrical SOFC, Int. J. Hydrogen Energy. 42 (2017) 21930–21943. doi:10.1016/j.ijhydene.2017.07.062.

[47] D. Senff, P. Reutler, M. Braden, O. Friedt, D. Bruns, A. Cousson, F. Bourée, M. Merz, B. Büchner, A. Revcolevschi, Crystal and magnetic structure of $La_{1-x}Sr_{1+x}MnO_4$: Role of the orbital degree of freedom, Phys. Rev. B. 71 (2005) 1–8. doi:10.1103/PhysRevB.71.024425.

[48] P. Reutler, O. Friedt, B. Büchner, M. Braden, A. Revcolevschi, Growth of $La_{1-x}Sr_{1+x}MnO_4$ single crystals and characterization by scattering techniques, J. Cryst. Growth. 249 (2003) 222–229.

[49] W. Bao, C.H. Chen, S.A. Carter, S.-W. Cheong, Electronic phase separation and charge ordering in $(Sr,La)_2MnO_4$: indication of triplet bipolarons, Solid State Commun. 98 (1996) 55–59.

[50] J.-C. Bouloux, J.-L. Soubeyroux, A. Daoudi, Proprieties magnetiques de la phase $Sr_{1.50}La_{0.50}MnO_4$, Mater. Res. Bull. 16 (1981) 855–860. doi:https://doi.org/10.1016/0025-5408(81)90160-4.

[51] A. Benabad, A. Daoudi, Les phases $SrLnMnO_4$ (Ln=La, Nd, Sm, Gd), $BaLnMnO_4$ (Ln= La, Nd) et $M_{1+x}La_{1-x}MnO_4$ (M= Sr, Ba), J. Solid State Chem. 22 (1977) 121–126.

[52] I.K. Suh, H. Ohta, Y. Waseda, High-temperature thermal expansion of six metallic elements measured by dilatation method and X-ray diffraction, J. Mater. Sci. 23 (1988) 757–760. doi:10.1007/BF01174717.

[53] Y. Wang, K. Shih, X. Jiang, Phase transformation during the sintering of γ-alumina and the simulated Ni-laden waste sludge, Ceram. Int. 38 (2012) 1879–1886.

doi:10.1016/j.ceramint.2011.10.015.

[54] L. Thommy, O. Joubert, J. Hamon, M.T. Caldes, Impregnation versus exsolution: Using metal catalysts to improve electrocatalytic properties of LSCM-based anodes operating at 600 °C, Int. J. Hydrogen Energy. 41 (2016) 14207–14216. doi:10.1016/j.ijhydene.2016.06.088.

[55] P. Munnik, P.E. De Jongh, K.P. De Jong, Recent Developments in the Synthesis of Supported Catalysts, Chem. Rev. 115 (2015) 6687–6718. doi:10.1021/cr500486u.

[56] T. Jardiel, M.T. Caldes, F. Moser, J. Hamon, G. Gauthier, O. Joubert, New SOFC electrode materials: The Ni-substituted LSCM-based compounds $(La_{0.75}Sr_{0.25})(Cr_{0.5}Mn_{0.5-x}Ni_x)O_{3-\delta}$ and $(La_{0.75}Sr_{0.25})(Cr_{0.5-x}Ni_xMn_{0.5})O_{3-\delta}$, Solid State Ionics. 181 (2010) 894–901.

[57] I. Chen, S. Lin, D. Shiue, Calcination of Nickel / Alumina Catalysts, Ind. Eng. Chem. Res. 27 (1988) 926–929. doi:10.1021/ie00078a005.

[58] D. Neagu, T.S. Oh, D.N. Miller, H. Ménard, S.M. Bukhari, S.R. Gamble, R.J. Gorte, J.M. Vohs, J.T.S. Irvine, Nano-socketed nickel particles with enhanced coking resistance grown in situ by redox exsolution, Nat. Commun. 6 (2015) 1–8. doi:10.1038/ncomms9120.

[59] S. Tao, J.T.S. Irvine, S.M. Plint, Methane oxidation at redox stable fuel cell electrode $La_{0.75}Sr_{0.25}Cr_{0.5}Mn_{0.5}O_{3-\delta}$, J. Phys. Chem. B. 110 (2006) 21771–21776. doi:10.1021/jp062376q.

[60] A.G. Bhavani, W.Y. Kim, J.S. Lee, Barium substituted lanthanum manganite perovskite for CO_2 reforming of methane, ACS Catal. 3 (2013) 1537–1544. doi:10.1021/cs400245m.

[61] W.K.B.W. Ramli, Exsolved base metal catalyst systems with anchored nanoparticles for carbon monoxide (CO) and nitric oxides (NO_x) oxidation, Newcastle University, 2017.

[62] D. Zubenko, S. Singh, B.A. Rosen, Exsolution of Re-alloy catalysts with enhanced stability for methane dry reforming, Appl. Catal. B Environ. 209 (2017) 711–719. doi:10.1016/j.apcatb.2017.03.047.

[63] D. Papargyriou, D.N. Miller, J.T.S. Irvine, Exsolution of Fe-Ni alloy nanoparticles from $(La,Sr)(Cr,Fe,Ni)O_3$ perovskites as potential oxygen transport membrane catalysts for methane reforming, J. Mater. Chem. A. 7 (2019) 15812–15822. doi:10.1039/c9ta03711j.

[64] S. Tao, J.T.S. Irvine, Catalytic properties of the perovskite oxide $La_{0.75}Sr_{0.25}Cr_{0.5}Fe_{0.5}O_{3-\delta}$ in relation to its potential as a solid oxide fuel cell anode material, Chem. Mater. 16 (2004) 4116–4121. doi:10.1021/cm049341s.

[65] S. Singh, D. Zubenko, B.A. Rosen, Influence of $LaNiO_3$ Shape on Its Solid-Phase Crystallization into Coke-Free Reforming Catalysts, ACS Catal. 6 (2016) 4199–4205. doi:10.1021/acscatal.6b00673.

[66] B. Mutz, A. Gänzler, M. Nachtegaal, O. Müller, R. Frahm, W. Kleist, J.D. Grunwaldt, Surface Oxidation of Supported Ni Particles and Its Impact on the Catalytic Performance during Dynamically Operated Methanation of CO_2, Catalysts. 7 (2017) 279. doi:10.3390/catal7090279.

[67] B. Mutz, H.W.P. Carvalho, W. Kleist, J.D. Grunwaldt, Dynamic transformation of small Ni particles during methanation of CO_2 under fluctuating reaction conditions monitored by operando X-ray absorption spectroscopy, J. Phys. Conf. Ser. 712 (2016). doi:10.1088/1742-6596/712/1/012050.

[68] B. Mutz, H.W.P. Carvalho, S. Mangold, W. Kleist, J.D. Grunwaldt, Methanation of CO_2: Structural response of a Ni-based catalyst under fluctuating reaction conditions unraveled by operando spectroscopy, J. Catal. 327 (2015) 48–53. doi:10.1016/j.jcat.2015.04.006.

[69] T.S. Oh, E.K. Rahani, D. Neagu, J.T.S. Irvine, V.B. Shenoy, R.J. Gorte, J.M. Vohs, Evidence and Model for Strain-Driven Release of Metal Nanocatalysts from Perovskites during Exsolution, J. Phys. Chem. Lett. 6 (2015) 5106–5110. doi:10.1021/acs.jpclett.5b02292.

[70] K.Y. Lai, A. Manthiram, Evolution of Exsolved Nanoparticles on a Perovskite Oxide Surface during a Redox Process, Chem. Mater. 30 (2018) 2838–2847. doi:10.1021/acs.chemmater.8b01029.

[71] S.E. Wanke, P.C. Flynn, The Sintering of Supported Metal Catalysts, Catal. Rev. Sci. Eng. 12 (1975) 93–135. doi:https://doi.org/10.1080/01614947508067523.

[72] G. Palasantzas, T. Vystavel, S.A. Koch, J.T.M. De Hosson, Coalescence aspects of cobalt nanoparticles during in situ high-temperature annealing, J. Appl. Phys. 99 (2006) 024307(1)-024307(5). doi:10.1063/1.2163983.

[73] M.A. Asoro, P.J. Ferreira, D. Kovar, In situ transmission electron microscopy and scanning transmission electron microscopy studies of sintering of Ag and Pt nanoparticles, Acta Mater. 81 (2014) 173–183. doi:10.1016/j.actamat.2014.08.028.

[74] S.K. Ryi, J.S. Park, D.K. Kim, T.H. Kim, S.H. Kim, Methane steam reforming with a novel catalytic nickel membrane for effective hydrogen production, J. Memb. Sci. 339 (2009) 189–194. doi:10.1016/j.memsci.2009.04.047.

[75] J. Xu, C.M.Y. Yeung, J. Ni, F. Meunier, N. Acerbi, M. Fowles, S.C. Tsang, Methane steam reforming for hydrogen production using low water-ratios without carbon formation over ceria coated Ni catalysts, Appl. Catal. A Gen. 345 (2008) 119–127. doi:10.1016/j.apcata.2008.02.044.

[76] W.S. Dong, H.S. Roh, K.W. Jun, S.E. Park, Y.S. Oh, Methane reforming over Ni/Ce-ZrO_2 catalysts: Effect of nickel content, Appl. Catal. A Gen. 226 (2002) 63–72. doi:10.1016/S0926-860X(01)00883-3.

[77] H. Timmermann, D. Fouquet, A. Weber, E. Ivers-Tiffée, U. Hennings, R. Reimert, Internal reforming of methane at Ni/YSZ and Ni/CGO SOFC cermet anodes, Fuel

Cells. 6 (2006) 307–313. doi:10.1002/fuce.200600002.

[78] E. Demirel, N. Ayas, Thermodynamic modeling of the water-gas shift reaction in supercritical water for hydrogen production, Theor. Found. Chem. Eng. 51 (2017) 76–87. doi:10.1134/S0040579517010067.

[79] B. Mcbride, S. Gordon, M. Reno, Coefficients for Calculating Thermodynamic and Transport Properties of Individual Species, Nasa Tech. Memo. 4513 (1993) 98. http://ntrs.nasa.gov/archive/nasa/casi.ntrs.nasa.gov/19940013151_1994013151.pdf.

[80] J.R. Fair, J.W. Mayers, W.H. Lane, Commercial ethylene production by propane pyrolysis in a molten lead bath, Chem. Eng. Prog. 53 (1957) 433.438.

[81] J.R. Rostrup-Nielsen, I. Alstrup, Innovation and science in the process industry Steam reforming and hydrogenolysis, Catal. Today. 53 (1999) 311–316. doi:10.1016/S0920-5861(99)00125-X.

[82] S. Dangwal, R. Liu, S.V. Kirk, S.J. Kim, Effect of Pressure on Ethane Dehydrogenation in MFI Zeolite Membrane Reactor, Energy and Fuels. 32 (2018) 4628–4637. doi:10.1021/acs.energyfuels.7b03442.

[83] Y. Im, J.H. Lee, B.S. Kwak, J.Y. Do, M. Kang, Effective hydrogen production from propane steam reforming using M/NiO/YSZ catalysts (M = Ru, Rh, Pd, and Ag), Catal. Today. 303 (2018) 168–176. doi:10.1016/j.cattod.2017.08.056.

[84] B.T. Schädel, M. Duisberg, O. Deutschmann, Steam reforming of methane, ethane, propane, butane, and natural gas over a rhodium-based catalyst, Catal. Today. 142 (2009) 42–51. doi:10.1016/j.cattod.2009.01.008.

[85] B. Anzelmo, J. Wilcox, S. Liguori, Hydrogen production via natural gas steam reforming in a Pd-Au membrane reactor. Comparison between methane and natural gas steam reforming reactions, J. Memb. Sci. 568 (2018) 113–120. doi:10.1016/j.memsci.2018.09.054.

[86] J. Saavedra-Lopez, V.L. Dagle, C.A. Deshmane, L. Kovarik, R.S. Wegeng, R.A. Dagle, Methane and ethane steam reforming over $MgAl_2O_4$-supported Rh and Ir catalysts: catalytic implications for natural gas reforming application, Catalysts. 9 (2019) 801.

[87] J. Wei, E. Iglesia, Isotopic and kinetic assessment of the mechanism of reactions of CH_4 with CO_2 or H_2O to form synthesis gas and carbon on nickel catalysts, J. Catal. 224 (2004) 370–383. doi:10.1016/j.jcat.2004.02.032.

[88] A.A. Latimer, A.R. Kulkarni, H. Aljama, J.H. Montoya, J.S. Yoo, C. Tsai, F. Abild-Pedersen, F. Studt, J.K. Norskov, Understanding trends in C-H bond activation in heterogeneous catalysis, Nat. Mater. 16 (2017) 225–229. doi:10.1038/nmat4760.

[89] B. Ruscic, Active Thermochemical Tables: Sequential Bond Dissociation Enthalpies of Methane, Ethane, and Methanol and the Related Thermochemistry, J. Phys. Chem. A. 119 (2015) 7810–7837. doi:10.1021/acs.jpca.5b01346.

[90] M. Lo Faro, V. Modafferi, P. Frontera, P. Antonucci, A.S. Aricò, Catalytic behavior of Ni-modified perovskite and doped ceria composite catalyst for the conversion of odorized propane to syngas, Fuel Process. Technol. 113 (2013) 28–33. doi:10.1016/j.fuproc.2013.03.010.

[91] V.R. Choudhary, V.H. Rane, A.M. Rajput, Simultaneous thermal cracking and oxidation of propane to propylene and ethylene, AIChE J. 44 (1998) 2293–2301. doi:10.1002/aic.690441018.

[92] N. Moreau, S. Pasquiers, N. Blin-Simiand, L. Magne, F. Jorand, C. Postel, J.R. Vacher, Propane dissociation in a non-thermal high-pressure nitrogen plasma, J. Phys. D. Appl. Phys. 43 (2010) 1–14. doi:10.1088/0022-3727/43/28/285201.

[93] M.V. Sandoval, S. Durán, A. Prada, C. Pirovano, O. Gardoll, P. Roussel, G.H. Gauthier, Synthesis and preliminary study of $Nd_xAE_{2-x}MnO_{4\pm\delta}$ (AE: Ca, Sr) for symmetrical SOFC electrodes, Solid State Ionics. 317 (2018) 194–200. doi:10.1016/j.ssi.2018.01.025.

[94] M.V. Sandoval, C. Cárdenas, E. Capoen, C. Pirovano, P. Roussel, G.H. Gauthier, Performance of $La_{0.5}Sr_{1.5}MnO_{4\pm\delta}$ Ruddlesden-Popper manganite as electrode material for symmetrical solid oxide fuel cells. Part A. The oxygen reduction reaction, Electrochim. Acta. 304 (2019) 415–427. doi:10.1016/j.electacta.2019.03.037.

Chapter 3
Methane steam reforming in water-deficient conditions on a new Ni exsolved Ruddlesden-Popper manganite: coke formation and H_2S poisoning

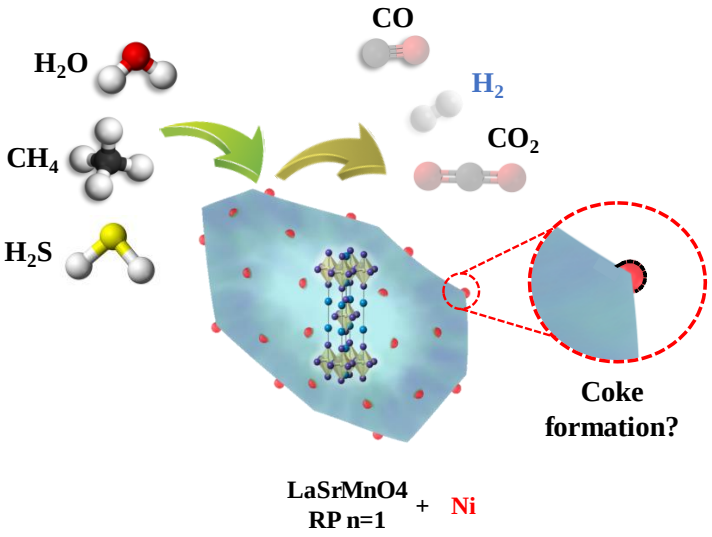

3.1. **Abstract**

The present research deals with the catalytic behavior for the methane steam reforming reaction over a new Ni exsolved Ruddlesden-Popper (RP) manganite for a long period of time (100h) with special focus on the possible carbon deposition and H_2S poisoning. The material, of $La_{1.5}Sr_{1.5}Mn_{1.5}Ni_{0.5}O_{7\pm\delta}$ composition, was synthesized by the Pechini method and reduced in diluted hydrogen to induce the Ni exsolution on the surface of a n=1 Ruddlesden-Popper (RP) phase. The behavior of the as-obtained material was compared to Ni impregnated manganite of similar $(La,Sr)_2MnO_{4\pm\delta}$ composition and to state-of-the-art Ni/YSZ cermet. The catalytic measurements for the steam reforming reaction were carried out at 850 °C in low steam-to-carbon conditions (S/C = 0.15). During the first hours of operation, the cermet material exhibits the best catalytic performance (with higher conversion, conversion rate, and H_2 production rate) followed by the exsolved material and, finally, the impregnated catalyst. However, for longer reaction times, the activity drops in the case of cermet and impregnated materials due to coking, as evidenced by TEM and TGA/MS analysis, while the exsolved material behavior remains stable even with 100 h of reaction. All the studied materials are susceptible to H_2S poisoning, forming undesired sulfide compounds with dramatic consequence for the reforming reaction. However, the stability of the exsolved catalyst over a long period of time is a noticeable advantage in view of a possible use as SOFC anode fed with Colombian natural gas free of H_2S.

3.2. **Introduction**

Solid Oxide Fuel Cell (SOFC) is recognized as one of the most attractive energy conversion technology with simplified design, high efficiency, low emission of pollutant gases and fuel flexibility, being able to operate not only with H_2 but also with hydrocarbon fuels. Currently, natural gas (basically methane) has been considered as a fuel of highest interest due to its relatively low cost, availability (naturally found) and facility to be stored and transported [1–4].

The methane steam reforming (MSR) is a catalytic highly endothermic reaction for commercial H_2 production (H_2/CO molar ratio of 3) as described by Equation 3.1. The excessive addition of steam will promote the CO conversion into CO_2 by the slightly exothermic water gas shift (WGS) reaction (Equation 3.2). In a SOFC operating with natural gas (methane), these reactions occur in the anode region and the H_2 obtained is

simultaneously consumed by the electrochemical reaction to produce electricity [5,6]. Also, steam will be formed as a by-product which will be used in the reforming reactions as reactive, reducing the amount of injected H_2O and then improving the efficiency of the electrochemical system.

$$CH_4 + H_2O \leftrightarrow CO + 3H_2 \quad \Delta H^o = 206.1 \text{ kJ mol}^{-1} \qquad \textbf{Equation 3.1}$$

$$CO + H_2O \leftrightarrow CO_2 + H_2 \quad \Delta H^o = -41.2 \text{ kJ mol}^{-1} \qquad \textbf{Equation 3.2}$$

Nevertheless, the direct internal reforming over Ni-based anodes is still facing two major issues: thermomechanical problems and carbon formation/deposition in the form of filaments on the particles via parasitic reactions such as methane cracking (Equation 3.3) or Boudouard reaction (Equation 3.4) [7]. According to the literature, the steam to carbon ratio (S/C) must be higher than 1 to avoid the coke formation/deposition on the anode surface. However, such high S/C ratios dilute the fuel composition and may lead to thermomechanical damages due to large temperature gradients at the anode side (reforming reaction is strongly endothermic, while electrochemical reactions are exothermic) and the requirements to produce steam in excess and condense the unreacted products are energetically unfavorable. Therefore, with low steam to carbon ratio (S/C), the process will need a small amount of steam at the inlet and the excess will be produced *in situ* by the electrochemical oxidation of the hydrogen obtained during the reforming reaction [8,9]. Such alternative strategy, called Gradual Internal Reforming – GIR has been proposed by Vernoux *et al*. [10], and potentially allows to circumvent the problems and improve the long-term stability of the cell operating without water excess, as already demonstrated theoretically and experimentally [11,12].

$$CH_4 \leftrightarrow C + 2H_2 \quad \Delta H^o = 75.6 \text{ kJ mol}^{-1} \qquad \textbf{Equation 3.3}$$

$$2CO \leftrightarrow C + CO_2 \quad \Delta H^o = -172.0 \text{ kJ mol}^{-1} \qquad \textbf{Equation 3.4}$$

In addition, the sulfur-containing compounds, generally in the form of hydrogen sulfide (H_2S) inherently present in hydrocarbon fuels such as natural gas, lead to catalysis inhibition by poisoning of metallic active sites, impacting irreversibly on SOFC performance and life-time [13–15].

Consequently, a correct operation of SOFC needs the development of new materials with specific properties (electrochemical and catalytic), which must be different to the

conventional cermet based on nickel and yttria-stabilized zirconia (Ni/YSZ) since the latter has shown unsatisfactory performances with natural gas [1,16,17], poor redox stability, tendency to nickel agglomeration (sintering), carbon deposition, sulfur poisoning, leaching and delamination of anode material after prolonged operation. All of this involves its deactivation, losses of cell performances and poor durability [18,19].

Currently, the Mixed Ionic and Electronic Conducting (MIEC) oxides are being developed as potential alternative anode materials, due to their varied and exceptional transport (ionic and electronic) and structural properties, together with their high thermal and mechanical stabilities, essential features for the correct operation of the SOFC [20–29]. Besides, the electrochemical characteristics and catalytic behavior of those materials can be improved by the addition on the surface of small metallic nanoparticles (Ni, Ru, Rh, others) deposited by different techniques such as impregnation by a solution or a suspension, vapor deposition, electroless deposition or hybrids [30]. However, in several of the aforementioned techniques, the weak particle - MIEC interaction can lead to sintering problems, carbon deposition, and even sulfur poisoning and others [31,32].

Interestingly, during the last years, several research studies have reported an alternative way to obtain metallic active particles through a single-step reduction treatment called metal exsolution, providing resistance to agglomeration and coking in comparison to other routes of particle deposition [32–36], as well as a considerably improved H_2S poisoning resistance [37–39]. This stability is related to the strong particle - MIEC oxide interaction. Those exsolved nanoparticles are well-dispersed and partially embedded (socketed) into the oxide surface, showing promising performance for SOFC anode. It is worth mentioning that exsolution has been reported with many transition-metals including Ru, Pd, Co, Fe, and Ni; the last one is of especial interest for the desired application due to its versatility in steam reforming reaction and low cost [32,40–44].

The synthesis, exsolution and catalytic study of a new MIEC material ($La_{1.5}Sr_{1.5}Mn_{1.5}Ni_{0.5}O_{7\pm\delta}$) with Ruddlesden-Popper (RP) structure have been presented in previous studies [45]. Those works report the formation of a biphasic material based on electrocatalytic Ni metallic active nanoparticles decorating the RP n= 1 $LaSrMnO_{4\pm\delta}$ manganite after exsolution in SOFC anode conditions. Satisfactory results for the steam reforming of methane and other light hydrocarbon components of natural gas allow to consider the material as a potential anode for SOFC (Chapter 2). The present work provides continuity to the aforementioned research studies and deals with the resistance to carbon formation/deposition and H_2S poisoning of the exsolved $La_{1.5}Sr_{1.5}Mn_{1.5}Ni_{0.5}O_{7\pm\delta}$ material, *i.e.* Ni/ $LaSrMnO_{4\pm,}$ in comparison to a conventional Ni impregnated material of similar composition and to the state of art Ni/YSZ cermet.

The study was performed at a longer reaction time of MSR in water-deficient conditions and using Colombian natural gas (methane as the main component).

3.3. **Methodology**

3.3.1. ***Synthesis***

Ruddlesden-Popper (RP) powder of $La_{1.5}Sr_{1.5}Mn_{1.5}Ni_{0.5}O_{7\pm\delta}$ (LSMN n= 2) and $La_{0.5}Sr_{1.5}MnO_{4\pm\delta}$ (LSMO n= 1) were synthesized by a Pechini o citrate complexation route [46]. The synthesized LSMO n= 1 powder was impregnated with Ni (active phase) using Incipient Wetness Impregnation (IWI) technique, also known as pore volume impregnation. The synthesis and impregnation procedures were described in Chapter 1 Section 1.3.1 [45], Chapter 2 Section 2.3.1 and Chapter 2 Section 2.3.3. Fresh powder characterization (XRD, TEM-EDS, SEM, XRF), reduction study and catalytic tests were previously presented (Chapter 1 [45] and 2). The commercial NiO/YSZ (fuel cell materials, SKU: 132301, nickel oxide – YSZ anode powder for general applications, 60 wt% NiO, 40 wt% $(Y_2O_3)_{0.08}(ZrO_2)_{0.92}$) was employed as a reference SOFC anode material.

3.3.2. ***MSR at longer reaction time: the study of carbon formation/deposition resistance***

A series of catalytic tests were performed during a long time at atmospheric pressure and 850 °C to evaluate the resistance to carbon formation of the synthesized materials. Thereby, MSR reaction was performed in the experimental set-up described in Chapter 1 section 1.3.4.1 [45]. Individual tests were carried out using 50 mg of catalyst diluted in SiC (SiC:catalyst 10:1 weight ratio) to minimize heat-transfer effects, which was introduced in the reactor as fixed-bed between catalyst-free SiC and two pieces of quartz wool. Considering the previous results (Chapter 1 [45] and Chapter 2), the catalyst was reduced *in situ* (55 mL (STP) min^{-1} of 3 mol% H_2/N_2 mixture (Cryogas) at 850 °C during 4 h to guarantee the complete Ni exsolution from LSMN n= 2 material (thereafter referred to as Ni/LSM n= 1 exsolved material), as well as the complete NiO reduction for both impregnated LSMO n= 1 (referred to as Ni/LSMO n= 1 impregnated material) and NiO/YSZ (referred to as Ni/YSZ).

The reaction mixture corresponds to 82 mol% CH_4 in N_2 as balance, (Cusiana gas, Colombia [47]) humidified to achieve a carbon ratio (S/C) of 0.15 according to the SOFC

anode conditions which are suggested by the Gradual Internal Reforming concept or GIR [10]. The moisture content was adjusted by flowing 128 mL (STP) min^{-1} (dry basis) of CH_4-N_2 mixture (the volume hourly space velocity value – VHSV was kept constant at 172000 mL (STP) g^{-1} h^{-1} throughout a bubbler containing distilled water warmed exactly at 46 °C). The molar composition for each compound (CH_4, CO, H_2, CO_2, and N_2) was measured each 20 min using an on-line gas chromatograph (GC, SRI instruments 8610C) using He (grade 5.0, CRYOGAS) as mobile phase, equipped with a solenoid gas sampling valve heated at 60 °C, two packed columns (molecular sieve 13X 6 in and hayesep D 6 in), a thermal conductivity detector (TCD) heated at 150 °C and controlled by PeakSimple 4.44 free software (method described in Appendix B). Standard gas cylinders with different gas compositions were employed for the outlet products quantification. The CH_4 conversion, CH_4 conversion rate, and H_2 formation rate were calculated using the equations presented in Chapter 1 (Equation 1.1, Equation 1.2 and Equation 1.3, respectively).

A microstructural characterization post-reaction was performed on the spent catalysts by transmission electron microscopy in the TEM FEI TITAN Themis 300 equipped with a Super-X quad EDS for elemental analysis. The powders were crushed and dropped in the form of alcohol suspension on carbon-supported copper grids followed by evaporation under ambient conditions.

In addition, thermogravimetric analysis (TGA) was used to quantify the carbonaceous species formed on the spent catalysts. The experiments were performed on a TA 2960 SDT 2960 V3.0F instrument. The samples were heated from room temperature (RT) to 1000 °C at 10 °C min^{-1} under a diluted O_2 stream (20 mol% in He). A mass spectrometer was used to identify effluent gas. The signal at m/z = 18, 28 and 44, was used to track the generation of H_2O, CO, and CO_2 during the measurements, respectively.

3.3.3. *Tolerance tests of materials to H_2S exposure*

The resistance to hydrogen sulfide (H_2S) poisoning of synthesized materials was evaluated using a two steps methodology. First, the materials were exposed to H_2S during a defined time. Then, once the materials have been poisoned, they were tested on MSR reaction in water-deficient conditions to evaluate their catalytic performances. For the first step, the experimental set-up illustrated in Figure 3.1 was used. It is divided into 2 main sections: feeding and reduction/poisoning zones. In the first zone, N_2 (grade 5.0, Cryogas), 3 mol% H_2/N_2 mixture (Cryogas) and 500 ppm H_2S/N_2 mixture (Linde) cylinders are available. Each pipeline has an analog manometer (Bourdon-Haenni® 0-100 psi and Ashcroft® 0-100 psi) and a Cole-Parmer® 150 mm correlated and calibrated

flowmeter with a high-resolution valve for the precise control flow. Finally, the N_2 - H_2S/N_2 mixture passes through the second zone (reduction/poisoning zone) which is constituted by a tubular quartz reactor ($ø_I$: 9 mm, $ø_E$: 12 mm and L: 300 mm) heated by a tubular furnace (CARBOLITE MTF 10/15/130). The preparation of catalyst fixed bed (50 mg of catalyst diluted in SiC) and its pretreatment (*in situ* reduction 55 mL (STP) min^{-1} of 3 mol% H_2/N_2 mixture, (Cryogas) at 850 °C during 4 h) was similar to the procedure explained in Section 3.3.2. Once the catalyst has been reduced, it was put in contact with an N_2 - H_2S/N_2 mixture containing 50 ppm of H_2S (128 mL (STP) min^{-1} dry basis) during 8 h at 850 °C. As in the case of the carbon formation study, the poisoning tests were performed in severe conditions, *i.e*. at the higher H_2S composition observed for Cusiana gas [47].

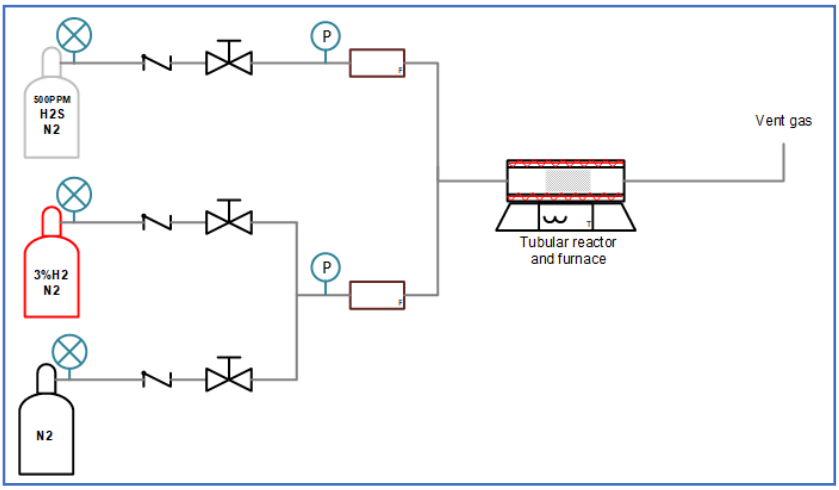

Figure 3.1 Experimental set-up for H_2S poisoning.

After the sample exposure to H_2S, the test was stopped, and the reactor was isolated at room temperature under N_2. Finally, it was carefully coupled with the experimental set-up described and used in Chapter 1 Section 1.3.4.1 [45], and MSR test was started. A mixture of gases was fed into reactor containing 82 mol% CH_4 in N_2 as balance, (Cusiana gas, Colombia [47]) humidified to achieve a carbon ratio (S/C) of 0.15 according with the SOFC anode conditions which are suggested by the Gradual Internal Reforming concept or GIR [10]. The moisture content was adjusted by flowing 128 mL (STP) min^{-1} (dry basis) of CH_4-N_2 mixture (the volume hourly space velocity value – VHSV was kept constant at 172000 mL (STP) g^{-1} h^{-1}) throughout a bubbler containing distilled water warmed exactly at 46 °C. The molar composition for each compound (CH_4, CO, H_2, CO_2, and N_2) was measured each 20 min using an on-line GC/TCD (method described

in Appendix B). The CH_4 conversion, CH_4 conversion rate, and H_2 formation rate were calculated using the equations presented in Chapters 1 and 2.

X-ray diffraction (XRD) experiments were carried out at room temperature (RT) using a Bruker D8-ADVANCE powder diffractometer operated in Bragg-Brentano geometry, equipped with a Lineal LynxEye detector and a beam of $CuK_{\alpha 1,2}$ radiation (λ= 1.5418 Å). The diffractometer was operated over the angular range 2θ = 10 - 70° with a measurement step of 0.020353° (2θ). The qualitative identification of crystalline phases was performed by comparing the measured profile reflections with the diffraction profiles reported in the Powder Diffraction File (PDF-2) database of the International Center of Diffraction Data (ICDD), using Crystallographica Search-Match Software [48] and processed using JANA 2006 software package [49].

X-ray photoelectron spectroscopy (XPS) experiments were performed for impregnated and exsolved materials after treatment in H_2S using a SPECS® XPS/ISS/UPS Surface Characterization Platform provided with an energy analyzer PHOIBOS 150 2DDLD (analysis chamber at 1×10^{-9} Pa). The samples were analyzed by using a monochromatized Al Kα source (FOCUS 500) operated at 100W. The pass energy of the hemispherical analyzer was set to 100 and 15 eV and for the high-resolution spectra. Step-size was adjusted to 0.05 eV, Dwell time was set at 0.1 s. The samples were mounted on carbon conducting tape over the metallic sample holders. Surface charge compensation was controlled with Flood Gun (FG 15/40-PS FG 500) operated at 58µA-2.5eV. The reference scale was adjusted to the C 1s core level at 284.8 eV. Peak fitting was processed with Casa XPS version 2.3.16Dev52 software, using a mixed Gaussian/Lorentzian shape.

Finally, the exsolved and impregnated materials after the treatment in H_2S at high temperature were analyzed by a micro-Raman spectrometer (HORIBA LabRAM XploRA Plus) with a 638 nm laser as the excitation source (red light). Raman spectra were collected in micro Raman configuration with a 50× objective, a grating of 2400 lines mm^{-1}, an entrance slit of 50 to 200 µm, a confocal hole of 100 to 500 µm, spectrometer filter used for 1 % power, 10 accumulations and 25 s of acquisition time. The spectrometer was calibrated before and after each analytical session using the well-known Raman stretching vibrations of pure silicon (520.6 cm^{-1} at 20 °C).

3.4. **Results**

3.4.1. ***Carbon formation resistance***

The MSR reaction of a CH_4 - H_2O mixture containing an important excess of methane respect to steam (molar S/C ratio= 0.15) was performed at 850 °C using different catalysts to compare their catalytic behavior in the same operating conditions during long reaction time. The samples used in this study were the exsolved and impregnated material and Ni/YSZ (reference anode material). In all cases, the materials were previously reduced at 850 °C during 4 h under diluted H_2 to compare the behavior. The trend of the catalytic performance for each material is presented in Figure 3.2.

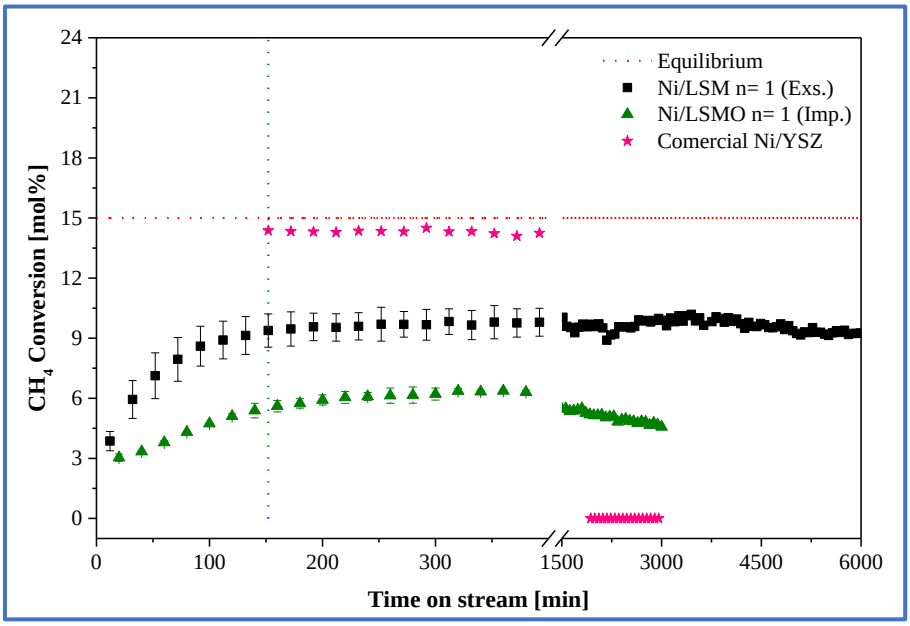

Figure 3.2 Catalytic behavior at T= 850 °C of Ni/LSM n= 1 (exsolved material), Ni/LSMO n= 1 (impregnated material) and Ni/YSZ over long reaction time (reduction pretreatment: 850 °C during 4h in diluted H_2).

During the first 8 h (480 min), the CH_4 conversion for the exsolved and impregnated materials follows a similar trend to that reported in Chapter 2; an unstable region in which the conversion increases until a maximum value maintained constant and associated to steady-state conditions. In these conditions, the achieved CH_4 conversion

is 9.71 ± 0.50 mol% using exsolved material while the conversion rate is 8.17 ± 0.48 mmol min^{-1} g^{-1} and the H_2 formation rate 23.5 ± 1.31 mmol min^{-1} g^{-1}. Those values are greater than those observed with impregnated material, for which a CH_4 conversion of 7.89 ± 0.20 mol% is calculated with a rate of 6.65 ± 0.16 mmol min^{-1} g^{-1} and an H_2 formation rate of 19.60 ± 0.52 mmol min^{-1} g^{-1}. Conversely, the reference material (Ni/YSZ) shows a CH_4 conversion (14.00 ± 0.44 mol%) close to the equilibrium value (15 mol%), a calculated conversion rate of 11.70 ± 0.41 mmol min^{-1} g^{-1} and an H_2 formation rate of 33.41 ± 1.68 mmol min^{-1} g^{-1}. It is worth noting that the behavior of CH_4 conversion observed for this reference material is stable from the beginning of the test and during the first hours, although only the values at longer reaction time are presented in Figure 3.2 to compare with the other studied materials. Concerning the CH_4 conversion, the difference observed between Ni/YSZ and the other two samples is associated to its higher Ni content, which exhibits around 10 times more nickel than the exsolved and impregnated (5 wt%), resulting, in much more metallic active sites per gram of catalyst (high surface area).

At longer reaction time, the activity performance over the materials decreases. The CH_4 conversion over Ni/YSZ is almost null after 30 h (1800 min). In the case of impregnated material, it is worth noting an important decrease of CH_4 conversion close to 42 %, achieving a value of 4.57 mol%, whilst the conversion rate and the H_2 formation rate decrease to 3.86 mmol min^{-1} g^{-1} and 11.60 mmol min^{-1} g^{-1}, respectively. For both materials, this phenomenon is associated to a catalyst deactivation as result of particle growth (sintering or coalescence) caused by a non-uniform size, a non-homogenous Ni distribution on the surface and carbon/coke formation on the catalyst surface, which are favored by the high operating temperature, the low S/C ratio in the feed gas and the Ni grain size. The literature shows that this behavior is commonly observed in Ni-based catalyst prepared by wet impregnation technique as well as cermet materials such as Ni/YSZ [50–52].

In the case of exsolved material, the catalytic behavior remains stable even after 100 h (6000 min) of reaction. This exceptional stability is sign of a less sensitivity to carbon formation/deposition in severe operating conditions (S/C= 0.15), which are the result of the joint interactions of the main properties of the exsolved material: small amount of exsolved Ni [53] (5 wt% Chapter 1 [45]), fine metal dispersion on the surface, small particles size, strong nanoparticles – support interaction (socketed particles), less sintering effect [32,40,54,55] and strong basicity of the La/Sr-containing support [51].

TGA/MS analysis, under diluted O_2 atmosphere, performed on the spent catalyst (Figure 3.3 – A) confirms the negligible carbon formation/deposition on the exsolved material after long reaction time (100 h). Three weight losses are visible in this material: the first

one, at a temperature ranging from 100 °C to 200 °C corresponds to some H_2O evaporation (ion 18) [56]. The other two weight losses (1.45 wt%) around 500 °C - 650 °C and 700 °C - 850 °C are related to the oxidation of some carbonaceous species deposited on the surface as confirmed by the presence of CO and CO_2 signals (ions 28 and 44) in MS spectrum, which coincide with the same temperature range, they are attributed to the catalyst contamination during the sample handling (reactor discharge, TGA/MS sample manipulation). This hypothesis is confirmed, apart from catalytic behavior, by the analysis of TEM image (Figure 3.4 - A), from which it is possible to observe the embedded Ni nanoparticles without traces of any kind of carbonaceous formations on the surface. This result is coherent with the high tolerance against carbon/coke formation/deposition described in other studies of Ni exsolution over different materials for similar applications [32,37,38,41,54]. Finally, in the exsolved sample a weight gain is slightly visible between 350 and 450 °C, which is linked to the Ni nanoparticles oxidation as described by other authors [56–59].

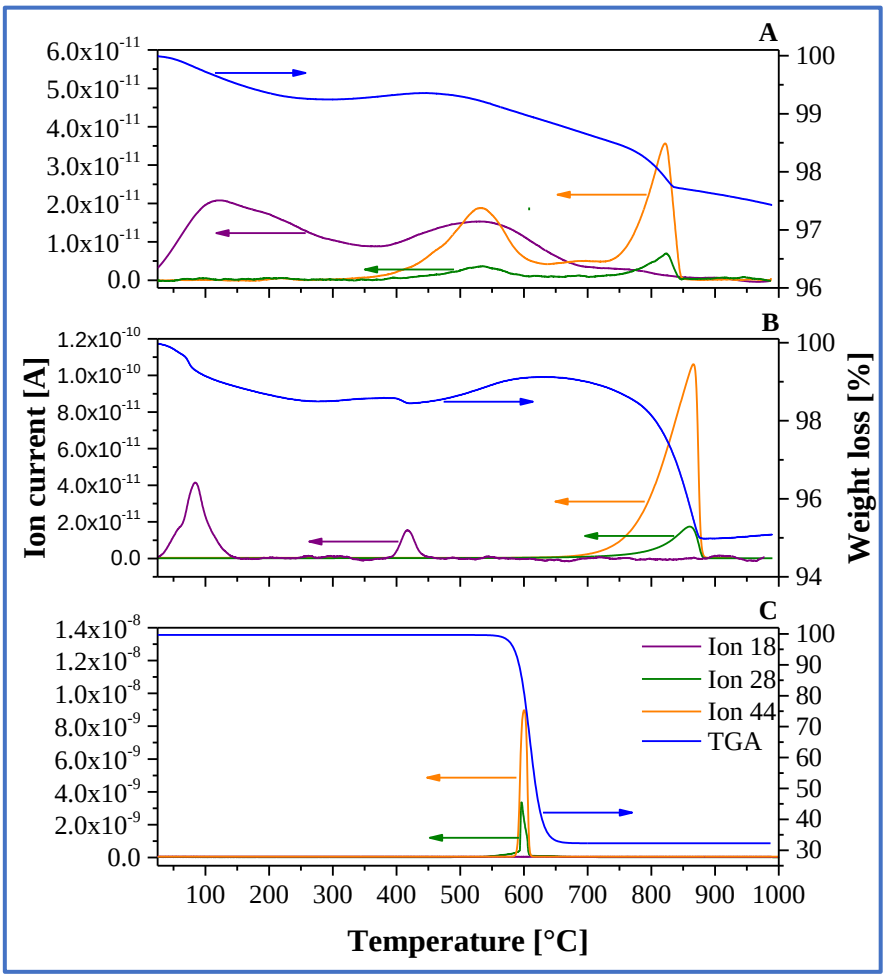

Figure 3.3 Weight loss and MS signal of spent catalysts A) exsolved material B) impregnated material C) reference material: Ni/YSZ.

TGA/MS analysis of spent impregnated material shows 3 weight losses (Figure 3.3 - B), the first two can be ascribed to the loss of moisture (ion 18) due to the desorption of physisorbed and chemisorbed water. The last weight loss, at temperature ranging from 650 to 900 °C, is due to the oxidation of the carbonaceous species formed/deposited on the surface (4.13 wt%) producing CO and CO_2, as evidenced by ions 28 and 44 signals in MS trace. TEM image confirms those results: small fibers on the surface of this material can be observed (Figure 3.4 – B), which progressively have started to accumulate encapsulating the active sites and deactivating them. These carbonaceous

deposits might be associated with the cracking of methane (coke) and/or disproportionation of CO (carbon) during the MSR reaction. Their formation depends on the temperature, the partial pressure of the steam, Ni crystallite size, the support, and other factors [60,61]. According to the literature [62–64], initially, single carbon atoms are formed and deposited (adsorbed) on the catalyst surface due to the parasitic reactions presented in Equation 3.3 and Equation 3.4; these reaction products are referred to as C_α or surface carbide. At reaction temperatures over 500 °C, the C_α species can polymerize to form carbonaceous amorphous films (C_β) that deactivate the catalyst and, over a period of time and at high temperature, they can be transformed into a more stable and crystalline graphitic form (C_φ), only oxidized at high temperatures [62,63] and commonly observed on low area catalysts [64]; it seems to be the case of the impregnated material due to the low Ni loading (5 wt% Chapter 2) in association with the low dispersion of the Ni particles resulting from the metal sintering, as reported in the literature [41,44]. In this second sample, it is worth noting a slight weight gain above 500 °C, similar to the case of the exsolved material, which can be attributed to the Ni particles oxidation [57].

Finally, the Ni/YSZ sample shows an expected behavior. Only one important weight loss (67.36 wt%) between 370 - 700 °C is observed in TGA/MS (Figure 3.3 - C), definitively linked with a large amount of carbon formation during the steam reforming reaction. It has been demonstrated in previous studies that Ni/YSZ cermet is not stable in hydrocarbon fuels *e.g*. methane in coking conditions. Large amounts of carbonaceous species deposited on the Ni surface would, in turn, lead to a rapid degradation and even collapse of the cell performance by covering the catalytic metallic active sites, blocking the gas transportation as well as causing some cracks in the anode layer [1,7,65–67].

In TEM image (Figure 3.4 - C), a carbon layer was observed surrounding the Ni particles separated from the zirconia in a phenomenon similar to the metal dusting effect described by Chen *et.al*. [68]. This effect is a catastrophic form of corrosion, in which the nickel particles can be disintegrated into fine powders by deposited carbon due to the exposition to reducing atmosphere, highly carburizing gases and high temperature (T > 400 °C). The most accepted mechanism is based on the following sequence: first, the carbon is successively formed and deposited on the nickel surface, randomly oriented on its different lattice planes. Then, the carbon, in a graphitic form, grows into the metal through a certain nickel lattice surface, using as driving force the difference between the supersaturated activity at the gas-metal interface and the activity of the matrix at the precipitation site. Eventually, the nickel disintegration occurs. The continuous metal dusting effect will be the cause of breaking the contact of nickel particles of the zirconia surface, which generates, in the application as SOFC anode, a drop in the electrical conductivity and the introduction of extra stress producing the fracture of the cell [68–71].

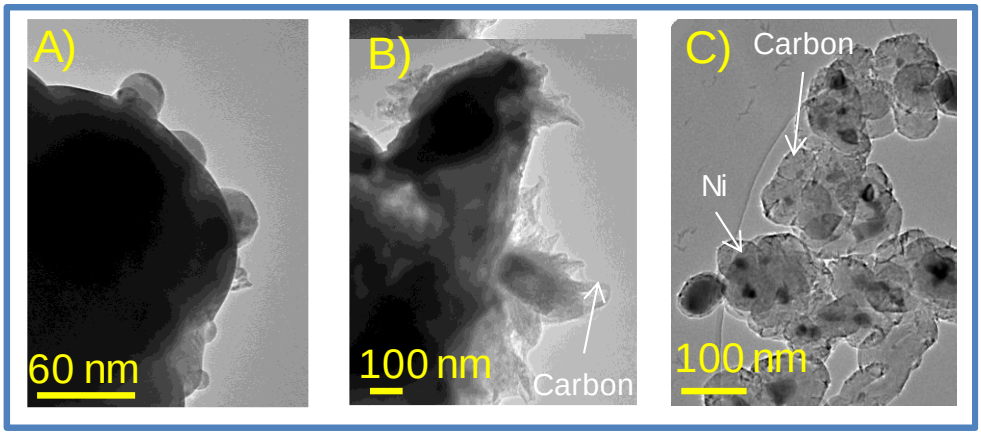

Figure 3.4 *Post mortem* TEM image after long reaction time A) Ni/LSM (Exsolved material), B) Ni/LSMO (Impregnated material) and C) Ni/YSZ.

The CO selectivity calculated for all materials once the steady-state condition is reached is presented in Table 3.1. The exsolved material shows a CO selectivity slightly upper than the value for impregnated material: 0.86 ± 0.01 against 0.80 ± 0.01 respectively. In both cases, these results together with the reduced presence of CO_2 in the products indicate that the MSR reaction (Equation 3.1) becomes more predominant, and the WGS reaction (Equation 3.2) has a low contribution. This hypothesis is confirmed by calculating the H_2/CO ratio: for exsolved material, the value is 3.32 ± 0.03 against 3.60 ± 0.04 for the impregnated sample. Those values are higher than 3 (stoichiometric H_2/CO value for MSR reaction), suggesting than the WGS reaction is slightly present during the catalytic test, consuming CO and producing H_2 as well as CO_2; low S/C ratii increase the CO selectivity while higher ratii the CO_2 selectivity [19], as presented and discussed in Chapter 3. In the case of Ni/YSZ, the CO selectivity is 0.99 ± 0.02 and H_2/CO ratio 2.92 ± 0.07, confirming that only the MSR reaction is occurring over this catalyst. However, for long reaction time, the selectivity values over the reference material (Ni/YSZ) are null due to the complete deactivation of the catalyst. In the case of the impregnated material, while the CH_4 conversion slowly decreases, the behavior of CO and CO_2 selectivity is reversed due to the fact that the material produces more CO_2 than CO, as shown with the rising H_2/CO value, in relation with the formation of carbon by the disproportionation of CO (Boudouard reaction Equation 3.4). On the other hand, the exsolved material shows different behavior, for which neither the selectivity values nor the H_2/CO ratio change even after 100 h of reaction, the latter case being of higher interest for an SOFC anode application fed with hydrocarbon fuels such as natural gas.

		Impregnated	Exsolved	Ni/YSZ
S_{CO}	S.S.	0.80 ± 0.01	0.86 ± 0.01	0.99 ± 0.02
	L.R.	0.29[a]	0.87[b]	0[a]
S_{CO_2}	S.S.	0.20 ± 0.01	0.14 ± 0.01	0.01 ± 2x10^{-3}
	L.R.	0.71[a]	0.13[b]	0[a]
H_2/CO ratio	S.S.	3.60	3.32	2.92
	L.R.	4.24[a]	3.31[b]	-[a]

*S.S.: steady-state conditions

*L.R.: long reaction time, a:30 h (1800 min), b: 100 h (6000 min)

Table 3.1 Values of selectivity and H_2/CO ratio for impregnated, exsolved and reference (Ni/YSZ) materials in steady-state condition during long reaction time.

3.4.2. *H_2S poisoning*

After H_2S treatment over the exsolved and impregnated materials, the catalytic behavior for the MSR reaction is practically null with CH_4 conversion values of 1.45 ± 0.30 mol% and 1.50 ± 0.12 mol%, respectively. These results suggest that both materials are irreversibly susceptible to sulfur poisoning.

As described in the methodology section, the sulfur sensitivity of both exsolved and impregnated materials was tested by pretreatment in an atmosphere containing 50 ppm H_2S during 8 h at 850 °C. The poisoning in Ni/YSZ reference material was not studied in the present work, considering that many works have demonstrated that this anode material is easily poisoned with H_2S, in a wide range of concentrations and temperatures [72–74].

The XRD patterns of impregnated and exsolved materials after H_2S poisoning are presented in Figure 3.5 and Figure 3.6, respectively. The negative effect of H_2S is clear in both materials, as the starting diffraction patterns have changed, and new phases are formed due to the adsorption of sulfur on the surface and the generation of sulfide and/or sulfate compounds. These results are not really positives for the application, and in particular from the point of view of the MSR catalytic behavior in the presence of sulfides. According to XRD analysis and Rietveld refinement, the resulting phases after H_2S poisoning are: $La_{0.5}Sr_{1.5}MnO_4$ (ceramic support), Ni (active phase), nickel sulfide (Ni_3S_2), lanthanum oxy-sulfate (La_2O_2S) and other metallic sulfides such as SrS and MnS for the impregnated material and $LaSrMnO_4$ (ceramic support), Ni (active phase),

Ni_3S_2, La_2O_2S, SrS, MnS and a $La_xSr_{1-x}MnO_3$-type phase with perovskite structure for the exsolved material, being coherent with previous reports [75–78]. The formation of the additional phase in the poisoned exsolved sample could be associated with the stoichiometric difference of both support materials ($LaSrMnO_4$ against $La_{0.5}Sr_{1.5}MnO_4$).

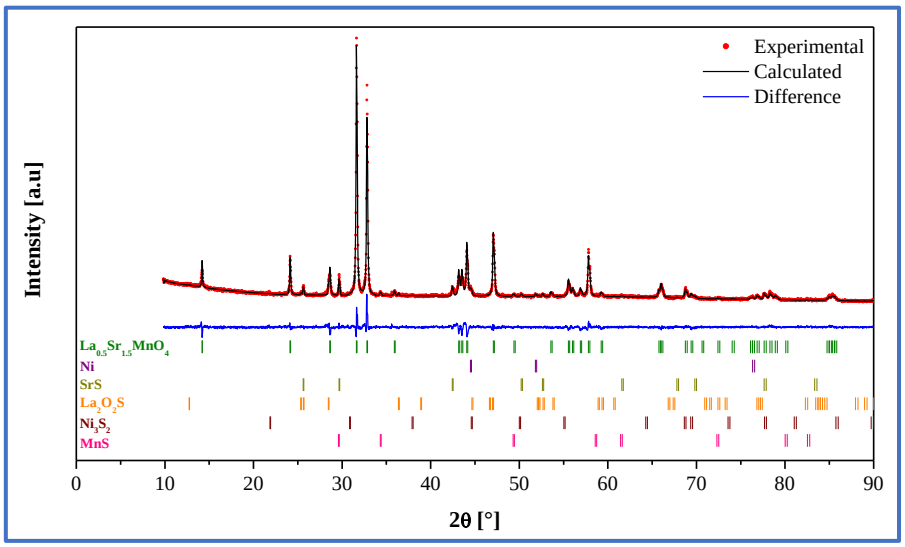

Figure 3.5 Graphical result of Rietveld refinement for impregnated material (Ni/LSMO n= 1) after H_2S treatment.

Sulfur poisoning mechanism has been described as made of two sequential surface steps. When H_2S molecules touch the Ni surface, the first step occurs, *i.e.* a dissociative adsorption of H_2S begins. The formed sulfur radicals are strongly adsorbed and quickly cover and block the metallic active sites, suppressing later the CH_4 and H_2O adsorption, dissociation, oxidation and diffusion necessary for the MSR reaction (inhibition). Subsequently, a gradual degradation of the material occurs, inducing the formation of inactive Ni-S compounds, mainly Ni_3S_2 [62,79,80].

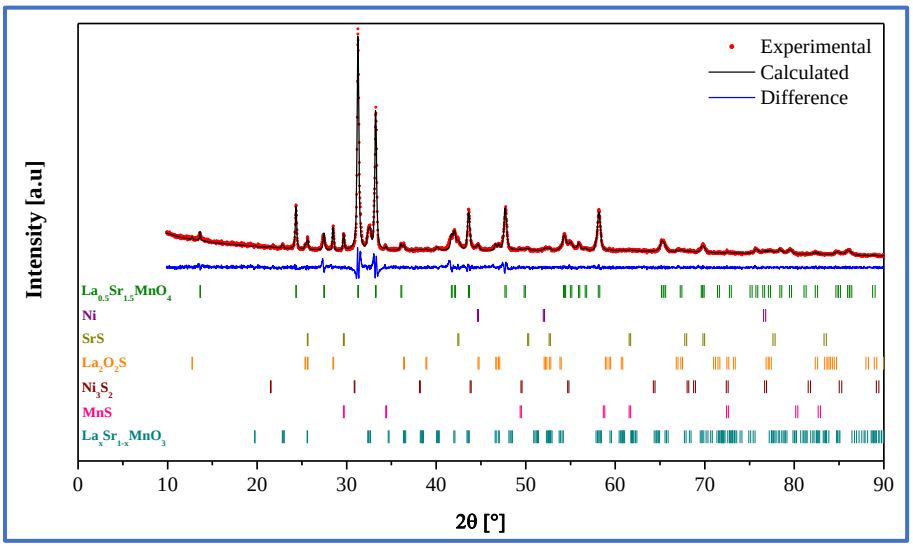

Figure 3.6 Graphical result of Rietveld refinement for exsolved material (Ni/LSM n= 1) after H_2S treatment.

Additionally, the materials poisoning confirmed by the catalytic tests and XRD results has been also examined using surface XPS and Raman analysis. Figure 3.7 shows the XPS spectra of impregnated and exsolved material after H_2S treatment at high temperature. The core level region examined for both materials were S(2p) and Ni(3p); nickel could not be analyzed properly in Ni(2p) region due to the low concentration of metal in both materials (low signal intensity), the overlapping between Ni(2p) and La(3d) signals, even with the procedure proposed by Amaya *et al.* and described in [81] for a nickel lanthanum catalyst with similar Ni content.

About sulfur, the S(2p) spectra of both materials were successfully decomposed notwithstanding the low signal intensity. The peak doublet with low binding energy (around 162 eV) on sulfur $2p_{3/2}$ can be assigned to S bonded as sulfides (S^{2-}) such as metal sulfides *e.g.* N_xS_y, SrS, or MnS and oxysulfides *e.g.* La_2O_2S [82–85], the same compounds found during XRD analysis. On the other hand, the peak doublet at high binding energy (around 168 eV) is associated to surface sulfur-oxygen impurity species characteristic of S bonded as sulfates (SO_4^{2-}), probably $La_2O_2SO_4$ which contaminates the signal in the case of La_2O_2S due to its oxidation.

The decomposition of the XPS spectra in the case of Ni 3p for the only reduced materials (exsolved or Ni/LSM and impregnated or Ni/LSMO) evidences low binding energies

with values of 66.30 and 66.20 eV, respectively (Appendix N); those values agree well with the literature [86–88]. However, once the reduced materials have been treated with H_2S at high temperature, the observed binding energies are shifted to higher values, *i.e.* 67.8 eV for the impregnated material and 66.90 eV for the exsolved material (Figure 3.7). Such results are very close to XPS decomposition lines of as-synthesized material, with 66.8 and 66.9 eV for $La_{1.5}Sr_{1.5}Mn_{1.5}Ni_{0.5}O_{7\pm\delta}$ and NiO/LSMO respectively (Appendix N), and consistent with the data reported by other authors [86,89–91]. It confirms the presence of nickel in an oxidized state that would be coherent with the nature of formed nickel sulfide.

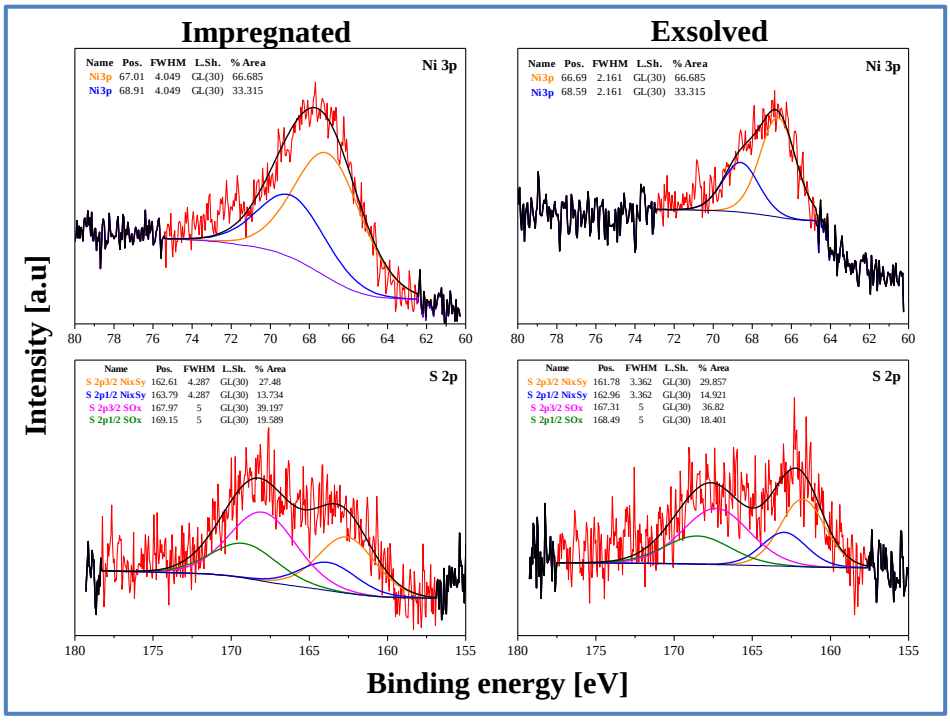

Figure 3.7 XPS spectra of Ni(3p) and S(2p) of the impregnated and exsolved materials after H_2S treatment at 850 °C during 8 h.

To further confirm those results, the Raman spectra of both materials after H_2S treatment are presented in Figure 3.8. The characteristic bands of the supports, $LaSrMnO_4$ and $La_{0.5}Sr_{1.5}MnO_4$, are present as the higher signals at 490 and 700 cm^{-1} on the one hand [92] and 532 and 640 cm^{-1} on the other hand [93,94], respectively. The difference between the vibration frequencies in both materials is related to the difference of material

composition and the huge signal broadening is associated with the Jahn-Teller distortion of the MnO_6 octahedra due to the excess of charge introduced by La doping [93,94]. Concerning the presence of other phases, the analysis of the low-frequency range allows evidence the presence of characteristics vibrations of Ni_3S_2, MnS and La_2O_2S, based on literature reported values [95–100].

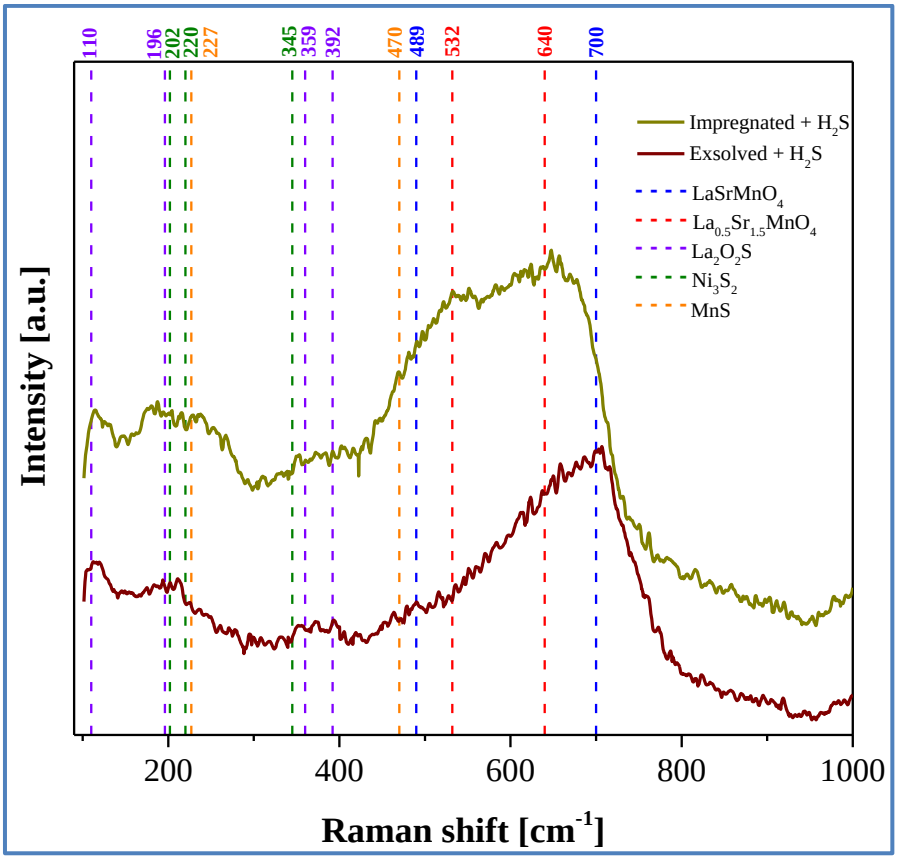

Figure 3.8 Raman spectra of impregnated and exsolved materials after treatment with H_2S at 850 °C.

3.5. **Conclusions**

The present research demonstrates that the Ni exsolution technique applied to the $La_{1.5}Sr_{1.5}Mn_{1.5}Ni_{0.5}O_{7\pm\delta}$ complex oxide to produce a Ni-decorated Ruddlesden-Popper manganite provides a performant and long-term stable catalyst for the steam reforming of methane in deficient steam conditions, in comparison to an analogue impregnated material and to the Ni/YSZ cermet, the state-of-the-art SOFC anode. The resulting behavior is explained by the well dispersed and socketed Ni nanoparticles on the oxide surface in the case of exsolved catalyst, being highly active and stable even up to 100 h of reaction without carbon deposition. Such approach provides a promising way for enhancing the catalytic (and probably the electrochemical) properties of RP manganites for SOFC anodes. However, all three materials exhibit a high level of sensitivity to H_2S (50 ppm), with an almost complete catalyst poisoning for H_2S content characteristic of natural gas. Therefore, its possible application as SOFC anode material would be limited to sulfur-free hydrocarbon fuels.

3.6. **References**

[1] S. McIntosh, R.J. Gorte, Direct hydrocarbon solid oxide fuel cells, Chem. Rev. 104 (2004) 4845–4865. doi:10.1021/cr020725g.

[2] G.J. Saunders, J. Preece, K. Kendall, Formulating liquid hydrocarbon fuels for SOFCs, J. Power Sources. 131 (2004) 23–26. doi:10.1016/j.jpowsour.2004.01.040.

[3] T. Matsui, T. Iida, R. Kikuchi, M. Kawano, T. Inagaki, K. Eguchi, Carbon Deposition over Ni–ScSZ Anodes Subjected to Various Heat-Treatments for Internal Reforming of Solid Oxide Fuel Cells, J. Electrochem. Soc. 155 (2008) B1136. doi:10.1149/1.2975337.

[4] G. Postole, K. Girona, J. Toyir, A. Kaddouri, P. Gélin, Catalytic steam methane reforming over Ir/Ce 0.9 Gd 0.1 O 2-x : Resistance to coke formation and sulfur poisoning, Fuel Cells. 12 (2012) 275–287. doi:10.1002/fuce.201100079.

[5] M. Andersson, H. Paradis, J. Yuan, B. Sundén, Review of catalyst materials and catalytic steam reforming reactions in SOFC anodes, Int. J. Energy Res. 35 (2011) 1340–1350. doi:10.1002/er.1875.

[6] K. Li, L. Jia, X. Wang, J. Pu, B. Chi, L. Jian, Methane on-cell reforming in nickel-iron alloy supported solid oxide fuel cells, J. Power Sources. 284 (2015) 446–451. doi:10.1016/j.jpowsour.2015.03.062.

[7] A. Atkinson, S. Barnett, R.J. Gorte, J.T.S. Irvine, A.J. McEvoy, M. Mogensen, S.C.

Singhal, J. Vohs, Advanced anodes for high-temperature fuel cells., Nat. Mater. 3 (2004) 17–27. doi:10.1038/nmat1040.

[8] K. Girona, S. Sailler, P. Gélin, N. Bailly, S. Georges, Y. Bultel, Modelling of gradual internal reforming process over Ni-YSZ SOFC anode with a catalytic layer, Can. J. Chem. Eng. 93 (2015) 285–296. doi:10.1002/cjce.22113.

[9] J. Toyir, P. Gélin, H. Belatel, A. Kaddouri, Ir/$Ce_{0.9}Gd_{0.1}O_{2-x}$ as a new potential anode component in solid oxide fuel cells integrating the concept of gradual internal reforming of methane, Catal. Today. 157 (2010) 451–455. doi:10.1016/j.cattod.2010.03.066.

[10] P. Vernoux, J. Guindet, M. Kleitz, Gradual Internal Methane Reforming in Intermediate-Temperature Solid Oxide Fuel Cell, J. Electrochem. Soc. 145 (1998) 3487–3492.

[11] S.D. Nobrega, M. V. Galesco, K. Girona, D.Z. De Florio, M.C. Steil, S. Georges, F.C.Fonseca, Direct ethanol solid oxide fuel cell operating in gradual internal reforming, J. Power Sources. 213 (2012) 156–159. doi:10.1016/j.jpowsour.2012.03.104.

[12] J.-M. Klein, M. Hénault, C. Roux, Y. Bultel, S. Georges, Direct methane solid oxide fuel cell working by gradual internal steam reforming: Analysis of operation, J. Power Sources. 193 (2009) 331–337. doi:10.1016/j.jpowsour.2008.11.122.

[13] H.P. He, A. Wood, D. Steedman, M. Tilleman, Sulphur tolerant shift reaction catalysts for nickel-based SOFC anode, Solid State Ionics. 179 (2008) 1478–1482. doi:10.1016/j.ssi.2007.11.009.

[14] T.R. Smith, A. Wood, V.I. Birss, Effect of hydrogen sulfide on the direct internal reforming of methane in solid oxide fuel cells, Appl. Catal. A Gen. 354 (2009) 1–7. doi:10.1016/j.apcata.2008.10.055.

[15] Y. Matsuzaki, I. Yasuda, The poisoning effect of sulfur-containing impurity gas on a SOFC anode: Part I. Dependence on temperature, time, and impurity concentration, Solid State Ionics. 132 (2000) 261–269. doi:10.1016/s0167-2738(00)00653-6.

[16] Y.S. Chung, T. Kim, T.H. Shin, H. Yoon, S. Park, N.M. Sammes, W.B. Kim, J.S. Chung, In situ preparation of a $La_{1.2}Sr_{0.8}Mn_{0.4}Fe_{0.6}O_4$ Ruddlesden-Popper phase with exsolved Fe nanoparticles as an anode for SOFCs, J. Mater. Chem. A. 5 (2017) 6437–6446. doi:10.1039/c6ta09692a.

[17] Y. Sun, J. Li, Y. Zeng, B.S. Amirkhiz, M. Wang, Y. Behnamian, J. Luo, A-site deficient perovskite: the parent for in situ exsolution of highly active, regenerable nano-particles as SOFC anodes, J. Mater. Chem. A. 3 (2015) 11048–11056. doi:10.1039/C5TA01733E.

[18] C.M. Finnerty, R.M. Ormerod, Internal reforming over nickel/zirconia anodes in SOFCs operating on methane: Influence of anode formulation, pre-treatment and operating conditions, J. Power Sources. 86 (2000) 390–394. doi:10.1016/S0378-

7753(99)00498-X.

[19] H. Timmermann, D. Fouquet, A. Weber, E. Ivers-Tiffée, U. Hennings, R. Reimert, Internal reforming of methane at Ni/YSZ and Ni/CGO SOFC cermet anodes, Fuel Cells. 6 (2006) 307–313. doi:10.1002/fuce.200600002.

[20] V.V. Kharton, A.A. Yaremchenko, A.L. Shaula, M. V. Patrakeev, E.N. Naumovich, D.I. Logvinovich, J.R. Frade, F.M.B. Marques, Transport properties and stability of Ni-containing mixed conductors with perovskite- and K_2NiF_4-type structure, J. Solid State Chem. 177 (2004) 26–37. doi:10.1016/S0022-4596(03)00261-5.

[21] S.J. Skinner, J.A. Kilner, Oxygen diffusion and surface exchange in $La_{2-x}Sr_xNiO_{4+\delta}$, Solid State Ionics. 135 (2000) 709–712. doi:10.1016/S0167-2738(00)00388-X.

[22] P. V. Balachandran, D. Puggioni, J.M. Rondinelli, Crystal-chemistry guidelines for noncentrosymmetric A_2BO_4 ruddlesden-popper oxides, Inorg. Chem. 53 (2014) 336–348. doi:10.1021/ic402283c.

[23] C. Autret, C. Martin, M. Hervieu, R. Retoux, B. Raveau, G. André, F. Bourée, Structural investigation of Ca_2MnO_4 by neutron powder diffraction and electron microscopy, J. Solid State Chem. 177 (2004) 2044–2052. doi:10.1016/j.jssc.2004.02.012.

[24] J. Dailly, S. Fourcade, A. Largeteau, F. Mauvy, J.C. Grenier, M. Marrony, Perovskite and A_2MO_4-type oxides as new cathode materials for protonic solid oxide fuel cells, Electrochim. Acta. 55 (2010) 5847–5853. doi:10.1016/j.electacta.2010.05.034.

[25] H. Zhao, F. Mauvy, C. Lalanne, J.M. Bassat, S. Fourcade, J.C. Grenier, New cathode materials for ITSOFC: Phase stability, oxygen exchange and cathode properties of $La_{2-x}NiO_{4+\delta}$, Solid State Ionics. 179 (2008) 2000–2005. doi:10.1016/j.ssi.2008.06.019.

[26] M. Al Daroukh, V. V. Vashook, H. Ullmann, F. Tietz, I. Arual Raj, Oxides of the AMO_3 and A_2MO_4-type: Structural stability, electrical conductivity and thermal expansion, Solid State Ionics. 158 (2003) 141–150. doi:10.1016/S0167-2738(02)00773-7.

[27] S.Y. Jeon, M.B. Choi, H.N. Im, J.H. Hwang, S.J. Song, Oxygen ionic conductivity of La 2NiO 4δ via interstitial oxygen defect, J. Phys. Chem. Solids. 73 (2012) 656–660. doi:10.1016/j.jpcs.2012.01.006.

[28] H.W. Nie, T.L. Wen, S.R. Wang, Y.S. Wang, U. Guth, V. Vashook, Preparation, thermal expansion, chemical compatibility, electrical conductivity and polarization of $A_{2-\alpha}A'_\alpha MO_4$ (A = Pr, Sm; A′ = Sr; M = Mn, Ni; α = 0.3, 0.6) as a new cathode for SOFC, Solid State Ionics. 177 (2006) 1929–1932. doi:10.1016/j.ssi.2006.01.003.

[29] Y.S. Yoo, M. Choi, J.H. Hwang, H.N. Im, B. Singh, S.J. Song, $La_2NiO_{4+\delta}$ as oxygen electrode in reversible solid oxide cells, Ceram. Int. 41 (2015) 6448–6454. doi:10.1016/j.ceramint.2015.01.083.

[30] V. Meille, Review on methods to deposit catalysts on structured surfaces, Appl.

Catal. A Gen. 315 (2006) 1–17. doi:10.1016/j.apcata.2006.08.031.

[31] B. Mitra, X. Gao, I.E. Wachs, A.M. Hirt, G. Deo, Characterization of supported rhenium oxide catalysts: Effect of loading, support and additives, Phys. Chem. Chem. Phys. 3 (2001) 1144–1152. doi:10.1039/b007381o.

[32] D. Neagu, T.S. Oh, D.N. Miller, H. Ménard, S.M. Bukhari, S.R. Gamble, R.J. Gorte, J.M. Vohs, J.T.S. Irvine, Nano-socketed nickel particles with enhanced coking resistance grown in situ by redox exsolution, Nat. Commun. 6 (2015) 1–8. doi:10.1038/ncomms9120.

[33] R. Shiozaki, A.G. Andersen, T. Hayakawa, S. Hamakawa, K. Suzuki, M. Shimizu, K. Takehira, Partial oxidation of methane over a Ni/BaTiO3 catalyst prepared by solid phase crystallization, J. Chem. Soc. - Faraday Trans. 93 (1997) 3235–3242. doi:10.1039/a701383c.

[34] W. Kobsiriphat, B.D. Madsen, Y. Wang, L.D. Marks, S.A. Barnett, $La_{0.8}Sr_{0.2}Cr_{1-x}Ru_xO_{3-\delta}$-$Gd_{0.1}Ce_{0.9}O_{1.95}$ solid oxide fuel cell anodes: Ru precipitation and electrochemical performance, Solid State Ionics. 180 (2009) 257–264. doi:10.1016/j.ssi.2008.12.022.

[35] D. Zubenko, S. Singh, B.A. Rosen, Exsolution of Re-alloy catalysts with enhanced stability for methane dry reforming, Appl. Catal. B Environ. 209 (2017) 711–719. doi:10.1016/j.apcatb.2017.03.047.

[36] J. Li, B. Wei, X. Yue, L. Zhe, A Highly Efficient and Robust Perovskite Anode with Iron–Palladium Co-exsolutions for Intermediate-Temperature Solid-Oxide Fuel Cells, ChemSusChem. 11 (2018) 2593–2603. doi:10.1002/cssc.201800641.

[37] E.I. Papaioannou, D. Neagu, W.K.W. Ramli, J.T.S. Irvine, I.S. Metcalfe, Sulfur-Tolerant, Exsolved Fe–Ni Alloy Nanoparticles for CO Oxidation, Top. Catal. (2018) 1–8. doi:10.1007/s11244-018-1053-8.

[38] Y.F. Sun, J.H. Li, L. Cui, B. Hua, S.H. Cui, J. Li, J.L. Luo, A-site-deficiency facilitated in situ growth of bimetallic Ni-Fe nano-alloys: a novel coking-tolerant fuel cell anode catalyst, Nanoscale. 7 (2015) 11173–11181. doi:10.1039/c5nr02518d.

[39] T. Luo, X. Liu, X. Meng, H. Wu, S. Wang, Z. Zhan, In situ formation of $LaNi_{0.6}Fe_{0.4}O_{3-\delta}$-carbon nanotube hybrids as anodes for direct-methane solid oxide fuel cells, J. Power Sources. 299 (2015) 472–479. doi:10.1016/j.jpowsour.2015.09.035.

[40] D. Neagu, G. Tsekouras, D.N. Miller, H. Menard, J.T. Irvine, In situ growth of nanoparticles through control of non-stoichiometry, Nat Chem. 5 (2013) 916–923. doi:10.1038/nchem.1773.

[41] J.T.S. Irvine, D. Neagu, M.C. Verbraeken, C. Chatzichristodoulou, C. Graves, M.B. Mogensen, Evolution of the electrochemical interface in high-temperature fuel cells and electrolysers, Nat. Energy. 1 (2016) 1–13. doi:10.1038/nenergy.2015.14.

[42] T.S. Oh, E.K. Rahani, D. Neagu, J.T.S. Irvine, V.B. Shenoy, R.J. Gorte, J.M. Vohs,

Evidence and Model for Strain-Driven Release of Metal Nanocatalysts from Perovskites during Exsolution, J. Phys. Chem. Lett. 6 (2015) 5106–5110. doi:10.1021/acs.jpclett.5b02292.

[43] Y. Li, W. Zhang, Y. Zheng, J. Chen, B. Yu, Y. Chen, M. Liu, Controlling cation segregation in perovskite-based electrodes for high electro-catalytic activity and durability, Chem. Soc. Rev. 46 (2017) 6345–6378. doi:10.1039/c7cs00120g.

[44] O. Kwon, S. Sengodan, K. Kim, G. Kim, H.Y. Jeong, J. Shin, Y.W. Ju, J.W. Han, G. Kim, Exsolution trends and co-segregation aspects of self-grown catalyst nanoparticles in perovskites, Nat. Commun. 8 (2017) 1–7. doi:10.1038/ncomms15967.

[45] S. Vecino-Mantilla, P. Gauthier-Maradei, M. Huvé, J.M. Serra, P. Roussel, G.H. Gauthier, Nickel exsolution-driven phase transformation from an n = 2 to an n= 1 Ruddlesden-Popper manganite for methane steam reforming reaction in SOFC conditions, ChemCatChem. 11 (2019) 4631–4641. doi:10.1002/cctc.201901002.

[46] M.P. Pechini, Method of preparing lead and alkaline earth titanates and niobates and coating method using the same to form a capacitor, US Patent no. 3330697 A, U.S. Patent No. 3330697 A, 1967.

[47] Ecopetrol, Composición del gas entregado al SNT desde la planta de gas Cusiana, Dep. Logística Energía y Gas-Gerencia Logística y Contratación. (2019). https://www.ecopetrol.com.co/wps/portal/es (accessed April 11, 2019).

[48] T. Siegrist, Crystallographica - a software toolkit for crystallography , J. Appl. Crystallogr. 30 (1997) 418–419. doi:10.1107/s0021889897003026.

[49] V. Petrícek, M. Dušek, L. Palatinus, Crystallographic computing system JANA2006: General features, Zeitschrift Fur Krist. 229 (2014) 345–352. doi:10.1515/zkri-2014-1737.

[50] M.S. Fan, A.Z. Abdullah, S. Bhatia, Utilization of greenhouse gases through carbon dioxide reforming of methane over Ni-Co/MgO-ZrO_2: Preparation, characterization and activity studies, Appl. Catal. B Environ. 100 (2010) 365–377. doi:10.1016/j.apcatb.2010.08.013.

[51] C. Arrivé, T. Delahaye, O. Joubert, G. Gauthier, Exsolution of niquel nanoparticles at the surface of a conducting titanate as potential hydrogen electrode materialfor solid oxide electrochemical cells, J. Power Sources. 223 (2013) 341–348. doi:10.1016/j.jpowsour.2012.09.062.

[52] M.C.J. Bradford, M.A. Vannice, CO_2 reforming of CH_4, Catal. Rev. - Sci. Eng. 41 (1999) 1–42. doi:10.1081/CR-100101948.

[53] F. Rahbar Shamskar, M. Rezaei, F. Meshkani, The influence of Ni loading on the activity and coke formation of ultrasound-assisted co-precipitated Ni–Al_2O_3 nanocatalyst in dry reforming of methane, Int. J. Hydrogen Energy. 42 (2017) 4155–4164. doi:10.1016/j.ijhydene.2016.11.067.

[54] T. Wei, L. Jia, H. Zheng, B. Chi, J. Pu, J. Li, $LaMnO_3$-based perovskite with in-situ exsolved Ni nanoparticles: a highly active, performance stable and coking resistant catalyst for CO_2 dry reforming of CH_4, Appl. Catal. A Gen. 564 (2018) 199–207. doi:10.1016/j.apcata.2018.07.031.

[55] A. Yaqub, N.K. Janjua, C. Savaniu, J.T.S. Irvine, Synthesis and characterization of B-site doped $La_{0.20}Sr_{0.25}Ca_{0.45}TiO_3$ as SOFC anode materials, Int. J. Hydrogen Energy. 40 (2015) 760–766. doi:10.1016/j.ijhydene.2014.08.083.

[56] V.M. Shinde, G. Madras, Catalytic performance of highly dispersed Ni/TiO_2 for dry and steam reforming of methane, RSC Adv. 4 (2014) 4817–4826. doi:10.1039/c3ra45961f.

[57] J. Zhu, X. Peng, L. Yao, J. Shen, D. Tong, C. Hu, The promoting effect of La, Mg, Co and Zn on the activity and stability of Ni/SiO_2 catalyst for CO2 reforming of methane, Int. J. Hydrogen Energy. 36 (2011) 7094–7104. doi:10.1016/j.ijhydene.2011.02.133.

[58] L. Yao, J. Shi, C. Hu, The structure, carbon deposition and stability of a ZrO_x/Ni-MnO_x/SiO_2 catalyst for the CO_2 reforming of methane, RSC Adv. 5 (2015) 90168–90177. doi:10.1039/c5ra19195e.

[59] C. Tanios, C. Gennequin, M. Labaki, H.L. Tidahy, A. Aboukaïs, E. Abi-Aad, Evaluation of a catalyst durability in absence and presence of toluene impurity: Case of the material $Co_2NvMg_2Al_2$ mixed oxide prepared by hydrotalcite route in methane dry reforming to produce energy, Materials (Basel). 12 (2019). doi:10.3390/ma12091362.

[60] J.R.H. Ross, Metal catalysed methanation and steam reforming, The Royal Society of Chemistry, 1985. doi:10.1039/9781847553195-00001.

[61] W. Wang, C. Su, Y. Wu, R. Ran, Z. Shao, Progress in solid oxide fuel cells with nickel-based anodes operating on methane and related fuels, Chem. Rev. 113 (2013) 8104–8151. doi:10.1021/cr300491e.

[62] C.H. Bartholomew, Mechanism of catalyst deactivation, Appl. Catal. A Gen. 212 (2001) 17–60. doi:https://doi.org/10.1016/S0926-860X(00)00843-7.

[63] C.H. Bartholomew, Carbon deposition in steam reforming and methanation, Catal. Rev. Sci. Eng. 24 (1982) 67–112. doi:http://dx.doi.org/10.1080/03602458208079650.

[64] A. Lanzini, P. Leone, C. Guerra, F. Smeacetto, N.P. Brandon, M. Santarelli, Durability of anode supported Solid Oxides Fuel Cells (SOFC) under direct dry-reforming of methane, Chem. Eng. J. 220 (2013) 254–263. doi:10.1016/j.cej.2013.01.003.

[65] J. Hanna, W.Y. Lee, Y. Shi, A.F. Ghoniem, Fundamentals of electro- and thermochemistry in the anode of solid-oxide fuel cells with hydrocarbon and syngas fuels, Prog. Energy Combust. Sci. 40 (2014) 74–111.

doi:10.1016/j.pecs.2013.10.001 Review.

[66] J.W. Fergus, Oxide anode materials for solid oxide fuel cells, Solid State Ionics. 177 (2006) 1529–1541. doi:10.1016/j.jpowsour.2007.08.011.

[67] S.P. Jiang, S.H. Chan, A review of anode materials development in solid oxide fuel cells, J. Mater. Sci. 39 (2004) 4405–4439. doi:10.1023/b:jmsc.0000034135.52164.6b.

[68] T. Chen, W.G. Wang, H. Miao, T. Li, C. Xu, Evaluation of carbon deposition behavior on the nickel/yttrium-stabilized zirconia anode-supported fuel cell fueled with simulated syngas, J. Power Sources. 196 (2011) 2461–2468. doi:10.1016/j.jpowsour.2010.11.095.

[69] Y. Nishiyama, K. Moriguchi, N. Otsuka, T. Kudo, Improving metal dusting resistance of transition-metals and Ni-Cu alloys, Mater. Corros. 56 (2005) 806–813. doi:10.1002/maco.200503883.

[70] J. Zhang, P. Munroe, D.J. Young, Microprocesses in nickel accompanying metal dusting, Acta Mater. 56 (2008) 68–77. doi:10.1016/j.actamat.2007.09.010.

[71] D.J. Young, J. Zhang, C. Geers, M. Schütze, Recent advances in understanding metal dusting: A review, Mater. Corros. 62 (2011) 7–28. doi:10.1002/maco.201005675.

[72] B. Shri Prakash, S. Senthil Kumar, S.T. Aruna, Properties and development of Ni/YSZ as an anode material in solid oxide fuel cell: A review, Renew. Sustain. Energy Rev. 36 (2014) 149–179. doi:10.1016/j.rser.2014.04.043.

[73] L. Zhang, S.P. Jiang, H.Q. He, X. Chen, J. Ma, X.C. Song, A comparative study of H_2S poisoning on electrode behavior of Ni/YSZ and Ni/GDC anodes of solid oxide fuel cells, Int. J. Hydrogen Energy. 35 (2010) 12359–12368. doi:10.1016/j.ijhydene.2010.08.067.

[74] Z. Cheng, M. Liu, Characterization of sulfur poisoning of Ni-YSZ anodes for solid oxide fuel cells using in situ Raman microspectroscopy, Solid State Ionics. 178 (2007) 925–935. doi:10.1016/j.ssi.2007.04.004.

[75] M. Florea, S. Somacescu, G. Postole, A. Urdă, F. Neaţu, Ş. Neaţu, L. Massin, P. Gélin, $La_{0.75}Sr_{0.25-X}O_3$ (X = Fe, Mn or Cr) with coking tolerance for CH_4/H_2O reaction: Effect of H_2S on catalytic performance, Catal. Sci. Technol. 9 (2019) 2351–2366. doi:10.1039/c9cy00065h.

[76] Y. Li, Z. Wang, J. Li, X. Zhu, Y. Zhang, X. Huang, Y. Zhou, L. Zhu, Z. Lü, Sulfur poisoning and attempt of oxidative regeneration of $La_{0.75}Sr_{0.25}Cr_{0.5}Mn_{0.5}O_{3-\delta}$ anode for solid oxide fuel cell, J. Alloys Compd. 698 (2017) 794–799. doi:10.1016/j.jallcom.2016.12.313.

[77] Y. Li, L. Na, Z. Lü, Z. Jiang, Regeneration of sulfur poisoned $La_{0.75}Sr_{0.25}Cr_{0.5}Mn_{0.5}O_{3-\delta}$ anode of solid oxide fuel cell using electrochemical oxidative method, Electrochim. Acta. 304 (2019) 342–349. doi:10.1016/j.electacta.2019.03.027.

[78] S. Zha, P. Tsang, Z. Cheng, M. Liu, Electrical properties and sulfur tolerance of $La_{0.75}Sr_{0.25}Cr_{1-x}Mn_xO_3$ under anodic conditions, J. Solid State Chem. 178 (2005) 1844–1850. doi:10.1016/j.jssc.2005.03.027.

[79] S. Zha, Z. Cheng, M. Liu, Sulfur poisoning and regeneration of ni-based anodes in solid oxide fuel cells, J. Electrochem. Soc. 154 (2007) 201–206. doi:10.1149/1.2404779.

[80] H. Chen, F. Wang, W. Wang, D. Chen, S.D. Li, Z. Shao, H_2S poisoning effect and ways to improve sulfur tolerance of nickel cermet anodes operating on carbonaceous fuels, Appl. Energy. 179 (2016) 765–777. doi:10.1016/j.apenergy.2016.07.028.

[81] Á.A. Amaya, C.A. González, M.E. Niño-Gómez, F. Martínez O., XPS fitting model proposed to the study of Ni and La in deactivated FCC catalysts, J. Electron Spectros. Relat. Phenomena. 233 (2019) 5–10. doi:10.1016/j.elspec.2019.03.007.

[82] W.H. Shen, S. Naito, Easy precipitation method for preparation of cerium added $La_2O_2SO_4$ used for oxygen storage, Adv. Mater. Res. 886 (2014) 196–199. doi:10.4028/www.scientific.net/AMR.886.196.

[83] Y. Jiang, Y. Wu, Y. Xie, Y.-T. Qian, Synthesis and Characterization of nanocrystalline lanthanide oxysulfide via a $La(OH)_3$ gel solvothermal route, J. Am. Ceram. Soc. 83 (2000) 2628–2630.

[84] B.M. Jaffar, H.C. Swart, H.A.A. Seed Ahmed, A. Yousif, R.E. Kroon, Cathodoluminescence degradation of Bi doped La_2O_3 and La_2O_2S phosphor powders, Phys. B Condens. Matter. 574 (2019) 411659. doi:10.1016/j.physb.2019.411659.

[85] J.F. Moulder, W.F. Stickle, P.E. Sobol, K.D. Bomben, Handbook of X-ray photoelectron spectroscopy, Perkin-Elmer Corporation, Eden Prairie, Minnetsoa, USA, 1992.

[86] A. Nenning, J. Fleig, Electrochemical XPS investigation of metal exsolution on SOFC electrodes: Controlling the electrode oxygen partial pressure in ultra-high-vacuum, Surf. Sci. 680 (2019) 43–51. doi:10.1016/j.susc.2018.10.006.

[87] S.K. Kulkarni, M.G. Thube, A.S. Nigavekar, Electronic-structure study of $Ni_{81}Cr_{15}B_4$ metallic glass using photoemission spectroscopy, Phys. Rev. B. 37 (1988) 6723–6730. doi:10.1103/PhysRevB.37.6723.

[88] N.S. Mcintyre, M.G. Cook, X-Ray Photoelectron Studies on Some Oxides and Hydroxides of Cobalt, Nickel, and Copper, Anal. Chem. 47 (1975) 2208–2213. doi:10.1021/ac60363a034.

[89] J.F. Marco, J.R. Gancedo, J. Ortiz, J.L. Gautier, Characterization of the spinel-related oxides $Ni_xCo_{3-x}O_4$ (x = 0.3, 1.3, 1.8) prepared by spray pyrolysis at 350 °C, Appl. Surf. Sci. 227 (2004) 175–186. doi:10.1016/j.apsusc.2003.11.065.

[90] G.C. Allen, S.J. Harris, J.A. Jutson, J.M. Dyke, A study of a number of mixed transition metal oxide spinels using X-ray photoelectron spectroscopy, Appl. Surf.

Sci. 37 (1989) 111–134. doi:10.1016/0169-4332(89)90977-X.

[91] K.K. Lian, D.W. Kirk, S.J. Thorpe, Investigation of a “two-state” tafel phenomenon for the oxygen evolution reaction on an amorphous ni-co alloy, J. Electrochem. Soc. 142 (1995) 3704–3712. doi:10.1149/1.2048402.

[92] K.Y. Choi, P. Lemmens, D. Heydhausen, G. Güntherodt, C. Baumann, R. Klingeler, P. Reutler, B Büchner, Anomalous orbital dynamics in $LaSrMnO_4$ observed by Raman spectroscopy, Phys. Rev. B - Condens. Matter Mater. Phys. 77 (2008) 1–5. doi:10.1103/PhysRevB.77.064415.

[93] P. Postorino, A. Congeduti, E. Degiorgi, J.P. Itié, P. Munsch, High-pressure behavior of $La_xSr_{2-x}MnO_4$ layered manganites investigated by Raman spectroscopy and x-ray diffraction, Phys. Rev. B - Condens. Matter Mater. Phys. 65 (2002) 2241021–2241028. doi:10.1103/PhysRevB.65.224102.

[94] K. Yamamoto, T. Kimura, T. Ishikawa, T. Katsufuji, Y. Tokura, Raman spectroscopy of the charge-orbital ordering in layered manganites, Phys. Rev. B - Condens. Matter Mater. Phys. 61 (2000) 14706–14715. doi:10.1103/PhysRevB.61.14706.

[95] A. V. Sotnikov, V. V. Bakovets, Kinetics of lanthanum oxide sulfurization in ammonium rhodanide vapor, Inorg. Mater. 50 (2014) 1212–1216. doi:10.1134/S002016851412019X.

[96] M. Mikami, S. Nakamura, Electronic structure of rare-earth sesquioxides and oxysulfides, J. Alloys Compd. 408–412 (2006) 687–692. doi:10.1016/j.jallcom.2005.01.068.

[97] C.R. Gopinath, I.D. Brown, Normal coordinate analysis of the Raman and infrared vibrations of the alpha phases of RE_2O_3 (RE=La, Pr, Nd) and RE_2O_2S (RE=La and Yb), J. Raman Spectrosc. 12 (1982) 278–280. doi:10.1002/jrs.1250120315.

[98] Z. Cheng, H. Abernathy, M. Liu, Raman spectroscopy of nickel sulfide Ni_3S_2, J. Phys. Chem. C. 111 (2007) 17997–18000.

[99] N. Feng, D. Hu, P. Wang, X. Sun, X. Li, D. He, Growth of nanostructured nickel sulfide films on Ni foam as high-performance cathodes for lithium ion batteries, Phys. Chem. Chem. Phys. 15 (2013) 9924–9930. doi:10.1039/c3cp50615k.

[100] J.R.L. Fernandez, M. Souza-Parise, P.C. Morais, Structural characterization and simulation of colloidal MnS, Mater. Res. Express. 2 (2015) 95019. doi:10.1088/2053-1591/2/9/095019.

Conclusions

1. Conclusions

Through the development of our scientific trip, started few chapters ago and known as Ph.D. thesis, many results have been obtained concerning the study of the Ni exsolution in the Ruddlesden-Popper (RP) phase $La_{1.5}Sr_{1.5}Mn_{1.5}Ni_{0.5}O_{7\pm\delta}$, most of them interesting and appropriate for the desired application (SOFC anode material). Therefore, considering the proposed objectives, the results presented in this book led to the following conclusions:

The new material with n= 2 Ruddlesden-Popper structure (RP), $La_{1.5}Sr_{1.5}Mn_{1.5}Ni_{0.5}O_{7\pm\delta}$ (LSMN), was successfully synthesized as a single phase at 1300 °C in the air using the Pechini route, as confirmed by an in-depth structural characterization by Rietveld refinement using X-ray powder diffraction data (XRD). In reducing atmosphere and high temperature (750, 800 and 850 °C) for 4 to 8 h, the complete Ni exsolution from the RP structure is evidenced. As a result, a new stable RP phase corresponding to only one perovskite-layer (n=1) is formed that corresponds to $LaSrMnO_{4\pm\delta}$ (LSM) composition, decorated with metallic Ni nanoparticles socketed on the manganite surface without any other impurity phase as shown by complementary techniques (XRD, TEM, and SEM). This particular heterogeneous phase transformation from RP n=2 to RP n= 1 + Ni had not been previously reported before, neither for catalyst preparation nor for SOFC anode material.

Once the exsolution has been demonstrated, the first litmus test of the as-obtained Ni/LSM was performed: the catalytic tests for the steam reforming of the main light hydrocarbon compounds present in Colombian natural gas (CH_4, C_2H_6, and C_3H_8) in low steam conditions. As expected for a Ni-supported catalyst, a clearly effective CH_4 conversion and H_2 production was observed even better than Ni-impregnated material, of similar stoichiometry, and prepared for comparison, and comparable with the state-of-the-art material for SOFC anode, the Ni/YSZ cermet. This important catalytic behavior is largely related to a lower propensity to Ni coarsening of the exsolved manganite because the metallic particles are embedded in the ceramic support; in comparison, for the impregnated material, the particles are only deposited on the surface and makes them easily mobile, leading to coarsening issues.

Similar exceptional results were obtained during the catalytic test with hydrocarbon mixtures. However, the ethane and propane reforming reactions are favored with respect to methane. The presence of the latter molecules in the reactive mixture promotes faster parallel reactions over the methane reforming, producing the desired H_2 but additionally

more methane. Therefore, the methane steam reforming is not kinetically favored in mixture with other hydrocarbon fuels.

Surprisingly, the catalytic behavior of the new exsolved material was exceptionally satisfactory and stable during 100 h of reaction without formation of carbonaceous species, this long-term stability is much better than for Ni/YSZ or Ni-impregnated materials, whose catalytic behavior dropped to become almost null due to carbon deposition on the metallic active phase, as proved by TEM and TG/MS analysis.

However, despite the stable catalytic stability and the resistance to coking evidenced for the exsolved material, the catalyst is strongly affected by the presence of 50 ppm H_2S causing its irreversible poisoning, which corresponds to the formation of sulfide phases: the catalytic behavior is lost, limiting the material´s possible application as anode material in SOFC fed with sulfur-free hydrocarbon fuels.

In summary, despite the sensibility to H_2S impurity, the newly developed material, based on the Ni exsolution mechanism in which the remaining oxide (the catalytic support) is a Mixed Ionic and Electronic Conductor with interesting electrochemical properties as SOFC anode, is very promising as SOFC anode in a system that would operate with the main hydrocarbon compounds present in a clean natural gas. Considering the results we obtained in this work, electrochemical tests of complete cells in a real anode atmosphere are more than requested to not only complete the material´s characterization but also definitely confirm its potential as anode material in replacement of Ni/YSZ (and other analogue) cermets, giving a step forward in the development of SOFC technology.

Scientific contributions

Scientific contributions

Publications

- Vecino-Mantilla, S., Gauthier-Maradei, M. P., Gauthier, G., Serra, J. M., Huvé, M., Roussel, P., *Nickel exsolution-driven phase transformation from an n=2 to a n=1 Ruddlesden-Popper manganite for methane steam reforming reaction in SOFC conditions.* ChemCatChem, 11(18), 4631-4641. (2019). https://doi.org/10.1002/cctc.201901002.

- Vecino-Mantilla, S., Gauthier-Maradei, M. P., Gauthier, G., Quintero, E., Fonseca, C., *Catalytic steam reforming of natural gas over a new Ni exsolved Ruddlesden-Popper manganite in SOFC anode conditions*. ChemCatChem. (2020). https://doi.org/10.1002/cctc.201902306.

Congress participation

Oral presentations

- Vecino-Mantilla, S., Gauthier-Maradei, M. P., Gauthier, G., Silva, K., Gelin, P., Sandoval-Rincón, M. V., *Catalytic behavior in internal steam reforming of methane in SOFC conditions over $La_xSr_{2-x}MnO_4$ materials*. 2016 AIChe Annual Meeting, San Francisco, United States (2016).

- Vecino-Mantilla, S., Gauthier-Maradei, M. P., Gauthier, G., Serra, J. M., Fabuel, M., Huvé, M., Gardoll, O., Roussel, P., *Assessment of a novel exsolved Ni-doped manganite in the steam reforming of methane under water deficient conditions*. French Conference on Catalysis 2019, Frejus, France (2019).

- Pirovano, C., Vecino-Mantilla, S., Gauthier-Maradei, M. P., Gauthier, G., Cárdenas-Velandia, C., Sandoval-Rincón, M. V., Roussel, P., *Study of $La_{1.5}Sr_{1.5}Mn_{1.5}Ni_{0.5}O_{7\pm\delta}$ as solid oxide fuel cell anode material*. 22nd

International Conference on Solid State Ionic (SSI-22), PyeongChang, South Korea (2019)

Poster presentations

- Vecino-Mantilla, S., Gauthier-Maradei, M. P., Gauthier, G., Serra, J. M., N*ickel exsolution effect on the catalytic behavior of Ruddlesden-Popper manganites in solid oxide fuel cells conditions using Colombian natural gas.* Catalysis: fundamentals and practice summer school, Liverpool, United Kingdom (2017)

- Gauthier-Maradei, M. P., Vecino-Mantilla, S., Gauthier, G., Serra, J. M., Fabuel, M., Huvé, M., Gardoll, O., Roussel, P., *Excellent catalytic performance of a novel exsolved Ni-doped manganite for the steam reforming of methane in SOFC operating conditions*. XIV HYPOTHESIS: HYdrogen POwer THeoretical and Engineering Solutions International Symposium. Foz Do Iguazu, Brazil (2019).

Degree projects (co-direction)

- Iván Eliecer Suárez Acelas and Santiago Páez Duque, E*valuación de una unidad piloto a escala laboratorio de vaporreformado usando bajas concentraciones de agua,* Universidad Industrial de Santander (2016).

- Maria Margarita Vecino Mantilla and Laura Carolina Cárdenas Velandia, *Estudio catalítico de la exsolución in situ de ni en el material* $La_{1.5}Sr_{1.5}Mn_{1.5}Ni_{0.5}O_7$ *en la reacción de reformado de metano con vapor a bajas concentraciones de agua,* Universidad Industrial de Santander (2017).

- Erika Tatiana Quintero Pacheco and Jeison Camilo Fonseca Marquez, *Estudio comparativo de la actividad catalítica del Ni soportado sobre manganitas tipo Ruddlesden-Popper obtenido por impregnación y exsolución en el reformado de metano con vapor a condiciones de pila SOFC,* Universidad Industrial de Santander (2018).

Appendices and supplementary information

Appendix A

Jana2006 is a crystallographic program focused to solution, refinement and interpretation of difficult, especially modulated structures. It calculates structures having up to three modulation vectors from powder as well as single crystal data measured with X-ray or neutron diffraction. The input diffraction data can be unlimitedly combined, the combination of powder neutron data with single crystal X-ray data being a typical example. The structure solution can be done using the built-in charge flipping algorithm or by calling an external direct methods program. Jana can handle multiphase structures (for both powder and single crystal data), merohedric twins as well as twins with partial overlap of diffraction spots, commensurate and composite structures. It contains powerful transformation tools for symmetry (group-subgroup relations), cell parameters and commensurate-supercell relations. Wide scale of constrains and restrains is available including a powerful rigid body approach and possibility to define a local symmetry affecting only part of the structure. The latest development of Jana concerns magnetic structures.

Rietveld refinement

The Rietveld refinement method* is a complex minimization procedure that allows to slightly modify a preconceived model based on prior external knowledge, in order to adjust it to an experimental pattern. The starting parameters for this model must be similar to the final values, bearing in mind that the sequence in which the different parameters are refined, have a marked influence on the result. This method is a process of structural refinement that uses each point of the pattern as an observation data.

The adjustment of the diffraction profiles is carried out point by point in the diffractogram, allowing to perform an iterative adjustment process until reaching a convergence between the theoretical and the experimental. In this thesis, the refinements were made using Jana 2006 software. The values of standard deviations were calculated considering the correction of the Berar and Lelann equations.

The algorithms implemented to the Rietveld method use all information contained in the diffractogram, including the one that is outside the diffraction peaks. Some of these very useful variables are:

-The characteristics of the instrument (the resolution curve of the diffractometer, displacement parameters concerning the imbalances of the goniometer, experimental geometry, characteristics of the detector).

-Structural parameters (unit cell parameters, atomic positions, atomic occupations, atomic displacements).

-Microstructural parameters (average crystalline size and microtensions, structural defects).

-Parameters of the sample (preferential orientation, residual stress, eccentricity, thickness, transparency, absorption and phase fractions) The refined parameters were: background function, zero-point position, scale factor, unit cell parameters, contributions to peak shape U, V, W parameters and asymmetric coefficients.

The Rietveld method is based on a least square function, which seek to find the lowest possible value of the was S_y which is defined as:

$$S_y = \sum_i w_i (y_i - y_{ci})^2 \quad (1)$$

Where; $w_i = {}^{1}/_{y_i}$, y_i is the experimental intensity observed in the *i* step of the diffractogram and y_{ci} in the intensity calculated for the *i* step. The mathematic definition of y_{ci} is shown in equation (2), which includes all the data that determine the intensity of a signal and that depend on the refined parameters.

$$y_{ci} = y_{bi} + \sum_{f=1}^{N} S_f \sum_{k=k_1}^{k_2} j_{fk} \,.\, Lp_{fk}.O_{fk}.M.\left|F_{fk}\right|^2.\Omega_{ifk} \quad (2)$$

Where:

y_{bi}= represents the intensity of the background at the point 2θ.

S_f= represents the scale factor of phase *f*.

j_{fk}= is the multiplicity factor of the k_i reflection.

Lp_{fk}= contains the correction factors of Lorentz-Polarization.

F_{fk}= is the structure factor corresponding to the peak *k* of phase *f*.

Ω_{ifk}= describes the shape function of the peaks.

The first sum corresponds to all the crystalline phases present in the sample and the second summation to all the reflections k_1 to k_2 that contribute to the *i* step.

Peak parameters

The shape of the peak is an important factor when studying a sample by powder diffraction. The correct refinement of the peak shape is fundamental, not only for a reasonable visual adjustment between the calculated and the observed intensity, but also so that the values of the structural parameters of the sample, dependent on the integrated intensity, have a physical sense. Although, in a diffraction profile is observed that H (the maximum width at the average height of the peak) is a function of the dispersion vector module, in absence of anisotropy by crystal size or reticular stresses, the H function can be modeled empirically. This means that the H parameter of each peak is not one of the variables in the adjustment, instead the coefficients of the equations that describe the variation of the maximum width to the average height of the peak. Fo example, the case of equation of Cagliotti, Pauletti and Ricci, that describes the variation of H with θ for Gaussian profiles (3):

$$(FWHM)_G = H_k^2 = Utan^2(\theta) + Vtan(\theta) + W \quad (3)$$

Rietveld's refinement employs a profile function that models the diffraction peaks, by means of width at average height, asymmetry, preferential orientation, background, etc., the most commonly used functions are Gaussian (G), Lorentzian (L), Pseudo-Voigt and Pearson VII.

Generally, the practical procedure used to adjust the model to the data and avoid false minimums requires working with increasingly complex partial models where a series of reasonable values $(x_1,...x_{m-n})$ of the initial parameters are left fixed, allowing the subset $(x_{m-n+1},...x_m)$ to vary until reaching the minimum. The model expands as the adjustment improves and the minimization function approaches the absolute minimum unit, in a reasonable way, all parameters of the model can be free to vary simultaneously in a stable

manner. The selection of the different structural models of the respective phases to be refined by the Rietveld method, can be taken from the different database of crystalline structures, such as the ICSD (International Centre Structural Database, see http://barns.ill.fr/dif/icsd), the Cambridge Structural Database System (see http://www.ccdc.cam.ac.uk), and the IUCr (International Union Chrystallographic, see http://www.iucr.ac.uk/iucr-top/comm/cpd/QARR/data-kit.htm).

Adjustment/Fix criteria

To achieve a precise adjustment of the measured intensities, it is necessary tha the model used considers all the factors involved in the formation of the diffraction profile. The use of an incomplete model will inevitably lead to incorrect parameters *($x_1, \ldots x_{m-n}$)*. However, even with an adequate model, the experimental errors in the measurement to produce imbalances that cannot be avoided. To advise on the degree of adjustment of the model to the data (quality of matching results), it is necessary to use a series of numbers that indicate different relationships between the intensities observed (y_i) and those calculated (y_{ci}). This series of numbers are called refinement adjustment criteria, and are calculated from the residual values R_p (pattern factor), R_{wp} (weighted pattern factor) and the goodness of fit (GOF or χ^2), defined by the following equations:

$$R_p = \frac{\sum|y_i - y_{ci}|}{\sum|y_i|} \quad (4)$$

$$R_{wp} = \sqrt{\frac{\sum w_i(y_i - y_{ci})^2}{\sum w_i y_i{}^2}} \quad (5)$$

$$GOF = \chi^2 = \sqrt{\frac{\sum w_i(y_i - y_{ci})^2}{N-P}} = \sqrt{\frac{S_y}{N-P}} \quad (6)$$

R_p represents the direct relationship between the intensities observed and the experimental ones without any kind of weight between them. It is a very reliable parameter to observe during the minimization process since it responds to small changes in the degree of adjustment, both in the background and in the maxim. However, its value is always low since it is not heavy and, usually represents more than the background (most of the points in a diffraction profile) than to the diffraction maxima.

R_{wp} is the main parameter to adjustment to be observed since in its numerator is the function that is minimized by the least squares method. Unlike the R_p includes a function of weight on the intensities that gives greater importance to the imbalances in the high

intensities (diffraction peaks) than in the low ones (background). It is the most significant parameter that is usually reported when publishing the results, since it gives an indication of how good the refinement of the diffraction pattern.

The "Goodness of fit (GOF)" or χ^2 value, numerically equal to the square root of S_y divided by the difference in the number of observations (N) and the number of adjusted parameters (P), will be equal to one in an ideal refinement. However, in an actual situation, the background and peak profile mismatch lead to GOF > 1. A GOF value between1.0 and 2.9 is generally considered satisfactory.

Although, these numerical parameters have been mentioned that advise on the quality of the adjustment, the best indication of this can be obtained during the experiment, tha is by visual inspection of the curve y_i vs 2θ when it is represented along with the curve y_{ci} vs 2θ, which also allows to analyzed details of it in specific regions of the diffractogram. Additionally, it is very useful to represent the intensity difference $(y_i - y_{ci})$ vs 2θ. In the latter, it is very easy to detect errors in the adjustment of the intensity, the shape of the peak, the background, etc., in specific zones of the diffraction profile that affect the global adjustment parameters. Therefore, all Rietveld refinement programs have a graphic interface that updates the result of each refinement cycle automatically

*RIETVELD H. M. (1969) A profile refinement method for nuclear and magnetic structures, Journal of Applied Crystallographic, 2, 65-71

Taken from:
SANDOVAL, Mónica V., Personal notes (UIS, 2012)

Appendix B

Chromatographic method in Peaksimple 4.39:

Events table

Time [min]	Events
0	Zero
0.1	G-ON (valve in “Inject”)
6.4	G-OFF (valve in “Load”)

Channel 1 program

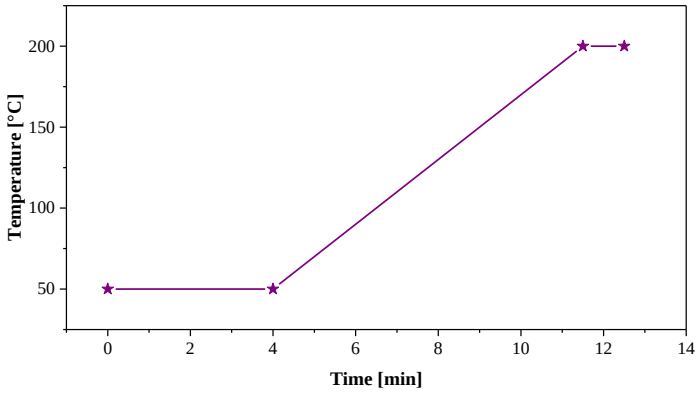

Initial temperature [°C]	Hold [min]	Ramp [°C min^{-1}]	Final temperature [°C]
50	4	20	200
200	1	0	200

Channel 2 program

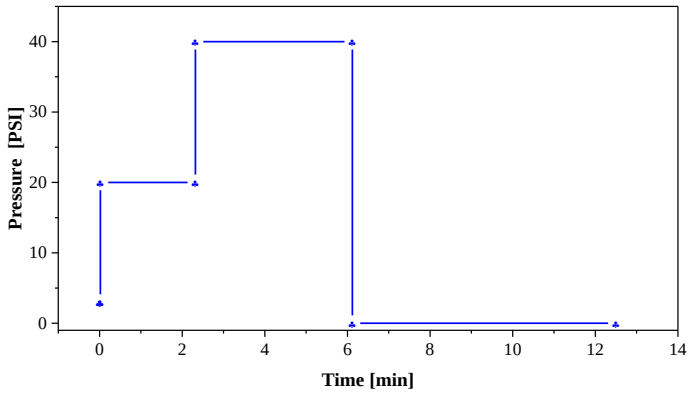

Initial pressure [PSI]	Hold [min]	Ramp [PSI min^{-1}]	Final pressure [PSI]
3	0.02	0	3
20	2.3	0	20
40	3.8	0	0
0	6.38	0	0

Appendix C

During the first part of this work, a total of 24 samples of LSMN n= 2 material were synthetized. They were analyzed individually by XRD. The refined lattice parameters are shown below:

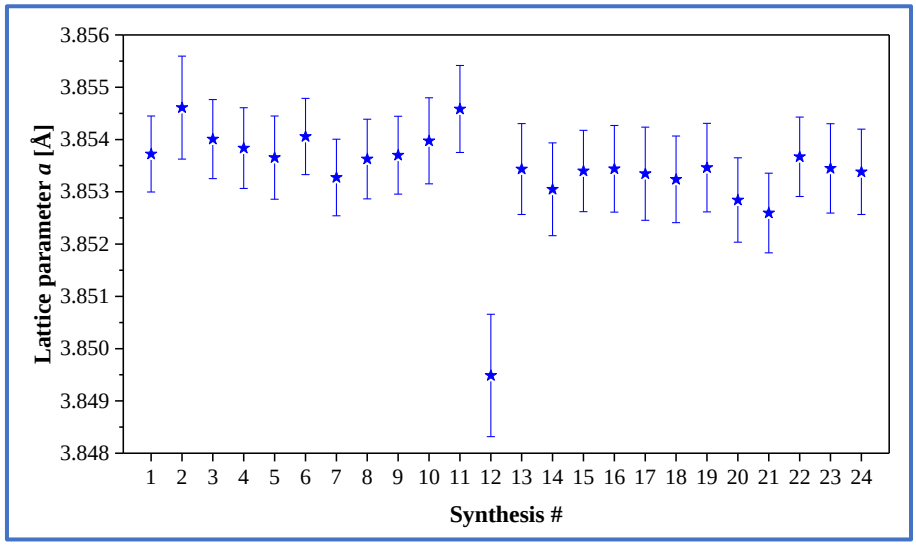

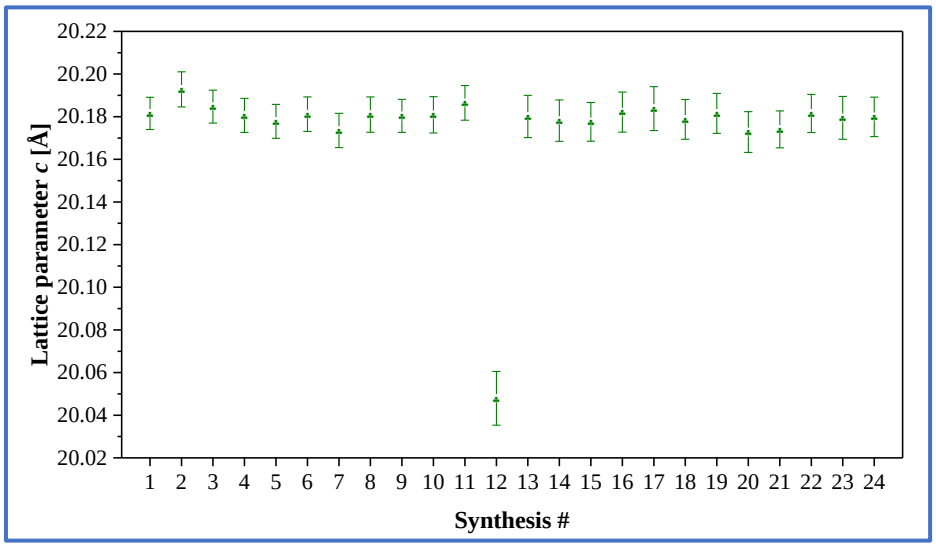

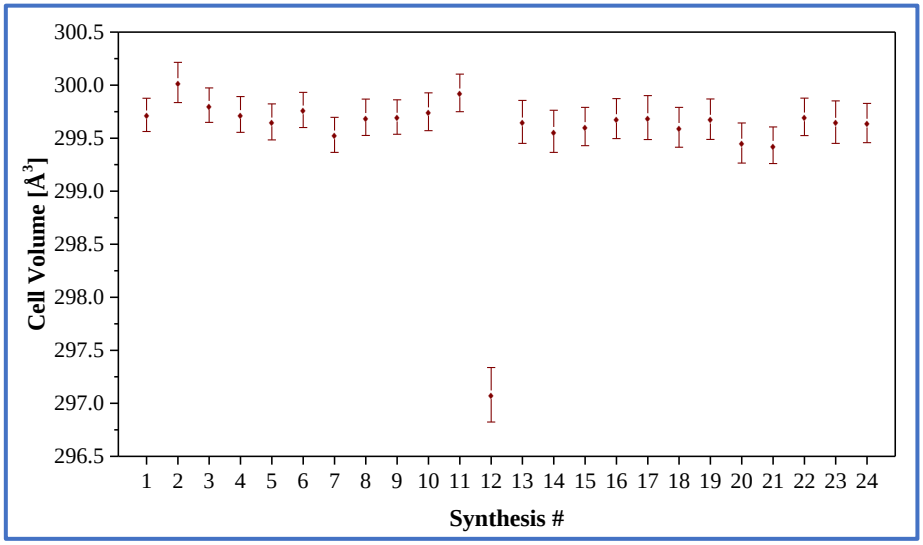

Synthesis #	χ^2	R_p	R_{wp}
1	1.22	5.05	6.43
2	1.2	5.03	6.47
3	1.32	5.33	6.89
4	1.35	4.57	5.96
5	1.44	4.76	6.25
6	1.36	4.65	6.04
7	1.38	4.54	5.98
8	1.33	4.61	6.05
9	1.36	4.54	5.96
10	1.39	4.84	6.34
11	1.28	4.58	5.9
12	1.68	4.59	7.01

Synthesis #	χ^2	R_p	R_{wp}
13	1.36	4.72	6.11
14	1.38	4.73	6.23
15	1.37	4.73	6.13
16	1.36	4.70	6.17
17	1.40	4.88	6.34
18	1.41	4.82	6.31
19	1.44	4.95	6.50
20	1.39	499	6.48
21	1.38	4.82	6.38
22	1.37	4.89	6.3
23	1.45	5.15	6.72
24	1.42	5.11	6.67

Appendix D

The X-ray fluorescence (XRF) is a common analytical technique non-destructive to identify and quantify, with proper calibration, the elemental composition of a sample. Each element in the periodic table has characteristic fluoresced X-ray photon emission energies relating to their periodic number and they are the key for the identification. In this research was employed an S2 Ranger Bruker spectrometer equipped with a Pd X-ray tube. Below, the LSMN n= 2 spectra by XRF with the main characteristic emission energies, which signifies the presence of La, Sr, Mn an Ni in the material. The amount of metallic Ni was confirmed as 0.057 ± 0.002 in mass fraction.

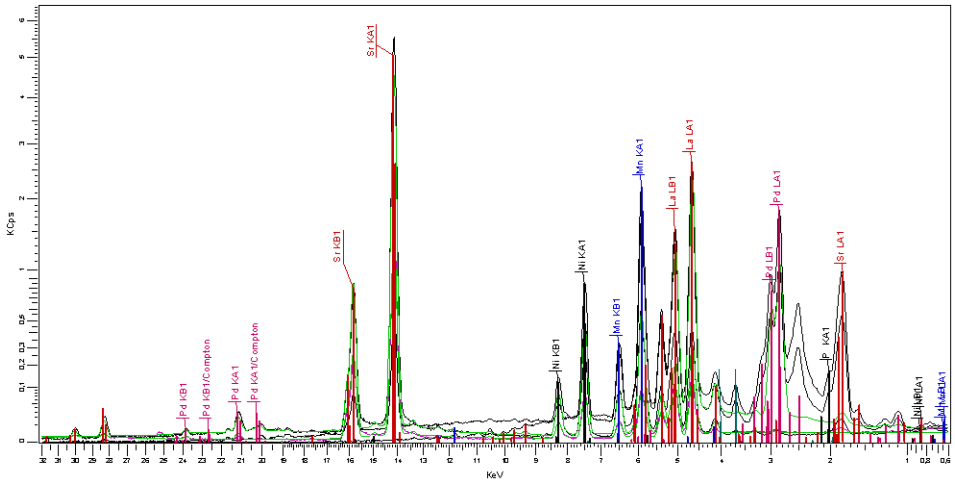

Appendix E

Even if the structure type and the presence of other elements have an influence on a metal redox behavior (and in particular its reducibility in diluted H_2), the theoretical value of reduction Gibbs free energy for the binary metal oxide corresponding to each constituting cations in LSMN n= 2 phase can confirm this qualitative reduction behavior, in particular the order of metal reduction as a function of temperature in fixed conditions [Eq. (S1)]. Such values were calculated at different temperatures using the standard thermodynamic properties of chemical substances*****, as shown in following figure. In the case of manganese oxides, the four characteristics oxides MnO, Mn_3O_4, Mn_2O_3 and MnO_2 were considered.

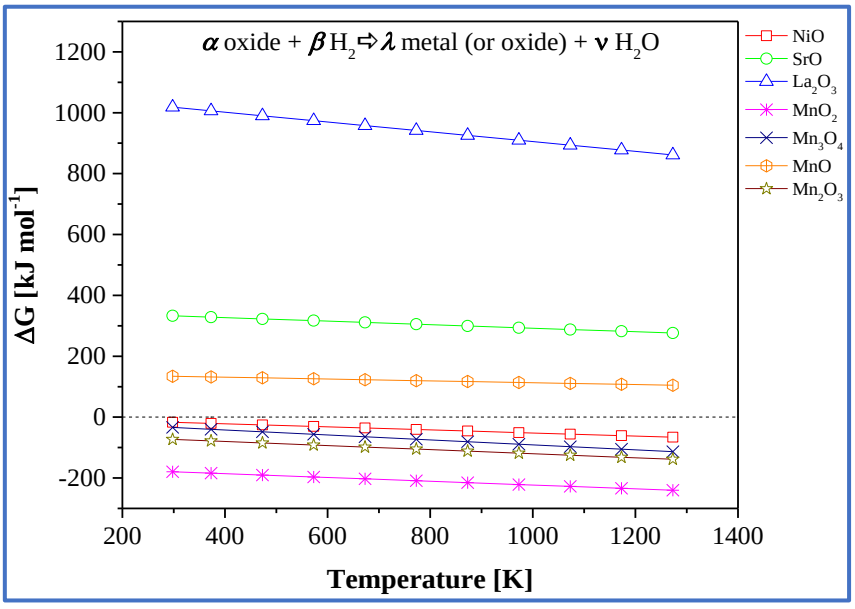

*****D.R. Lide, Standard thermodynamic properties of chemical substances, in: D.R. Lide (Ed.), CRC Handb. Chem. Phys., 81st ed, Taylor & Francis, Boca Raton, USA, 2000. http://www.update.uu.se/~jolkkonen/pdf/CRC_TD.pdf.

Appendix F

Ni particle size distribution was determined using, in each case, 100 particle diameters measured from SEM micrographs. The data were treated in Origin pro 8 employing an Orthogonal Distance Regression as iteration algorithm, adjusted to a lognormal function defined as:

$$f(D) = \frac{A}{(2\pi)^{0.5} w D} e^{-\frac{\ln ({}^{D}/_{D_0})^2}{2w^2}}$$

Where A is the area of the sized distribution, w the scale parameter defining the width of the size distribution and D_0 the median radius

The average particle size ($\overline{D}_p$) and its standard deviation (σ_{ln}) of the lognormal distribution were determined using the following equations:

$$\overline{D}_p = D_0 e^{\frac{w^2}{2}}$$

$$\sigma_{ln} = D_0 \sqrt{e^{2w^2} - e^{w^2}}$$

And then:

$$\overline{D}_p \pm z_{95\%} * \frac{\sigma_{ln}}{\sqrt{N}}$$

Where:
$z_{95\%}$ is the inverse normal probability distribution function with 95% of confidence interval and *N* is the sample size (100 particles).

750 °C 8h

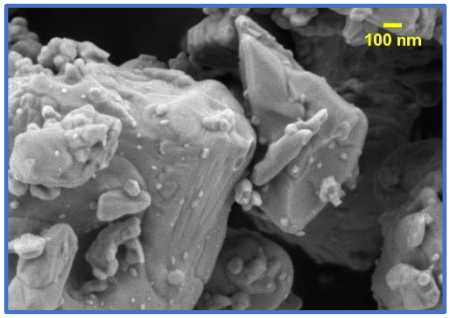

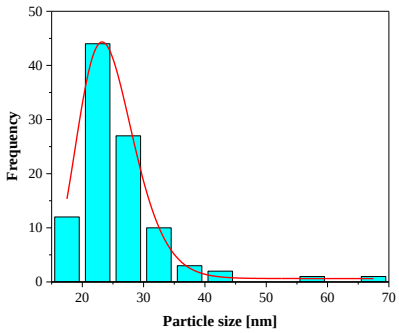

	Value	Standard error
D_0	24.09931	0.41154
w	0.19194	0.01322
A	497.48442	27.77524
$\bar{D}_p$	24.54 nm ± 1.02 nm (95% C.L.)	
Adj. R^2	0.99954	

C.L: Confidence Level

750 °C 16h

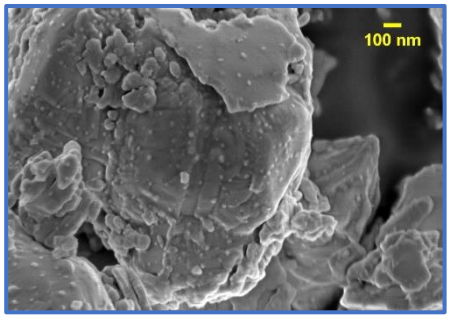

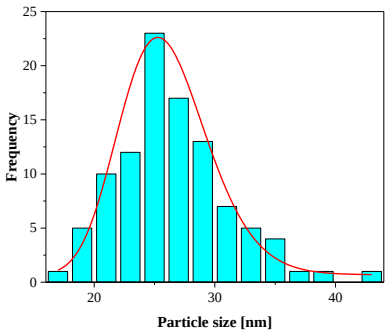

	Value	Standard error
D_0	25.78957	0.31993
w	0.14135	0.01078
A	198.33283	16.82939
$\bar{D}_p$	26.05 nm ± 0.73 nm (95% C.L.)	
Adj. R^2	0.99825	

C.L: Confidence Level

750 °C 24 h

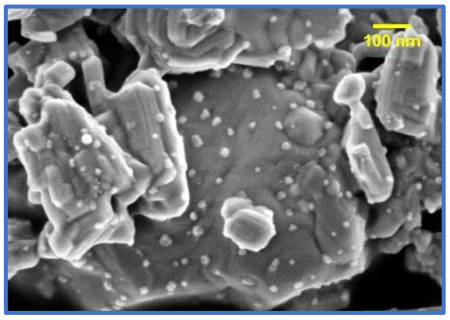

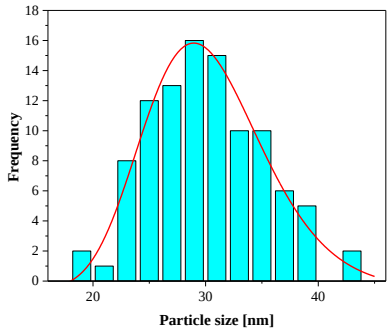

	Value	Standard error
D_0	29.90329	0.38258
w	0.18017	0.0187
A	217.01708	30.38041
$\bar{D}_p$	30.39 nm ± 1.08 nm (95% C.L.)	
Adj. R^2	0.99784	

C.L: Confidence Level

750 °C 48 h

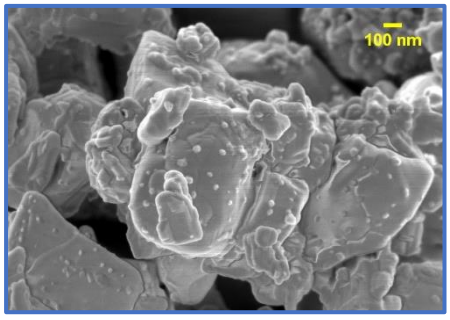

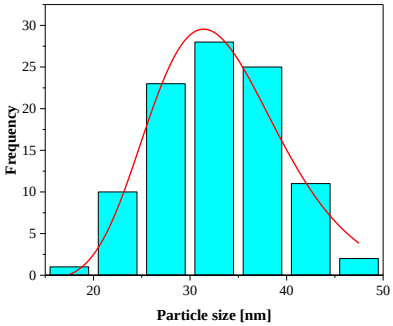

	Value	Standard error
D_0	32.83872	0.87442
w	0.21115	0.03599
A	512.06581	118.56161
$\bar{D}_p$	33.58 nm ± 1.40 nm (95% C.L.)	
Adj. R^2	0.99419	

C.L: Confidence Level

800 °C 4 h

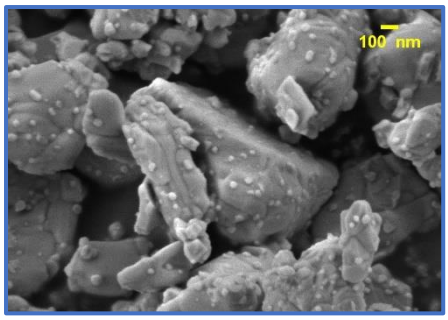

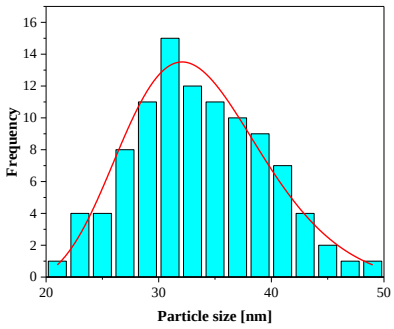

	Value	Standard error
D_0	33.2855	0.45476
w	0.19241	0.02534
A	220.40243	46.3347
$\bar{D}_p$	33.91 nm ± 1.29 nm (95% C.L.)	
Adj. R^2	0.99853	

C.L: Confidence Level

800 °C 8 h

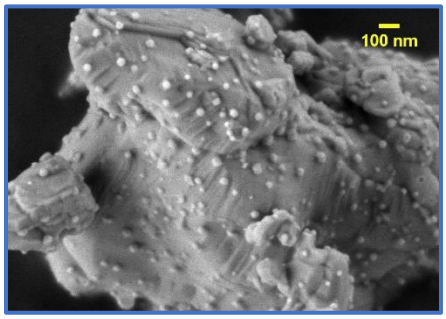

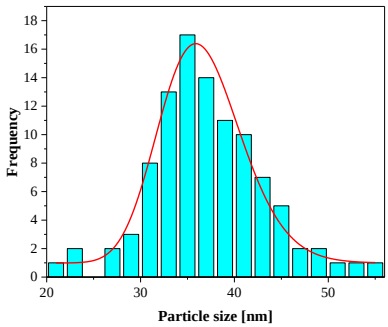

	Value	Standard error
D_0	36.40712	0.28915
w	0.1207	0.00834
A	168.37281	12.62505
$\bar{D}_p$	36.67 nm ± 0.87 nm (95% C.L.)	
Adj. R^2	0.99922	

C.L: Confidence Level

800 °C 16 h

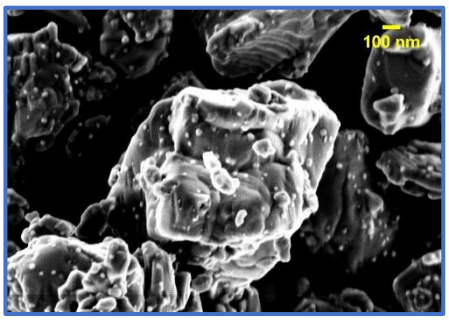

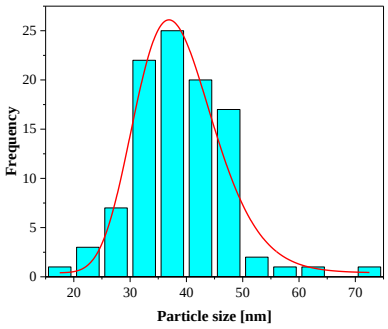

	Value	Standard error
D_0	38.21809	0.83918
w	0.18734	0.02136
A	453.287	58.85319
$\bar{D}_p$	38.90 nm ± 1.43 nm (95% C.L.)	
Adj. R^2	0.99782	

C.L: Confidence Level

800 °C 24 h

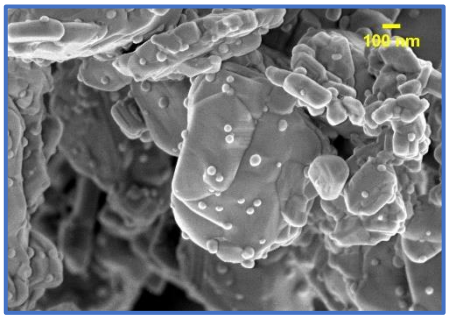

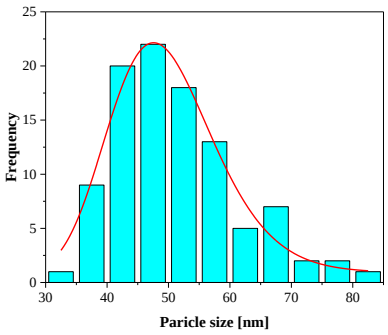

	Value	Standard error
D_0	49.07053	0.80735
w	0.17612	0.02087
A	452.65289	66.94783
$\bar{D}_p$	49.84 nm ± 1.73 nm 95% C.L.)	
Adj. R^2	0.99865	

C.L: Confidence Level

800 °C 48 h

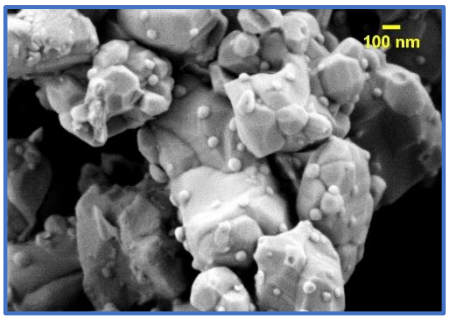

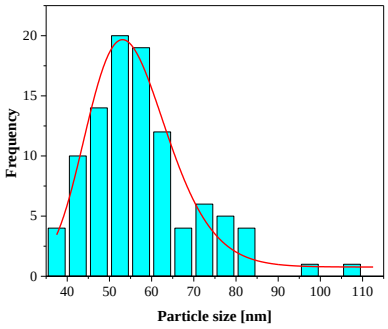

	Value	Standard error
D_0	54.76533	0.65592
w	0.17597	0.01661
A	449.62361	49.15741
$\bar{D}_p$	55.62 nm ± 1.93 nm (95% C.L.)	
Adj. R^2	0.9992	

C.L: Confidence Level

850 °C 4 h

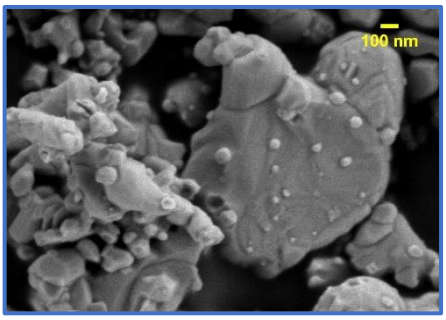

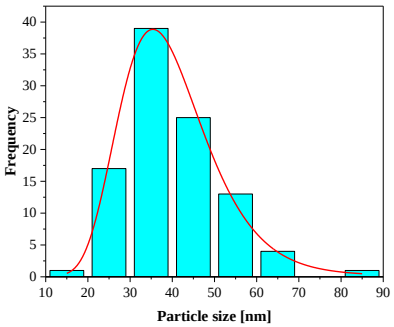

	Value	Standard error
D_0	38.29653	0.64184
w	0.28049	0.01917
A	1000.88789	72.42415
$\bar{D}_p$	39.83 nm ± 2.21 nm (95% C.L.)	
Adj. R^2	0.99936	

C.L: Confidence Level

850 °C 8 h

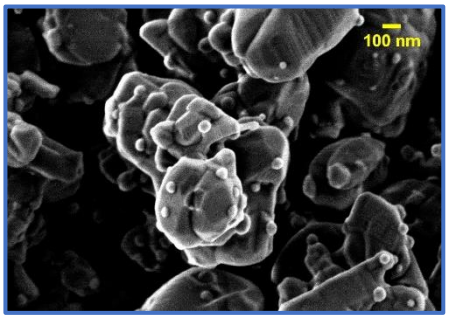

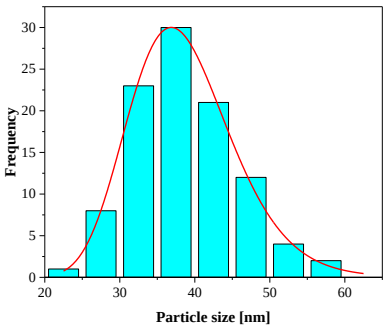

	Value	Standard error
D_0	38.08154	0.21998
w	0.18056	0.00638
A	508.16226	22.28162
$\bar{D}_p$	38.70 nm ± 1.38 nm (95% C.L.)	
Adj. R^2	0.99978	

C.L: Confidence Level

850 °C 16 h

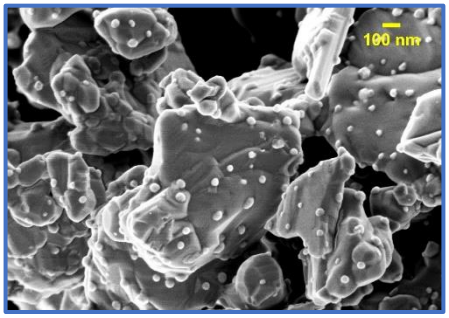

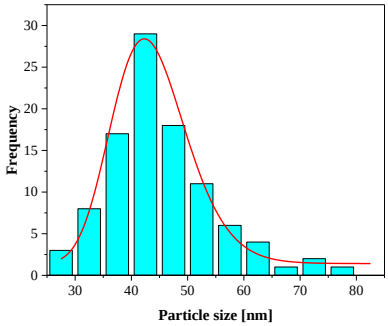

	Value	Standard error
D_0	43.32375	0.60363
w	0.15467	0.01191
A	447.88126	39.05683
$\bar{D}_p$	43.85 nm ± 1.34 nm (95% C.L.)	
Adj. R^2	0.99911	

C.L: Confidence Level

850 °C 24 h

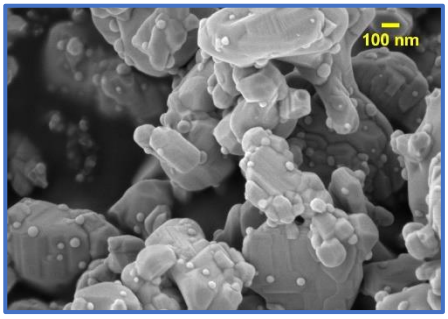

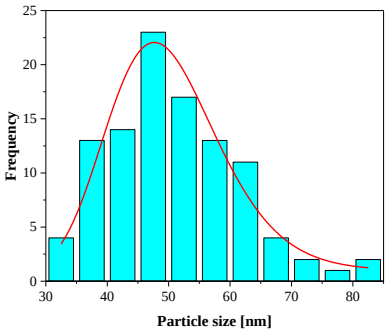

	Value	Standard error
D_0	49.32348	0.86563
w	0.18478	0.02276
A	473.13866	75.18778
$\bar{D}_p$	50.17 nm ± 1.98 nm (95% C.L.)	
Adj. R^2	0.99845	

C.L: Confidence Level

850 °C 48 h

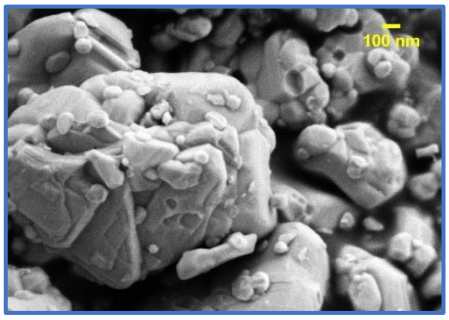

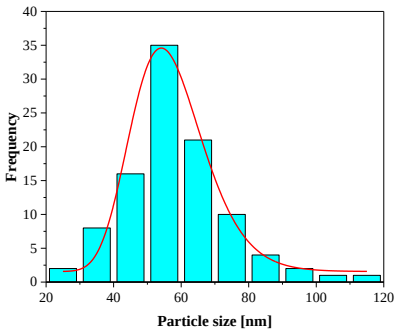

	Value	Standard error
D_0	56.19256	1.02016
w	0.19435	0.01504
A	887.03112	81.80526
$\bar{D}_p$	57.26 nm ± 2.20 nm (95% C.L.)	
Adj. R^2	0.99915	

C.L: Confidence Level

Appendix G

An important technique for analyzing the effect of categorical factors on a response is to perform an Analysis of Variance. An ANOVA decomposes the variability in the response variable amongst the different factors. Depending upon the type of analysis, it may be important to determine: (a) which factors have a significant effect on the response, and/or (b) how much of the variability in the response variable is attributable to each factor.

Y: one or more numeric columns containing the *n* observations for the dependent variables Y.

Quantitative factors: numeric columns containing the *n* values of any quantitative factors X (Temperature, reduction time)

Analysis of Variance: a decomposition of the sum of squares for Y into components for the model and for the residuals. The F-test tests the statistical significance of the model as a whole. A small p-value (less than 0.05 if operating at the 5% significance level) indicates that at least one factor in the model is significantly related to the dependent variable.

Type III Sums of Squares: decomposition of the model sum of squares into components for each factor. Based on the settings specified on the Analysis Options dialog box, either Type III or Type I sums of squares are displayed. Type III sums of squares test the marginal significance of each factor, assuming it was the last to be entered into the model. Small p-values indicate significant effects.

Degree of freedom (D.F.): In statistics, the D.F. is the number of values in the final calculation of a statistic that are free to vary.

Mean square: represents an estimate of population variance. In ANOVA, mean squares are used to determine whether factors (treatments) are significant.

*The treatment mean square is obtained by dividing the treatment sum of squares by the degrees of freedom. The treatment mean square represents the variation between the sample means.

*The mean square of the residual (MSR) is obtained by dividing the sum of squares of the residual error by the degrees of freedom. The MSR represents the variation within the samples.

F-test: To test if a relationship exists between the dependent and independent variable, a statistic based on the F distribution is used

p-Value: The p-value is the level of marginal significance within a statistical hypothesis test representing the probability of the occurrence of a given event.

Taken from:
http://www.statgraphics.com/analysis-of-variance#General%20Linear%20Models
Visited 03/03/2019

Appendix H

The LSMO ($La_{0.5}Sr_{1.5}MnO_4$) synthesis is given by de following reaction:

$$0.25La_2O_3+1.5SrCO_3+0.5Mn_2O_3 \rightarrow La_{0.5}Sr_{1.5}MnO_{4\pm\delta}$$

Then, the amount of each precursor is calculated taking as calculation base 1 g of LSMO:

$$1\text{ g LSMO}\times\frac{1\text{ mol LSMO}}{381.83\text{ g LSMO}}\times\frac{0.25\text{ mol }La_2O_3}{1\text{ mol LSMO}}\times\frac{325.81\text{ g }La_2O_3}{1\text{ mol }La_2O_3}=0.2133\text{ g }La_2O_3$$

$$1\text{ g LSMO}\times\frac{1\text{ mol LSMO}}{381.83\text{ g LSMO}}\times\frac{1.5\text{ mol }SrCO_3}{1\text{ mol LSMO}}\times\frac{147.63\text{ g }SrCO_3}{1\text{ mol }SrCO_3}=0.5799\text{ g }SrCO_3$$

$$1\text{ g LSMO}\times\frac{1\text{ mol LSMO}}{381.83\text{ g LSMO}}\times\frac{0.5\text{ mol }Mn_2O_3}{1\text{ mol LSMO}}\times\frac{157.87\text{ g }Mn_2O_3}{1\text{ mol }Mn_2O_3}=0.2067\text{ g }Mn_2O_3$$

In this synthesis was employed $MnCO_3$, so it was made a "test of fire" at 700 °C during 4 h in air to find the mass loss factor, which corresponded to 1.5219 g$MnCO_3$ per gMn_2O_3. In this way, it was calculated the amount of $MnCO_3$ to obtain the stoichiometric amount of Mn_2O_3.

$$0.2067\text{ g }Mn_2O_3\times\frac{1.5219\text{ g }MnCO_3}{1\text{ g }Mn_2O_3}=0.3146\text{ g }MnCO_3$$

Thus, 0.3146 g of $MnCO_3$, 0.5799 g of $SrCO_3$ and 0.2133 g of La_2O_3 are required for each g of LSMO.

It was calculated the amount of citric acid to use in Pechini method considering the total number of cations in the precursors and multiplying by 3 (citric acid molecule has 3 carboxyl groups).

$$0.3146\text{ g }MnCO_3\times\frac{1\text{ mol }MnCO_3}{114.94\text{ g }MnCO_3}\times\frac{1\text{ mol cation }Mn^{+2}}{1\text{ mol }MnCO_3}=0.0027\text{ mol cation }Mn^{+2}$$

$$0.2133\text{ g }La_2O_3\times\frac{1\text{ mol }La_2O_3}{325.81\text{ g }La_2O_3}\times\frac{2\text{ mol Cation}La^{+3}}{1\text{ mol }La_2O_3}=0.0013\text{ mol cation}La^{+3}$$

$$0.5799\text{ g }SrCO_3\times\frac{1\text{ mol }SrCO_3}{174.62\text{ g }SrCO_3}\times\frac{1\text{ mol cation}Sr^{+2}}{1\text{ mol }SrCO_3}=0.0033\text{ mol cation}Sr^{+2}$$

0.0033 mol cation Sr^{+2} + 0.0013 mol cation La^{+3} + 0.0027 mol cation Mn^{+2} = 0.0073 mol cations

$$0.0073 \text{ mol cations} \times 3 = 0.0220 \text{ mol } C_6H_8O_7$$

$$0.0220 \text{ mol } C_6H_8O_7 \times \frac{192.12 \text{ g } C_6H_8O_7}{1 \text{ mol } C_6H_8O_7} = 4.2194 \text{ g } C_6H_8O_7$$

Now, it was calculated the amount (volume) of HNO_3 65 vol% considering the following reactions.

$$La_2O_3 + 6HNO_3 \rightarrow 2La(NO_3)_3 + 3H_2O$$
$$SrCO_3 + 2HNO_3 \rightarrow Sr(NO_3)_2 + CO_2 + H_2O$$
$$MnCO_3 + 2HNO_3 \rightarrow Mn(NO_3)_2 + CO_2 + H_2O$$

$$0.2133 \text{ g } La_2O_3 \times \frac{1 \text{ mol } La_2O_3}{325.81 \text{ g } La_2O_3} \times \frac{6 \text{ mol } HNO_3}{1 \text{ mol } La_2O_3} \times \frac{63.01 \text{ g } HNO_3}{1 \text{ mol } HNO_3} = 0.2475 \text{ g } HNO_3$$

$$0.5799 \text{ g } SrCO_3 \times \frac{1 \text{ mol } SrCO_3}{174.62 \text{ g } SrCO_3} \times \frac{2 \text{ mol } HNO_3}{1 \text{ mol } SrCO_3} \times \frac{63.01 \text{ g } HNO_3}{1 \text{ mol } HNO_3} = 0.4185 \text{ g } HNO_3$$

$$0.3146 \text{ g } MnCO_3 * \frac{1 \text{ mol } MnCO_3}{114.94 \text{ g } MnCO_3} * \frac{2 \text{ mol } HNO_3}{1 \text{ mol } MnCO_3} * \frac{63.01 \text{ g } HNO_3}{1 \text{ mol } HNO_3} = 0.3449 \text{ g } HNO_3$$

$$0.2475 \text{ g } HNO_3 + 0.4185 \text{ g } HNO_3 + 0.3449 \text{ g } HNO_3 = 1.0109 \text{ g } HNO_3$$

$$\frac{1.0109 \text{ g } HNO_3}{0.65} = 1.5553 \text{ g } HNO_3$$

Then, for the synthesis are required 1.5553 g of HNO_3 65 vol% (1.2 mL). The ethylene glycol used at the end of the synthesis correspond to 1.5 mL/gLSMO.

The synthetized LSMO n= 1 powder was impregnated with Ni using Incipient Wetness Impregnation (IWI) method also known as pore volume impregnation. Also, to be comparable, the Ni content selected was the same obtained by the exsolution, (~0.05 mass fraction). To impregnate 1 g of LSMO and obtain Ni 5 wt%, it was calculated the Ni mass.

$$1 \text{ g LSMO} \times \frac{0.05 \text{ g Ni}}{0.95 \text{ g LSMO}} = 0.0526 \text{ g Ni}$$

Using the stoichiometry of the following reaction, it was calculated the necessary NiO mass:

$$NiO + H_2 \rightarrow Ni + H_2O$$

$$0.0526 \text{ g Ni} \times \frac{1 \text{ mol Ni}}{58.7 \text{ g Ni}} \times \frac{1 \text{ mol NiO}}{1 \text{ mol Ni}} \times \frac{74.69 \text{ g NiO}}{1 \text{ mol NiO}} = 0.0669 \text{ g NiO}$$

It was made a "test of fire" of $NiCO_3$ at 700 °C during 4 h in air to find the mass loss factor, which corresponded to 1.7907 g$NiCO_3$ per gNiO. In this way, it was calculated the amount of $NiCO_3$ to obtain the stoichiometric amount of NiO.

$$0.0669\ \text{g NiO} \times \frac{1.7907\ \text{g NiCO}_3}{1\ \text{g NiO}} = 0.1198\ \text{g NiCO}_3$$

Now, it was calculated the stoichiometric HNO_3 65 vol% volume.

$$NiCO_3 + 2HNO_3 \rightarrow Ni(NO_3)_2 + H_2O + CO_2$$

$$0.1198\ \text{g}NiCO_3 \times \frac{1\ \text{mol NiCO}_3}{118.7\ \text{g NiCO}_3} \times \frac{2\ \text{mol HNO}_3}{1\ \text{mol NiCO}_3} \times \frac{63\ \text{g HNO}_3}{1\ \text{mol HNO}_3} \times \frac{1\ \text{mL HNO}_3}{1.5129\ \text{g HNO}_3} = 0.0840\ \text{mL pure HNO}_3$$

$$\frac{0.0840\ \text{mL pure HNO}_3}{0.65} = 0.1293\ \text{mL HNO}_3$$

Thus, to prepare the $Ni(NO_3)_2$ solution, 0.1198 g $NiCO_3$ per g LSMO and 129.3 µL HNO_3 per g LSMO are required. Now, to guarantee the complete $NiCO_3$ reaction, 8 % HNO_3 excess was added.

The ethanol-water 20 mol% solution was prepared using the commercial ethanol solution 70 vol%.

$$\frac{0.2\ \text{mol } C_2H_5OH}{1\ \text{mol Sol.}} \times \frac{46.07\ \text{g } C_2H_5OH}{1\ \text{mol } C_2H_5OH} \times \frac{1\ \text{mL } C_2H_5OH}{0.789\ \text{g } C_2H_5OH} = 11.8377 \frac{\text{mL pure } C_2H_5OH}{\text{mol Sol.}}$$

$$\frac{11.8377\ \text{mL pure } C_2H_5OH/\text{mol Sol.}}{0.7} = 16.91 \frac{\text{mL } C_2H_5OH}{\text{mol Sol.}}$$

$$\frac{0.8\ \text{mol } H_2O}{1\ \text{mol Sol}} \times \frac{18\ \text{g } H_2O}{1\ \text{mol } H_2O} \times \frac{1\ \text{mL } H_2O}{0.9993\ \text{g } H_2O} = 14.41 \frac{\text{mL } H_2O\ \text{total}}{\text{mol Sol.}}$$

The volume of water contained in HNO_3 65 vol% was subtracted from the volume of total water.

$$14.41\text{-}16.91\text{+}11.83 = 9.33 \frac{\text{mL } H_2O}{\text{mol Sol}}$$

$$\frac{16.91\ \text{mL}\ C_2H_5OH/\ \text{mol Sol.}\times 100}{(16.91+9.33)\ \text{mL Sol./mol Sol.}}=64.44\frac{\text{mL}\ C_2H_5OH}{\text{mL Sol.}}$$

The $Ni(NO_3)_2$ solubility in water is 99.6 g $Ni(NO_3)_2$ per gH_2O, so the water volume necessary to dilute the amount of $Ni(NO_3)_2$ available in the solution was

$$0.1198\ \text{g}NiCO_3\times\frac{1\ \text{mol}\ NiCO_3}{118.7\ \text{g}\ NiCO_3}\times\frac{1\ \text{mol}\ Ni(NO_3)_2}{1\ \text{mol}\ NiCO_3}\times\frac{182.7\ \text{g}\ Ni(NO_3)_2}{1\ \text{mol}\ Ni(NO_3)_2}=0.1843\ \text{g}Ni(NO_3)_2$$

$$0.1843\ \text{g}\ Ni(NO_3)_2\times\frac{1\ \text{g}\ H_2O}{0.996\ \text{g}\ Ni(NO_3)_2}\times\frac{1\ \text{mL}\ H_2O}{0.9993\ \text{g}\ H_2O}=0.1852\ \text{mL pure}\ H_2O$$

Assuming the ethanol dilute Ni(NO3) 2 and does not affect the water solubility, the volume of water-ethanol solution to be used is:

$$0.1852\ \text{mL}\ H_2O\ \text{Pura-}(0.125\times 0.35)\ \text{mL}\ H_2O\ \text{en}\ HNO_3=0.1414\ \text{mL}\ H_2O\ \text{Pura}$$

$$\frac{14.41\ \text{mL}\ H_2O\ \text{Total}}{1\ \text{mol Sol.}\ C_2H_5OH\text{-}H_2O}\times\frac{1\ \text{mol Sol.}\ C_2H_5OH\text{-}H_2O}{(16.91+9.33)\text{ml Sol.}\ C_2H_5OH\text{-}H_2O}=\frac{0.5491\ \text{mL}\ H_2O\ \text{Total}}{1\ \text{mL Sol.}\ C_2H_5OH\text{-}H_2O}$$

$$0.1414\ \text{mL}\ H_2O\times\frac{1\ \text{mL Sol.}\ C_2H_5OH\text{-}H_2O}{0.5491\ \text{mL}\ H_2O\ \text{Total}}=0.2575\ \text{mL Sol. EtOH-}H_2O$$

The minimum required volume of ethanol-water solution is 275.5 µL per g LSMO. The saturation volume of the LSMO, experimentally found, corresponded to 286 µL per g LSMO. Then, as the total volume of $Ni(NO_3)_2$ solution, considering the minimum amount of ethanol-water solution is higher than 286 µL per g LSMO (347.5 µL per g LSMO), incipient wet impregnation should be carried out in two steps; thus to complete 2-fold volume of 286 µL $Ni(NO_3)_2$ solution (572 µL per g LSMO), it was added 447 µL per g LSMO of ethanol-water solution. 286 µL of the prepared solution is impregnated on LSMO and after that, it is dried at 110 °C during 15 min, macerated and then, the remaining solution is impregnated, dried again during 12 h and calcinated at high temperature.

Appendix I

During the first stage of this thesis, a total of 9 sets of LSMO n = 1 material, were synthetized. They were analyzed individually by XRD. The refined lattice parameters are shown below

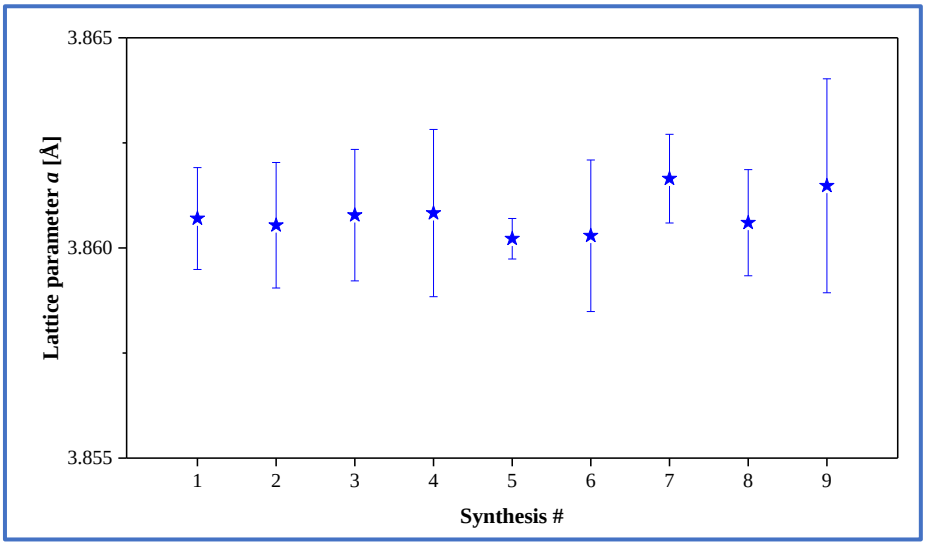

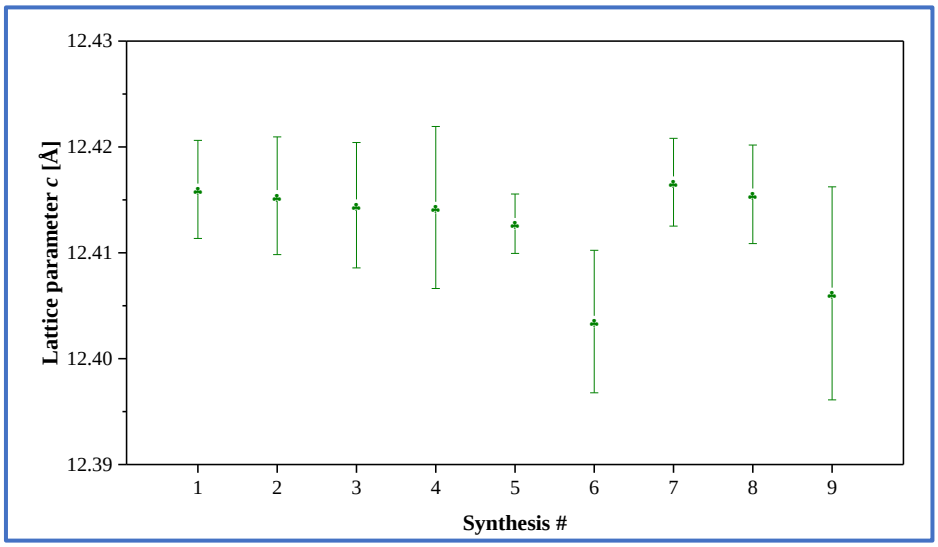

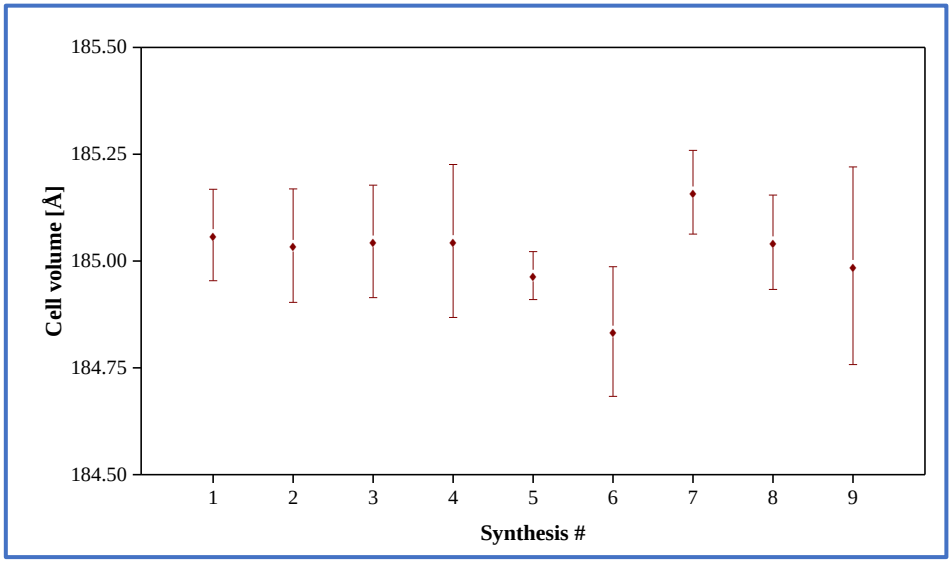

Synthesis #	χ^2	R_p	R_{wp}
1	2.44	6.87	9.77
2	2.55	5.49	6.98
3	2.62	5.33	6.98
4	2.40	6.08	7.67
5	2.37	5.85	7.48
6	2.59	6.69	7.76
7	1.92	5.46	7.03
8	2.10	5.72	7.20
9	2.12	7.09	9.68

Appendix J

In this research was employed an S2 Ranger Bruker spectrometer equipped with a Pd X-ray tube. Below, the XRF spectra of the impregnated LSMO n= 1 reduced ad 850 ºC during 4 h, it is visible the main characteristic emission energies which signifies the presence of La, Sr, Mn an Ni in the material. The amount of metallic Ni impregnated on the LSMO n= 1 surface was confirmed as 0.059 ± 0.004 in mass fraction.

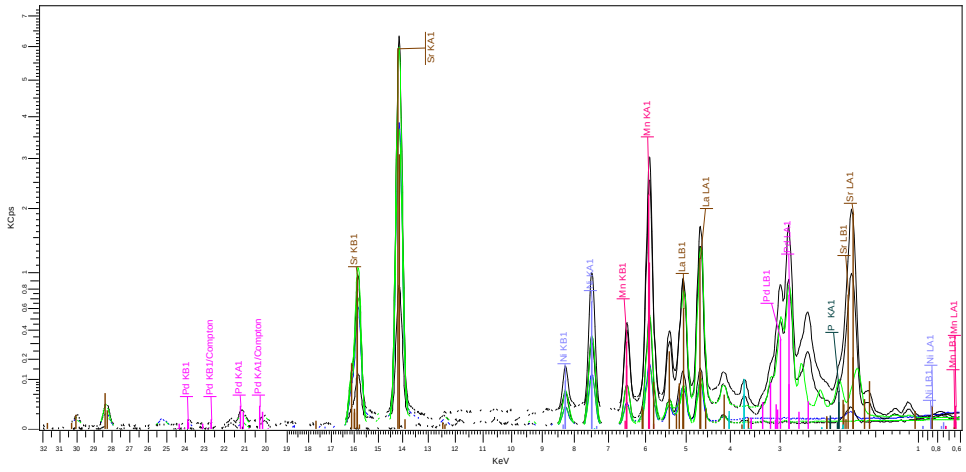

Appendix K

750 °C 8 h

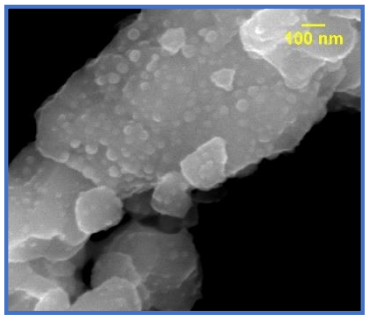

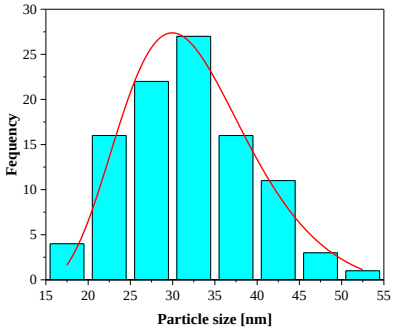

	Value	Standard error
D_0	31.8555	0.91809
w	0.24845	0.04289
A	547.80521	140.9954
$\bar{D}_p$	32.85 nm ± 1.62 nm (95% C.L.)	
Adj. R^2	0.99611	

C.L: Confidence Level

800 °C 4 h

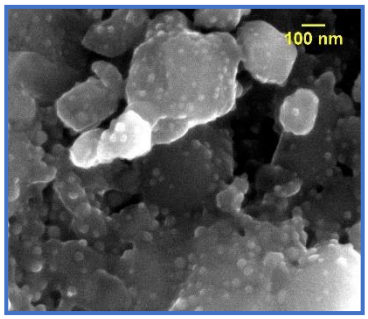

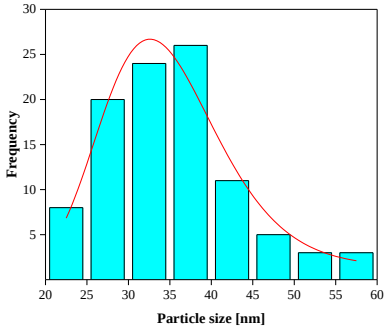

	Value	Standard error
D_0	34.0944	0.9246
w	0.2114	0.0407
A	446.4868	60.8654
$\bar{D}_p$	34.86 nm ± 1.46 nm (95% C.L.)	
Adj. R^2	0.9549	

C.L: Confidence Level

850 °C 4 h

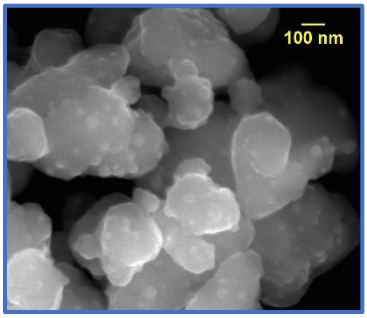

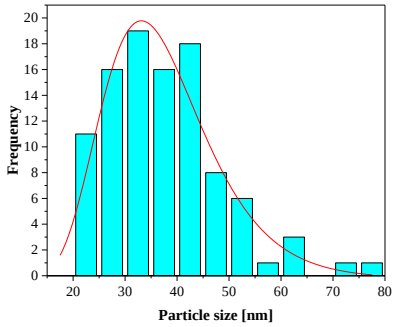

	Value	Standard error
D_0	36.04801	1.07283
w	0.29063	0.004035
A	503.1878	87.91494
$\bar{D}_p$	38.20 nm ± 2.43 nm (95% C.L.)	
Adj. R^2	0.9978	

C.L: Confidence Level

850 °C 8 h

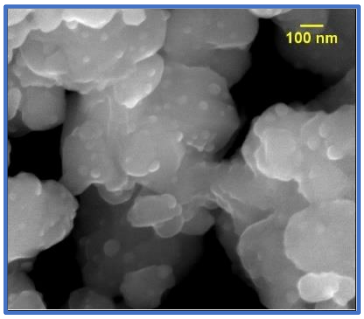

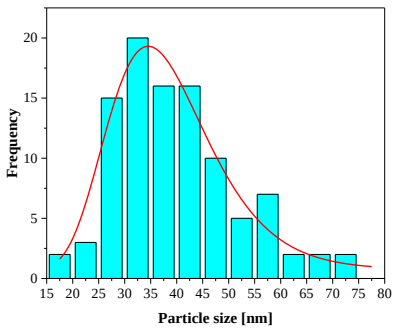

	Value	Standard error
D_0	37.2462	1.0107
w	0.2750	0.0378
A	459.0195	79.5126
$\bar{D}_p$	38.68 nm ± 2.13 nm (95% C.L.)	
Adj. R^2	0.9981	

C.L: Confidence Level

Appendix L

Ni/LSMO n= 1 (impreg.) reduced at 850 °C during 4 h and post reaction at 850 °C

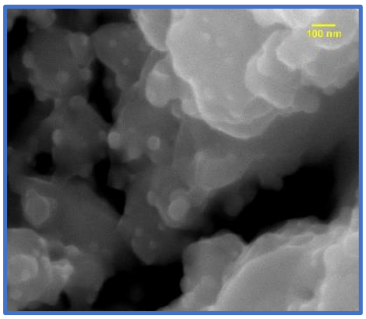

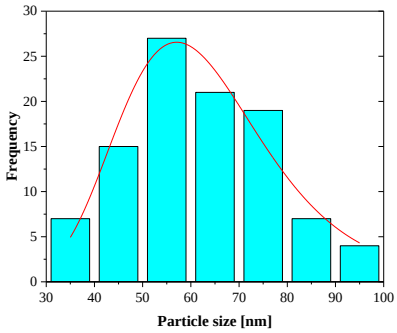

	Value	Standard error
D_0	60.94566	2.88916
w	0.25655	0.0849
A	979.76751	50.764
$\bar{D}_p$	62.97 nm ± 3.02 nm (95% C.L.)	
Adj. R^2	0.99698	

C.L: Confidence Level

Ni/LSMO n= 1 (impreg.) reduced at 800 °C during 4 h and post reaction at 800 °

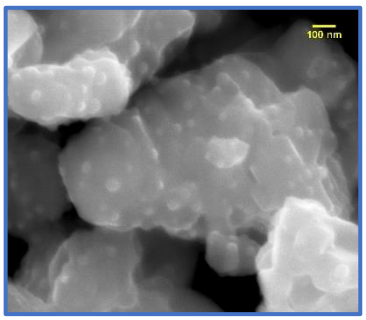

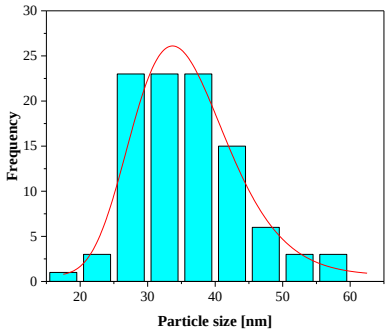

	Value	Standard error
D_0	35.14208	0.74124
w	0.20584	0.03019
A	452.0699	67.31806
$\bar{D}_p$	35.62 nm ± 1.62 nm (95% C.L.)	
Adj. R^2	0.99716	

C.L: Confidence Level

Ni/LSM n= 1 (exsolv.) reduced at 850 °C during 4 h and post reaction at 850 °

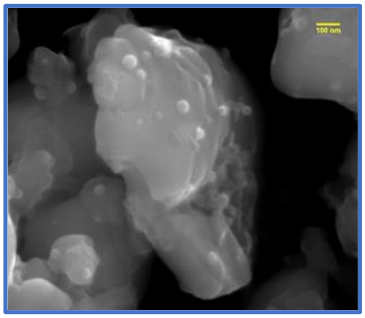

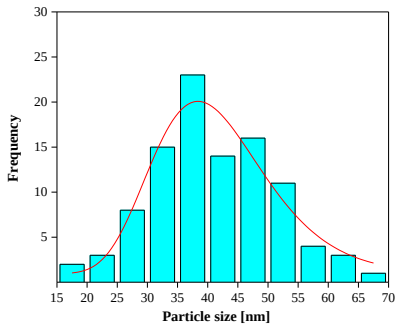

	Value	Standard error
D_0	40.6486	1.1672
w	0.2389	0.03999
A	452.4645	55.3176
$\bar{D}_p$	41.83 nm ± 1.99 nm (95% C.L.)	
Adj. R^2	0.92643	

C.L: Confidence Level

Appendix M

Operating conditions for the MSR at new methane inlet composition. CH_4 43.26 mol% - N_2 balance, S/C: 0.15, reaction temperature: 850 °C, catalyst: LSMN n= 2 reduced at 850 °C during 4 h (exsolved material).

CH_4 conversion [mol%]		9.67 ± 0.10	
CH_4 conversion rate [mmol min^{-1} g^{-1}]		4.39 ± 0.04	
H_2 production rate [mmol min^{-1} g^{-1}]		11.20 ± 0.32	
Outlet gas composition [mol%]		**H_2/CO ratio**	
N_2	53.93 ± 0.24	3.04 ± 0.01	
H_2	9.12 ± 0.11	**Selectivity**	
CH_4	33.33 ± 0.12	**CO**	0.83 ± 0.01
CO	3.01 ± 0.10	**CO_2**	0.17 ± 0.01
CO_2	0.61 ± 0.01		

Operating conditions for the ESR at ethane composition in Colombia natural gas. C_2H_6 10 mol% - N_2 balance, S/C: 0.6, reaction temperature: 850 °C, catalyst: LSMN n= 2 reduced at 850 °C during 4 h (exsolved material)

C_2H_6 conversion [mol%]		92.62 ± 0.10	
C_2H_6 conversion rate [mmol min^{-1} g^{-1}]		10.70 ± 0.17	
H_2 production rate [mmol min^{-1} g^{-1}]		29.10 ± 0.59	
Outlet gas composition [mol%]		**H_2/CO ratio**	
N_2	66.80 ± 0.22	2.57 ± 0.04	
H_2	20.65 ± 0.18	**Selectivity**	
CH_4	0.43 ± 0.01	**CH_4**	0.03 ± $1.3x10^{-3}$
CO	8.03 ± 0.12	**CO**	0.53 ± 0.02
CO_2	0.24 ± 0.02	**CO_2**	0.02 ± $1.0x10^{-3}$
C_2H_4	3.24 ±0.05	**C_2H_4**	0.43 ± 0.01
C_2H_6	0.61 ± 0.01		

Operating conditions for the PSR at propane composition in Colombia natural gas. C_3H_8 4 mol% - N_2 balance, S/C: 1, reaction temperature: 850 °C, catalyst: LSMN n= 2 reduced at 850 °C during 4 h (exsolved material)

C_3H_8 conversion [mol%]		98.30 ± 0.17	
C_3H_8 conversion rate [mmol min^{-1} g^{-1}]		4.42 ± 0.03	
H_2 production rate [mmol min^{-1} g^{-1}]		16.30 ± 0.59	
Outlet gas composition [mol%]		**H_2/CO ratio**	
N_2	77.61 ± 0.30	2.15 ± 0.05	
H_2	12.75 ± 0.29	**Selectivity**	
CH_4	2.07 ± 0.03	**CH_4**	0.20 ± $3.4x10^{-3}$
CO	5.93 ± 0.21	**CO**	0.58 ± 0.02
CO_2	0.85 ± 0.02	**CO_2**	0.08 ± $1.2x10^{-3}$
C_2H_4	0.64 ±0.06	**C_2H_4**	0.12 ± 0.01
C_2H_6	0.05 ± $1.0x10^{-3}$	**C_2H_6**	0.01 ± $1.0x10^{-3}$
C_3H_6	0.03 ± $4.3x10^{-3}$	**C_3H_6**	0.01 ± $1.3x10^{-3}$
C_3H_8	0.06 ± 0.01		

The amount of C_2H_6 and C_3H_8 in Colombian natural gas is much lower than CH_4, in SOFC operating conditions these gas will not correspond to the same S/C ratio than the majority compound; their dry gas saturation were performed at the same temperature as described in CH_4, keeping steam deficient conditions in agreement with the GIR concept.

Appendix N

XPS spectra of impregnated and exsolved material as synthesized (NiO/LSMO n= 1 and LSMN n= 2) and after reducing treatment at 850 °C during 4 h in diluted H_2 (Ni/LSMO n= 1 (Imp.) and Ni/LSM n= 1 (Exs.)).

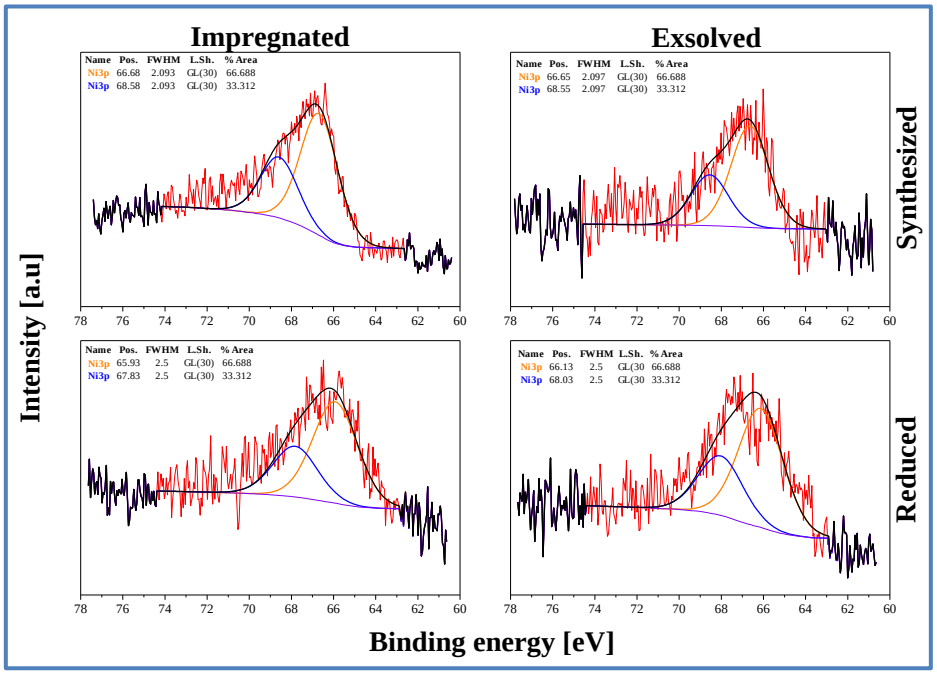

	Ni binding energy level 3p [eV]
$La_{1.5}Sr_{1.5}Mn_{1.5}Ni_{0.5}O_{7\pm\delta}$ (LSMN n= 2)	66.8
Reduced $La_{1.5}Sr_{1.5}Mn_{1.5}Ni_{0.5}O_{7\pm\delta}$ (Ni/LSM n= 1)	66.3
NiO/LSMO n= 1	66.9
Reduced NiO/LSMO n= 1 (Ni/LSMO n= 1)	66.2